Cold air pools over complex terrain

Bradley Colin Jemmett-Smith

Submitted in accordance with the requirements for the degree of
Doctor of Philosophy

The University of Leeds
School of Earth and Environment
April 2014

Declaration of Authorship

The candidate confirms that the work submitted is his own, except where work which has formed part of jointly-authored publications has been included. The contribution of the candidate and the other authors to this work has been explicitly indicated below. The candidate confirms that appropriate credit has been given within the thesis where reference has been made to the work of others.

The sensible heat flux data in Appendix C of the thesis, has appeared in publication as follows: Cold pool formation in a narrow valley, 2013, Vosper, S., Hughes, J., Lock, A., Sheridan, P., Ross, A., **Jemmett-Smith, B.**, and Brown, A. Quarterly Journal of the Royal Meteorological Society.

I was responsible for supplying data and interpretation of observations. The contribution of the other authors was: Vosper: Led the paper and did much of the data analysis as well as initial modelling. Lock: Technical advice on the modelling and interpretation of the results. Contributed comments on the manuscript. Sheridan: Contributed to the modelling and interpretation of the results. Brown: Contributed to the overall research plan, and interpretation of the results. Hughes: Conducted most of the model simulations and some of the data analysis and figures. Ross: Contributed to the overall research plan and structure of the paper. Discussion and interpretation of the results. Contributed to the writing of the paper.

Acknowledgements

I must start by thanking my supervisors Andrew Ross, Peter Sheridan and Stephen Mobbs, your input and ideas have helped me no end. I'd like to thank Ian Brooks for the critical feedback and additional guidance that he has given throughout my postgraduate years. I give further thanks to Andrew Ross, I am very grateful for the help, guidance and encouragement given over the many years of supervision. I extend my thanks to all Met Office and University of Leeds staff who took part in COLPEX, specifically John Hughes, Simon Vosper, Jeremy Price and Volker Horlacher.

Thank you David Tupman, Michael Holloway and Sarah Wallace, there's always time for just one, need I say more. Thank you to all my friends from ESS undergraduate education, with special mentions to James Clarke, Rachel Berman, Christopher Kelsey, Rob Whittleston and Lucy Clement, you're all exceptional people and I look forward to many more years of friendship.

Thank you room 11.121, both past and present; Matt Woodhouse, Sophie Cowie, Kathryn Nicklin, Bastiaan Brak, Ann-Kristin Koehler, Nick Dixon, Catherine Birch, Louis Garcia-Carreras and Phil Rosenberg, thank you all for your cheery banter and happy research faces. Special thanks to the 09:30 UTC ($\pm$10 mins ish) morning coffee group, past and present; Jim Watson, David Dufton, Kerstin Schepanski, Stephanie Fiedler and briefly Nathan. The short breaks provide great light conversations, a brief respite and strong coffee, whatever the weather. Thank you James Pope, Jenn Brooke, Cat Scott, Amber Leeson, Ryan Hossaini and to all my sporting buddies.

To all my family (including Mendhams and Holidays); June Jemmett (Mum), Colin Smith (Dad), Wesley Jemmett-Smith, Lawrence Jemmett Miller, Ross Smith, Chantel Smith, Wendy Mendham, Paul Mendham and Ricky Mendham, thank you for your continued support and interest that you have all shown throughout my studies. You all give me encouragement and drive. Special thanks must go to the better half of me, Stevie Mendham, your encouragement, patience, love and support is unfounded and I can never thank you enough.

Funding for this research was provided by a Doctoral Training Grant from the Natural Environmental Research Council and a CASE award from the Met Office.

Abstract

Cold air pools (CAPs) over complex terrain have rarely been investigated in hilly regions that are typical across the UK. This thesis gives a detailed account of CAP observations gained during the COLd air Pooling EXperiment (COLPEX), conducted in the Clun Valley region of Shropshire, England.

A short 9–month climatology study reveals that weak CAPs, defined as temperature inversions larger than 1°C across a valley depth of ∼170 m, occur 45% of all nights. Strong CAPs, defined as temperature inversions larger than 4°C, occur 12% of all nights. Strong CAPs are found to occur when the following "ideal" conditions are met: (1) mean sea level pressures >1029 hPa, (2) pressure gradients <1.5 Pa km^{-1}, (3) mean night-time ambient wind speeds <3 m s^{-1}, (4) mean night-time ambient wind directions from the N, (5) low values of F_{lw}, i.e., <0.80, where F_{lw} is the ratio of incoming to outgoing LW radiation. Using this criteria a case study investigation is conducted. The case study highlights the sensitivity of CAPs to nocturnal phenomena, which have rarely been documented before. The CAP is disturbed by; a gravity wave, an acceleration of the ambient wind (∼4.6 x 10^{-4} m s^{-2}) and by an increase in the ambient wind speed associated with a developing nocturnal low level jet (NLLJ). The final breakup of the CAP occurred some 3.5hrs after local sunrise and the NLLJ appears to play a role. Further investigations indicate that NLLJs occur during other CAP nights also.

A wind climatology study is conducted investigating the relationship between ambient winds and valley winds. Four forcing mechanisms for valley winds are proposed by Whiteman & Doran (1993), and these are; forced channeling, downward momentum transport, pressure driven channeling and thermally driven flows. Downward momentum transport preferentially occurs in less sheltered regions and forced channeling in narrow valley regions. The valley wind behaviour is notably different from day to CAP nights, with thermally driven down-valley winds prominent during CAP nights. Pressure driven channeling and daytime thermally driven flows (anabatic winds) are not seen.

High resolution model simulations of five CAP nights, show that drainage flows develop frequently. However, the timing, structure and strength of drainage flows differs from case to case. Two regimes stand out: (1) For low ambient wind speed nights the development of strong drainage flows leads to increased mixing in valley bottom regions, resulting in

weaker stability. (2) For high ambient wind speed nights, weaker drainage flows form initially, which result in stronger stability and stronger temperature gradients in valley bottom regions. This result suggest a negative feedback on near surface stability caused by stronger drainage flows that preferentially form during strong CAP nights. This highlights a potential misunderstanding of CAP characteristics in valleys. Here it is shown that stronger CAPs do not have stronger near surface temperature gradients.

An investigation into the affects of ambient wind on local sheltering/decoupling in valley bottom regions is conducted. Results suggest that quantifying the amount of sheltering/decoupling of valley bottom regions can be a useful indicative tool for understanding the timing and amount of cooling that is occurring during CAP formation. However, future attempts to use NH/U as a downscaling tool should endeavour to integrate other factors, such as; changes in the ambient wind, drainage flows, gravity waves and NLLJs.

Contents

List of Figures

List of Tables

Chapter 1

Introduction

Cold air pools (CAPs) in complex terrain are a well documented meteorological phenomena associated with stable boundary layers. Broadly speaking, research on stable boundary layers is lagging behind those of convective boundary layers, subsequently stable boundary layer phenomena are less documented and less well understood. The motivations for studying CAPs are numerous, but most importantly CAPs can have direct implications on road safety and health. CAPs can be associated with the heightened risk of prolonged cold weather, persistence of lying snow, frost, fog and pollution episodes. Mitigation through gritting roads or issuing hazard warnings depends on the ability of weather forecasting models to predict the occurrence of CAP outbreaks successfully. There is also some concern over temperature representation by climate models in complex terrain. An improved representation of CAPs in numerical weather prediction models may lead to an improvement in climate model representation of regional minimum and maximum temperature.

CAPs have been extensively investigated in the past using both numerical models and field observations; however, in the past these studies have focused on CAPs in large mountainous regions or basins. Few studies have been concerned with smaller scales, where valley or basin widths are less than a few kilometres and depths less than a few hundred metres, which are common in the UK. At this present moment in time there is a gap in knowledge of CAP occurrences over smaller scales and there remains a lack of understanding of CAP dynamics generally.

Current operational weather forecasting models cannot yet represent CAPs over these small scales without the aid of downscaling or parametrisation techniques. At this present moment in time these approaches are rather novel for complex terrain regions and there is a need to develop and test them further. By documenting the occurrence of CAPs over smaller valley regions and by improving our understanding of CAP dynamics generally, an improvement of CAP representation can occur. This knowledge can lead to the development of alternative forecasting methods.

The main aim of this research is to improve the knowledge and understanding of CAPs for a small system of valleys typical of the UK, through the use of field observations and model investigations. Specifically this will be achieved by:

1. Conducting a short climatology study of CAP occurrences (chapter 4):
   (a) When and how often do CAPs occur?
   (b) What synoptic conditions are favoured for CAP occurrences?
   (c) How do synoptic conditions affect/characterise valley winds across the Clun Valley region during the daytime, night-time and CAP nights?
2. A case study investigation of an "ideal" CAP forming night (chapter 5):
   (a) What is the timing and structure of CAP formation during the evening transition.
   (b) How does the CAP evolve during synoptic conditions that are "ideal" for CAP formation. Is the CAP evolution uninterrupted and insensitive to small changes in the synoptic conditions?
   (c) What is timing and structure of CAP breakup during the morning transition. What are the processes that lead to CAP breakup?
3. Comparison of multiple CAP nights (chapter 6). The emphasis is on understanding the structure, timing of formation, evolution and breakup of CAPs, for a number of CAP forming nights. This will give some perspective to the case study investigation conducted in chapter 5.
4. Understand the potential affects of wind direction on sheltering/decoupling of valley bottom regions during the early stages of CAP formation (chapter 6).

The structure of the remaining thesis is as follows. Chapter 2 provides a background of the relevant material and a review of the current literature. The majority of the analysis in this thesis is based on measurements obtained as part of a field campaign conducted in the Clun Valley region of Shropshire, England. The field campaign forms part of the COLd air Pool EXperiment (COLPEX). Chapter 3 gives a description of the field campaign, data processing and data products used. Chapter 4 presents the first results chapter, which is a small 9-month climatology study of CAP occurrences. Chapter 5 is a case study of an "ideal" CAP forming night, investigating the processes of CAP formation, evolution and breakup. Investigations in Chapter 6 are focused on understanding a number of CAP nights. Chapter 7 provides a summary of the findings from this thesis, highlighting the implications of the research findings and thoughts on future work.

Chapter 2

Background

2.1 Introduction

This literature review provides a broad understanding of the physical processes that define the occurrence of cold-air-pools (CAPs) in complex terrain, a subject within the field of boundary-layer (BL) meteorology. Initial discussions are focused on the diurnal cycle and the associated characteristics of the atmospheric boundary-layer (ABL) over complex terrain. Thereafter discussions include CAP formation, evolution, break-up, dependence on topography and external effects, both environmental and meteorological. CAP forecasting and the use of models to do so, are discussed as their use will undoubtedly contribute to future understanding of this phenomena.

2.2 ABL structure in complex terrain

At night the ABL structure is defined by the amount of radiative cooling of the surface and is characterised by the nocturnal boundary layer (NBL) (see figure 2.1), which is a common form of the stable boundary layer (SBL) (Fernando & Weil, 2010). The convective boundary layer (CBL) collapses with the establishment of the the NBL during the "evening transition". The break-up of the NBL occurs during the "morning transition" as the CBL grows. The NBL tends to be stably stratified over land surfaces and forms readily under clear skies and low synoptic wind speeds, which are more likely to occur during high

pressure situations. The existence of turbulence in the NBL is driven by shear instabilities – rather than convective/thermal instability associated with the daytime CBL – which are suppressed by buoyancy. With less turbulence in the system and therefore less turbulent kinetic energy (TKE), the vertical transfer of heat and water vapour are restricted. The vertical profiles of wind speed and potential temperature θ in the NBL are more complex than those seen in the CBL. Eddies are also much smaller and intermittent in the NBL than those seen in the CBL (Wyngaard, 1990).

Over complex terrain, the structure of the CBL and NBL are markedly different from that seen over flat homogeneous terrain. Representations of the diurnal cycle over flat and complex terrain are shown in figure 2.1(a) and 2.1(b) respectively. In each case there remains three distinct components; (1) the mixed layer or CBL, (2) the residual layer, and (3) the SBL. The residual layer is less turbulent than the well developed CBL and contains the former mixed layer air which is detrained from the surface as the SBL grows during the evening transition. The residual layer is often considered neutrally stratified with turbulence nearly equal in intensity in all directions (Stull, 1988).

The ABL over complex terrain (figure 2.1(b)) often leads to the development of thermal flows which modify the structure of the ABL so that it appears different to that seen over flat terrain (figure 2.1(a)). The thermal flows follow the pattern of the diurnal cycle with the development and break-up of the NBL. During the day, warm up-valley anabatic winds can develop, which remain attached to the slope due to two forces, a pressure gradient force pushing the column of air towards the slope and a buoyancy force driving the air parcel upwards. The resulting net force causes air to move approximately parallel to the slope with air being replaced from lower elevations (Reuten *et al.*, 2005).

Differences in valley geometry, narrow or wide valleys (Rotach & Zardi, 2007), irregularities in opposing slope angle and the orientation of the slope to the sun (Weigel & Rotach, 2004), all have impacts on both the characteristics of thermally driven flows and the ABL structure. At night during NBL conditions the opposite occurs to that seen during the day; in this instance down-valley katabatic winds occur, forced by the drainage of negatively buoyant cold air. In future these katabatic winds will also be referred to as drainage flows.

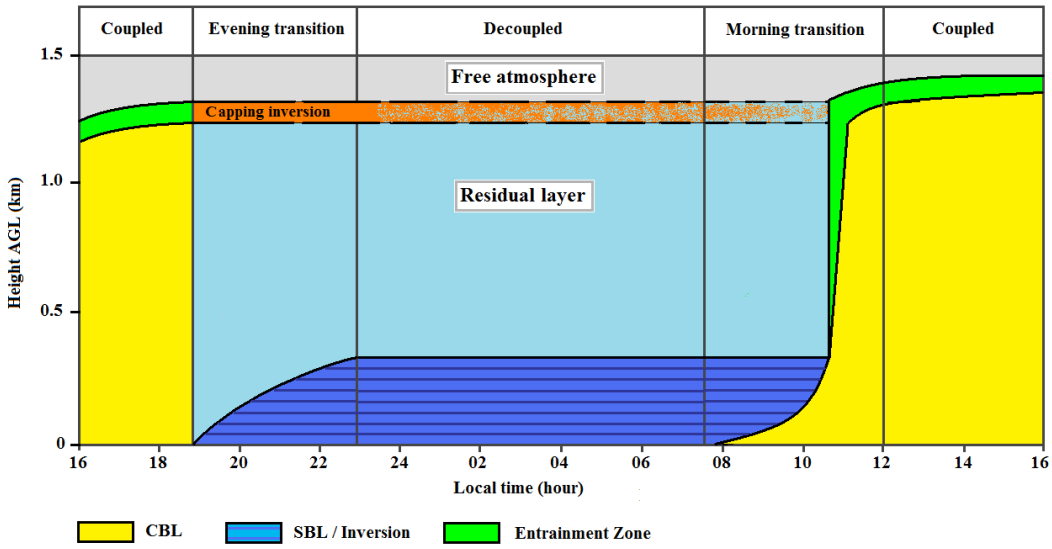

(a)

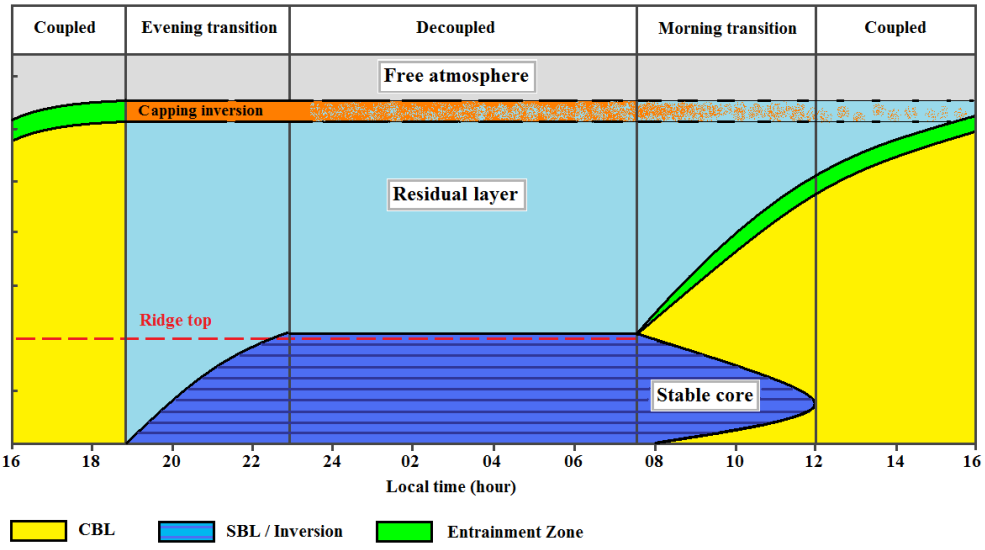

(b)

FIGURE 2.1: *Diurnal cycle showing the temperature and wind structure over; (a) flat terrain, and (b) complex terrain. Figure (a) is adapted from Whiteman (2000); Stull (1988) and figure (b) from Whiteman (2000).*

2.2.1 Temperature and humidity

From day to night the ABL characteristics of the surface energy budget can be very different and in turn this affects the vertical profile of air temperature, sub-soil temperature and specific humidity (M_r). The evolution and vertical structure of temperature within the ABL, over flat or complex terrain, is unvaried under cloudless or relatively clear skies,

responding to the upward (daytime) and downward (night-time) sensible heat flux (Whiteman, 2000). Typical ABL profiles of daytime and night-time θ, M_r and saturation mixing ratio (W_s) are shown in figure 2.2. Measurements are from the Clun Valley in Shropshire, England, taken on the 30 July 2009 during clear calm conditions when high atmospheric pressure prevailed. The daytime θ profile taken at 16:06 UTC is relatively uniform from the hill tops up to ∼1,200 m; above this there is an inversion with θ increasing with height. The valley atmosphere is slightly unstable in the lowest regions where warmer temperatures reside near the surface. This turbulent surface layer of the CBL (the lowest ∼10% of the ABL) is typically super adiabatic, i.e., a negative environmental temperature lapse rate (ELR) with height (Oke, 1987). The relatively warm near surface air is caused by turbulent exchange with the warmer radiatively heated surface below, which diminishes with time as the sun sets. During the night under SBL conditions a positive ELR occurs and temperature increases with height; this is shown in terms of θ in figure 2.2(a). In this particular instance θ increases with height in the ABL. Very strong near surface inversions can form, which are caused by mechanically derived turbulence that remove the heat from the lowest layers (Oke, 1987). The strong inversions that form within complex terrain such as dips, valleys or basins, are referred to as CAPs.

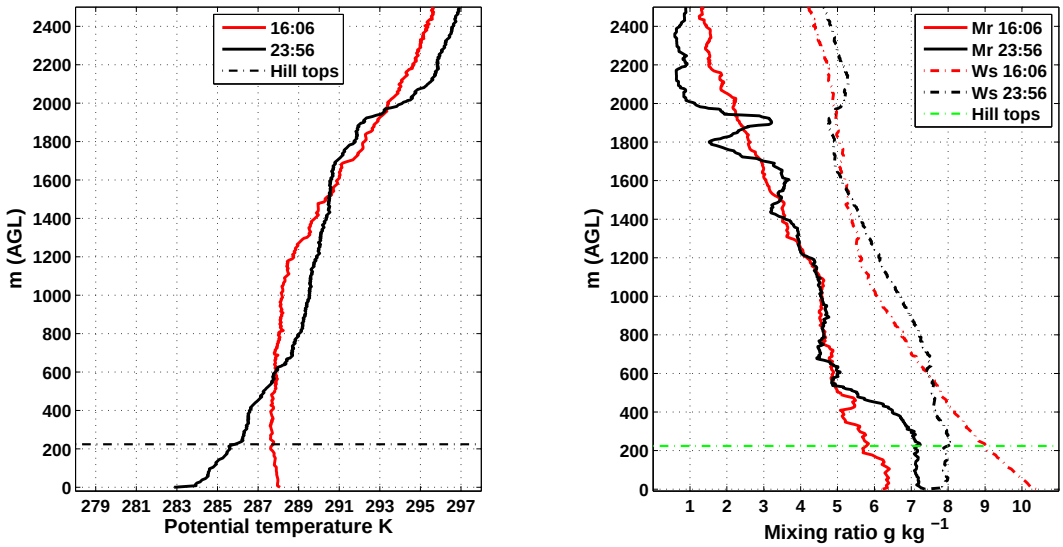

(a) (b)

FIGURE 2.2: *Radiosonde profile of; 2.2(a) θ, 2.2(b) water vapour mixing ratio (M_r) and saturation mixing ratio (W_s), during convective boundary layer (red) and nocturnal boundary layer (black) conditions. Radiosonde measurements taken on 30 July 2009 from Duffryn in Clun Valley, Shropshire, England, as part of the COLPEX field experiment (see Price* et al., *2011).*

The humidity of the ABL is driven by the exchange of moisture between the surface and the atmosphere. During the day the flux of moisture is upwards away from the surface and the vapour concentration decreases with height. An example of this daytime lapse in moisture is shown by the 16:06 UTC profile of M_r in figure 2.2(b). At night the moisture flux can be upwards but the magnitude of the flux is much reduced (Oke, 1987). Observations by Manins & Sawford (1979) show that M_r decreases with height through the night-time near surface inversion and the moisture flux is therefore upwards, in opposition to the sensible heat flux (H), which is in contrast to the usual daytime situation. At night the moisture flux can be towards the surface when dew fall occurs. As the NBL is established during the evening transition, the stability of the atmosphere in the lowest layers increases and the up-ward moisture flux in to the free atmosphere through entrainment is reduced with time (Oke, 1987). As the air cools its ability to hold moisture is reduced and the relative humidity (RH) can rise; this is clearly seen by the example in figure 2.2(b), where the difference between M_r and the saturation mixing-ratio (W_s) in the lowest 500 m AGL, is much larger during the daytime profile at 16:06 UTC compared to the night-time profile at 23:56 UTC. Therefore in the lowest regions RH is higher at night compared to the day, appearing almost saturated near the surface at night where the cooling is most prominent. Above 600 m (AGL) the θ and RH profiles remain similar during both the CBL and NBL periods, which is characteristic of a residual layer (see figure 2.1(b)).

2.2.2 Wind, atmospheric stability and flow

The near surface wind profile differs depending on the prevailing weather conditions and time of day. Example idealised profiles of wind speed are shown for stable, unstable and neutral atmospheres in figure 2.3. Under neutral conditions the near surface wind speed exhibits a classic logarithmic profile. The logarithmic wind speed profile is only valid during neutral stability; any deviation towards stable or unstable conditions will cause a departure from the logarithmic profile. A simple formula for the wind speed profile in a neutrally stratified atmosphere is given by equation 2.1 from Kaimal & Finnigan (1994).

$$\overline{u}(z) = \frac{u_*}{k}\, ln\Big(\frac{z}{z_0}\Big) \tag{2.1}$$

$$Ri_b = \frac{N^2}{(\Delta\overline{u}/\Delta z)^2} \tag{2.2}$$

$$N^2 = \left(\frac{g}{\theta_0}\right).\left(\frac{\partial\overline{\theta}}{\partial z}\right) \tag{2.3}$$

In equation 2.1 the mean wind speed $\overline{u}$ at height z is given where; z_0 is the roughness length or constant of integration at which $\overline{u}$ disappears when extrapolated downward; k is the Von Karman constant, a dimensionless constant which is used to describe the logarithmic velocity profile of a turbulent flow near a surface or wall, generally accepted to be 0.40 (Stull, 1988); u_* is the friction velocity, a characteristic for the amount of shear stress that is occurring.

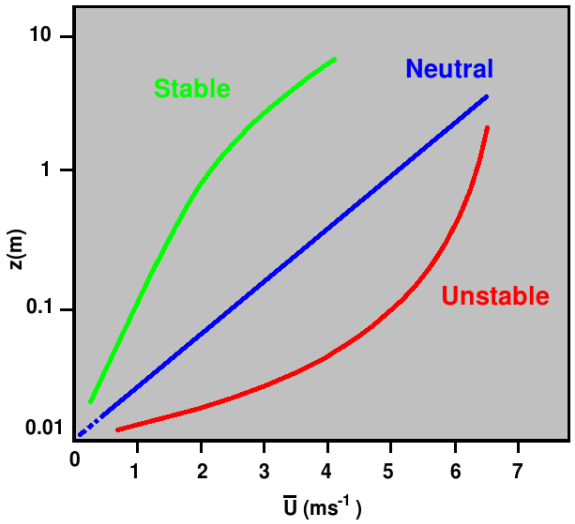

FIGURE 2.3: *Idealised wind profiles under the influence of stable (green), neutral (blue) and unstable (red) air masses. Diagram adapted from Kaimal & Finnigan (1994).*

The wind speed profile during strong CBL conditions is characterised by the unstable profile in figure 2.3. The occurrence of a strong near surface temperature inversion experienced during a CAP episode is characteristic of the stable wind speed profile shown in figure 2.3, which is decoupled from the ambient wind.

For the majority of stability studies conducted within the ABL, the stability is characterised using the Richardson number (Ri), a dimensionless number. The value of Ri is dependent on the amount of buoyancy and mechanically driven turbulence that is occurring – or the ratio of static stability to the square of the mean shear. Negative values reflect unstable stratification, where an increase in the wind speed gradient during the presence of a temperature gradient, increase the negative value. Positive values reflect stable stratification and are favoured by weak wind speed gradients, reducing the amount of shear between layers.

Ri can be defined in a number of ways, which include the flux Richardson number Ri_f, the gradient Richardson number Ri_g and the bulk Richardson number Ri_b. Ri_f is a measure for the rate of production of turbulent buoyancy to the production of turbulence by shear. Ri_g gives an accurate instantaneous measure of Ri. Ri_b is used as a preference to other methods close to the ground surface, particularly during low wind speed conditions (see Kaimal & Finnigan, 1994, p. 14). Ri_b is defined in equation 2.2, where; N is the Brunt-Väisälä or buoyancy frequency (equation 2.3) and $\Delta\overline{u}$ is the change in wind speed across the layer ∂z. In equation 2.3 g is the acceleration due to gravity (9.81 m s^{-2}), θ_0 is the potential temperature at z_0 and $\partial\overline{\theta}$ is the change in potential temperature across the layer ∂z.

The ABL is said to be neutrally stratified (figure 2.3) as Ri approaches zero (Oke, 1987; Kaimal & Finnigan, 1994). Ri can be used to measure the likelihood of Kelvin-Helmholtz (KH) instability. When wind shear is strong enough breaking waves can form: these occur when Ri is below a critical value Ri_c, often 0.25 (for inviscid flow). At this point the flow undergoes a transition from laminar flow to turbulent flow and Kelvin-Helmholtz instability can occur (Kaimal & Finnigan, 1994).

In BL meteorology the characteristic flow of an air parcel is often characterised by the Froude number F, which is a dimensionless number. One definition of F is given by equation 2.4, where U_0 is the characteristic velocity of approach flow at a given height, N is the Brunt-Väisälä frequency (see equation 2.3) and H_z is the characteristic height. H_z may be substituted for the length scale L_1 (Pal Arya, 1988). In equation 2.3 the Brunt-Väisälä frequency N is the natural frequency of internal gravity waves or lee waves (Pal Arya, 1988, p. 256).

$$F = \frac{U_0}{NH_z} \tag{2.4}$$

2.2.3 Turbulence in the SBL

When SBL conditions prevail it is often observed that turbulence is not continuous in space and time (Van de Wiel *et al.*, 2002). Patchy turbulence can occur in thin layers within the atmosphere and turbulent bursting can cause sporadic vertical mixing, which contradicts the expressions of Monin-Obukhov (MO) similarity theory that assumes the SBL is continuously turbulent in space and time, with no gaps or patches of non-turbulent

air (Stull, 1988). Furthermore Mahrt (2008a) states 'that the bulk formulation for surface fluxes based on surface-layer similarity theory is found to be a poor approximation for weak-wind stably-stratified conditions', where turbulence is typically weak and intermittent.

The large wind direction shifts during weak large-scale flow present a serious problem for predicting dispersion since the variation in wind direction during these 'light and variable' conditions are not predictable and their physical causes are usually unknown (Mahrt, 2008b). Observations by Moraes *et al.* (2005) of wind at valley bottom locations, found that weak SBLs still exhibit MO similarity; however, MO similarity rules do not apply when either windy or calm conditions occur during wind directions above the valley that are perpendicular to the valley axis. For windy conditions, rapid distortion of the flow permits local equilibrium – local equilibrium occurs when there is a balance between turbulence production and dissipation – rapid distortion occurs when the mean flow changes rapidly, and local equilibrium is impossible. For calm conditions the turbulence intensities were too small for MO similarity theory to appropriately describe the turbulent characteristics. When the wind directions above the valley were parallel to the valley axis MO similarity rules are met.

This global intermittent and discontinuous turbulence causes changes in the mean evolution of the near-surface temperature and wind speed, which may result in oscillatory type behaviour and large negative heat fluxes during clear nights (Van de Wiel *et al.*, 2002). This can lead to difficulties in closing the surface energy budget, which is integral for understanding both SBL and CAP dynamics (Mahrt, 2008a).

The small scale intermittent turbulence can occur as numerous narrow zones of shear with uncertain relationship to the main coherent structures (Mahrt, 1989). It is speculated that in non-turbulent SBLs, wind shear can increase due to the dynamic forcings and lack of mixing: this shear can eventually become strong enough that when a critical point is reached (i.e., Ri crit $= 0.25$), turbulence is initiated. This intermittent burst is enough to cause some level of vertical mixing of momentum and heat, thus leading to a weakening in shear, suppressing the turbulence until it can no longer occur. Such a pattern can continue with intermittent bursts of turbulence (Stull, 1988). Even with weak sporadic and patchy turbulence within a SBL, over long enough time intervals the flow-state can be transferred

throughout the BL depth and over a long period of time the turbulence may seem to be acting as a single entity rather than a group of decoupled layers (Stull, 1988).

2.2.4 The surface energy budget

The surface energy exchange is a combination of the soil heat flux (Q_G), the sensible heat flux (Q_H, in future this will also be referred to as H), the latent heat flux (Q_E) and the total radiative heat flux (Q_R), which combined form the surface energy balance (Q^*) shown in equation 2.5 (Oke, 1987). All of these surface exchange elements strongly affect CAP formation, evolution and break-up by modifying the surface temperature. A net divergence of these terms will lead to a surface temperature decrease (cooling) and a net convergence will lead to a surface temperature increase (warming). In equation 2.5 all positive values are fluxes toward the surface and away from the ground or atmosphere (Whiteman *et al.*, 1989b). These fluxes vary with time and have a strong diurnal signature due to the initial energy supply of long wave (LW) and short wave (SW) radiation. The daytime net all-wave radiation (Q_R) is shown by equation 2.6 (Oke, 1987).

$$Q^* = Q_G + Q_H + Q_E + Q_R \tag{2.5}$$

$$Q_R = SW\downarrow - SW\uparrow + LW\downarrow - LW\uparrow \tag{2.6}$$

$$Q_R = LW\downarrow - LW\uparrow = LW^* \tag{2.7}$$

$$LW\uparrow = \epsilon_0 \sigma T^4 + (1 - \epsilon_0) L\downarrow \tag{2.8}$$

The net all-wave radiation at night does not include terms for SW since there is no SW radiation supply. This new term is shown by equation 2.7, where the resultant LW^* is the net LW radiation (Oke, 1987). LW radiation is the largest and most consistent supplier of energy to valley ecosystems over a 24hr period, where the LW radiation emitted by ecosystems is the largest of all averaged radiative fluxes (Whiteman *et al.*, 1989a). The LW radiation at the surface is governed by the surface temperature and emissivity, as represented by equation 2.8. When $\epsilon_0 = 1$ the surface acts as a full radiator. LW in this case is the amount of reflected LW radiation away from the surface (Oke, 1987). Topographically induced temperature differences at night primarily depend on the LW radiation balance

and the degree of turbulent mixing, i.e., the sensible heat flux H (Bootsma, 1976). Investigations by Whiteman *et al.* (1989a), of Colorado's deep semi arid Brush Creek Valley (650 m depth), show that more exposed ridgetop sites, which have unobstructed views of the sky, had a higher average positive net radiation during the day and a higher average negative net radiation during the night than the valley stations.

2.3 Cold-air-pools over complex terrain

The occurrence of CAPs can have impacts on the environment, health and economy. CAPs form under stably stratified conditions with little turbulence, which inhibits CBL growth. CBLs, when present, help mix-up and transfer both pollution and moisture out of the valley into the free atmosphere above, which otherwise remain trapped by valley circulations during SBL conditions (Whiteman *et al.*, 1989b). Without this process any pollution or moisture within the CAP will undergo limited dispersion and can result in severe pollution episodes (Whiteman *et al.*, 2001). Aerosols and other pollutants emitted at night will rise because of their thermal buoyancy, but the rise will be inhibited by the stable stratification. During winter, stable conditions are more frequent, therefore heightened risk of both CAPs and pollution episodes increase (Savov *et al.*, 2002).

Whiteman *et al.* (1989a) emphasise the relevant stress that is put on ecosystems by CAP events that initiate frost during clear nights. CAPs can lead to delays in the melting of snow and the break-up of ice on rivers, which can affect transport networks (Whiteman *et al.*, 2001). Another dangerous hazard for traffic obstructions may occur because of freezing rain, which often accompanies wintertime warm front movements when CAPs keep the low-level temperatures below freezing while positive temperatures exist above (Zängl, 2005b).

The variability of low summer night temperatures is of crucial concern for the survival and progress of young trees (Lindkvist *et al.*, 2000). Furthermore, vineyards located in regions at the limit of viticulture, are particularly vulnerable to frost damage that can be caused by CAP events, this is a particular concern during early spring after bud burst (Madelin & Beltrando, 2005).

2.3.1 Previous field experiments

Studies within the scale of micrometeorology have always relied heavily on field experiments in order to learn more about BL processes and phenomena (Stull, 1988). Many field experiments focused on SBLs and CAPs have been conducted before, in an array of geographical locations, different types of topography and spatial scales. However, most studies have been conducted in large mountainous regions. Some examples include; the study by Clements *et al.* (2003) of the Peter Sinks Mountain Basin in Utah, USA; an investigation of spatial and seasonal variations in temperature lapse rates across the Italian and Austrian Alps by Rolland (2003); investigations by Whiteman *et al.* (1999) of the Colorado Plateau Basin; and the Stable Atmospheric Boundary-Layer Experiment in Spain (SABLES 98) by Cuxart *et al.* (2000). In fact very few field campaigns have focused on smaller valley systems where valley widths can be less than 1 km, which are common in the UK. SBL experiments focused on scales less than 1 km include; the Meteor Crater Experiment (METCRAX) in Arizona, USA, by Whiteman *et al.* (2008); a study by Bodine *et al.* (2009) using the Lake Thunderbird Micronet in Norman, Oklahoma, USA; and tethered balloon investigations by Holden *et al.* (2000) of the Llanthony Valley in South Wales; however, none of these investigate a system of valleys. Two exceptions, which investigate temperature differences across a number of valleys, are; the field experiment by Gustavsson *et al.* (1998), in the Skaraborg County in Sweden; and an experiment using an instrumented car by Smith *et al.* (2010), in the county of Devon in south west England. Unfortunately both experiments lack a full array of instrumentation and have limited aerial coverage in terms of studying an entire valley system – both investigations are essentially one transect of instrumentation.

2.3.2 Governance of temperature

A general expression for the conservation of energy (q) is given by equation 2.9, where c_v is the specific heat of air at constant volume (718 J kg^{-1} K^{-1}), T is temperature and $p\partial\alpha$ is an expression for the work done per unit mass of air (specific work). In the atmosphere many of the temperature changes can be be approximated as they are adiabatic, this can be achieved using the equation of state shown by equation 2.10, where c_p is the specific heat capacity of dry air held at constant pressure (1005 J kg^{-1} K^{-1}), R' is the

gas constant for dry air (287 J kg^{-1} K^{-1}) and p is pressure. A common thermodynamic variable used in atmospheric science is potential temperature (equation 3.4), which can be used to estimate the temperature of an air parcel that has been subject to an adiabatic compression or expansion from an initial pressure p and temperature T, to a final pressure p_0, where $k = R'/c_p$ (Rogers, 1979, pp. 2–7).

$$\partial q = C_v \partial T + p \partial \alpha. \tag{2.9}$$

$$c_p \partial T = R' T \frac{\partial p}{p} \tag{2.10}$$

$$\theta = T \left(\frac{p_0}{p} \right)^k \tag{2.11}$$

In the absence of cloud cover, and ignoring any contribution from phase changes, the main components of the heat budget that contribute to a net change of an air parcel in terms of θ with time ($\partial\theta/\partial t$), can be summarised by equation 2.12, where $\partial\theta/\partial t_{adv}$ is the contribution from advection, $\partial\theta/\partial t_H$ is the contribution from the vertical heat flux (H) divergence, $\partial\theta/\partial t_{Rnet}$ is the contribution from the radiative heat flux divergence.

$$\frac{\partial \theta}{\partial t} = \frac{\partial \theta}{\partial t}_{adv} + \frac{\partial \theta}{\partial t}_{H} + \frac{\partial \theta}{\partial t}_{rad} \tag{2.12}$$

All terms in the surface energy balance (equation 2.5) are governed by the nature of the surface and the relative abilities of the soil and atmosphere to transport heat. By night the effectiveness of convection as a means to distribute energy is dampened by the atmospheric temperature stratification associated with the SBL (Oke, 1987). All the surface energy exchange elements shown in equation 2.5 strongly affect CAP formation, evolution and break-up (Barr & Orgill, 1989). The contribution of each term in equation 2.12 on the amount of cooling (warming) is likely to be site-specific depending on height, the underlying soil characteristics, the morphology of the surrounding topography and both local and atmospheric stability.

The total amount of cooling observed within a CAP at any specific site is largely determined by the amount of in-situ cooling (warming) that is occurring as well as the net cooling (warming) contribution by advection. The main in-situ contributors are the vertical heat flux divergence (H) and the net radiative heat flux divergence $\partial\theta/\partial t_{Rnet}$, although

in the lowest region closest to the ground, the net latent heat flux may be important when dew or frost deposition occurs providing a warming term; see section 2.3.5.

In the past a number of studies have investigated the radiative flux divergence of a layer, Garratt & Brost (1981) and Hoch *et al.* (2007) are two such examples. Using the net radiative flux of two opposing layers at heights z and $z+\Delta z$, the warming (convergence) or cooling (divergence) of a layer of air over time, caused by radiative properties alone, can be calculated from the principle of conservation of energy (Pal Arya, 1999). The net change in radiation across this layer gives the radiative flux divergence $\partial\theta/\partial t_{rad}$ (see equation 2.13). The net cooling (warming) resulting from the radiative flux divergence (convergence) of a surface layer can be referred to as the amount of in-situ cooling (warming) that the radiation budget contributes to the overall temperature change that is observed.

$$\left(\frac{\partial\theta}{\partial t}\right)_{rad} = \left(\frac{1}{\rho c_p}\right)\left(\frac{\partial R_N}{\partial z}\right) \tag{2.13}$$

2.3.3 Role of topography

The atmosphere of valleys and basins has higher ground-surface-area to air-volume ratios than equivalently deep atmosphere over homogeneous terrain and this has large implications on the surface energy exchange (Whiteman *et al.*, 2007). For example, a v-shaped valley which has planar sidewalls, has twice the air volume over a homogeneous plane surface with the same width and depth (Whiteman, 2000). The actual valley or basin surface-to-volume ratio is further enhanced by small-scale irregularities that are often present on complex terrain surfaces (Whiteman *et al.*, 2007).

Cold air accumulates at low points, such as valley bottoms, due to the fact that cold air is denser than warm air, i.e., negative buoyancy of the cold air causes it to sink. Generally steep and elevated slopes drain most effectively to form CAPs under clear skies and weak ambient winds (Neff & King, 1989). Despite the numerous variations in geographical parameters, Gustavsson *et al.* (1998) found that cooling in separate valleys within the same region after dusk is simultaneous, with no sign of cooling slower or faster in larger valleys.

A two year study by Bodine *et al.* (2009) looked at temperature and wind data using the Lake Thunderbird Micronet located near Oklahoma, USA. The micronet covered an

area 120×320 m, located in a region with patchy vegetation and gently sloped terrain – from a lake shoreline (south) to a small hill (north) – with a maximum elevation change of ∼25 m. The study showed that strong CAP events were frequently observed at this location. Temperature differences during CAP events were typically in the order of 3–4°C over elevation changes as small as 6 m (0.5–0.6°C m^{-1}). In this case the strength of the CAPs appeared to be much stronger than those seen in the study by Gustavsson *et al.* (1998), which was conducted over much larger scales.

Basins on the other hand are generally found to have minimum temperatures lower than those experienced in adjacent or nearby valleys (Clements *et al.*, 2003). Valleys produce their own local wind systems as a result of thermal differences on opposing slopes which can generate horizontal pressure and temperature gradients causing winds (Oke, 1987). In contrast basins lack an along-valley wind system, which can be a means of warm air advection in to the valley system and this allows the basin air to cool more rapidly since it is essentially decoupled from the free atmosphere above (Clements *et al.*, 2003). Large temperature differences between cooler and warmer regions in valleys have been recorded by Gustavsson *et al.* (1998) to be up to 15°C, these large temperature differences occur despite the fact that the topography in their study is described as moderate.

The ELR can be used as an indicator for measuring the strength of temperature gradients with height (°C km^{-1}). The ELR for temperature inversions associated with CAP events would appear negative, as apposed to daytime positive ELRs. In complex terrain ELRs can be extremely variable, whereby the local ELR on sloped terrain is affected by radiative and turbulent heat fluxes modifying the temperature structure, which therefore differ from the free atmosphere depending on the time, day or night (Barry, 2008). A long term study by Rolland (2003), comparing temperature measurements with height using linear regression, looked at the variability of ELRs in several valley type regions across Northern Italy using 269 observation sites. Variations in ELRs proved to be strongly regional within valley systems. During nocturnal hours the differences in minimum temperature gradients are strongly associated with CAP events. These diurnal variations in surface temperature have been further defined by Mahrt (2006). Findings by Mahrt (2006) suggest that temperature gradients are larger on sloped terrain surfaces with weaker down-valley slopes, which have a favoured tendency for CAP formation than sloped surfaces on isolated and exposed hills.

The orientation of the valley is also important for solar radiation influences and therefore the surface energy budget. Direct solar radiation can play a key role in the formation of micro-climates in valley systems, as apposed to diffuse radiation from either the sky or reflected from the surrounding terrain. Generally the strength of the incoming solar radiation is much stronger than the diffuse radiation, which changes very little from site to site. The direct incoming solar radiation is predominantly a vector quantity with strong contrasts generated by the difference in the orientation and angle of a slope in relation to the direct beam of light (Whiteman *et al.*, 1989a). The direct solar radiation can therefore have consistent long term (vegetation differences) and short term (differences in the surface energy budget) effects on the terrain that result in differences in the surface energy budget across a valley, this in turn affects diurnal temperature cycles on sloped surfaces and can produce lateral density gradients that drive local circulations within a valley/basin affecting the formation and evolution of CAPs (Barr & Orgill, 1989).

Theoretical calculations by Whiteman *et al.* (1989a) show that a south-facing slope of $30 - 50^{o}$ would receive roughly 35% more radiation than at ridge top (in the northern hemisphere). Investigations by Whiteman (1982) investigated the relationship between total radiation and sage brush ecosystem in a valley setting with results showing that the radiation balance is characterised by an excess of SW radiation gain over a 24hr period, with LW loss amounting to 109 Wm^2. This net all-wave radiation excess must therefore be balanced by non-radiative fluxes, i.e., the surface energy balance; see equation 2.8 (Whiteman, 1982).

The amount of incoming solar radiation is the key in determining the possibilities for temperature variations to develop during the day. The incoming solar radiation can be calculated using equation 2.14 on a homogeneous flat surface, the variation between a flat and sloping surface can be calculated combining equation 2.14 with equation 2.15 (Bogren *et al.*, 2000b). In (2.14) I is the intensity of the direct solar radiation, α is the solar elevation and D is the diffuse solar radiation from clear sky, clouds and other objects. In equation (2.15), θ is the angle between direct-beam and a normal to the slope surface (Bogren *et al.*, 2000b).

$$S_0 = Isin\alpha + D \tag{2.14}$$

$$S = S0cos\theta \tag{2.15}$$

It is easy to understand how a valley system, with numerous tributary valleys orientated at different angles, will have an energy budget with much more local variations than a basin or crater.

Land use types have strong effects on the SBL locally through the existence of different density gradients and ground friction seen from site to site. Furthermore the land type can affect the ground heat capacity, conductivity and evapotranspiration. This can lead to local pressure gradients and subsequent horizontal circulations, which are particularly prominent during low wind speed conditions. Stable stratification is also stronger over deforested land than over forested areas. Over regions of water near-neutral conditions can persist late in to the evening (Fernando & Weil, 2010). Relatively small differences in soil moisture can also affect local circulations over flat and complex terrain as illustrated by Ookouch *et al.* (1984).

2.3.4 CAP formation and evolution

Temperature patterns of CAP formation within a valley or basin system often reoccur from one occasion to the next (Gustavsson *et al.*, 1998). The development of the temperature pattern with time is highly dependent on the shape and width of the topography type, i.e., large enclosed basin or elongated valley system. Observations by Clements *et al.* (2003) of the Peter Sinks Basin in Utah, USA, observed a CAP that had fully developed to the rim of the basin within two–three hours following sunset. Gustavsson *et al.* (1998) also noted the rapid development of temperature differences between hill top and valley bottom in more modest terrain in the county of Skaraborg. Observations by Gustavsson *et al.* (1998) are shown in figures 2.4 and 2.5. Their study, in more modest terrain, investigated a valley measuring 700 m bottom width, 3030 m top width and 88 m depth, in the county of Skaraborg, Sweden, from 11-12 April 1994. Figure 2.4 illustrates the lateral extension of the CAP development with time after sunset. Within 1 hr of sunset the differences in temperature varied from a maximum of 7.8°C to a minimum of 3.3°C. Under ideal synoptic conditions for CAP occurrence, cooling starts soon after sunset with the cold air building up from the valley floor. As the CAP continues to grow it spreads out laterally up the slopes with the isotherms of θ parallel to the valley floor (Gustavsson *et al.*, 1998), as illustrated by figure 2.5.

CAPs without interruption by either increasing wind speed, incoming cloud, or fog, can be maintained throughout the night and temperature differences from peak to basin can continue to grow until sunrise in this case; however, the increase in temperature gradient is much reduced when compared to the initial formation at sunset (Gustavsson *et al.*, 1998), as seen in figure 2.5.

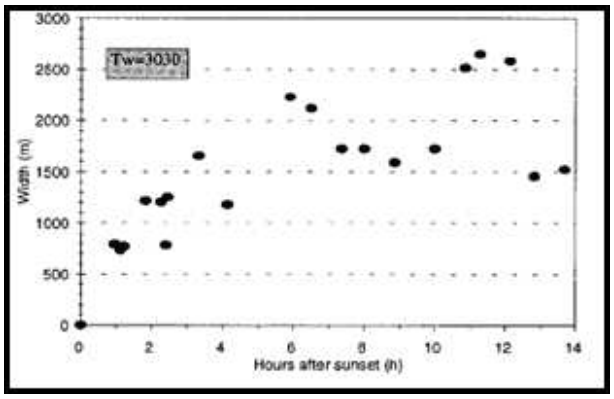

FIGURE 2.4: *Figure from Gustavsson* et al. *(1998) shows the width in metres (m) of the cold pool as it grows up the valley sides with time in hours (h), (Valley top width = 3030m)*

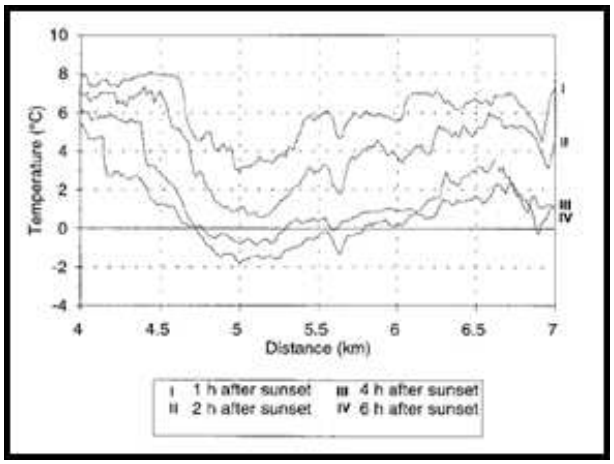

FIGURE 2.5: *Figure from Gustavsson* et al. *(1998) shows 2 m temperature (^oC) evolution along the valley floor (km) at time intervals of; (i) 1 hr, (ii) 2 hr, (iii) 4 hr, and (iv) 6 hr, after sunset.*

CAP formation, in both basin and valley terrain types, occurs shortly after sunset. Depending on time, location and the stability of the atmosphere, CAP formation tends to be associated with either the drainage of cool air, in the form of drainage or katabatic flows, or caused through sheltering from the atmosphere above, with cooling occurring in-situ with little or no horizontal advection of cold air. Both of these regimes can occur

simultaneously or independent from one another. Drainage of cold air from above and in-situ cooling are dependent on many factors, including slope angle, temperature gradient, net radiation and the net surface energy budget, i.e., the sum of sensible, latent and soil heat fluxes. Both drainage flows and in-situ cooling are discussed further in the following sections.

2.3.4.1 Drainage winds

Winds that form as a consequence of cold dense air, which is then accelerated downslope by gravity are called drainage winds, gravity flows, slope flows, or katabatic winds (Stull, 1988). These type of flows have been observed and documented over a very long period of time. One of the first well documented studies was conducted by Heywood (1933), aptly titled 'Katabatic winds in a valley'. The basic driving force behind cold-air drainage flows to the bottom of valleys is the cooling of air by LW radiative flux divergence above a sloping surface. Rapid cooling of the air in contact with elevated slopes occurs around sunset following the shut down of the daytime sensible heat flux away from the surface. This air becomes negatively buoyant and is accelerated down the slopes towards the bottom of the valleys (Vosper & Brown, 2008). During the day incoming SW radiation causes the surface to warm, this leads to unstable sub-layers forming immediately above the ground on the sidewalls of basins and valleys, this leads to a positive heat flux away from the surface, which prevents the drainage of cold air from occurring (Barr & Orgill, 1989).

Investigations of the Great Salt Lake basin by Banta *et al.* (2004) showed that the timing of a down basin flow was sensitive to the large scale pressure situation. When a weak pressure gradient existed, local drainage flows were well developed. Drainage flows tend to be associated with weaker or more intermittent flows that occur over shallower sloped terrain than those that occur in steeper terrain types (Neff & King, 1989).

Manins & Sawford (1979) define a flow arising from local sustained cooling as a true katabatic flow. A flow, in part at least, of cold air drainage from an elevated plateaux or remote slope, is often referred to as a mountain wind as well as a katabatic wind or drainage flow. Over smaller scales, observations of mist and smoke from chimneys by Heywood (1933), suggest that drainage flows appear to start in the upper regions of the valley, such as near valley heads, rather than in hill sided regions (slope flows). From literature it

appears that katabatic winds and drainage flows tend to represent cold downslope flows that form on different scales. However, there is no clear definition between the two. In the following text, drainage flows will allude to smaller down-slope and down-valley flow winds in smaller valley systems. On occasions, when the author chooses to use the term katabatic winds/flows, this will be referred to instead. A review of observational work undertaken on small-scale katabatic winds is given by Poulos & Zhong (2008).

Observations by Manins & Sawford (1979) summarise the vertical structure of katabatic flows observed over a gentle slope (average slope 4.5°) in the Jeeralang Hills of Western Australia, into four distinct parts:

1. A skin flow no more than several metres deep in which the effects of surface stress are largely confined.

2. The major downslope-flowing layer – in their observations 40 m thick – characterised by an exceptionally strong thermal inversion, a maximum in wind speed and little directional wind shear. The maximum wind speed appears just above a strong near surface temperature inversion.

3. The mixed region, which is above the downslope-flowing layer outlined by 2. This is the intersection between the katabatic flow and the free atmosphere above. Its thickness is much greater than that of the surface shear layer 1. Within this region the wind direction changes.

4. The ambient air flow, which lies above the mixed region highlighted by 3. Manins & Sawford (1979) suggest that the katabatic flow is the region below the height where the wind direction changes, therefore includes regions 1, 2 and partly 3.

The strength of katabatic and drainage flows appear in part to be dependent on the scale of the topography in which it is formed, the slope angle, as well as the synoptic conditions that prevail at the time (Barr & Orgill, 1989). A climatology study of a recurring katabatic wind in Coats Land Antarctica by Renfrew & Anderson (2002), shows that the mean wind speed is 7.5 m s^{-1} at the steepest part of the slope (slope angle 5.5°) and 5.1 m s^{-1} where the slope angle is less (1.0°). Furthermore investigations by Kouznetsov *et al.* (2012), over a gently sloped (∼0.6°) glacier in Antarctica, show that the thickness of a recurring katabatic flow varied from a few tens to several hundreds of meters. The wind speed maximum

was observed to be as low as 5 m s^{-1}. The shallower and weaker katabatic flows were associated with stronger near surface temperature inversions (1 K/m) and smaller surface heat fluxes. Whiteman (1982) observed down-valley winds in the deep mountain valleys of western Colorado, which ranged in speed from 8–11 m s^{-1}. In contrast, observations by Heywood (1933), in a more modest valley located in the Cotswold Hills of the UK, noted that down-valley drainage winds rarely exceeded 1 m s^{-1}.

According to observations by Orgill *et al.* (1992) of multiple valleys in West Colorado, drainage flows are shallow at upper valley regions and large at lower valley regions. Smaller drainage flows merge with other drainage flows from other tributary valleys to form larger deeper flows. In the upper valley regions, the drainage flows appear to be related to the size of the source region and terrain channeling (Orgill *et al.*, 1992). According to Heywood (1933), flows appeared different in different tributary valleys, i.e., in one instance the flow appeared stagnant in the main NW–SE trending valley and appeared to block part of a deep katabatic flow that had formed in the N–S tributary valley. Furthermore, trees appeared to block these weak drainage flows (evidence from observations of mist and smoke from chimneys).

Haiden & Whiteman (2005) show that downslope flows over a low angle slope were deeper and stronger than those reported previously by other investigations, which tend to investigate steeper slopes and in many cases, slopes on the sidewalls of isolated mountains where the down-slope flows are not subject to the influence of night-time buildup of ambient stability within a valley. There are two main factors that drive the strength, depth and structure of cold air drainage flows on slopes in valley terrain, and these are; the reduction of the driving force behind the drainage flow and the erosion of the system that already exists (Holden *et al.*, 2000). The upper level of a drainage flow is very susceptible to breakdown, through turbulent mixing by its proximity to the free atmosphere, lack of terrain sheltering and generally weaker density gradients than within the valley. Additionally, drainage along upper slopes, where terrain shielding is minimal, is greatly influenced by the large-scale ambient winds (Gudiksen *et al.*, 1992). Under weak stability, strong along-slope increase of downward momentum flux and heat deficit can occur with a slight deepening of the katabatic layer (Haiden & Whiteman, 2005).

The initiation of down-valley drainage flows means that the air needs to be replaced by potentially warmer air above that sinks into the valley. The warm sinking, or advected

air, can act as a brake on the katabatic wind system and reduce the night-time cooling in a valley (Clements *et al.*, 2003). For complex terrain problems, where the valley meanders and is joined by tributary valleys, these drainage flows are likely to be important in terms of the redistribution of the cold air in a valley system (Vosper & Brown, 2008). Drainage flows can also weaken as the stronger down-valley flow expands and the temperature inversion in the valley grows and strengthens (Haiden & Whiteman, 2005). Drainage flows can be attributed to smaller warming/mixing events within valleys, and these are likely to be caused locally by one of the following; (a) local shear, (b) local pulsations, (c) local obstacle effects, or (d) the convergence or divergence of local drainage flows, as outlined by Banta *et al.* (2004). The continued growth of a CAP in a valley can lead to further pooling of elevated major tributary cool drainage flows entering the valley system, as shown by Neff & King (1989): their study in Book Cliffs, Colorado, shows that a neighbouring tributary, De Beque Canyon, had its own temperature inversion which would itself fill over several hours and later overflow a barrier.

If any factor were to reduce the net radiative cooling on adjacent slopes the breakdown of the cold drainage flows may occur and thus affect CAP evolution (Barr & Orgill, 1989). According to Orgill *et al.* (1992), wind erosion processes of drainage flows appear to be especially active when above-valley wind speeds exceed 5 m s^{-1} and accelerations exceed 4 x 10^{-4} m s^{-2}. Furthermore, Gudiksen *et al.* (1992) found that when up-valley ambient winds above 5 m s^{-1} occur, surface cooling was not able to develop and drainage flows were non existent. Observations by Heywood (1933) also observed that cold drainage flows were only observed when above valley winds were below 5 m s^{-1}. Coulter *et al.* (1989) show that there was increased drainage from a tributary valley when the wind direction was opposite to the drainage direction, than when the ambient wind was aligned with the drainage flow.

According to Gudiksen *et al.* (1992), other factors that can cause variable or disrupt drainage flow depths are; precipitation-evaporation effects causing non-radiative drainage events, wind shear above the valley, cloudiness, frontal passages and synoptic winds directed in the down-valley direction. Additionally Haiden & Whiteman (2005) highlight that small slope irregularities or curvature along slopes, which are unseen to most observers, can play an important role in flow changes. This is particularly important when investigating/predicting along slope flow variations. Comparison of observations to models

using point source data should be avoided, instead volume-averaged measurements, such as remote sensing technology, should be used for these purposes.

2.3.4.2 Sheltering effects and in-situ cooling

CAPs are known to occur within small valleys or local dips in more modest terrain; in this case it is likely that cooling takes place in-situ within the valley itself under sheltered conditions, being independent from the transport of cold air from elevated areas (Vosper & Brown, 2008). For continued in-situ cooling to occur, all turbulent processes must be suppressed with absolute atmospheric stability.

Drainage flows are shown to aid CAP formation (Barr & Orgill, 1989) and lead to their increased lateral extension during the night; however, evidence for a contribution to CAP formation by cold drainage flows could not be found in forested areas where flow is stagnant (Gustavsson *et al.*, 1998). The study by Gustavsson *et al.* (1998) investigated CAPs in moderate valley terrain, with elevations varying from 165 m to 240 m above mean sea level. Gustavsson *et al.* (1998) noted that the cooling in separate valleys occurred at the same time. Further to this, the investigation showed that the lowest temperatures recorded during CAP episodes occurred in the forested regions at the bottom of valleys. This led to the argument that in-situ cooling, in this case, was the dominant process for CAP formation where drainage of cold air from above appeared to play no role. Gustavsson *et al.* (1998) suggests that if CAPs are the result of the accumulation of drainage flow alone, they will have a considerably high speed to establish the large temperature differences recorded after sunset.

Observations by Whiteman *et al.* (2008) during the METCRAX field experiment, investigating CAP occurrences within the Meteor Crater in South Arizona, USA. During light synoptic wind speeds above the crater rim, soon after sunset they identified the existence of a shallow but particular strong super-adiabatic layer on the crater floor. The inversion developed over the following 2.5 hrs to a depth of 50 m, with especially strong cooling still persisting near the crater floor.

Another study by Clements *et al.* (2003) of the Peter sinks basin in Utah, gives an account of how both drainage flows and in-situ cooling through sheltering, are observed. Soon after sunset a cold down-slope flow become detached from the sidewalls of the basin and

ran down in to the centre of the basin and flowed over the top of a cooler dense sheltered layer: at this point there was a clear two-layer CAP structure formed by two dynamically different regimes. Weak horizontal winds within the basin cause weak advection into the basin from its surroundings; however, the lowest elevations within the basin remain effectively isolated from the warmer air at the same elevation surrounding the basin, i.e., the cooling was in-situ only. After two hours the cold drainage flow had ceased but the CAP continued to grow vertically and horizontally until reaching the top of the basin, and at this point the CAP ceased to grow any further. It is presumed this halted due to cold air flowing out over the basin rim. Similarly Whiteman (1982) also found that the inversion top associated with valley systems, was also lower than the surrounding ridge tops.

This sheltering mechanism for CAP formation relies on the reduction of turbulent mixing of cold near-surface air with the warmer air aloft, which under clear conditions leads to a higher rate of cooling of the air that is in contact with the radiatively cooling surface (Vosper & Brown, 2008), this shelter can be in the form of topography, e.g., narrow valleys, small hills, or in the form of vegetation, such as tree strands or lines of trees (Lindkvist *et al.*, 2000). The cooling mechanism that occurs in forested areas is caused by the trees preventing any turbulent mixing between the surface cooled air and the warmer air aloft, i.e., there is a reduction in the amount of turbulence generated by wind shear. The forested areas are therefore less sensitive to more turbulent winds than the open air, and this process may in fact be operating to cool the air at the bottom of the forest canopy, despite the fact that the canopy shelter prevents LW radiation loss from leaving the system (Gustavsson *et al.*, 1998).

Holden *et al.* (2000) used a gradient Richardson number (Ri_g) to observe flow regimes within a valley during neutral and stable conditions. Their observations showed that under fairly neutral conditions Ri_g was high (Ri_g >0.25) and the flow would remain attached to the valley as it would under weakly stratified conditions, but when more stratified conditions occurred, small values of Ri_g (Ri<0.25) were observed, turbulence was reduced and flow separation occurred from the mean flow aloft. These results suggest that under more dynamically stable conditions flow separation is favoured and drainage flows occur within the valley, i.e., the valley becomes decoupled from the ambient flow aloft.

Using numerical simulations, Vosper & Brown (2008) investigated the inverse Froude number (F_r) dependence on flow separation in an idealised valley (see equation 2.16), with a width and depth of 1 km and 50 m respectively. Their 2D model study, using the Met Office BLASIUS model (see Wood & Mason, 1993), showed that a sheltering mechanism in moderate terrain is capable of forming CAPs that formed temperatures much less than that compared to other regions outside the valley; reflecting the results from Gustavsson *et al.* (1998) using observations. The most intense CAP regions – in terms of the difference in θ between valley top and valley bottom – are directly related to the non dimensional valley depth F_r (see equation 2.16); however, beyond a critical valley depth ($F_r = 0.35$–0.64) the CAP intensity remained unchanged (see figure 2.6).

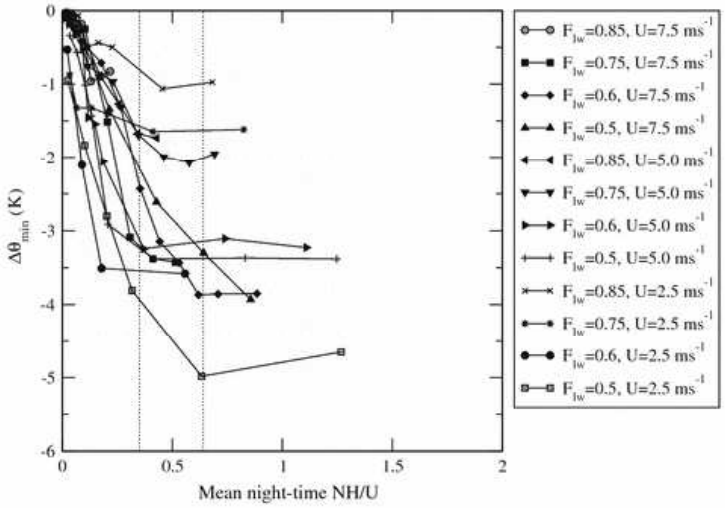

FIGURE 2.6: *$\Delta\theta_{min}$ data are plotted against the mean nightime non-dimensional valley depth $\widetilde{N}H/\widetilde{U}$, for a various simulations with a range of F_{lw} and U values. Values of $\Delta\theta_{min}$ for the case $U = 2.5\ ms^{-1}$ and $F_{lw} = 0.5$, are divided by two. Figure from Vosper & Brown (2008).*

$$F_r = NH/U \tag{2.16}$$

Two dimensional numerical simulations of CAPs by Vosper & Brown (2008) show that the sheltering mechanism leads to a divergence in the sensible heat flux (H) in the lowest regions of the valley, which promotes a rapid cooling of the air adjacent to the ground. The small amount of downward sensible heat flux is unable to compensate for the radiative

cooling surface, therefore adding to the surface cooling. Vosper & Brown (2008) characterised this layer at the bottom of the valley as a decoupled slack flow, which has little or no influence from the ambient wind above.

Furthermore, investigations by Sheridan *et al.* (2013) applied the 2-D model findings by Vosper & Brown (2008) to observations of multiple CAP episodes. Sheridan *et al.* (2013) looked at the observed strength of CAPs during the COLPEX field experiment that took place in a system of valleys in moderate terrain (valley depths ∼200 m, peak to peak widths of ∼1,000–2,000 m). The observational study by Sheridan *et al.* (2013) proved to be relatively consistent with the findings of Vosper & Brown (2008). In both studies, Vosper & Brown (2008) and Sheridan *et al.* (2013) show that the variability in the wind speed (U) and the radiative conditions (F_{lw}), mostly determine the cold pool strength. Additionally, the results by Sheridan *et al.* (2013) suggest that decoupling occurs when a critical value of F_r is close to 1, rather than between 0.35–0.64 as found by Vosper & Brown (2008); however, in both investigations a range of critical values of F_r were found for various combinations of F_{lw} and U (see Sheridan *et al.*, 2013, figure 10).

Sheridan *et al.* (2013) highlights a number of other factors that may affect F_r that are not accounted for, including drainage flows, the effect of external wind, the quality of UK4 forecast data and topographical differences between the two measurement sites used in their study.

2.3.5 Effects of moisture, cloud, frost, fog and snow

Clouds have major effects on temperature within valleys and basins. The type, elevation, time and length of cloud existence, strongly affect whether they have a negative, positive or neutral effect on CAPs. The amount of LW radiation emitted (LW_{up}) and received (LW_{dn}) at the surface is controlled by the amount and type of cloud cover and the concentration of CO_2 and water vapour in the atmospheric column above. The presence of atmospheric moisture increases LW_{dn} radiative flux, thus decreasing the net radiation and the subsequent cooling rate at the ground surface (Gudiksen *et al.*, 1992).

Bogren *et al.* (2000b) illustrate how maximum nocturnal air temperature between valley top and bottom, changes as a as a function of cloud cover, as shown in figure 2.7 (for calculations see Bogren *et al.*, 2000b, pp. 155). Barr & Orgill (1989) suggest that middle

and high clouds have little effect on CAPs in the form of drainage flows, as they are maintained by enough long-wave radiation loss. Additionally, Bogren *et al.* (2000b) find that a sky filled by at least 6 octas had a significant affect on the possible development of temperature variations across topography at night.

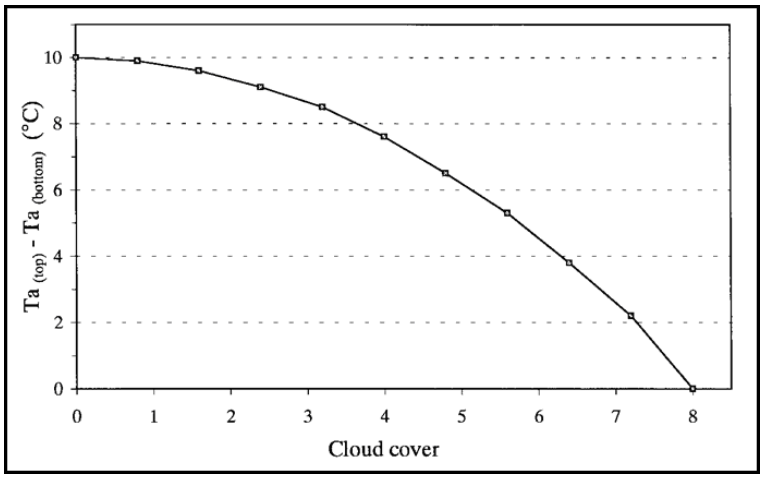

FIGURE 2.7: *Calculated effect of cloud cover on the maximum nocturnal air temperature potential difference as a result of cold air accumulation. Figure from Bogren* et al. *(2000b).*

During cloudy, windy conditions, the counter radiation and high percentage of diffuse radiation can lead to a smoothing of local temperature variation. Furthermore, the wind itself will aid in this process by increasing turbulence (Lindkvist *et al.*, 2000). These conditions will either destroy an already existing CAP or inhibit the formation of one. The radiative effects of high and mid level cloud on the surface energy budget are very complex and have a high amount of uncertainty. Further discussion on this subject is beyond the scope of this review: some investigations into radiative cloud effects on topography are discussed further by Barr & Orgill (1989); Bogren *et al.* (2000b); Whiteman *et al.* (2001).

Moisture condensation at the ground and the accompanying latent heat release has a number of practical implications such that they affect the forecasting of minimum temperatures (Whiteman *et al.*, 2007). The effects of moisture and frost are very important when considering the effects that they can have on the surface energy budget (Barr & Orgill, 1989). These factors directly influence soil properties such as the thermal conductivity and diffusivity (Gustavsson *et al.*, 1998). Moisture processes at the bottom of valleys often lead to fog formation which will affect the radiative cooling and limit the surface to air temperature differences (Vosper & Brown, 2008). Dew-fall occurs when vegetation cools radiatively below the dew-point temperature of the adjacent air and the water vapour

condenses. The rate of dew deposition is tied to the rate of heat release (through the latent heat of vaporisation). The condensation of dew and the consequent release of latent heat reduce the total nocturnal cooling relative to a night with no dew (Whiteman *et al.*, 2007).

Water vapour may be added to the valley interior by drainage flows that cause draw down and advection of air from above. Stronger drainage flows may enhance the rate of condensation due to the introduction of new moisture in to the system (Whiteman *et al.*, 2007). Additionally, Gudiksen *et al.* (1992) made a correlation between the upper-level downslope wind speeds and the radiation levels.

Stagnation under stably stratified conditions can often lead to the buildup of aerosol concentrations, which can increase the risk of fog formation during mornings. The presence of fog and aerosol pollution can further reduce solar heating at the surface: this is important because the process can prolong the presence of CAPs after sunrise (Savov *et al.*, 2002). Whiteman *et al.* (2007) investigated CAPs in the Gruenloch Basin in Austria: they found that on two successive days, air confined inside the enclosed lower basin dried during the night as dew-fall and frost-fall occurred on the basin sidewalls and floor, and this deposition led to the releases of latent heat. Their calculations suggested that the latent heat release on these nights was 33% to 53% of the total sensible heat lost from the basin. If the air had been sufficiently dry that the night-time temperature falls did not reach the dew-point, no frost-fall would have occurred and the sensible cooling would have been substantially larger.

The presence of snow cover dramatically modifies the components of the energy budget. The high albedo of snow prevents much of the incoming SW radiation being absorbed in the snowpack, with little transfer of heat to the soil taking place when the snow pack is sufficiently thick. Fresh snow has a higher albedo than old snow, therefore less SW radiation is absorbed as the snow ages. Results by McKay & Thurtell (1978) show that during snow cover, neither latent heat nor sensible heat fluxes have a diurnal periodicity, which is the normal situation in non snow covered conditions during summer. Furthermore, the flux of heat into the snowpack is found to be a major component of the energy balance. Specifically, large sensible and latent heat fluxes are seen when cold air masses replace warm air masses. During these periods both the sensible and latent heat fluxes are greater than the net radiation, which results in a rapid loss of energy from the snow pack. The

net radiation was the controlling component of the energy budget during periods when the air mass was well established.

Results by Whiteman (1982) of the Yampa Valley in Colorado, US, show that inversion strength within valleys is increased with the presence of snow cover. As snow melt occurs, and the distribution becomes less homogeneous, north facing slopes are likely to retain snow cover for longer periods (in the Northern Hemisphere) and CAPs are likely to evolve and break up differently during these regimes (Whiteman, 1982).

During CAP events the persistence of lying snow or frost can be particularly localised and patchy in screened areas away from direct sunlight (Bogren *et al.*, 2000a) and wind sheltered locations (Gustavsson, 1995). A study by Lindkvist *et al.* (2000) used a numerical model to assess frost in an area of diverse topography and vegetation cover in the Southern Swedish mountains. This study concluded that more than 90% of the frost situations that occurred in the study period were due to radiation-type frost events, this variation being closely related to the terrain type during these situations with frost occurring most frequently in narrow valleys.

2.3.6 CAP Break-up during the morning transition

An important aspect of CAPs is understanding how CAP break-up occurs and what causes the contributing factors that lead to break-up, which is believed to be due to a number of mechanisms including surface heating induced turbulent fluxes (Whiteman, 1982) and upper-level wind speeds (Bogren *et al.*, 2000b). The understanding of CAP formation, evolution and break-up is not only dependent on the meteorological conditions such as stability, moisture, cloud and fog, but also on diurnal and seasonal meteorological cycles, i.e., in the UK high pressure systems are more dominant during the summer than in winter, therefore it can be argued that ideal conditions for CAP occurrence are more likely in the summer.

According to Whiteman (1982), inversion break-up in valleys follows three patterns of temperature structure. The first is characterised by an up-ward growth from the ground of a warming CBL and describes inversion behaviour over flat terrain. The second, seen during snow covered conditions, is accompanied by a warming of the valley atmosphere from the ground up, by the development of a CBL that is arrested once a height of between

20-50 m is obtained. The inversion is then destroyed as the top the NBL descends in to the valley. The third most common pattern seen, being a more generic case of the first and second patterns, is attributed by the continued growth of the CBL from the valley floor upwards and the continuous descent of the inversion top, this is shown in figure 2.8. At sunrise (t1) an inversion is present (CAP). Soon after sunrise (t2) incoming *SW* radiation warms the valley floor and slopes. By t3 the development of upslope anabatic flows are seen and the inversion top is beginning to be eroded. By t4 only a small inversion layer remains and anabatic flows have decreased. By tD the inversion layer is completely eroded and replaced by a fully developed CBL.

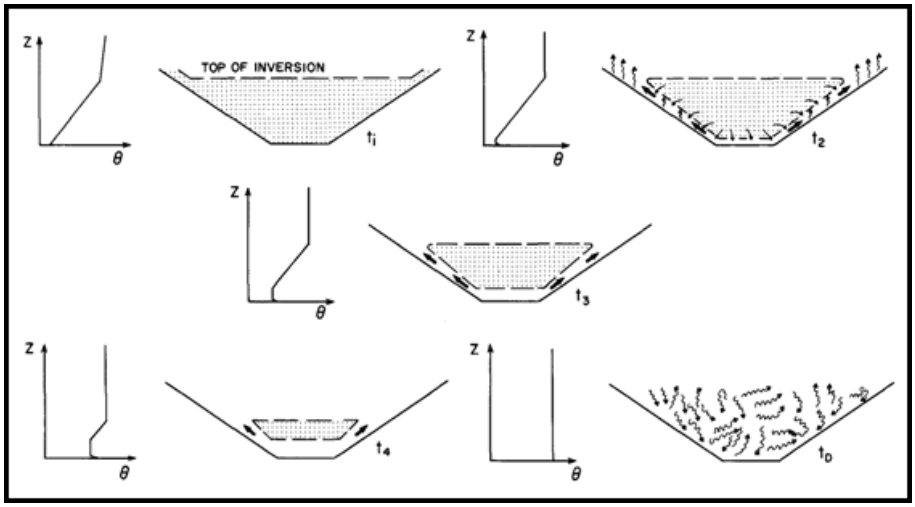

FIGURE 2.8: *Inversion destruction as outlined by Whiteman (1982). The order is from top left t1, to bottom right tD. Small plots shoe idealised θ profiles with height (z) AGL.*

Before sunrise the existence of a horizontal flow above the hill-tops can occur with a CAP forming in the valley or basin beneath. This flow is kinematically and dynamically possible, although in practice turbulent coupling is likely to occur at some point between the flows if strong winds are sustained after sunrise. This can lead to CAP break-up by the recirculation of air within the valley (Holden *et al.*, 2000). This process is known as turbulent erosion and removes the stable air layer by layer at the top of a CAP through turbulent eddies, which are generated by the wind shear between the weak intermittent stable air within the CAP and the stronger winds just above the stable transition layer at the top of the CAP. Another form of turbulent erosion can occur by warm air, caused by solar heating, advecting over the CAP top (Whiteman *et al.*, 2001). Turbulent forced mixing by strong winds at hill top level can also delay CAP formation as well as cause it to breakup (Clements *et al.*, 2003). These turbulent processes relate to the second CAP

break-up process outlined by Whiteman (1982). However, Zängl (2005a) suggests that CAP erosion by turbulent mixing from above plays a comparatively minor role in deep valley systems. Furthermore, findings by Zängl (2003) suggest that turbulent mixing can be important for shallow CAPs, particularly in basins having no significant outflow.

Tethered balloon observations of the Eagle Valley in the US by Whiteman (1982) illustrate the third process of inversion break-up (figure 2.8), which looked at the vertical wind profile of the valley in the region. During the night down-valley katabatic winds were present which differed greatly in speed from valley to valley. Shortly after sunrise the top of the inversion started to descend and the surface heat flux – initiated by excess sensible heat flux from increased short wave radiation (Whiteman *et al.*, 1989b) – caused up-slope anabatic winds to form within the CBL that grew over the side walls and with time along the valley floor also. At the same time down-valley winds are sustained within the remnant temperature inversion layer until it is fully destroyed, as seen in figure 2.9. Once this occurs a deep CBL is present in the valley and couples with the atmosphere outside the valley, at which point up-valley, up-floor and up-slope flows are difficult to differentiate in the fully developed CBL (Whiteman, 1982).

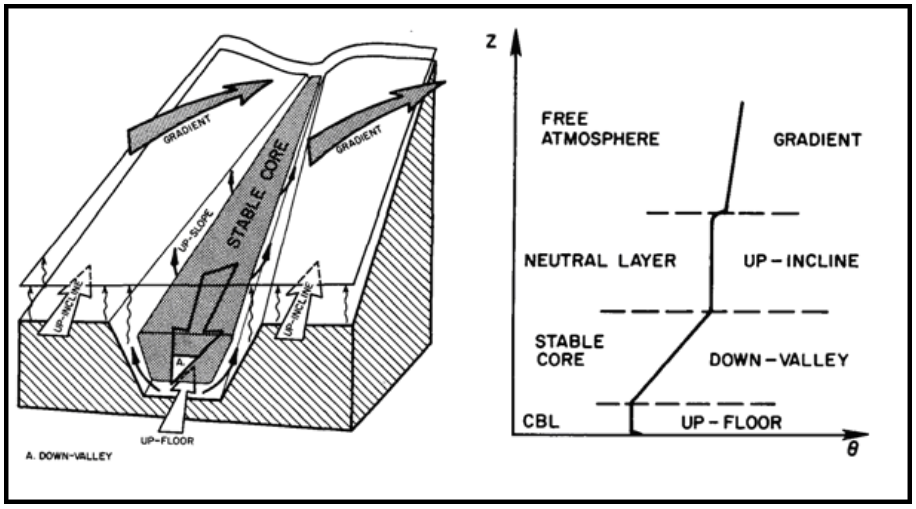

FIGURE 2.9: *Left shows the typical wind system development during mid-valley temperature inversion break up. Right illustrates the relationship between potential temperature (θ) and wind structure with height (z), during inversion break up. Figures from Whiteman (1982).*

According to Whiteman (1982) observations of twenty different locations saw temperature inversion break-up start to occur within 30-40 minutes after sunrise and the total break-up of CAPs varied between 3.5 to 5 hours. The average break-up time observed was

4hrs 35min. Considering both seasonal and topographic differences across the valleys, this difference was relatively small. Whiteman *et al.* (2001) gives an account where the first process of CAP inversion break-up occurs as outlined by Whiteman (1982). On this occasion the CAP break-up was initiated by the above-mountain geostrophic winds turning perpendicular to the crest of the mountain, this caused a strong hydraulic lee wave flow that caused warmer air to descend destroying the CAP, although there were remnants of cold air trapped for some time.

It should be noted that the three processes hypothesised by Whiteman (1982) are idealised examples of CAP break-up during the morning transition. In reality CAP break-up is likely to be more complex and may not follow the processes outlined by Whiteman (1982). One example is given by Whiteman *et al.* (1999). An inspection of individual wind soundings of the Colorado Plateau Basin in the US showed that strong winds from travelling storm systems often penetrate into the upper levels of the basin, but do not often extend throughout the basin floor. Their findings suggested that the temperature inversion build-up and break-up in the Colorado Plateau Basin differs significantly when compared to build-up and break-up in smaller valleys and basins.

The existence of induced strong turbulent fluxes of energy (i.e. by solar heating at dawn) in a valley can also break down the temperature inversion layer of CAPs (Barr & Orgill, 1989). It is therefore clear that surface heat fluxes have strong effects on the wind profiles within valley systems also. Observations by Whiteman & McKee (1982) show that latent and sensible heat fluxes differ strongly across opposite sidewalls of a valley controlled by the time of day, orientation to the sun and the soil characteristics, the differences in these rates of heating and supply of moisture to the atmosphere between the two opposing slopes leads to horizontal temperature and humidity gradients that create cross valley circulations towards the warmer slope, this type of flow may induce shear and create turbulence which may lead to or enhance CAP break-up.

2.3.6.1 Effects of ambient wind on CAPs.

In the past a number of investigations have highlighted the importance of the above valley ambient wind on CAPs: these include Barr & Orgill (1989); Orgill *et al.* (1992); Iijima & Shinoda (2000); Whiteman *et al.* (2001); Bogren *et al.* (2000b); Vosper & Brown (2008).

Over a period of 88 days, Bogren *et al.* (2000b) looked at night-time minimum air temperatures between two stations with differing altitudes in the county of Älvsborg, one located at a hill top (station 1512), at 330 m above sea level (ASL) and the other at the bottom of a broad valley (station 1513), at 295 m ASL. The minimum temperature difference ($T_{a(top)} - T_{a(bottom)}$) is compared to the hilltop wind speed, the result is shown in figure 2.10. From their results it is clear that the development of air temperature difference between stations is very much dependent on the hilltop wind speed. In this instance inversions larger that 1°C did not occur when the wind speed exceeded 2 m s^{-1}.

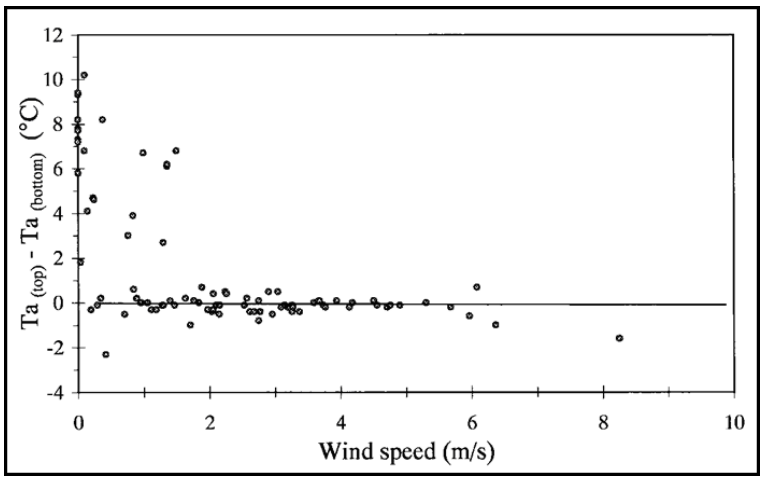

FIGURE 2.10: *Observed difference in minimum night-time air temperature between the hilltop (station 1512) and valley bottom (station 1513) over versus mean night-time hilltop wind speed. Figure from Bogren* et al. *(2000b).*

Orgill *et al.* (1992) shows results gathered as part the Atmospheric Studies in Complex Terrain (ASCOT) field experiment, conducted across the Mesa Creek Valley and surroundings. Valley widths were up to 10 km and valley depths up to 1500 m. It was noted that whenever winds exceeded 5 m s^{-1}, even well established drainage flows, particularly along the upper slopes, were significantly affected. One dimensional model investigations suggested that the stronger the ambient flow is, the more difficult it is to maintain the temperature inversion, therefore there is a greater tendency to override the nocturnal drainage flows.

Investigations by Iijima & Shinoda (2000) of a hollow in a subalpine area of the Yatsugatake Range Japan, found that the majority of inversions formed when the mean night-time wind speed at the local mountain top was between 0–6 m s^{-1}. However, on rare occasions inversions were seen to occur for mean night-time winds exceeding 6 m s^{-1}, and in this

instance Iijima & Shinoda (2000) suggest that this may be related to a high-level inversion created by anticyclonic subsidence (Yoshino (1972) cited Iijima & Shinoda (2000, p. 11)).

Results by Barr & Orgill (1989) suggest that an up-valley ridge wind speed above 8 m s^{-1} (tower Froude number $0.3 - 0.6$) is sufficient to totally override any drainage conditions present thus hindering any cold pool formation, although this research did not determine what the maximum cross valley ridge wind would be needed to eliminate the valley drainage wind (Barr & Orgill, 1989).

Model studies by Zängl (2005a) show that for a given valley geometry and a given strength of the ambient flow, the probability for persistent cold-air pools mainly depends on the ambient wind direction. In this study the maintenance of CAPs in the deep Alpine valleys, is favoured when the large-scale flow is towards the Alpine foreland. Furthermore, CAP maintenance was not favoured when the large scale flow was from the SW, when the main valley mouth is directed to the NW, i.e., the PG is along the valley axis in a down-valley direction. A number of contributing factors lead to this conclusion, including; drainage efficiency, related to the geometry and possible flow pathways into the foreland region; lateral constrictions along the valley, which greatly restrict CAP outflow. Combined, the optimal conditions for CAP drainage are given when the connecting valley or pass has a large width and points down the pressure gradient related to the ambient (geostrophic balanced) flow.

2.3.7 Other nocturnal boundary layer phenomena

One meteorological phenomenon that can influence the above valley wind, is the development of a nocturnal low level jet (NLLJ). Blackadar (1957) was the first to outline the theory for NLLJ existence, suggesting the shut down of frictional forces close to sunset leads to supergeostrophic wind speeds several hours later. NLLJs favour conditions when a surface inversion is present. They form inland during the night-time under fine weather conditions with little presence of cloud cover – often associated with high atmospheric pressure – conditions that allow the formation of a stable inversion layer near the ground.

These conditions are synonymous with CAP formation in complex terrain. A pronounced supergeostrophic wind maximum is seen within a few hundred meters of the ground. The jet maximum occurs at, or slightly above the nocturnal inversion layer. Whether the

maximum supergeostrophic wind speed occurs by dawn is dependent on the length of night relative to a half inertial period, at this point the NLLJ may have a significant effect on the development of the NBL (Thorpe & Guymer, 1977).

The generation of turbulence by convection at the ground surface following sunrise, plays a large role in breaking up the NLLJ (Thorpe & Guymer, 1977). Most notably NLLJs with these characteristics have been seen to occur often in the Great Plains of the US (see Whiteman, 2000, p. 168) and has been well documented to occur in Australia by May (1995), with the NLLJ said to be continental in scale covering most of northern Australia. Thorpe & Guymer (1977) suggest that wind speeds of 5 m s^{-1}, at least 100 km of up wind, are required for the optimal formation of a NLLJ.

Another phenomenon that has been noted to occur during SBL conditions, when atmospheric wind speeds decrease below a certain value (1–2 m s^{-1}), is an apparent meandering of the wind that is associated with large horizontal wind oscillations, which are unexplained by any initial trigger (Oettl *et al.*, 2005). According Oettl *et al.* (2005), the appearance of wind meandering is a phenomenon related to the structure of the Navier Stokes equations, where the equilibrium between the Coriolis force and the pressure gradient force generates a solution that shows oscillatory characteristics, particularly when a flow approaches or is near approximate geostrophic balance, i.e., the pressure gradient force and the Coriolis force are in balance, which results in a geostrophic wind that moves parallel to the isobars, and counterclockwise round a low pressure system in the northern hemisphere. Furthermore their numerical simulations show that a small flow perturbation is sufficient to initiate this meandering, which otherwise appear not to be related or generated by atmospheric stability, specific topographic features, season (Anfossi *et al.*, 2005) or gravity waves (Oettl *et al.*, 2005).

Increases in wind speed – caused by increases in geostrophic pressure gradient – lead to increased turbulence through wind shear, which dampen out the meandering (Oettl *et al.*, 2005). The wind directions related to this meandering oscillate with periods on the order of half an hour or more, which results in difficulties calculating a precise mean wind direction (Anfossi *et al.*, 2005).

The formation of gravity waves in the atmosphere are highly likely to affect CAPs. Formation of orographic gravity waves can accelerate airflow down into a valley inducing turbulent erosion, maintaining a very strong vertical shear on top of a CAP (Zängl, 2005a). Adler *et al.* (2012) hypothesises that warm air intrusions into CAPs that formed in the Arizona's Meteor Crater, are associated with hydraulic jumps. Numerical model results by Lee *et al.* (1989) also highlighted that CAP presence down-stream of a bell shaped mountain can act very much like terrain with a similar shape, which may cause mountain waves to be significantly modified in the atmosphere above.

Lalas & Einaudi (1980) suggest that one of the best ways to reveal gravity wave activity in the troposphere is to use rawinsonde rate of ascent. Observations in Aberystwyth, Wales by Worthington (1999), found that on average the mountain wave vector is biased 20° clock-wise near the ground from the background surface wind direction.

One other meteorological phenomenon that has been documented to occur over complex terrain during NBL conditions, is the existence of a turbulent meso-flow (TMF), as documented by Parker & Raman (1993) near Augusta Georgia. The TMF occurred in the lowest few hundred metres of the complex terrain. The TMF was associated with a persistent elevated turbulent layer, dual low-level wind maxima and dual inversions. However, the cause of the TMF was not well understood, with little evidence of any synoptic causes.

2.4 Relationship between ambient wind and valley winds

Many studies have looked at the the relationship between the ambient winds (or geostrophic winds) above a valley and the winds within the valley, including Gross & Wipperman (1987), Fitzjarrald & Lala (1989), Whiteman & Doran (1993), Weber & Kaufmann (1998), Rampanelli *et al.* (2004), Mayr *et al.* (2004), Drobinski *et al.* (2007), Zhong *et al.* (2008), Carrera *et al.* (2008) and Schmidli *et al.* (2009). All of these studies are focused in large mountainous regions with no investigations to date conducted in more moderate complex terrain.

Whiteman & Doran (1993) proposed that four physical mechanisms account for the relationships that exists between the above-valley ambient winds and those that are observed within the valley. The four physical mechanisms outlined by Whiteman *et al.* (1996) are:

(1) thermally driven (or thermal forcing), (2) downward momentum transport, (3) forced channeling, and (4) pressure-driven channeling. Each of the four physical mechanisms produces a distinct distribution pattern in plots of above valley wind versus valley wind. The distinct distribution patterns associated with each of these mechanisms are shown for a NE to SW orientated valley, located in the northern hemisphere, by figure 2.11, examples for (1) north–south, and (2) west–east orientated valleys, are given in Appendix A.

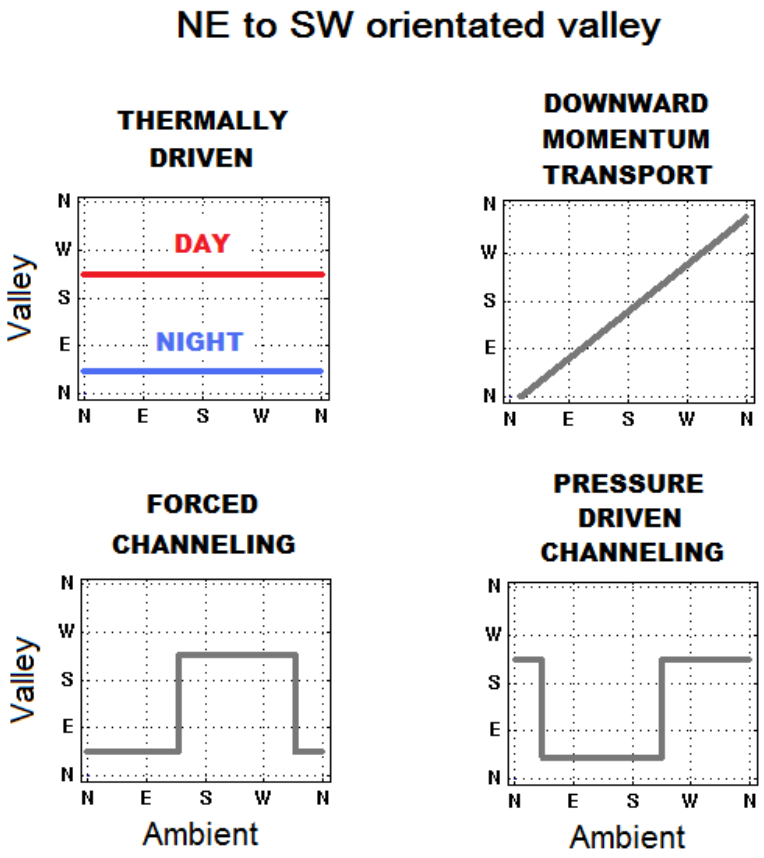

FIGURE 2.11: *Patterns of ambient wind verses valley wind for the four physical forcing mechanisms outlined by Whiteman & Doran (1993) for a NE to SW orientated valley in the northern hemisphere. The four mechanisms are; thermally driven, downward momentum transport, forced Channelling and pressure driven channeling. Figure adapted from Whiteman & Doran (1993).*

The thermal forcing mechanism in valleys develops as a hydrostatic response to temperature differences that develop along the valley axis, which results in an along-valley pressure gradient (Carrera *et al.*, 2008; Whiteman & Doran, 1993). This type of valley flow has been associated with many valleys with numerous observations made by Stewart *et al.* (2002) across the Inter Mountain West region of the US. They are favoured when ambient wind speeds above the valley are weak. The typical thermal forcing scenario results in

up-valley anabatic winds during the daytime and down-valley katabatic or drainage winds during the night-time. They are common in areas with strong diurnal cycles of the surface sensible heat flux (Whiteman & Doran, 1993). Thermal forcing mechanisms are likely to be more frequent when light ambient winds occur during stable or neutral conditions.

The forced channeling mechanism occurs when the ambient winds above the valley are in geostrophic balance but are forced to flow along the valley. The valley wind direction and speed within the valley are a function of the sign and magnitude of the above valley wind projected along the valley axis. Horizontal mixing of momentum from frictional drag on the valley side walls, is likely to play a large in determining factor on the occurrence of the forced channeling mechanism, for this reason you may expect the forced channeling mechanism to be more prominent throughout a narrow valley than a wide valley, where the momentum from frictional drag has a higher potential to be mixed out through other turbulent processes away from the side walls in a wide valley. A unique feature of this mechanism is the reversal in wind directions within the valley, up-valley to down-valley and vise-versa, when the above valley wind crosses perpendicular to the valley axis below. This mechanism is expected to be important for narrow valleys during unstable or neutral conditions (Whiteman & Doran, 1993; Weber & Kaufmann, 1998).

Downward momentum transport is characteristic of valley wind directions that are almost completely aligned with the above valley wind, with a slight turning of the winds expected ($\sim$24°) towards the low pressure as the ground approaches (i.e., through frictional drag). This is a result of strong downward transport of momentum from the above ambient winds in to the interior of the valley that can be caused by either vertical turbulent mixing or by gravity waves. You may expect to see this forcing mechanism in more exposed regions of the valley that are less sheltered by the local orography or vegetation. Downwarm momentum transport is likely to occur during unstable and neutral atmospheric conditions, which favour strong coupling between the free atmosphere and the valley atmosphere. The thermal forcing of valley winds would be less likely to develop during these conditions and channeling along the valley axis by the valley sidewalls would be relatively ineffective. Valley geometry also plays an important role, wide and flatter valley floors and low relief valley side walls favour downward momentum transport (Whiteman & Doran, 1993).

The pressure-driven channeling mechanism for valley winds is driven by the component of the geostrophic pressure gradient imposed along the length of the valley. This mechanism

can be prominent in wide and shallow valleys, as shown by Gross & Wipperman (1987); Whiteman & Doran (1993); Weber & Kaufmann (1998); Kossmann & Sturman (2003). One unique feature associated with pressure driven channeling is the presence of counter currents, as noted by Gross & Wipperman (1987); Whiteman & Doran (1993) in the Rhine and Tennessee Valleys respectively. In this case winds flip 180° when the above valley winds are aligned along the valley axis, the result is an up-valley or down-valley flow, with the valley winds blowing in opposition to the above valley ambient winds. The influence of pressure driven flows is zero only when the ambient wind is aligned along the valley axis – with the presumption that the wind is supergeostrophic the pressure gradient would be perpendicular to the valley axis – or when there is no geostrophic pressure gradient (Whiteman & Doran, 1993).

Whiteman & Doran (1993) demonstrate that the pressure gradient induced by a typical synoptic pressure (5 Pa km^{-1}) is likely to be larger than the internal valley pressure gradient that forms as a consequence of thermal differences within the valley (thermal forcing mechanism). However, Whiteman & Doran (1993) also point out that narrow valleys and steeper terrain may result in thermal gradients that are sufficiently large enough to impose a thermal forcing that may be greater and more dominant that any pressure driven flow. Therefore you may expect pressure-driven channeling to be less prominent in smaller valleys, where the pressure change along the length of the valley is less. Additionally, pressure-driven channeling is more likely to occur under less turbulent conditions, i.e., more stable conditions, including low wind speeds and limited cloud cover; turbulence can be generated by the descent of cooling air at cloud tops, which subsequently sinks through negative buoyancy.

2.5 CAP forecasting, modelling and uncertainties in the field of research

Many studies of CAPs, both past and present, have used computer model simulations as a resource to further understand their occurrence. The ability to predict CAPs using current computer models remains a difficult and complex task to undertake. Forecasts of precipitation type and timing, temperature maximum and minimum, and the effects of these parameters on transportation and other activities depend critically on the CAP

forecast (Whiteman *et al.*, 2001). The computational expense of resolving such fine scales using an operational forecast model, in which CAPs often occur, has led to alternative numerical methods such as down-scaling (Sheridan *et al.*, 2010) and machine learning methods (Pozdnoukhov *et al.*, 2009).

Over larger scales some basic knowledge is well established at mid and high latitudes. Wintertime high pressure situations are frequently associated with persistent CAPs (Zängl, 2005b). Temperature inversion breakup is seen in all seasons throughout the year during undisturbed clear weather conditions dominated by high pressure, but is more dominant during summer and autumn (Whiteman, 1982). Findings by Whiteman *et al.* (1999) suggested that the evolution cycle of CAPs is primarily driven by synoptic-scale weather events in midwinter, but becomes more and more influenced by diurnal radiation-induced BL processes inside basins by late winter and early spring. Another study by Bootsma (1976) estimated that on Prince Edward Island in Canada, average freeze dates in hollows within hilly terrain occur 34 days later in spring and 39 days earlier in the autumn than on hilltops.

A 3-year observational study by Iijima & Shinoda (2000) of CAP occurrence in a hollow, in the subalpine area of the Yatsugatake Range Japan, found that CAPs occurred on more than half of the observational days and the frequency of CAP occurrence was strongly related to anticyclone pressure situations with weak pressure gradients. This result is shared by Kiess & Riordan (1987). Findings by Kiess & Riordan (1987) show a strong correlation between inversion strength to anticyclone pressure situations in North and South Carolina in the USA, specifically when anticyclones were centred over the region and when centred south west of the measurement sites. Furthermore, Iijima & Shinoda (2000) found that CAPs exhibited a seasonal variability. Strong CAPs ($>10°$C) frequently occurred during migratory anticyclone pressure situations that were accompanied by dry air and were dominant during early summer and autumn. Weaker CAPs ($<10°$C) frequently occurred when the North Pacific anticyclone dominated during summer. Iijima & Shinoda (2000) concluded that the weaker forming CAP regime in summer was predominantly caused by the delayed development of the temperature inversion. This was caused by local circulation patterns in the afternoon that were enhanced in spring and summer. This led to higher water vapour content in the late afternoon – possibly resulting in cloud cover at

times – which led to a subsequent increase in downward long-wave radiation, inhibiting CAP formation.

All of the above findings give some idea of the large scale weather phenomena and time dependency that drive CAP evolution, in reality the majority of the problems associated with CAP prediction occur over smaller scales. Much of the variability that is of practical importance, such as the change in air temperature across a narrow valley or along a road, occur on scales that are too small to be resolved by current operational forecast models. This is likely to remain the case for the foreseeable future, for this reason it is important to understand these effects so that alternative forecasting or downscaling techniques can be developed (Vosper & Brown, 2008).

In the past and in the present the large number of processes and complex numerical problems associated with forecasting CAP formation and breakup present significant challenges for numerical modeling (Whiteman *et al.*, 2001), although some interesting hypothesis have been documented in recent years using idealised numerical models. Recent attempts have been made using forecast models to predict the weather in complex terrain with limited success. Using the Pennsylvania State University-National Centre for Atmospheric Research Mesoscale Model (MM5), Billings *et al.* (2006) looked at forecasting of CAPs in the Yampa Valley, northwest Colorado. The model had a baseline simulation with a horizontal scale of 1 km, which is close to present operational resolution for regional mesoscale model forecasts. Their forecast model results did not reflect what was shown by observations incredibly well initially, by the inclusion of snow cover into the model the resolution was increased to 333 m and 111 m, which gave much better results (Billings *et al.*, 2006).

Hart *et al.* (2005) examined if forecast accuracy, as measured by traditional measures, improves with decreasing horizontal grid spacing over the fine-scale Inter-mountain West orography in Utah USA. Again the MM5 forecast model was used. The model results were compared to observations from nearly 200 temperature and wind sites. The results suggested that the 4 km wind forecasts were measurably better than those produced by the 12 km domain. This showed that the gains in cool-season forecast accuracy are possible if horizontal grid spacings are decreased.

More recently, Vosper *et al.* (2013a) show that increasing the vertical resolution of the Met Office Unified model, from 70 to 140 levels – from 10 to 20 levels in the bottom 1 km –

dramatically improved the ability of the model to simulate CAPs, in terms of temperature for the modest terrain setting of the Clun Valley region in Shropshire, England. This result clearly identify that decreasing model resolution, both horizontally and vertically, is especially needed to improve regional weather forecasts in future.

There are often exceptions in the literature which counteract the scientific understanding, and these exceptions further emphasise the need to understand CAP phenomena. Whiteman (1982) gives a good account of how CAP temperature inversions break up and the majority do so within 5hrs; however, their investigations also found an exception to the rule where a CAP is continually maintained in the snow-covered Yampa Valley throughout the day on 19th October 1978. In valleys the drainage flows and compensatory subsidence and warming greatly complicate the interpretation of atmospheric mass and heat-budget computations (Clements *et al.*, 2003). Poor model resolution is clearly hindering our ability to forecast in complex terrain regions and identify CAP evolution with any confidence. In the past Whiteman *et al.* (2001) has also highlighted the logistical problems and costs encountered in running wintertime field studies of CAPs.

A number of numerical modelling and field experiments have investigated CAPs, but few have focused on the formation and maintenance of CAPs and fewer still have resulted in climatology studies of CAPs (Dorninger *et al.*, 2011). Furthermore, comprehensive field experiments of CAPs have rarely been conducted over smaller complex terrain regions that are typical across the UK. Therefore there is little knowledge of CAP occurrences in these type of regions, where CAPs are shallower and likely to be more susceptible to external influences.

Model results by Zängl (2005a) highlight that CAPs can preferentially form and persist depending on the wind direction, suggesting that this could have interesting implications for local weather weather forecasting in mountainous regions. The same may be true for other regions and for smaller complex terrain also. This highlights the potential usefulness of climatology studies for use as a tool for CAP forecast predictions.

In future comparison of observational data with models of increased resolution will further improve our understanding of SBL phenomena and increased computer power will undoubtedly lead to the reduction in both horizontal and vertical resolution, further aiding our ability to forecast on ever smaller scales.

2.5.1 The Met Office Unified Model and COLPEX model

The following section provides a background on Met Office Unified Model (UM) and the COLd air Pool EXperiment (COLPEX) model configuration, which is used for studies within chapter 6 of this thesis. One of the key aims of COLPEX was to improve understanding and enable prediction of the local flow in complex terrain, given accurate knowledge of the larger-scale flow (Price *et al.*, 2011). Initial modelling investigations were aimed at developing the model and validating the configuration. To achieve this a COLPEX version of the Met Office Unified Model (UM) was developed. The final version of the COLPEX model is outlined in Vosper *et al.* (2013a).

The operational version of the Met Office UM has a grid length of 1.5 km, which is insufficient to represent the narrow valleys seen across the Clun Valley region (Vosper *et al.*, 2013a). The Met Office UM solves the non-hydrostatic, deep–atmosphere equations of motion on a rotated latitude-longitude grid, using a semi-implicit, semi-Lagrangian numerical scheme and Arakawa C staggering (Cullen *et al.*, 1997; Davies *et al.*, 2005). Additionally the model uses terrain-following hybrid-height vertical coordinates with Charney–Phillips staggering (Davies *et al.*, 2005).

The Met Office UM has an extensive set of optional parametrisations, which includes surface (Best *et al.*, 2011); boundary layer (Lock *et al.*, 2000), mixed phase cloud microphysics (Wilson & Ballard, 1999) and convection (Gregory & Rowntree, 1990); however, the convection parametrisation tends not to be used for horizontal grid spacings less than 1.5 km (Vosper *et al.*, 2013a). Recently the radiation scheme was updated taking in to account terrain aspect, shading and sky-view (Manners *et al.*, 2012), which is incorporated in the COLPEX model version of the Met Office UM.

The COLPEX model is adapted from the Met Office UM, to run with a 100 m horizontal grid length (Vosper *et al.*, 2013a). The COLPEX version of the Met Office UM has a number of one way nested domains. The horizontal grid lengths on the outermost domain are 4 km and the middle domain is 1.5 km. The 4 km resolution domain is based on the operational version of the Met Office UK4, which covers the whole of the UK. The 1.5 km resolution domain is based on the operational version of the Met Office UK 1.5 km model, which covers southern England and Wales only (Vosper *et al.*, 2013a). The 1.5 km model is run with the standard boundary-layer scheme for vertical sub-grid mixing, but is run

without a convection scheme (Lean *et al.*, 2008) and uses a Smagorinsky-Lilly diffusion scheme in the horizontal (Vosper *et al.*, 2013a).

The model inner domain has a variable resolution, is approximately 80 km x 80 km and is centred over the Clun Valley region (Vosper *et al.*, 2013a), (see figure 3.3). The variable resolution grid (Tang *et al.*, 2012), or stretched grid, means that the grid size changes from 1.5 km down to 100 m, which means there is no need for a nest between the two resolutions. The 100 m horizontal grid covers a regions of 30x30 km, and is also centred over the Clun Valley region (Vosper *et al.*, 2013a).

The 4 km and 1.5 km model versions use 70 vertical levels and the inner variable domain has 140 vertical levels, i.e., the grid spacing is halved for the inner domain. In all cases the vertical spacing of the levels increases quadratically, with most layers in the lowest regions of the domain (Vosper *et al.*, 2013a). There are roughly 40 vertical levels in the lowest 1 km of the 100, m version. The time step of the inner domain is 5 s and 50 s for the 1.5 km version (Vosper *et al.*, 2013a).

It was assumed that sub-grid variability of humidity would be less in the 100 m version of the model, therefore the critical value for relative humidity values for cloud formation (Smith, 1990), were increased in the 100 m model. In the lowest $\sim$0.5 km the critical value is set to 0.99, which then decreases smoothly to 0.91 at $\sim$3.5 km and above this is set to 0.91. This higher value is set in the lowest region to reduce the tendency for low-level cloud to form (Vosper *et al.*, 2013a).

The inner domain used a three-dimensional Smagorinsky turbulence parametrisation scheme and a stability function. The stability function was used to define the turbulent heat flux diffusivity, which cuts off when a critical value of Richardson number of 0.25 occurs (Vosper *et al.*, 2013a). The 100 m model was setup using a dynamical adaptation of the operational UK4 model, essentially testing the ability of the operational model for higher resolutions over complex terrain (Vosper *et al.*, 2013a). The nested model used the operational 3 h analysis to provide lateral boundary conditions for the 1.5 km domain, which was then used to drive the 100 m model. Both the 1.5 km and 100 m model domains are initialised using the 4 km operational analysis, but are free running thereafter (Vosper *et al.*, 2013a).

2.6 Summary

It seems that at this present time there is a much higher level of observational and dynamical understanding of CAPs than in our ability to model and predict them, and this has remained the case for some years. Additionally many studies of CAPs in the past have been concerned with larger mountainous terrain or idealised basin terrain types. Therefore there appears to be a current gap in knowledge with regard to observations of CAP occurrence over smaller horizontal and vertical scales, in the order of a kilometre or less. Furthermore there are very few climatological studies of CAP occurrence, which highlights a gap in knowledge with regards to the recurrence of CAPs under different synoptic regimes.

An improved understanding of CAP occurrence over these scales, in time and space, through modelling and observation, is likely to aid future efforts to better represent CAPs in numerical weather prediction models. In the short term this is likely to be achieved through downscaling or parametrisation techniques, rather than real time weather forecasts conducted using high resolution models, with horizontal grid lengths less than 100 m.

Chapter 3

Methodology

3.1 COLPEX field campaign

3.1.1 The Clun Valley region

The rolling hills and network of valleys in the Clun Valley region, Shropshire, typify many regions across the UK. The ground cover is mostly green pastures lined with hedgerows and trees. The terrain is modest with valley depths rarely exceeding 250 m. The valleys tend to be between 5–15 km in length. The main vein of the Clun Valley is ∼25 km in length. The many river valleys in the region provide the ideal conditions for CAP occurrences and associated meteorological phenomena. For this reason the Clun Valley is an ideal place to investigate CAPs in complex terrain. A view looking north across the Clun Valley is shown in figure 3.1.

The Clun Valley region is highlighted in figure 3.2. It is located on the western edge of England in the county of Shropshire and is in close proximity to the border with Wales. The main control on temperatures in the UK are the prevailing air masses. For regions not in direct interaction with the sea, such as the Clun Valley region, temperature changes are highly responsive to radiation input and losses, especially during low wind speed conditions. Newport in Shropshire holds one of the lowest minimum temperature records in the UK, occurring in January 1981, induced by cold Arctic air settling over the region that was already covered in snow. The Midland region of the UK, which includes Shropshire, is known to have a particularly high number of frost days each year compared to the

FIGURE 3.1: *Pictured is the Clun Valley running left to right (west to east) looking north.*

rest of the UK. Only sixty days are expected to remain frost free throughout the year (i.e. no ground frost occurring within the 24hr diurnal cycle) due to the cold nocturnal temperatures that prevail in the region (King & Giles, 1997).

Figure 3.3 shows a close-up of the Clun Valley region with the larger valleys identified. The land coverage is mostly pasture and hedgerows with <10% woodland (Price *et al.*, 2011). The valleys are typically V-shaped river valleys; however, some regions may appear more U-shaped. The largest valley is the main vein of the Clun Valley, identified by the black solid line in figure 3.3. The majority of the main Clun Valley is oriented west to east from Duffryn (245 m ASL) to Clun (185 m ASL). The western most part, from Anchor (400 m ASL) to Duffryn, is orientated north-west to south-east. The width of the valley from peak to peak increases from west to east and the valley floor has a gentle undulating slope down towards the east. The valley mouth lies ∼10 km east from Clun. The total length of the valley is estimated at 25 km. The highest peaks in the region are at an altitude of 470 m ASL (Masons Bank) and the lowest regions around 185 m ASL (Clun Castle). At the center of the Clun Valley, north of Springhill, the floor width is approximately 0.5 km and the peak to peak width approximately 1.5 km. There are a number of tributary valleys that feed into the main valley (black). The two largest tributary valleys feed into the main valley from the north near Bicton (highlighted red in figure 3.3), orientated north to south, and near Newcastle (highlighted blue in figure 3.3), orientated north-north-west to south-south-east. A third tributary valley (highlighted magenta in figure 3.3), orientated west-south-west to east-north-east, feeds into the main valley at Duffryn. Another valley

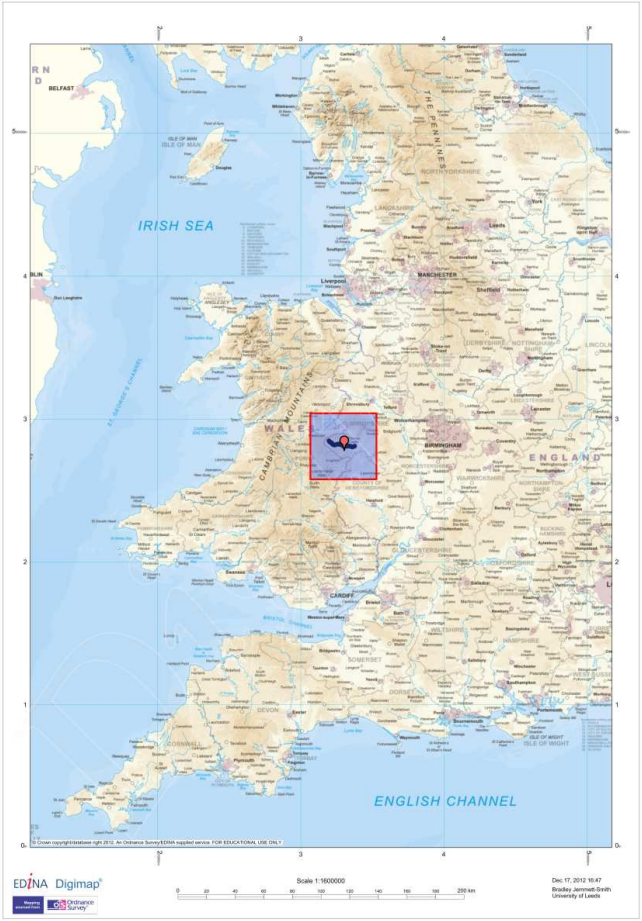

FIGURE 3.2: *Map of west England and Wales. The Clun Valley region is outlined by the blue filled square. The main vein of the Clun Valley is shown by the black line. The grid squares are 50×50 km^2. Co-ordinates are Great Britain (GB) Ordnance Survey (OS) grid reference. ©Crown Copyright/database right 2012. An Ordnance Survey/EDINA supplied service.*

of interest is the Burfield Valley, which is located south from the Clun Valley (highlighted yellow in figure 3.3). The head of the Burfield Valley is just south of Springhill. The total length of the Burfield Valley is approximately 15 km and is mostly orientated north-west to south-east. There are many smaller tributory valleys, the largest of these are highlighted grey in figure 3.3.

3.1.2 Design and instrumentation

COLPEX is a collaboration between the Met Office, University of Salford, University of Leeds, University of Surrey and the National Centre for Atmospheric Sciences (NCAS). This collaboration resulted in a comprehensive set of instrumentation deployed during the

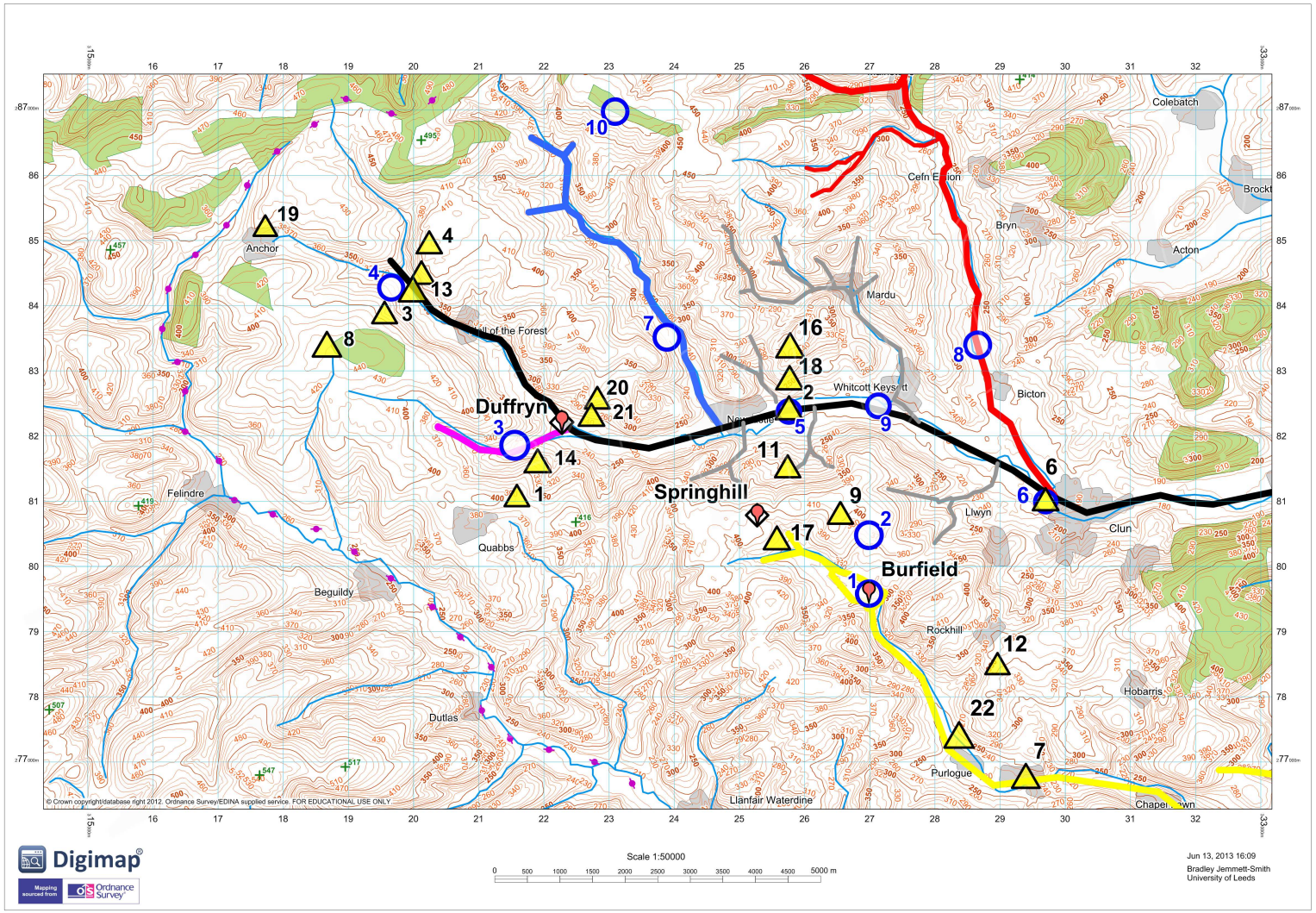

FIGURE 3.3: *Map of the Clun Valley region. AWS are highlighted by blue circles, HOBOs by yellow filled triangles, mast sites by red balloons. The main vein of the Clun Valley is highlighted black, AWS 8 tributary valley is red, AWS 7 tributary valley is blue, AWS 3 tributary valley is magenta and the Burfield Valley is yellow. Valley regions highlighted are below 350 m ASL. Highlighted in grey are smaller tributary valleys that have valley floors below 300 m ASL. Grid squares are 1×1 km^2. Co-ordinates are GB OS grid reference. ©Crown Copyright/database right 2013. An Ordnance Survey/EDINA supplied service. Note, detached laminated version supplied.*

COLPEX field campaign, as shown by figure 3.3. There are three main sites located at the Burfield Valley, Upper Duffryn and Springhill Farm, for simplicity these will be referred to as Burfield, Duffryn and Springhill respectively. Broadly they will be referred to as mast sites. Each mast site is identified in figure 3.3. A description of the three mast sites is given in table 3.1. Duffryn is located on the floor of the main Clun Valley roughly 5.5 km SE from the valley head. Burfield is located in a separate bowl shaped valley known as the Burfield Valley. The Burfield Valley is adjacent and to the south of the Clun Valley. The Burfield mast site is higher and shallower than much of the main Clun Valley floor. Springhill is sited on a hill top between the Burfield and Duffryn mast sites.

There are also 31 satellite weather stations made up of 21 HOBO data loggers (Onsett Computer, inc.), supplied and maintained by the Met Office, and 10 Automatic Weather Stations (AWS) that were developed and maintained by the University of Leeds and NCAS – AWS are discussed in 3.2. During the field campaign measurements were undertaken in two operational modes, Normal Operational Period (NOP) and Intensive Operational Period (IOP). NOP is the standard mode of operation used throughout the field campaign. IOP mode is initiated when CAP episodes are forecast and a more intensive period of observation takes place. Some instruments were deployed during IOPs only. In most cases the measurement frequency is between 1 and 60 measurements per minute. A higher frequency of measurements occurred during IOPs. The measurement frequency varies for different instruments, depending on the instrument logger capability, practicality and resources available, i.e., power supply and storing of data.

Site	Height	Slope	Description
Duffryn	246 m	Slight incline towards the NW	Located on the valley floor at the junction of two valleys in a grass field lined by hedgerows and trees. Duffryn is the largest site in terms of instruments deployed, including a 50 m flux tower, radiometers and a LIDAR.
Burfield	316 m	–	Located on a small, open, grass covered hill top, within the bowl shaped Burfield Valley. Instruments include a 30 m flux tower.
Springhill	402 m	–	Sited on the hill top between Clun and Burfield Valleys. Instruments include a 30 m flux tower.

TABLE 3.1: *Description of the three main instrument sites located across the Clun Valley region. Height is meters (m) ASL.*

3.1.3 Met Office mast sites

All instrumentation at the three mast sites, Burfield, Duffryn and Springhill, were maintained by Met Office instrument scientists. Before and after the field campaign instruments were calibrated and intercomparisons conducted. Quality control was conducted in accordance with Met Office protocol and quality control flags applied to all datasets. For all analysis, if the amount of poor data exceeded 25% over the averaging period, the data was flagged as bad. According to Price (2010) on occassions spikes and anomalies in the data arose due to power supply, damp conditions and cable integrity issues.

Table 3.2 shows instrumentation at each of the mast sites and identifies which are used during each operation mode (NOP and IOP) – note this does not include all instrumentation that was deployed, only those that are relevant to this study. Further descriptions are given in Price *et al.* (2011). To follow are descriptions that refer to instruments in table 3.2. During IOP mode Met Office instrument scientists conducted balloon Radiosonde launches at one hour intervals throughout the evening (before and after sunset) and in the morning (before and after sunrise). On occasions it was not possible to launch Radiosondes this frequently, mainly due to unavailability of staff. Data are recorded and logged using a Vaisala RS92 Radiosonde and a Vaisala MW15 sounding system. In the majority of IOPs Radiosonde launches took place simultaneously at two separate locations. One Radiosonde was launched from Duffryn and another from either Springhill or Burfield. Each Radiosonde is equipped with Vaisala RS92 sensor that records temperature, RH and pressure (see table 3.2 for errors). The Vaisala RS92 sensor is subject to; calibration errors; solar radiation error, caused by radiative heating of the sensor; and time-lag error, caused by slow sensor response during cold temperatures (Miloshevich *et al.*, 2009).

CG4 and CM21 Kipp and Zonen radiometers are used to measure the amount of incoming (down) and outgoing (up) short-wave (SW) and long-wave (LW) radiation. The radiometer errors are shown in table 3.2 and are based on the worse case scenario obtained from Kipp and Zonen CG4 and CM21 data sheets. The CNR2 net radiometers mounted at 50 m (Duffryn), are expected to have worse case scenario errors of ± 7.5 W m^{-2}, which is roughly equal to the combined incoming and outgoing errors for net LW and net SW from the CG4 and CM21 sensors. According to Price (2010) the SW radiometer devices

Duffryn				
Instrument	Height (m AGL)	Error	Operating range	Mode
Sonic Anemometers (Gill HS 50)	50, 25, 10, 2	few cm^{-1}	−40 to +60°C	IOP/NOP
Temperature (platinum resistance)	50, 25, 10, 1.2	0.1-0.15 °C	−60 to +260°C	IOP/NOP
Visibility (Birall HSS VPF-730 Present weather sensor)	2	–	−50 to +60°C	IOP/NOP
Radiometers (Kipp and Zonen CG4, CM21 and CNR2)	50, 2	*SW* ±4 Wm^{-2} *LW* ±4 Wm^{-2}	−40 to +80°C	IOP/NOP
Halo photonics Doppler LIDAR (Hatpro RPG microwave radiometer)	50-2,000 (variable)	–	–	IOP/NOP
Radiosonde (Vaisala RS92)	0-20,000		−90 to +60°C	IOP
Temperature		0.5 °C		
RH		5 %		
Pressure (1080-100 hPa)		1 hPa		

Burfield				
Instrument	Height (m AGL)	Error	Operating range	Mode
Sonic Anemometers (Gill HS 50)	30, 10	few cm^{-1}	−40 to +60°C	IOP/NOP
Temperature (platinum resistance)	30, 10, 1.2	0.1-0.15 °C	−60 to +260°C	IOP/NOP
Radiometers (Kipp and Zonen CG4, CM21 and CNR2)	2	*SW* ±4 Wm^{-2} *LW* ±4 Wm^{-2}	−40 to +80°C	IOP/NOP
Radiosonde (as above)	0-20,000		−90 to +60°C	IOP

Springhill				
Instrument	Height (m AGL)	Error	Operating range	Mode
Sonic Anemometers (Gill HS 50)	30, 10	few cm^{-1}	−40 to +60°C	IOP/NOP
Temperature (platinum resistance)	30, 10, 1.2	0.1-0.15 °C	−60 to +260°C	IOP/NOP
Radiometers (Kipp and Zonen CG4, CM21 and CNR2)	2	*SW* ±4 Wm^{-2} *LW* ±4 Wm^{-2}	−40 to +80°C	IOP/NOP
Visibility (Birall HSS VPF-730 Present weather sensor)	2		−50 to +60°C	IOP/NOP
Radiosonde (as above)	0-20,000		−50 to +60°C	IOP

TABLE 3.2: *Description of instrumentation used in this thesis, from the three mast sites; Burfield, Duffryn and Springhill. Operating range of each instrument (column 4) is given in °C. Instruments operate during IOP, NOP or both modes.*

typically agree to 2 W m^{-2} and *LW* to approximately 3-4 W m^{-2}. *SW* domes are aspirated and heated at Springhill and Duffryn, and aspirated but not heated at Burfield.

Possible data quality issues experienced during the field campaign include dome wetting during precipitation and icing which may bias the radiation to the surface regime (Price, 2010).

Measurements from the 3D sonic anemometers (Gill HS 50) are used for high frequency measurements of the 3D wind field and for vertical flux calculations using eddy covariance. Combined with high frequency temperature measurements calculations of the sensible heat flux are obtained.

At Duffryn a Halo Photonics 1.5 micron pulsed Doppler LIDAR (LIght Detection And Ranging) was deployed throughout the period from October 2009 to March 2010. The LIDAR was provided by the Facility for Ground-based Atmospheric Measurements (FGAM) – a subsidiary of NCAS. LIDARs are particularly useful for studying the composition and structure of the boundary-layer. They use laser light to detect the amount of light reflected back by objects in the atmosphere (backscatter), such as aerosol and water vapour. The LIDAR was configured with 70 range gates that have a range gate length of ∼30 m giving a maximum vertical measurement of ∼2 km AGL with the lowest measurements obtained at ∼100 m AGL. Vertical stare scans were taken approximately once every 40 seconds. Additionally wind profile scans were taken once an hour that consist of a vertical profile and two profiles at 30 degrees from the vertical pointing north and east, combined these profiles give a doppler wind profile. Additionally a velocity azimuth display (VAD) scan was taken at an elevation of 30 degrees from the horizontal, with bearings taken at 30° intervals starting from north. Pearson *et al.* (2009) gives an analysis of the LIDAR performance for observations of the BL.

All LIDAR data products and graphical images were processed by Dr. Andrew Ross (Lecturer at the University of Leeds).

3.1.4 Met Office satellite weather stations; HOBOs

In total 21 HOBOs were deployed across the Clun Valley region as part of the Met Office contribution. Each HOBO takes measurements of temperature and RH. All HOBOs are identified by the yellow filled triangles in figure 3.3. A number of the HOBOs were deployed across three transects that cross the Clun Valley near Anchor, at Duffryn and at Springhill. A number of the HOBOs are located near hill tops above the valley. HOBOs are also sited

along the Burfield Valley floor. Temperature accuracy is approximately ±0.15°C and RH ±1.5%, when sensors are operating correctly. Each HOBO records an instantaneous measurement once per minute, with the exception of HOBO 22 that records data once every 2 minutes and takes measurement of wind and pressure also. HOBOs were installed away from obstruction wherever possible. Temperature sensors performed well; however, the HOBOs were unaspirated and may have had a tendency to over-read by up to 1-2°C in strong sunlight and light winds. RH sensors tended to fail after prolonged exposure to water from condensation forming on the sensor. On occasions this caused sensors to fail completly without recovery, which unfortunately was quite common. Sensors did recover in some instances but tended to be bias to low values of RH. Poor data are flagged appropriately by Met Office scientists according to their protocols (Price, 2010).

3.2 University of Leeds AWS

3.2.1 Instrumentation and deployment

The University of Leeds contributed and maintained 10 AWS as part of the COLPEX field campaign. An example AWS set-up in the field is pictured in figure 3.4. The AWS were designed and engineered by instrument scientists Matthew Hobby and Matt Gascoigne (at the time both employed by the University of Leeds and NCAS). The AWS are located throughout the Clun Valley region and are identified by the blue circles in figure 3.3. Table 3.3 gives a description of each AWS location. On occasions the AWS were co-located with Met Office HOBOs, this was for two reasons: (1) so a calibration between the two sets of instruments could be conducted, (2) as a contingency for instrument failure at locations deemed more important than others. Due to funding restrictions and instrument deployment strategy, it is neither possible nor practical to have HOBOs co-located with all AWS.

The main purpose of AWS deployment was to provide an understanding of the flow dynamics across the Clun Valley region, as well as provide further measurements of temperature, RH and pressure. Each AWS was installed with a data logger developed by Matthew Hobby. The loggers recorded data onto an SD card. Data was collected during regular visits (on average every 10 days) throughout the field campaign using a laptop computer.

AWS	Location	Height	Latitude/ Longitude	Valley orientation	Slope (from-to)	Site description
1	Burfield	317	52.4095/-3.0750	N/A	N/A	Co-located at the Burfield mast site, sited on a small, well exposed grass hill-top.
2	Weston Hill	376	52.4176/-3.0745	N/A	N-S	Well exposed location close to the hill-top between Burfield and Clun Valley. Situated at the edge of irrigated farm land; 30 cm crop growth by the end of the campaign. Located next to a clearing in a hedgerow to the west.
3	Moor Hall	283*	52.4290/-3.1548	WSW-ENE	WSW-ENE	Located in a tributary valley that feeds into the main Clun Valley at Duffryn. The AWS is sited within a garden with a hedgerow ∼5 m to the north. Some trees are in close proximity.
4	Weals Farm	345	52.4500/-3.1836	NW-SE	SW-NE	Close to the head of Clun Valley. A fairly well exposed site located on the edge of grazed farmland with a hedgerow ∼3 m SW.
5	Offa's Dyke	204	52.4348/-3.0934	W-E	N/A	Located in the middle of the Clun Valley floor. Sited on grazed farmland and well exposed. Forms part of the Offas Dyke transect.
6	Clun Castle	182	52.4224/-3.0349	NW-SE	N/A	Located on the floor of the Clun Valley. Straddling a ditch between two grazed fields.
7	Caldu	253	52.4448/-3.1215	NNE-SSW	WSW-ENE	Well exposed location. Sited in a large tributary that feeds into the Clun Valley at Newcastle.
8	Biston Farm	207	52.4440/-3.0510	N-S	N/A	Well exposed location and very flat. Sited in a large tributary valley that feeds into the Clun Valley at Whitcott Keysett.
9	Whitcott Keysett	197	52.4352/-3.0729	W-E	N/A	Located on the Clun Valley floor. In close proximity to a river and sheltered by tree cover above and to the west.
10	Masons Bank	468	52.4750/-3.1334	N/A	N-S	Well exposed site in one of the highest regions.

TABLE 3.3: *A description of the AWS sited across the Clun Valley region. Height is measured by differential GPS, given in metres (m) ASL. ∗AWS 3 height was measured using GPS, which is expected to have an error of ±10 m in the vertical and horizontal; however, using OS GB maps, the grid reference and height given here gives a good approximation, therefore the height and vertical co-ordinate error is expected to be smaller than ±3 m.*

		AWS			
Measurement	Key and Sensor	Accuracy	Precision	Range	Height
Temperature	TD* Sensirion SHT75	±0.4	±0.005	-40–124°C	1.8 ±0.1
	TT* BetaTHERM	±0.5	±0.04	-80–150°C	1.8 ±0.1
	TG BetaTHERM	±0.5	±0.04	-80–150°C	-0.1 ±0.04
	TB BetaTHERM	±0.5	±0.04	-80–150°C	1.75 ±0.1
RH	RH* Sensirion SHT	±1.5	±0.005	0–100% RH	1.8 ±0.1
Pressure	P MS5534A Barometer module	±1.5	±0.05	-20–70°C	0.0
Wind	Gill 2D WindSonic				2.3 ±0.1
Speed	WS/WV	±2%	±0.005	5–100% RH	
Direction	WD	±3%	±0.5	-35–70°C	

TABLE 3.4: *Unless stated otherwise, accuracy and precision units for temperature are given in °C, for RH as %, pressure in hPa, wind speed in m s^{-1} and wind direction in °. WS and WV are scalar and vector winds respectively. *sensors mounted in the aspirated unit. The accuracy (column 4) is the manufacturers guideline within the operational range (column 5). Sensor performace changes within the operational range. Refer to manufacturers instrument sheet for further details. The height of each instrument (column 6) is given by metres (m) AGL.*

The AWS loggers operate in both NOP and IOP mode. During NOP mode data are recorded instantaneously once every minute and in IOP mode once every second. Each AWS is equipped with instruments that measure ground temperature, 1.8 m air temperature, RH, pressure and two dimensional (2D) wind speed and direction (horizontal plane only). Details for each instrument installed on the AWS are given in table 3.4. Included is a short hand key for each instrument.

An aspirated unit was installed at ∼1.8 m AGL (±0.1 m), identified by the blue circle in figure 3.4. Within each aspirated unit is one Sensirion SHT75 humidity/temperature sensor (TD) and one BetaTHERM thermistor temperature sensor (TT). Two additional BetaTHERM thermistor sensors are used; (1) a ground temperature probe (TG), (2) an additional measure of air temperature (TB), not aspirated, which was mounted inside a white aluminium ventilated screen – a small type of Stevenson screen – identified by the yellow circle in figure 3.4. The ground temperature probe (TG) is a BetaTHERM sensor embedded inside a screw which is itself embedded into the side of a hollow aluminium pole ∼30 cm in length and 2 cm in diameter – this is to maximise the conductivity of the sensor in order to give the best representation of soil temperature. The ground temperature probe is then inserted into the ground with the sensor at a depth of ∼10cm. The TB temperature sensors were installed later in the field campaign at a height of ∼1.75 m (AGL) – a height similar to the HOBOs and other AWS air temperature sensors (TT and TD).

The winds are measured using a 2D Gill WindSonic installed at a height of ∼2.3 m (AGL), which is identified by the red circle in figure 3.4. The 2D Gill WindSonics are able to take accurate measurements of low wind speeds at high resolutions, which is particularly useful for taking measurements in low wind speeds.

Atmospheric pressure is measured at ground level. Air flows over a looped hollow foam tube, ∼30 cm across, which rests on the floor. The tubing has a diameter of ∼10 mm). The pressure measurement is taken using a MS5534A Barometer module that is mounted inside the logger unit and connected to the hollow foam tube via a hollow plastic tube (diameter ∼5 mm).

For time keeping each AWS is fitted with a GPS transmitter that updates the logger clock at least once every minute (more frequent during IOP mode). The main power supply for each AWS comes in the form of two solar panels that charge a 12V battery during the day, in return the 12V battery supplies power to the logger when the solar voltage is low, this means that the AWS are completely self sufficient, providing there is enough sun light during the day to charge the battery.

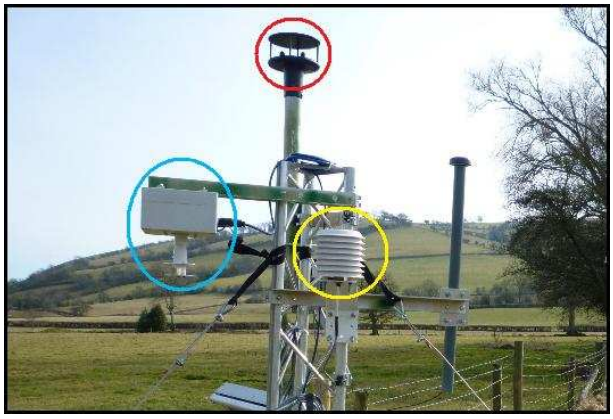

FIGURE 3.4: *Pictured is AWS 5 set up in the field. Highlighted in red is the 2D sonic anemometer. Outlined in blue is the aspirated unit, within are the SHT temperature, BetaTHERM thermistor temperature and relative humidity sensors. Highlighted in yellow is the TB BetaTHERM temperature sensor.*

Where possible AWS were installed in locations away from obstacles, such as trees and bushes, which may affect the local flow and distort wind measurements. Unfortunately in some cases this simply was not possible, since the region is dominated by working farmland, either being grazed on by cattle or sheep, or used for growing crops. On occasions AWS were found with chewed cables, the perpetrators expected to be sheep with a specific

appetite for GPS cables! For this reason, in some cases and with the farm owners permission, a barbed wire fence was erected. The AWS geographical coordinates and heights (see table 3.3), were obtained using differential GPS (DGPS). Due to obstructions limiting the signal received from satellites, DGPS measurements were not possible at AWS 3, in this case GPS measurements were used instead. DGPS is widely accepted to give extremely accurate measurements of both horizontal and vertical coordinates, with errors expected to be 10's of centimetres, as opposed to GPS errors that are in the order of 10's of meters. A comparison of the GPS measurements of AWS 3 location and height was made to a high resolution map of the region, in this case the GPS measurements appeared to be extremely accurate and correlated well to location of the AWS 3 site on the OS grid map.

3.2.2 Reliability of AWS instruments

3.2.2.1 Aspirated unit and sensors

During the field campaign issues arose with respect to the Sensirion SHT75 humidity (RH) and temperature sensor (TD), BetaTHERM thermistor (TT) and ground probe (TG). Fundamentally the RH, TD, TT and TG instruments failed to record data on many occasions. Most often this was related to sensor failure, caused by a combination of both cold and wet weather conditions, which were typical throughout the COLPEX field campaign – especially nearer valley floor locations where saturation occurred most often. The cold wet conditions highlighted a weakness in the design of the aspirated sensor units, which tended to trap moisture inside the unit causing enhanced corrosion of the sensors. RH can be a particularly difficult measurement to take at the best of times, especially when values approach 100% humidity and saturation occurs. The HOBO used the same SHT75 sensors and suffered a similar fate to that of the AWS, but the HOBO measurements tended to be more reliable than those recorded by the AWS. During the field campaign values of RH often approached saturation at night (100% RH), as a consequence night-time measurements of temperature and RH from the AWS were particularly poor.

The failing of the RH and temperature sensors on the AWS were easily identified by anomalously high and/or low values being recorded and/or the sensors failing completely. Treatment of all AWS erroneous data is discussed later in section 3.2.5. It was concluded by Hobby (2010) that a flaw in the hardware design caused the BetaTHERM temperature

measurement to stop recording when the SHT75 sensor failed. As a consequence there is a lack of temperature and RH data recorded by the AWS for much of the field campaign.

3.2.2.2 Ground probe and replacement with additional air temperature measurement

Unfortunately many of the ground temperature probes were saturated with water soon after the field campaign started. The sensors either failed as a direct consequence of this or through corrosion over time. On occasions this caused erroneous data to be recorded. Subsequently the failing ground temperature probes were replaced by an additional air temperature measurement (TB) mounted 1.8 m (±10 cm) AGL. The TB instruments were installed over a 2 day period from 22-23 February 2010. The aim was to improve the reliability and coverage of air temperature measurements. As explained previously, both TD and TT temperature sensors – both within the same aspirated unit – failed frequently. For the remainder of the field campaign the TB temperature sensors proved to be very reliable.

3.2.2.3 Pressure sensor issues

The pressure sensors (MS5534A Barometer module) appeared to be very reliable on the whole. However, pressure measurements recorded by AWS 9 post January 2010 appeared to be less reliable. The general trend of the pressure measurement was consistent with other AWS, but the measurement appeared to oscillate more than that observed by other AWS. AWS 9 was a particularly wet location and may have been subject to flooding since it was located near the bend of a river. Water entering the pressure tube may have caused this measurement anomaly. On rare occasions there were anomalous positive spikes in the pressure data across more than one AWS, an example of this is shown in figure 3.5 – occurrences of this were <5 in total. Reasons for these anomalous spikes are unknown; however, their occurrence appears to co-inside with sunrise after a cold night, therefore the pressure spike may in some way be related to previously trapped moisture – within the pressure sensor or part of the sensor apparatus – which froze during the cold night and rapidly thawed during daybreak. No further investigations were conducted and the exact reason for the pressure spike is not known.

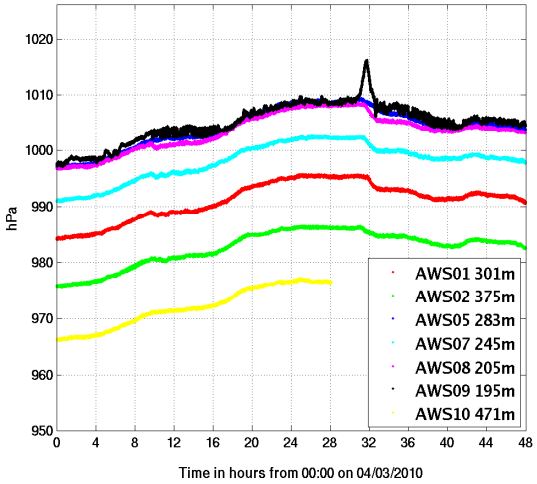

FIGURE 3.5: *Time series of AWS pressure (hPa) for the 48hr period from 00:00 UTC, 4 March 2010.*

3.2.2.4 Wind measurements

Over a 3 day period from 28–31 December 2009, the Gill WindSonic recorded anomalously high wind speeds/gusts at three separate sites; AWS 4, 9 and 10. These anomalous gust events are seen in figure 3.6 (Julian Day 362-365). This was a particularly cold period of weather during the 2009-2010 winter. Lying snow, ice and fog was present and noted during a site visit made between 28-29 December 2009. According to Nygaard & Wolff (2010), the Gill WindSonics are not suitable for use in areas prone to cold temperatures with problems associated with icing, rhyming and sleet or snow covering the sensor. Their study concludes that heavy snow/sleet events can lead to unrealistic values of gust events. This seems to be a likely cause of the high wind speed anomalies recorded by the AWS shown in figure 3.6. Subsequently these events were flagged appropriately and not included in any datasets or subsequent analysis. It is possible that rhyming, icing or snow accumulation on the Giil Windsonic sensors, may have caused other smaller gust anomalies at other times during the field campaign; however, none have been identified during quality checks and their occurrence is likely to be more ambiguous. Otherwise the Gill WindSonics performed well throughout the field campaign and proved to be one of the most reliable instruments used.

The Gill WindSonics intermittently failed to record data when logging in IOP mode. According to Hobby (2010), this is likely to have been due to the sampling rate being very high (one second intervals). Simply put the logger was unable to take a wind measurement

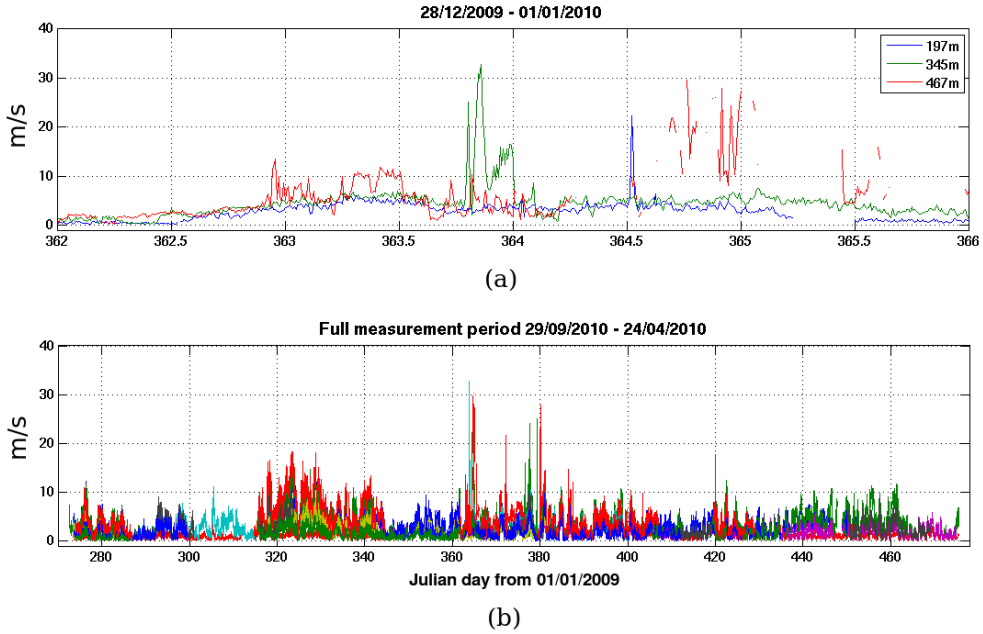

FIGURE 3.6: *Time series of wind speed (ms^{-1}). Figure 3.6(a) from 28 December 2009 to 1 January 2010 for; AWS 9 (197m), AWS 4 (345m) and AWS 10 (467m). Figure 3.6(b) is the entire AWS measurement period from 30 September 2009 to 22 April 2010. High wind speed anomalies are seen between Julian Days 360-380 (26 December'09 to 15 January'10) – this was a particularly cold period during the field campaign.*

from the Gill WindSonic at every one second interval over long periods of time. This did not occur often, for instance a wind measurement would be missed less than 1 in every 100 samples. Therefore missing wind data, caused directly by the high sampling rate, was much less than 1%.

During the first half of January 2010, wind measurements on AWS 10 were intermittent and on occasions missing all together. Again the reason for this may have been icing, rhiming, sleet or snow covering the Gill WindSonic Nygaard & Wolff (2010). However, this cannot be proved and the issue seemed to resolve itself over time. By the end of January 2010 the instrument continued to record as normal. This appeared to be an isolated event.

3.2.2.5 Other issues

Many of the data loggers (an essential part of the AWS) tended to fail within two weeks of operation, an issue not recognised before or during the first month of their deployment. According to Hobby (2010) it was suspected to be a hardware problem – rather than an

issue related to logger failure caused by the cold damp conditions – possibly related to the use of SD memory cards for data storage. However, this issue was not investigated further due to funding restrictions, limited time and resources. As a result of this issue site visits became more frequent, occurring at least every two weeks from November 2009, subsequently this strategy improved the amount of data obtained. Any breaks or disrepair found on inspection of the AWS during visits, were fixed when possible on site at the time.

Another issue caused by the AWS loggers and the recording of data to SD memory cards, was that on many occasions data had not been recorded in the correct format. On first view of the data – after copying the content of the SD cards to a laptop computer in the field – it appeared that the loggers had failed to record any data at all, or only recorded data in parts and was therefore incomplete. On occasions the data had been recorded but in a format unrecognised to some computer software. Thankfully much of this apparently lost data was recovered.

3.2.3 Calibration

This section describes the calibration procedures conducted for all AWS instruments. Instruments subject to calibration include the following:

TT 1.8 m air temperature BetaTHERM sensor (aspirated unit).

TD 1.8 m air temperature Sensirion SHT75 sensor (aspirated unit).

RH 1.8 m RH (aspirated unit).

TG 10 cm ground temperature.

P Ground level pressure.

TB 1.8 m air temperature, BetaTHERM sensor (ventilated).

When referring to specific instruments the acronym shown previously is used from here on, i.e. the 1.8 m air temperature, SHT75 sensor, will be referred to as TD. Each sensor is likely to have a mean negative or positive bias (offset), e.g. the TT sensor on AWS 1 may have a mean warm or cold temperature bias when compared to the mean temperature recorded by all TT sensors. The aim of the calibration exercise was to calculate the mean bias of each

sensor with respect to the average measurement across all sensors. Taking this mean bias into account provides improved measurement accuracy and reduces measurement error in future analysis.

Due to constraints on time and resources, it was not possible to conduct an intercomparison for sensors TD, TT, RH, TG and P, for all AWS (1 to 10) in one instance. As a consequence two separate intercomparisons took place. From here on the two intercomparison periods will be referred to as IP1 and IP2. A third intercomparison took place at the end of the field campaign primarily for the calibration of the TB sensors, this will be referred to as IP3. Further details regarding IP3 are discussed later in 3.2.3.2. Below are descriptions of each of the intercomparison periods, IP1, IP2 and IP3, including which sensors and AWS were calibrated in each intercomparison period:

IP1 From 25-27 September 2009. Sensors TD, TT, RH, TG and P, for AWS 1, 2, 3, 8, 9, and 10. Data recorded by Matthew Hobby.

IP2 From 29-30 September 2009. Sensors TD, TT, RH, TG and P, for AWS 4, 5, 6, 7, and 10. Data recorded by Matthew Hobby.

IP3 From 1-5 May 2010. Primarily for TB sensors. Included intercomparison for sensors installed as replacements during the field campaign, for all AWS. Conducted by myself.

3.2.3.1 Calibration; IP1 and IP2

In both IP1 and IP2, sensors TD, TT, RH, TG and P were calibrated. IP1 took place between 25-27 September 2009, with intercomparisons between sensors installed on AWS 1, 2, 3, 8, 9 and 10. IP2 took place between 29-30 September 2009, with intercomparisons between sensors installed on AWS 4, 5, 6, 7, and 10. During IP1, all sensors were huddled together and placed outside in view of direct sunlight – representative of conditions expected during the field campaign. For IP2 this setup was repeated, except the intercomparison took place inside, away from direct sunlight. During both IP1 and IP2 the loggers were set to record in IOP mode taking measurements at 1 second intervals.

For each sensor a mean bias (or calibration offset) was calculated with respect to the sample mean of all sensors within either IP1 or IP2 respectively. AWS 10 was used in

both IP1 and IP2, therefore AWS 10 sensors were used as a cross comparison between all AWS. IP1 has a longer measurement period than IP2 and as previously stated was conducted outside in conditions expected to be similar to those experienced during the field campaign. For these reasons the offsets calculated from IP1 will remain unchanged. Instead calibration offsets gained from IP2 will be adjusted relative to the mean value gained in IP1 using AWS 10 to cross calibrate e.g. $AWS03_{offset} = AWS03_{IP2} + \Delta AWS10$, where; $\Delta AWS10 = AWS10_{IP1} - AWS10_{IP2}$. This process is repeated for all sensors. The calculated offset value (bias) is then applied to all future datasets and before any analysis.

Figure 3.7 shows an example before (figures 3.7(a) and (b)) and after (figures 3.7(c) and (d)) the calibration offset is applied. In this case the TT sensors from IP1 are shown. One observation made during the initial stages of the calibration exercise was a divergence in temperature measurements as temperatures approached and exceeded ∼18°C between ∼08:00–15:45 UTC. This is clearly seen in figure 3.7(a) highlighted by the grey shaded regions. These biases are presumed to be caused by direct *SW* radiation, which warmed the sensors and sensor units. This effect is expected to be most prominent during summer, approaching midday when the incoming direct *SW* radiation is strongest.

Although some sensors were aspirated (TD, RH and TT sensors) it is not surprising that all sensors may be prone to radiation induced biases to some degree. As with the TT sensor, TD and TG sensors were also subject to biases when temperatures approached and exceed 18°C. Departures in RH (within the aspirated unit) and pressure (within the logger box) from the sample mean were also observed during warmer temperatures, but were less obvious than those observed by the temperature sensors. This was either due to the larger measurement error associated with the RH and P sensors relative to the temperature sensors, therefore masking the bias to some degree, or simply because both P and RH sensors were less prone to this type of bias.

The COLPEX project is focused on night-time phenomena, with the majority of the field campaign conducted during the autumn, winter and spring, as opposed to summer when temperature biases caused by *SW* radiation are expected to be strongest. With this in mind the period between 8:00 and 15:45 in IP1 and IP2, when temperatures approach and exceed ∼18°C, are excluded from all calibration intercomparison exercises for all sensors. Although this is likely to result in temperature, RH and pressure biases during warm

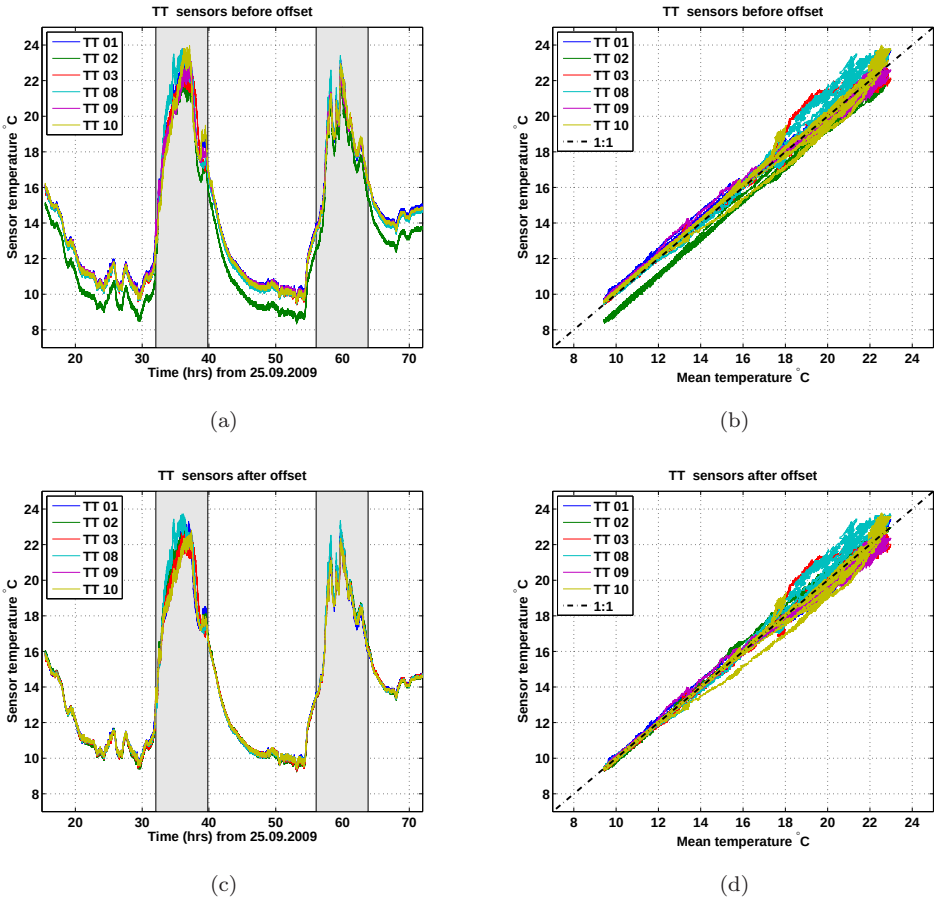

FIGURE 3.7: *TT sensor measurements before and after calibration during IP1. Figures (a) and (c) are time series before and after calibration respectively. Comparison of TT sensors before and after calibration, to the mean measurement of TT sensors during IP1, are shown by figures (b) and (d) respectively.*

daytime conditions, the reliability of night-time measurements, or cooler temperatures at least, are likely to be improved, which is more beneficial to the COLPEX field project as a whole.

By comparing the uncalibrated TT sensors in figures 3.7(a) and (b), to the calibrated TT sensors in figure 3.7(c) and (d), it is clear to see that without any calibration the temperature measurement from the TT sensors is more variable, especially at lower temperatures. The impact of excluding the warmer temperatures from the calibration exercise is clearly evident in figures 3.7(c) and (d). There is good agreement between all sensors after each offset is applied except, as expected, during warmer periods when more variation is seen.

The improvement made by the calibration exercise can be quantified by the root mean square (RMS) error, calculations of which are shown in table 3.5 for all AWS sensors,

before and after the calibration offsets are applied to measurements obtained during IP1, IP2 and IP3. For consistency, measurements between 8:00–15:45 are treated as NaN, since this period is prone to warm biases and was not included in the calibration exercise. For all sensors it is clear to see that the RMS error is greatly reduced after the calibration offset is applied. This indicates that the calibration exercise was successful at reducing the measurement variation (measurement error) across all sensors and instruments (for lower temperatures at least).

	Root mean square error											
	TD		TT		TG		RH		P		TB	
AWS	Before	After	Before	After	Before	After	Before	After	Before	After	Before	After
1	0.38	0.07	0.26	0.05	0.36	0.04	0.74	0.29	0.41	0.08	0.21	0.13
2	0.14	0.05	0.77	0.06	0.33	0.07	1.09	0.36	0.43	0.08	0.17	0.12
3	0.05	0.04	0.11	0.04	0.13	0.05	1.16	0.39	0.35	0.07	0.14	0.05
4	0.05	0.03	0.06	0.04	0.67	0.04	0.36	0.16	0.75	0.08	–	–
5	0.11	0.02	0.09	0.03	0.53	0.04	0.47	0.20	0.64	0.06	0.18	0.08
6	0.08	0.04	0.06	0.05	0.20	0.05	0.98	0.22	0.47	0.07	–	–
7	0.03	0.03	0.05	0.04	0.14	0.04	0.17	0.11	0.20	0.08	0.20	0.16
8	0.13	0.06	0.07	0.05	0.61	0.05	0.61	0.43	0.32	0.09	0.15	0.13
9	0.07	0.04	0.21	0.05	0.24	0.08	0.63	0.14	0.35	0.07	0.08	0.07
10	0.10	0.03	0.17	0.04	0.07	0.05	0.46	0.10	0.33	0.07	0.10	0.08

TABLE 3.5: *Root mean square error before and after calibration offsets are applied to data from IP1 (AWS 1, 2, 3, 8, 9 and 10), IP2 (AWS 4, 5, 6, and 7) and IP3 (all TB sensors). The RMS error is with respect to the sample mean for each measurement period (IP1, IP2 and IP3). Values are to 3 significant figures. Data between 8:00–15:45 UTC are excluded from all RMS error calculations in attempts to eliminate daytime radiation biases.*

Much variation away from the sample mean was seen when intercomparisons of RH were conducted. This is likely to reflect the large measurement error associated with this sensor (±1.5%, see table 3.4). After the calibration offset is applied the overall variability is improved; however, the error associated with the RH sensor does appear to be larger relative to other sensors (see table 3.5. Similarly the pressure sensor has large variation over small time scales, therefore the sensor appears to be more sensitive to change, which results in quicker response times. This also reflects the measurement accuracy of this instrument, which is relatively large (±1.5 hPa).

3.2.3.2 Calibration of TB sensors and post field campaign intercomparison; IP3

The TB sensors were assembled and installed at the end of February 2010 and intercomparison was not possible until the conclusion of the field campaign when all data loggers could be brought together. IP3 took place between 1–5 May 2010 following the conclusion of the field campaign. The objective of IP3 was to; (1) calibrate all TB sensors, (2) calibrate any additional or replacement sensors that were installed during the field campaign, (3) to see if any of the sensors experienced drift, i.e., a tendency to measure negative or positive biases different to that seen before the field campaign during IP1 and IP2.

Objective 3 only applied to sensors that were installed and continued to perform after the conclusion of the field campaign. Unfortunately all TT, TD and RH sensors failed at some point during the field campaign and most either failed to recover or suffered from corrosion that resulted in poor measurements. An intercomparison of the TT, TD and RH sensors after the field campaign proved to be a rather meaningless task. An intercomparison did take place, but is became apparent that the sensors were less likely to give accurate measurements after the field campaign in IP3 than before during IP1 and IP2, therefore measurements gained from IP3 may spoil the calibration rather than improve it. An assessment of P sensor drift was conducted and suggested that sensor drift was unlikely to be larger than the instrument error.

An additional temperature instrument TB was installed on each AWS over a two day period from 22-23 February 2010. An example of the instrument installed at 1.8 m AGL ($+/-10$ cm), is identified by the yellow circle in figure 3.4. The instrument is comprised of a ventilated white aluminium screen – similar to a Stevenson screen only smaller, dimensions roughly 25 cm height, 15 cm width and depth – with a BetaTHERM temperature sensor mounted inside. The measurement error and accuracy of the sensor is shown in table 3.4. The reason for installing the TB sensor was to provide an additional, reliable temperature measurement, needed as a result of data loss related to a fault that affected both TT and TD temperature sensors (discussed previously in 3.2.2.1).

Comparisons of TB before and after calibration are shown in figure 3.8 with the RMS error show in table 3.5. The calibration offset values for each are shown in table 3.6. A time series showing all TB sensors before and after the calibration offsets were applied are

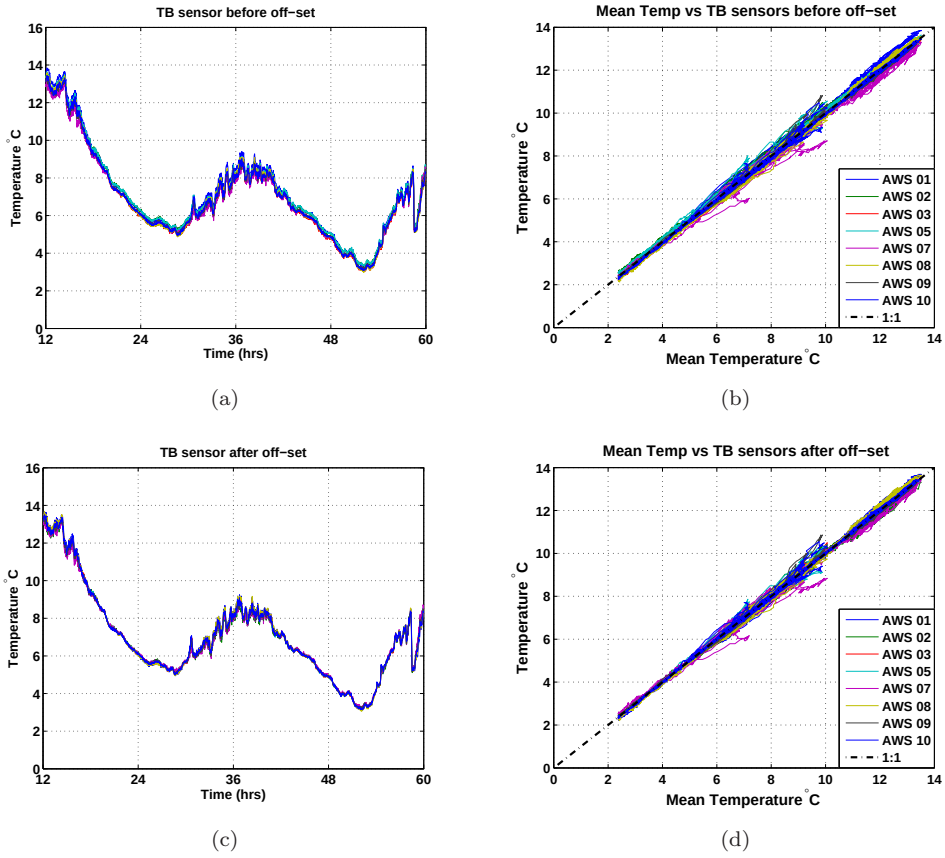

FIGURE 3.8: *Shows all TB sensors before, (a) and (b), and after calibration (c) and (d), during IP3.*

shown in figure 3.8(a) and (c) and comparisons to the sample mean before and after the calibration was applied in figures 3.8(b) and (d) respectively.

Two additional sensor platforms were installed during the field campaign to replace failed sensors. The two new sensor platforms were installed on AWS 2 and 3 on 12 November 2009 and included new TT, TD and RH sensors in each case. Unfortunately the new sensor platform on AWS 2 failed before the conclusion of the field campaign and could not be calibrated as a consequence. Data recorded from this sensor platform was appropriately flagged in all datasets and use of this data was left up to the users discretion. Successful calibration of the sensors installed on AWS 3 were conducted as part of IP3; however, as previously explained the reliability of TT, TD and RH sensors in IP3 are likely to be less reliable than during IP1 and IP2, before the field campaign started when the sensors were new. Treatment of all TT, TD, TG and RH data is discussed in 3.2.3.4.

3.2.3.3 HOBO and AWS intercomparison

To minimise error in any analysis, an attempt to calibrate the AWS instruments with respect to the HOBOs was conducted for measurements of temperature and RH. Throughout the field campaign AWS 5 and HOBO 2 are co-located. A comparison of temperature and RH between the two datasets is used to calibrate all AWS with respect to the HOBOs. The period from 1-10 October 2009 is used for a comparison of AWS 5 RH, TT, and TD, to HOBO 2 RH and temperature sensors. This period was chosen because there are no issues with data reliability in terms of availability and quality, the AWS had recently been installed and TD, TT and RH sensors were still performing well. An example comparison of RH is shown in figure 3.9.

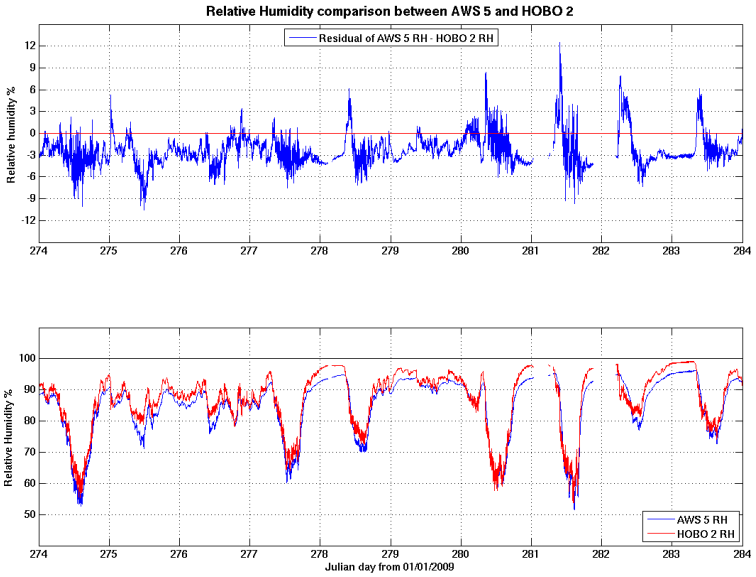

FIGURE 3.9: *Shown are time series of 2 m RH from AWS 5 and HOBO 2 (bottom) and the residual difference (top). AWS 5 and HOBO 2 are co-located (see figure 3.3). The measurement period is between 1-10 October 2009. The mean difference between the instruments is 2.321(%).*

Since the installation of all TB instruments did not take place until 24 February 2010, the period from 24–28 February 2010 is used for the comparison between AWS 5 TB and HOBO 2 temperature sensors. An example showing the intercomparison between TB and HOBO temperature is shown in figure 3.10. All results from this intercomparison are shown in table 3.6, row heading HOBO. This calibration offset is applied to the AWS prior to all datasets and analysis.

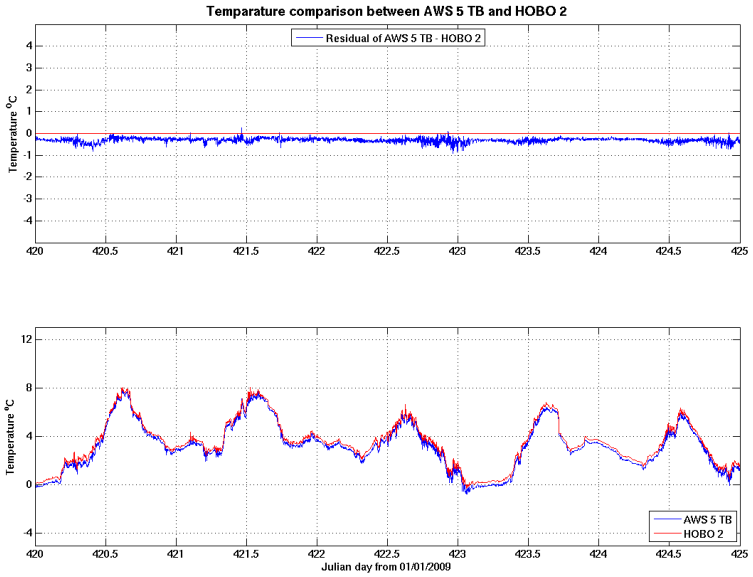

FIGURE 3.10: *As in figure 3.9, except for TB sensor 2 m temperature measured by AWS 5 and HOBO 2 (bottom) and the residual difference (top), for the measurement period 24-28 February 2010. The mean difference between the instruments is 0.305° C.*

3.2.3.4 Summary of AWS calibration

Table 3.6 shows the calibration offsets obtained from the calibration intercomparison exercises. The HOBO temperature offsets shown in table 3.6 are applied to all AWS temperature sensors before any analysis and dataset compilations. Following the conclusion of the field campaign and after the calibration exercises were completed, a full data quality exercise of the AWS was undertaken. After an assessment of the TT, TD and RH data quality, it was decided that the use of data from these sensors should be avoided, subsequently data recorded by the TD, TT and RH sensors is not used within this thesis and other collaborators were given the same advice. All collaborators were made aware of all AWS issues, concerns, calibration and data flagging procedures, in the form of a data quality report of the AWS. In addition, a presentation outlining the performance of the AWS instruments was given at a COLPEX meeting in July 2010.

3.2.4 Initiation of IOPs and data availability

The COLPEX field campaign was conducted over the 11 month period from June 2009 to April 2010. The deployment of all instrumentation took place during the months covering

AWS	Mean Offset					
	TD	TT	TG	RH	P	TB
	°C	°C	°C	%	hPa	°C
1	-0.101	0.287	0.418	0.850	0.483	0.157
2	0.164	-0.899	0.372	1.308	-0.487	0.121
3	-0.041	0.119	0.133	-1.306	0.398	-0.128
*3a	0.030	0.390	N/A	1.018	N/A	N/A
4	0.186	0.303	-0.774	-0.667	-1.070	-
5	0.008	0.151	0.395	-0.941	-1.000	0.157
6	0.222	0.290	-0.306	0.428	0.090	-
7	0.119	0.266	-0.009	-0.574	-0.149	-0.129
8	0.142	0.062	-0.717	0.430	-0.371	-0.079
9	0.066	0.238	-0.258	-0.755	-0.407	-0.038
10	0.114	0.193	0.051	-0.528	0.383	-0.062
HOBO	-0.023	0.008	N/A	-2.321	N/A	-0.305

TABLE 3.6: *Shows the calibration offsets applied to each instrument on the AWS. Values are to 3 d.p. HOBO offsets are applied to temperature sensors only. * Calibration offsets in row titled 3a are for a replacement sensor platform installed on 12 November 2009.*

October 2009 to April 2010. The University of Leeds AWS were installed at the end of September 2009. A list of the IOPs initiated during the COLPEX field campaign are displayed in table 3.7, which includes a description of observations made at the time recorded by Met Office scientists in the field at Duffryn. In total 17 IOPs were issued during the campaign. At least eight of the IOPs had a full deployment of instrumentation. Conditions were not always ideal for observing CAPs. Besides IOPs a number of ideal CAP episodes occurred when IOPs were not issued, most notably early in October 2009, early January 2010 and the two week period preceding the official end of the field campaign in early April 2010.

IOP observations taken at Duffryn			
IOP	Date	Fog	Observations
1	16.06.2009	No	Small ridge of high pressure over the region. 5-6 okta Cu at 17:00, reduces to 2 okta flat Cu by 19:00. By 21:30 0 Cu, thin cirrus haze above. Some stars visible thereafter.

2	23.06.2009	No*	Ridge of high pressure moving eastwards over region. 17:00: 8 okta low cloud. 19:11: 2 okta Cu, brief rain at 19:10. 20:10: Cu on western horizon. 21:06: Clear skies for remainder of IOP *22:30: Some misty patches observed. *01:15: lots of fog patches observed on journey back to Clun.
3	30.07.2009	No	Large high pressure over southern UK and France. 17:00: 3-4 Cu. 18:58: Thin Cu. 21:00: <1 okta thin Cu. Clear thereafter.
4	09.09.2009	No	Large high pressure over region with light winds. 19:34: Clear sky all night/-morning.
5	10.09.2009	No	Large high pressure light winds. Clear during evening 05:56 (11th): 3 okta Ci.
6	16.09.2009	No	Large high pressure over south UK with slackening winds. Cloudy. 13:21: 6 okta Sc. Mostly 7-8 okta during evening and night. 03:57 (17th): 8 okta Sc. No dew on grass. 04:12 (17th): Odd haze, star visible.
7	17.09.2009	No	Large high pressure over UK. 14:50: 8 okta Sc through to 16:50. 17:50: 7 okts Sc. 1850: 8 okta rest of evening. 04:30 (18th): 7 okta. Small amount of dew on grass.
8	13.10.2009	No	Large high pressure over southern England. Warm front to north is bringing some higher cloud to area. 15:40: 7 okta CiCu. 16:33: 7 okta Ci. 18:19: 7 okta Ci, 3 okta ACu. 19:04: 6 okta Ci, some ACu. 20:46: Some stars visible. 21:06: All starts visible–clear. 22:05: Stars visible. Lidar shows some cloud. 22:30: Stars visible, lidar shows clouds at 200m.
9	14.10.2009	No	High pressure, but stagnated warm front over region–partly cloudy. 16:11: 2 okta Cu, 5 okta Ac. 17:01: 7 okta Sc. 18:01: 7 okta Sc. 19:02: 7 okta Sc. 20:30: Some stars visible, remaining mostly cloudy for night. 04:40 (15th) 8 okta Sc/St.
10	10.12.2009	Yes	High pressure covering UK. Light winds. 15:30: 1 okta Ci remaining clear for evening. 06:10(11th): Thick fog at site and in Duffryn Valley. 07:20(11th): Fog lifted a little. 07:50(11th): At top of Springhill fog top just above ridge (photos taken). ∼10:30(11th): Fog top below ridge top by 100 feet. ∼12:00(11th): Fog top increases to above ridge top again and thickens and persists for rest of day.
11	14.01.2010	Yes	High pressure. Cold. Snow on ground 7-12 inches at Duffryn, more on hill tops. Fog intermittent early on. Higher cloud approached overnight with rain just starting by 06:00 at time of morning Sonde launch. Some issues with logging surface data–may be gaps in data.
12	18.01.2010	Yes	High pressure. Snow on ground. Initially cloudy–7 okta. 08:52 GMT: clear. 19:53: 8 okta low cloud. 20:50: 8 okta misty/foggy. 23:00: Fog reaches up to Springhill. 23:56: Foggy. 00:52: 8 okta St. 05:41: Foggy. 06:43: Fog starting to lift, then lifted suddenly. 07:40: 8 okts St. Cloud base below hill tops. 10:15: 8 okta Sc. Low cloud gone.

13	09.02.2010	No	Weather clear, cold, light winds. 19:03 GMT: Freezing, clear. 20:01: 3 okta cloud. 21:00: 3 okta. 22:02: 1 okta. 23:00: Clear no wind. 23:43: Clear. 00:28: Clear, light breeze.
14	10.02.2010	No	15:54 GMT: Snow shower. 1603: 7 okta Cu, no inversion. 17:03 4 okta Ci,Cu,Sc. 17:48: Snow shower until 17:56. 18:03: 2 okta Sc on horizon. 19:02: Clear sky. 20:03: Clear sky. 21:04: Clear sky. 22:02: Clear sky, dry. 23:02: Clear sky, dry. 01:03: clear sky, dry, light wind.
15	03.03.2010	No	16:01 GMT: 7 okta Ci, 1 okta Cu. 17:01: 7 okta Ci, 3 okta As. 18:03: 8 okta Ci, 7 okta As. 18:57: Some stars visible. 19:05: Stars visible overhead. 20:30: Part clear some stars visible. 22:02: stars visible, faintly. 23:09: Stars visible, faintly. 00:27: Stars visible. 05:45: Thin haze, stars visible, small amount of low cloud present.
16	04.03.2010	No	Clear, light winds and flippin' cold! 16:01: 1 okta Ci. 17:02: 1 okta Ci. 18:02: clear temp 0.0°C. 19:01: 1 okta Ci stars are bright. 20:31: Clear, bright stars. 22:02: Clear, bright stars. 23:01: Clear, bright stars, -4.6°C. 00:31: Clear, bright stars. 05:35: Clear (<1 okta Ci on horizon), -5.7°C, moonlight, very light winds, ground very hard, medium frost deposition. 09:00: Sunny, clear, frost in shadows. 11:00: Sunny, clear, no frost.
17	10.03.2010	No	14:30: 4 okta Sc + upper level haze. 15:30: 6 okta Sc. 16:02: 2 okta Sc. 17:05: 6-7 okta Sc. 19:02: 4-5 okta Sc. 20:29: 8 okta Sc. 21:30: 1-2 okta Sc. 22:01: Cloudy, a few stars visible. 23:01: Crystal clear! (0 okta). 05:00: Clear conditions (1 okta Ci at horizon). Moderate frost deposition on hard ground. No deposition on trees. Haze during morning to 09:00.

TABLE 3.7: *Table showing all IOPs initiated during the COLPEX field campaign. Observations were recorded at Duffryn by Met Office scientists.*

The University of Leeds AWS data – although incomplete – are available from the 29 September 2009 to 21 April 2010. Summary statistics of the AWS data availability is shown in table 3.8. In terms of data availability the most reliable instruments are the 2D Gill WindSonics (Wind) and the MS5534A Barometer modules (P). Both failed rarely when the loggers were operating, therefore the percentage of Wind and P data available mostly reflects the reliability of the loggers and not the 2D Gill WindSonics and MS5534A Barometer modules respectively. AWS 4, 6 and 9 have the least data availability. In all three cases the poor data coverage is due to all loggers being inoperable for long periods

of time. AWS 6 was believed to be overwhelmed by flood water on the 16 January caused by rapid snow melt – AWS 6 was located next to a stream at the lowest point in the valley just west of Clun. The logger on AWS 4 failed on 5 February immediately after re-booting the logger, which was standard procedure after retrieving data during site visits. Due to funding restrictions the failure of the AWS 4 logger was never determined and repairs not possible. Furthermore, replacement loggers were not available, therefore AWS 4 and 6 loggers were not replaced or repaired.

AWS	Location	P	RH	TB	TD	TG	TT	Wind
1	Burfield	68	30	16	30	7	24	68
2	Weston Hill	70	20	27	20	27	20	73
3	Moor Hall	72	48	27	48	34	48	72
4	Weals Farm	40	19	N/A	19	40	18	40
5	Offa's Dyke	72	19	26	40	23	40	73
6	Clun Castle	38	11	N/A	11	22	11	38
7	Caldu	70	20	27	20	26	20	73
8	Biston Farm	53	18	7	18	14	17	53
9	Whitcott Keysett	35	28	6	28	7	27	37
10	Masons Bank	48	22	5	22	4	16	45

TABLE 3.8: *Summary of available AWS data given as a whole percentage (%), over the period from 29 September 2009 to 20 April 2010.*

AWS 9 suffered from power loss some time in early January 2010. The logger stopped recording on 1 January. The loggers often failed and subsequently stopped recording data, therefore this does not necessarily indicate that the logger failed on 1 January due to power loss. AWS 9 was surrounded by many trees to the south, which restricted the amount of direct sunlight the solar panels received, especially during winter when the sun was setting behind surrounding hills earlier than at other times during the year. It was expected that the 12V batteries could be maintained and charged by the solar panels, even under low levels of sunlight and when operating in IOP mode – a higher sampling rate leads to higher energy consumption from the 12V battery. Unfortunately this was found not to be the case at AWS 9. As a consequence AWS 9 was not in operation between 1 January and 8 February 2010. This aside there were no other power issues for the remainder of the field campaign, in fact, with the exception of AWS 9, the solar panels performed better than expected.

Unfortunately for reasons unknown the loggers on AWS 8, 9 and 10 failed frequently towards the end of the field campaign, even with more frequent visits, which tended to improve the likelihood of data recovery. Detailed month by month tables of AWS instrument data coverage can be found in the Appendix A.

3.2.5 AWS ten minute mean dataset; flagging and treatment of erroneous data

The AWS data was compiled into a 10 minute mean dataset including both NOP and IOP sampled data. This dataset was then made available to all collaborators. At least 75% of the sampled data must be available for each 10 minute mean sample. The dataset includes variables for all instruments recorded by the AWS.

A flagging system was used to identify data that is good, not available or poor. A further data flag was given for data that had been averaged using IOP or NOP data. Full details of the AWS instrument reliability and issues are given in 3.2.2. A summary of how the flagging was conducted and how data was allocated to each flag follows.

Data was binned into each flag using both an automated system and manual allocation. The automated system was applied to flags that were allocated when flag = 0, flag = 1 and in most cases flag = 2. On occasions data was simply not recorded, i.e., the data flag = 1, a summary of reasons for this are:

- AWS logger failure.
- Gill WindSonic drop-out – AWS 10 in early January 2010.
- TG, TT, TD and RH instrument failure – caused by saturation of the sensor by water.

For the automated system, threshold values were used to remove data that had been recorded but gave unrealistic values (flag = 2). For each instrument an appropriate upper and lower threshold limit was applied, e.g. for all temperature measurements data is flagged as bad (flag = 2) and removed when values are above 35°C and below -30°C. For each measurement the upper and lower threshold values are set to eradicate data deemed highly unlikely to occur during COLPEX. This automated system was extremely efficient

at removing poor data, which occurred as a consequence of corrosion on the TG, TT, TD and RH sensors. To ensure poor data was flagged correctly, a manual check of all the AWS data took place – a tedious but necessary task – with the appropriate flag checked and the appropriate flag applied if necessary. Manual flagging of the data was conducted by viewing time series plots for the entire field campaign of all AWS data for each sensor, i.e. field campaign time series of all TT sensors from the ten AWS. This meant that the majority of erroneous data was easily identified since it did not fit the background trend of other instruments at the time. Data that was deemed to be poor and removed was subsequently flagged as flag = 2. In most cases this was due to instrument malfunction. The automated flagging system removed the majority of this data. Sensors that were commonly flagged in this way included:

TG – Ground temperature probe failures due to sensor being saturated by water.

RH – Sensor corroding with time due to saturation by water.

TD – SHT sensor corroding with time due to saturation by water.

TT – BetaTHERM sensor failing due to saturation by water.

WS/WV – Unrealistic values of gust events. Most likely caused by sensors being covered with frost, sleet and/or snow (Nygaard & Wolff, 2010).

P – Anomalous pressure measurements.

On occasions measurements appeared to be suspect and did not fit the background trend of other AWS measurements; however, there was insufficient evidence to disregard the data as poor, since the anomaly appeared to be either short lived, small relative to the background spread of measurements or within instrument error ranges. In these instances the data are flagged but not removed (flag = 3). Flags of this kind were rare and never removed by the automated system, instead being flagged manually, applying the flag using common sense and judgement. Flags of this kind were applied to the following instruments for the following reasons:

WS/WV – Realistic values of gust events that appear to be out of sync with other wind data. Possibly caused by sensors being covered with frost, sleet and/or snow (Nygaard & Wolff, 2010).

P – Anomalous pressure measurements recorded by AWS 9 post January 2010 (see 3.2.2.3 for full description.)

Unless stated otherwise all future representations of data, either in figures or tables, require at least 75% of data being available, i.e. if more than 25% of data is missing the data is treated as not a number (NaN). The accuracy and precision of the AWS instruments are displayed in table 3.4, for mast site instruments in table 3.2 and HOBO instruments are discussed in 3.1.4.

All datasets include scalar and vector averaged winds, in future these will be referred to as mean wind speed and vector averaged wind respectively. All representations of mean wind direction are calculated using vector averages.

3.3 Other data products and sources

3.3.0.1 Global model mean sea level pressure

The global model mean sea level pressure data are supplied by Dr. Peter Sheridan (Met Office Scientist). The data is a product of the UM global model (see Davies *et al.*, 2005) forecast simulations, which includes an analysis every 6 hours starting from 00:00 UTC. The model pressure data used in these analyses is taken at 00:00 UTC and is an analysis product. The advantage of using the UM Global model data over other higher resolution products, is that the complex terrain is unresolved, therefore the msl pressure serves as a measure of the background msl pressure, without the influence of the terrain over this region.

The data set covers the period from July 2009 to April 2010. Data are missing on occasions. For the majority of this period the resolution of the UM global model data is 40 km x 40 km; however, from 06:00 UTC on the 9 March 2010, the resolution of the data changes to a 25 km x 25 km grid. Data are extracted from four data points that surround the Clun Valley region. The data point co-ordinates, used before and after 06:00 (UTC) 9 March 2010, are given in table 3.9.

Using the global model pressure analysis data at 00:00 UTC each night, the following variables are calculated for the Clun Valley region:

Pre 06:00 9 March 2010		Post 06:00 9 March 2010	
Lat	Long	Lat	Long
52.125	-3.375	52.266	-2.813
52.125	-2.812	52.266	-3.516
52.500	-3.375	52.734	-2.813
52.500	-2.812	52.734	-3.516

TABLE 3.9: *Co-ordinates of UM global model grid points used for calculations of msl pressure, PG and PG direction. Co-ordinates are shown in decimal degrees.*

- The area average msl pressure.
- The msl pressure gradient.
- The msl pressure gradient direction (from high to low).
- The geostrophic wind.

The magnitude of the geostrophic wind is calculated using the global model mean sea level pressure and equation 3.1, where U_g is the resultant geostrophic wind, f is the Coriolis force, ρ is the density of air and $\bigtriangledown_H P$ is the pressure gradient.

$$U_g = \frac{1}{f\rho}\nabla_H P \tag{3.1}$$

In the absence of: (1) horizontal temperature gradients, (2) friction, and (3) no advected and local accelerations, the geostrophic wind is assumed to be in geostrophic balance between the pressure gradient and the Coriolis force, with the geostrophic wind assumed to be aligned parallel to the isobars and rotate clockwise round an anti-cyclone in the northern hemisphere (Pal Arya, 1988).

3.3.1 Shobdon dataset

The Shobdon dataset was obtained from the British Atmospheric Data Centre (BADC – badc.nerc.ac.uk). The Shobdon data form part of the Met Office Integrated Data Archive System (MIDAS) database, which includes an extensive record of surface observations over land in the UK. Observations at Shobdon are automated and are taken instantaneously once every hour on the hour. Observations include screen temperature, pressure, RH,

wind speed and direction. All observations are recorded in line with both Met Office and World Meteorological Organisation (WMO) standards.

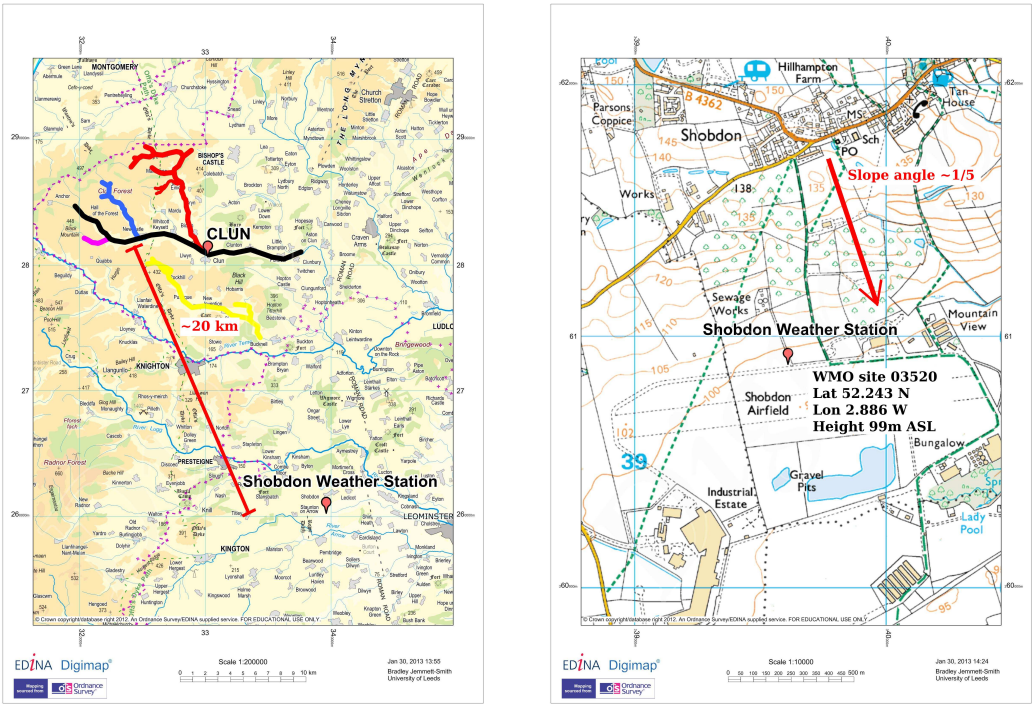

(a) (b)

FIGURE 3.11: *Figure (a) shows a regional map including the Clun Valley region and Shobdon weather station. Highlighted by the coloured solid lines are the major valleys in the Clun Valley region. The grid squares are 10 x 10 km^2. Figure (b) shows an area close up of the Shobdon weather station (red balloon). The grid squares are 1 x 1 km^2. Co-ordinates are GB OS grid reference. ©Crown Copyright/database right 2013. An Ordnance Survey/EDINA supplied service.*

Figure 3.11(a) shows the location of the Shobdon weather station (red balloon) with respect to Clun. Figure 3.11(b) is a close-up map indicating the location of the Shobdon weather station (red balloon). The Shobdon weather station is located roughly 20 km SSE from Clun. The weather station (WMO site number 03520) is located at GB OS grid co-ordinates SO 39607 60893 (latitude 52.2429° and longitude -2.8859, in decimal degrees) and at an elevation of 99 m ASL (roughly 100 m below Clun). The weather station is situated in a small fenced off grassland area, surrounded to the north, east and west by farmland and to the south by grassland and a small concrete pavement, which forms part of the Shobdon Airfield. As seen in figure 3.11(b), the weather station is situated in relatively flat terrain; however, there is a gentle slope ($\sim 1/5$) orientated roughly north to

south directly north of the site. This topographic feature may have some micro-climatic effect on the weather station, such as the generation of slope flows.

3.4 Processed data products

3.4.1 Calculating potential temperature at HOBO weather stations

The HOBO instruments do not have a pressure measurement; however, it is often beneficial to have a measure for pressure so that calculations of potential temperature can be conducted. The pressure can been inferred using a scale height (H_s) approximation using the hydrostatic relationship and a known measurement of pressure. In this instance the hydrostatic relationship can be expressed using equation 3.2, where P is the required pressure in hPa, P_0 is a reference pressure in hPa, z is the height in meters (m) and H_s is the scale height. The calculation of H_s is shown by equation 3.3, where k_s is the Stefan Boltzmann constant (1.38 x 10^{-23} JK^{-1}), R_d is the mean molecular mass for dry air (287.058 kg) and g is the acceleration due to gravity (9.81 ms^{-2}). Potential temperature (θ) is then calculated using equation 3.4, where P_0 is a reference pressure (such as 1000 hPa) and $k = 0.286$.

$$P = P_0^{\left(-\frac{z}{H_s}\right)} \tag{3.2}$$

$$H_s = \frac{k_s T v}{R_d g} \tag{3.3}$$

$$\theta = T\left(\frac{P_0}{P}\right)^k \tag{3.4}$$

An example of pressure calculated for all HOBOs using this method is shown by figure 3.12, comparing the approximated HOBO pressure to the in-situ measurements of pressure obtained from the AWS. This example clearly shows that the scale height approximation method produces satisfactory results. Using equation 3.2 and a reference pressure (P_0) from the AWS, a value for θ can then be obtained for any given HOBO.

3.4.2 Measurements of wind persistence

The persistence (P_w) is a measure of the tendency of the wind to blow in the same direction over a mean measurement period. It is the ratio of the mean scalar averaged wind (equation

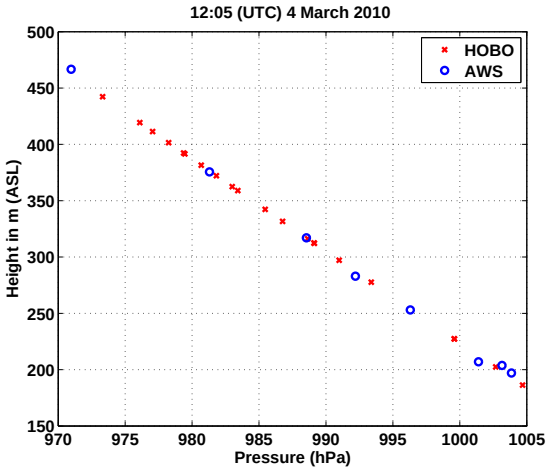

FIGURE 3.12: *Scatter plot of HOBO and AWS pressure using scale height to approximate the pressure at each HOBO.*

3.5) to the mean vector averaged wind (equation 3.6) and is calculated using equation 3.7. Values range from 0 to 1. The closer values are to 1, the more persistent the wind direction is (Farrugia & Micallef, 2006).

$$\overline{V} = n^{-1}\sum_{i=1}^{n} V_i. \tag{3.5}$$

$$|\overline{V}| = (\overline{V}_x^2 + \overline{V}_y^2)^{1/2}. \tag{3.6}$$

$$P_w = \frac{|\overline{V}|}{\overline{V}} \tag{3.7}$$

3.4.3 Measurements of Clun Valley environmental lapse rate

The ELR is calculated using linear regression of 1hr mean HOBO, AWS and mast 2 m temperature measurements. The gradient of the resulting regression is the ELR. Figure 3.13 shows examples of the Clun Valley region ELR calculated using linear regression (red solid line) of the 2 m temperature measurements (blue markers). The black solid lines show one standard deviation of the mean difference in temperature from the regression, which gives an indication of the amount of temperature variation across the sites for each 1hr mean sample. When available an ELR is calculated using radiosondes launched at Duffryn using the same method outlined here. In this instance measurements are used from 0–400 m AGL. The main reason for this approach is that this method of ELR calculation, using and comparing both 2 m temperature and radiosonde data, produced the most useful results for investigations conducted in Chapter 5. Further reasons include: (a) very few

radiosondes are launched during the campaign; (b) there are very few measurements of temperature at heights other than 2 m AGL; (3) the 2 m temperature data is relatively reliable, in terms of quantity and quality, and this method is at least consistent, i.e., all measurements are taken at $\sim$ 2 m AGL.

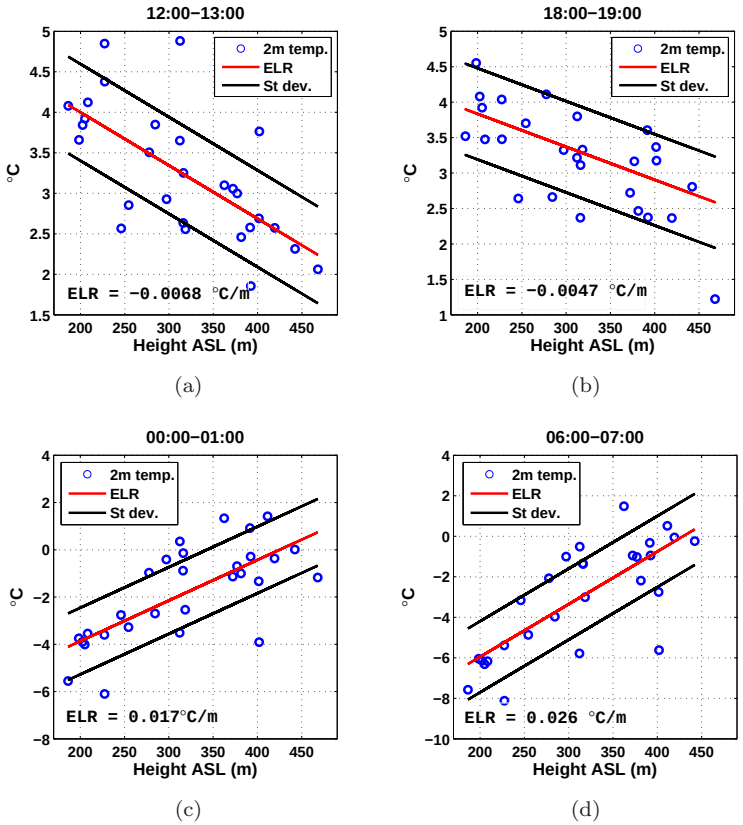

FIGURE 3.13: *Examples of 1hr mean environmental temperature against height for time periods; (a) 12:00–13:00, (b) 18:00–19:00, (c) 00:00–01:00, and (a) 06:00–07:00. The red line shows the ELR, calculated using linear regression. Black lines show the standard deviation.*

3.4.4 Calculation of other variables

Providing there are no concerns with data quality, the eddy correlation method gives the most reliable and direct measurements of turbulent exchanges of momentum and heat in atmospheric science (Pal Arya, 1999). Appropriate measurements of velocity and temperature are recorded at all mast locations; Burfield, Springhill and Duffryn, so that the eddy correlation method is used for investigations here.

3.5 Summary of the COLPEX field campaign

The reliability of the AWS loggers was a major hindrance to the availability of data during COLPEX. The loggers failed, appearing to turn off without reason. In most cases this occurred within two weeks of the loggers being rebooted after site visits and data collection. According to Hobby (2010) the majority of the logger problems stemmed from the use of SD cards that were used to store the data, although there are likely to be a number of contributing factors. As data is key for any field experiment, it is beneficial to use data loggers that are tried and tested prior to any field campaign. Unfortunately in this instance a sufficient amount of testing did not occur to find these potential issues.

Data retrieved from the AWS temperature and RH sensors installed within the aspirated unit was extremely poor, due to a combination of reasons. The two main reasons for poor data were caused by; (1) the sensors being saturated by water and failing, (2) a hardware design fault that caused all other sensors within the sensor unit to fail when any one of the sensors failed. The TB sensors that were installed later in the field campaign were not aspirated, being ventilated naturally by the wind, these sensors had no humidity related issues for the two month period in which they were deployed. The design of any aspirated unit should take into account the possibility of humidity and radiation effects, both of which are likely to be enhanced by a mostly enclosed unit with little ventilation, even if aspirated. The loggers and Sensirion SHT75 temperature and humidity sensors that were installed on the AWS, were showing signs of failure within the first two weeks of the AWS being deployed. On this occasion it appeared that there simply was not enough time devoted to testing both the loggers and sensors prior to their deployment.

The calibration of all AWS sensors was more taxing than it needed to be. Unfortunately due to constraints on time and resources, a comparison between all sensors could not be conducted at one time and had to be conducted at two separate time intervals with half the sensors being compared in each case. This led to a cross comparison of two data sets in order to gain calibration values. Had the calibration exercise been conducted as one data collection exercise, much time is likely to have been saved. It is more efficient to conduct any calibration exercise in one attempt if possible, even if the comparison is conducted over a shorter period of time.

One positive outcome from the field campaign was the successful design of the AWS in terms of power consumption. The AWS were completely self sufficient – with the exception of AWS 9, which was not located in the most ideal place to be powered by solar panels. Vertical profiles of the valley and above valley atmosphere through the LIDAR, Radiosonde launches and by masts, proved to be extremely valuable and generally a reliable data source throughout the field campaign, although again humidity sensors proved to be a problem on the masts. As a result of the problems associated with RH sensors during COLPEX, the Met Office, led by Dr. Jeremy Price, have planned a humidity experiment with the aim of improving RH sensor performance. It may have been beneficial to have a second mast located within the Clun Valley further down-valley from the Duffryn mast site.

A small reconnaissance type field campaign may be the most practical way of improving any field experiment plan and testing of some instrumentation prior to any major field campaign, which is likely to improve data quality and consequently research outcomes – this method formed part of the Convective Storm Initiation Project (see Browning *et al.*, 2007). Realistically, funding restrictions will always govern which instruments can be purchased, how much time can be spent testing prior to any field campaign and how many hours can be assigned to in-field data collection and IOP initiations. No matter how many contingency plans are in place, unexpected problems are always likely to occur.

Chapter 4

A short climatology study of cold-air-pools

4.1 Introduction

Many observational studies of CAPs have been conducted in the past, but these have mostly focused on individual case studies rather than a systematic analysis of CAP formation over a long period of time. Fewer still have been concerned with the occurrence of CAPs over small scales within a system of valleys, where valley or basin widths are less than a few kilometres, depths less than a few hundred meters and with multiple tributary valleys that have different orientations with respect to the ambient wind. Furthermore, there is a lack of climatology studies that focus on the relationship between synoptic conditions and CAPs, as well as understanding the relative importance of valley geometry and local valley flow properties.

Valley flows affect CAP formation in terms of their strength and morphology, primarily by redistributing cold air through advection and by affecting the amount of turbulent mixing generated by shear. Thus valley flows have an impact on the CAP formation mechanism, which is primarily driven by the synoptic conditions such as wind speed and cloud cover. Additionally, the structure of valley flows are also affected by the synoptic conditions above the valley, such as the ambient wind speed and direction.

This study provides a systematic summary of CAP occurrences over a 9–month period. The focus area of this study is the Clun Valley region in Shrophire, England and makes use of the COLPEX field experiment data. It is clear from literature that high wind speeds generally >5 m s^{-1} and cloud cover, limit the formation and growth of CAPs. However, there is a need to further understand how the synoptic conditions effect and interact with CAPs, specifically with regards to the ambient wind direction, the synoptic pressure situation and tributary valleys. The aims of this chapter are to understand;

- When and how often do CAPs occur.
- What synoptic conditions are favoured for CAP occurrences.
- How do synoptic conditions affect/characterise valley winds across the Clun Valley.

Conclusions from this chapter guide the investigations in subsequent chapters.

4.2 Clun Valley weather summary; July 2009 to April 2010

To follow is a summary of the prevailing weather conditions during the course of the COLPEX field campaign from 1 July 2009 to 15 April 2010. The summary draws on data shown in figures 4.1, 4.2 and 4.3. Figure 4.1 shows monthly average 24hr minimum, maximum and mean temperature for England, Wales, Shobdon and Clun. Values for England and Wales are area averages (data supplied by the Met Office http://www.metoffice.gov.uk/climate/uk/). Temperature for Clun is represented by HOBO 2 (2 m AGL and 202 m ASL). HOBO 2 is located on the floor of the Clun Valley ∼5 km WNW from Clun (see figure 3.3).

Figure 4.2 shows monthly sunshine and rainfall anomalies for England and Wales relative to the average period from 1971–2000. Figure 4.3 shows a time series of mean sea-level (msl) pressure, geostrophic wind speed and direction, valley floor and hill top 2 m air temperature – in each case values are representative of the Clun Valley region. Clun Valley region msl pressure is estimated at 13:00 UTC daily using data from the Met Office Unified Model global 1hr forecast simulations (data provided by Dr. Peter Sheridan, Met Office Scientist, see chapter 3 section 3.4.1). Wind speed, wind direction and temperature are 24hr averages. Wind speed and direction is measured at Springhill 30 m AGL (432 m

ASL), which is used as the local measure of the ambient wind at the hill top. Clun Valley temperatures are represented by the hill top site HOBO 17 (372 m ASL) and the valley bottom site HOBO 2 (202 m ASL).

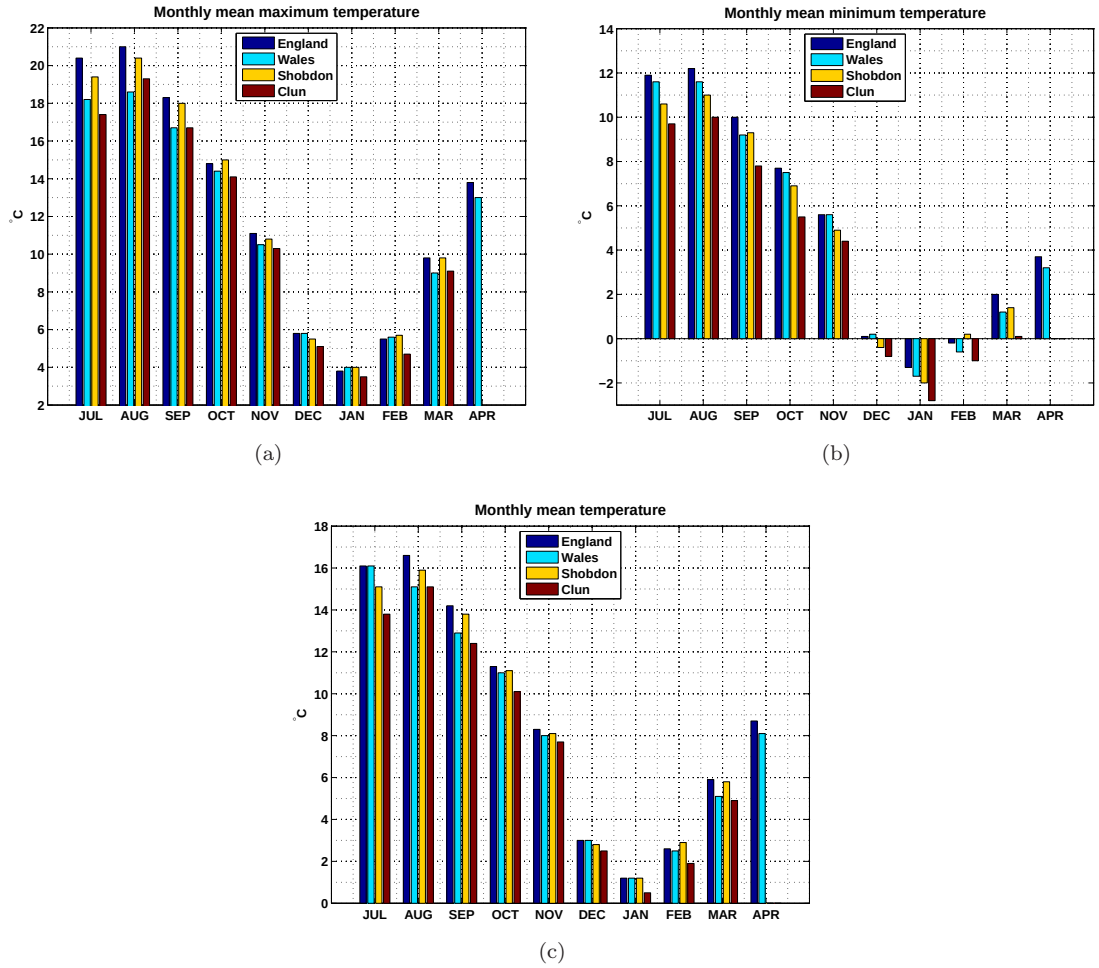

FIGURE 4.1: *Monthly averages of 24hr max, min and mean temperature (°C). Values for Clun are taken from HOBO 2. Values for England and Wales are area averages (supplied by the Met Office http://www.metoffice.gov.uk/climate/uk/). Due to lack of data no values for Clun and Shobdon are shown for April.*

July 2009 was a very cyclonic month for the UK with depressions crossing from the Atlantic and stagnating. At Springhill (30 m AGL) the mean monthly wind speed was 6.2 m s^{-1} from the SW (223°), which is similar in magnitude and direction to the field campaign mean of 6.22 m s^{-1} from the SW (230°). Across England and Wales temperatures tended to be below the 1971–2000 long-term average (Eden, 2009b).

August 2009 was the warmest month during the field campaign. The mean temperature at Clun was 19.3°C and temperatures across the UK tended to be above the 1971–2000

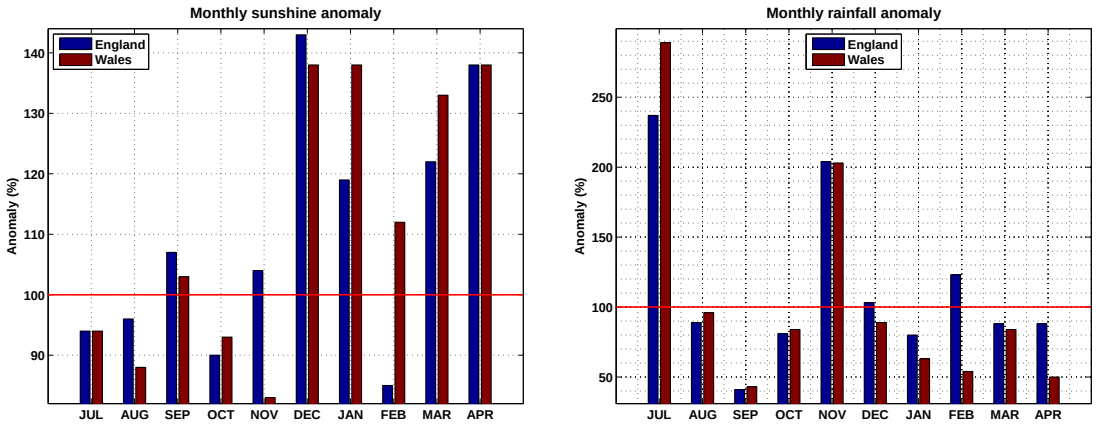

(a) (b)

FIGURE 4.2: *Monthly sunshine and rainfall anomalies for the area average regions of England and Wales relative to the average period from 1971–2000 (data supplied by the Met Office http://www.metoffice.gov.uk/climate/uk/).*

long-term mean. August was dominated by southerly winds, although changeable from W to S (Eden, 2009a).

The UK weather in September 2009 was predominantly anticyclonic (Eden, 2009e). The mean monthly msl pressure for the Clun Valley region was 1022 hPa – the highest monthly mean recorded during COLPEX. The lowest mean monthly wind speed measuring 4.6 m s^{-1} (NW wind directions) recorded at Springhill occur ed in September, which emphasises the anticyclonic tendency in this month. For England and Wales rainfall amounts were below (41% and 43%) and sunshine amounts above (107% and 103%) the 1971–2000 long-term mean (figure 4.2).

The UK weather during October 2009 can be summarised as dull, but dry, with a cyclonic tendency (Eden, 2009d). The lowest mean daily temperature recorded at Clun during the month coincided with a wind direction shift to the N and a drop in wind speed to values between 2–3 m s^{-1} (figure 4.3).

November 2009 was wet, mild and the most cyclonic month during COLPEX. An almost uninterrupted series of low pressure systems swept across the UK with few anticyclonic interludes (Eden, 2009c). The mean monthly msl pressure for the Clun Valley region was the lowest recorded, measuring 998 hPa. The mean wind speed at Springhill measured 8.9 m s^{-1} (SW wind direction) and was the highest monthly mean recorded. Rainfall for

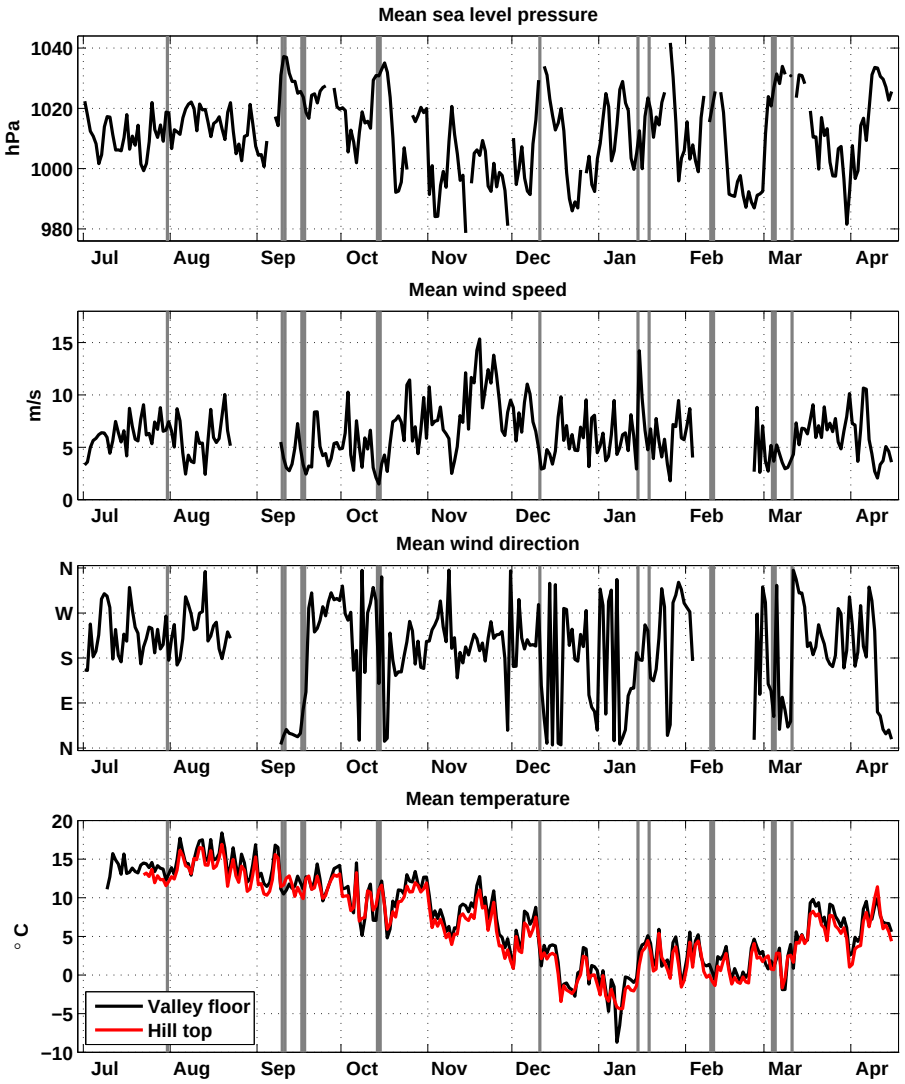

FIGURE 4.3: *Time series of daily msl pressure (*hPa*), mean wind speed (*m/s*), mean wind direction (°) and mean temperature (*°C*). Air temperature (*2 m *AGL) is represented by the Clun Valley floor site HOBO 2 in black (*202 m *ASL) and the hill top site HOBO 17 in red (*372 m *ASL). Solid vertical grey lines represent IOPs.*

England and Wales was much higher than the 1971–2000 long-term mean and sunshine in Wales well below (figure 4.2).

The first ten days of December continued the relatively warm and unsettled conditions experienced in November. However, much colder conditions followed (Eden, 2010b). Northerly winds, a drop in temperature, an increase in msl pressure and frequent snow showers set in from the middle of the month. The monthly mean minimum temperature at Clun was −0.8°C. Above average sunshine was seen across England and Wales measuring 143% and 138% respectively (figure 4.2(a)).

The cold conditions experienced over the UK in the second half of December 2009 continued into the first half of January 2010. An exceptional spell of cold weather followed, with snow cover across much of the UK; including the Clun Valley region. The second half of January was unremarkable (Eden, 2010d). A rapid temperature increase occurred in the middle of the month (14–15 January) causing a rapid thaw of the lying snow. This temperature jump is seen in figure 4.3. The coldest day throughout COLPEX occurred on the 7 January. The 24hr mean temperature recorded by HOBO 2 near Clun was $-8.7°$C (figure 4.3). The monthly average minimum, maximum and mean temperature for January at Clun (HOBO 2) was the lowest recorded during the field campaign (see figure 4.1). Accompanying the low temperatures was a relatively high monthly msl pressure, measuring 1015.1 hPa and a mean wind direction from the NW (316°) measured at Springhill. Sunshine was above average across both England and Wales (figure 4.2(a)).

February 2010 was broadly cyclonic with the exception of an anticyclonic period during the second week. The second half of February was exceptionally cyclonic (Eden, 2010c). A drop in msl pressure is clearly seen in figure 4.3 around 18 February (Julian day 412). Although February 2010 was relatively cyclonic it was a gale-free month with no gusts above 26 m s^{-1} observed (Eden, 2010c). The mean wind recorded at Springhill was 5.8 m s^{-1} from the W (279°).

The first half of March 2010 was predominantly anticyclonic and the second half cyclonic (Eden, 2010e). For the first two weeks the wind tended to be from the N and <5 m s^{-1}. Later in the month the wind tended to be from the S and >5 m s^{-1}. This change coincides with a jump in the mean daily temperature (figure 4.3). Monthly sunshine amounts for England and Wales were above the 1971–2000 long term mean; however, most of this coincided with the colder first half of the month (Eden, 2010e).

The COLPEX field campaign concluded in the middle of April 2010. Most of April was dominated by anticyclonic conditions with warm days and cold nights (Eden, 2010a). The period of high atmospheric pressure is clearly seen in figure 4.3 and was accompanied by a change in wind direction from the SW to the NE, and a drop in daily mean wind speed that persisted below 5 m s^{-1} until the end of the field campaign in mid-April. A direct comparison between Clun, England and Wales, was not possible for April.

To understand the phenomena of CAPs it is important to illustrate that during CAP episodes, regions within complex terrain, such as Clun, can be cooler than nearby regions in relatively flat terrain, such as Shobdon. Referring to figure 4.1, in all cases the monthly average minimum and mean temperature measured at Clun is less than observed at Shobdon, and the area means of England and Wales. The average minimum temperature recorded at Clun was lower than Shobdon, England and Wales, in all months. This suggests that night-time temperatures at Clun tended to be far lower in general. The average minimum temperature at Clun is notably cooler than other regions in September, October, January and March, when the monthly rainfall anomalies are below the long-term mean (figure 4.2(b)). The sunshine anomalies for September, January and March are also above the long term average.

During the winter months of December, January and February, the average minimum temperature near Clun was below 0°C, therefore night-time frosts were more likely at Clun throughout winter compared to Shobdon and many regions across England and Wales (figure 4.1). The colder conditions experienced at Clun are likely to increase the risk of: (1) hazardous driving conditions caused by icing on roads, (2) frost damage to crops or reduced seasonal growth/crop yield, (3) livestock health.

4.3 Cold-air-pool occurrence and strength

Throughout the field campaign the mean 2 m air temperature at the valley floor site HOBO 2 (see figure 3.3) is 6.3°C and at the hill top site HOBO 17 (directly south of HOBO 2) is 7.5°C. The coldest site is the valley floor site and a mean temperature difference of 1.2°C exists across the valley depth (170 m). This cold bias in the valley is predominantly caused by the formation of CAPs. CAP occurrence and strength can be defined in a number of ways. In the first instance this will be achieved here by comparing the difference in environmental temperature between a valley bottom site T_{bottom} and a nearby hill top site T_{top}. In this instance a comparison between the hill top site HOBO 17 (372 m ASL, T_{top}) and the valley bottom site HOBO 2 at (202 m ASL, T_{bottom}) is conducted.

A time-series of HOBO 2 and HOBO 17 temperature is shown in figure 4.3. HOBO 2 is located on a relatively flat horizontal surface. HOBO 17 is located on a relatively gentle slope at the head of the Burfield Valley. Slope effects such as thermally driven slope flows,

should be minimal; however, cannot be discounted, especially at HOBO 17. HOBO 2 and 17 are used as both are very reliable compared to other HOBOs, having an almost continuous data-set covering 9 months. For this reason HOBO 17 is chosen preferentially over other HOBOs in flatter regions (such as HOBO 9).

The CAP strength is defined by $T_{top} - T_{bottom}$. In future the CAP strength of a CAP night is defined by the maximum inversion that occurs during any 10 minute mean sample during the night (sunset to sunrise). CAP nights are defined as weak when an inversion between 1–4°C occurs and strong when an inversion larger than 4°C occurs. Using a 4°C threshold results in 12% of all nights being classed as "stong CAP nights", this seems to give a fair reflection of the more extreme CAP nights and yields enough strong CAP nights to conduct the analysis. Nights when an inversion smaller than 1°C occur are referred to as either very weak CAP nights or non CAPs nights.

There are a number of reasons why it may be argued that a comparison of environmental temperature difference conducted in this way may not be the most representative measure of the CAP strength. One such example is that the CAP top may exist above or below HOBO 17 (372 m AGL) – note that local peaks in the region are around 470 m ASL – therefore this investigation may not give a true representation of the total CAP strength. Local microclimatological differences in temperature are not important for investigations here, which are focused on understanding the general statistics of CAP occurrence and strength. This simple temperature comparison, should provide satisfactory results to aid further investigations.

A histogram showing the frequency distribution of night-time CAPs during COLPEX are shown in figure 4.4(a). CAP strength is divided into 1°C bins. CAPs with large temperature inversions occur less often than CAPs with small temperature inversions. Over the 264 night period, the total count of CAP nights with an inversion stronger than 1°C is 119 (45%) and for inversions stronger than 4°C is 31 (12%). Few nights have temperature inversions larger than 7°C. The most extreme CAP events observed measure 9.3°C and 9.9°C, which are clearly distinguishable from other CAP events in figure 4.4(a). These two extreme CAP nights occur back to back between 6–8 January 2010. The most extreme CAP event occurred between 7–8 January 2010. Both nights were very cold across, with widespread snow cover the UK, including the Clun Valley region.

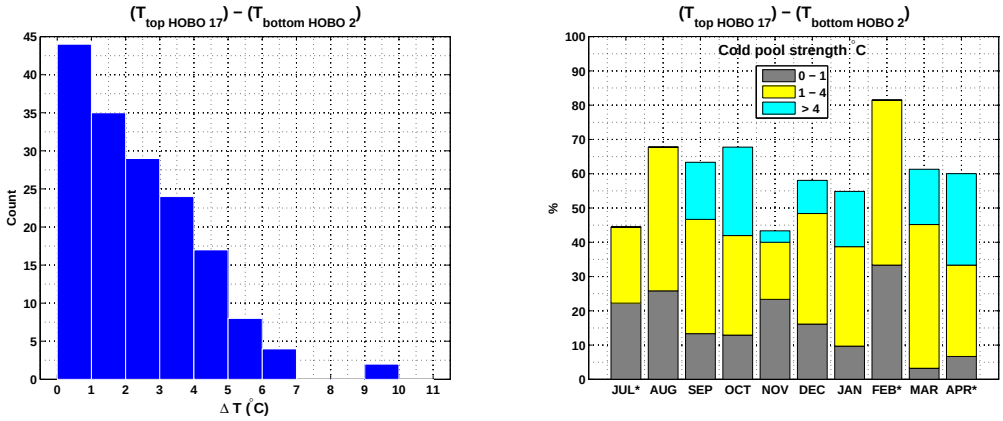

(a) All CAP occurrences

(b) Monthly CAP occurrences

FIGURE 4.4: *CAP occurrence between 23 July 2009 to 16 April 2010. Figure (a) shows the count of CAP occurrences, defined when a positive temperature difference ($T_{top} - T_{bottom}$) occurs during the night-time (based on local sunset and sunrise times). CAP strength is defined using HOBO 17 (372 m ASL) and HOBO 2 (202 m ASL) as T_{top} and T_{bottom} respectively. Figure (b) shows the occurrence of CAPs in each month as a percentage of total days in each month. CAP strength is divided into three bins; (1) 0–1° C (grey), (2) 1–4° C (yellow), (3) >4° C (blue). *There is no data for nights between 1–23 July, 11–12 February and 16–30 April.*

HOBO 6 recorded the lowest minimum temperature during both nights, which is the lowest measurement site at 186 m ASL (see figure 3.3). The minimum temperature were −17.9°C and −18.2°C for the two nights respectively. In comparison, the minimum temperature observed at HOBO 2 (202 m ASL), located ∼5 km up-valley to the west, was −13.8°C and −14.4°C respectively. This highlights the existence of a strong along valley temperature gradient during CAP nights.

Figure 4.4(b) shows the percentage of CAP occurrences during each month. In this case the strength of the CAP is categorised into three bins; grey represents very weak CAP nights (0–1°C), yellow are weak CAP nights (1–4°C) and blue are strong CAP nights (>4°C). The field campaign came to an end in mid April 2010; subsequently data here only represents the period up to 16 April 2010. No strong CAPs are observed in late July and August 2009, but some are seen during September 2009. CAP occurrences are less frequent during November – the most cyclonic month, with the highest mean monthly wind speed seen during COLPEX. Stronger CAP events occur most frequently during October 2009 and for the short period in April 2010. Although many CAPs occurred during February 2009, no CAPs with inversions greater than 4°C are observed, this may in part be due to the cyclonic tendency this month. Additionally the average msl pressure

over the Clun Valley region in February 2010 was 1002.6 hPa, the second lowest observed during COLPEX.

4.4 Relationship to synoptic conditions

To following results show relationships between synoptic conditions and CAP occurrence and strength. Figure 4.5 shows the distribution of wind speed, wind direction and the ratio of upwelling to downwelling LW radiative flux ($LWdn/LWup$), for different CAP strengths. The definition of CAP strengths is the same used in section 4.3.

The ratio of upwelling to downwelling LW radiative flux (F_{lw}) can be an indicator for the amount of cooling caused by the radiative flux divergence. It can also be an indicator for the amount of water vapour (greenhouse effect) and condensed water droplets (radiative effects of cloud) that are present in the atmosphere above. Measurements of F_{lw} are based on the mean night-time measurements obtained from Duffryn at 2 m AGL. Low values of F_{lw} (e.g. 0.75) indicate small amounts of condensed water and a reduced likelyhood of cloud cover. High values of F_{lw} (e.g. 1.0) indicate high amounts of condensed water and/or cloud cover is present. More importantly, in the absence of SW radiation at night, values of F_{lw} <1.0 indicate a divergence in the radiative heat flux i.e., a cooling contribution. This interpretation of F_{lw} is used by others, for example Sheridan *et al.* (2013).

In figure 4.5, 'non CAP nights' (grey histograms) represent all nights where no temperature inversion, or temperature inversions <1°C occur. 'All CAP nights' (yellow histograms) represent both weak and strong CAP nights where temperature inversions >1°C occur. 'Strong CAP nights' (blue histograms) are nights when temperature inversions >4°C occur. The red shaded histograms show the climatology of wind speed, wind direction and F_{lw} for all nights throughout the field campaign – providing data are available – between 23 July 2009 to 16 April 2010.

The distribution of wind speed is distinctly different during strong CAP nights (figure 4.5(c)) compared to non CAP nights (figure 4.5(a)) and all CAP nights (figure 4.5(d)). It is clear from the results shown here that strong CAPs are more likely to occur when the mean night-time wind speed is less than 7 m s^{-1}. Most strong CAPs occur when the wind speed is between 2–3 m s^{-1} and the likelihood of strong CAP occurrence increases

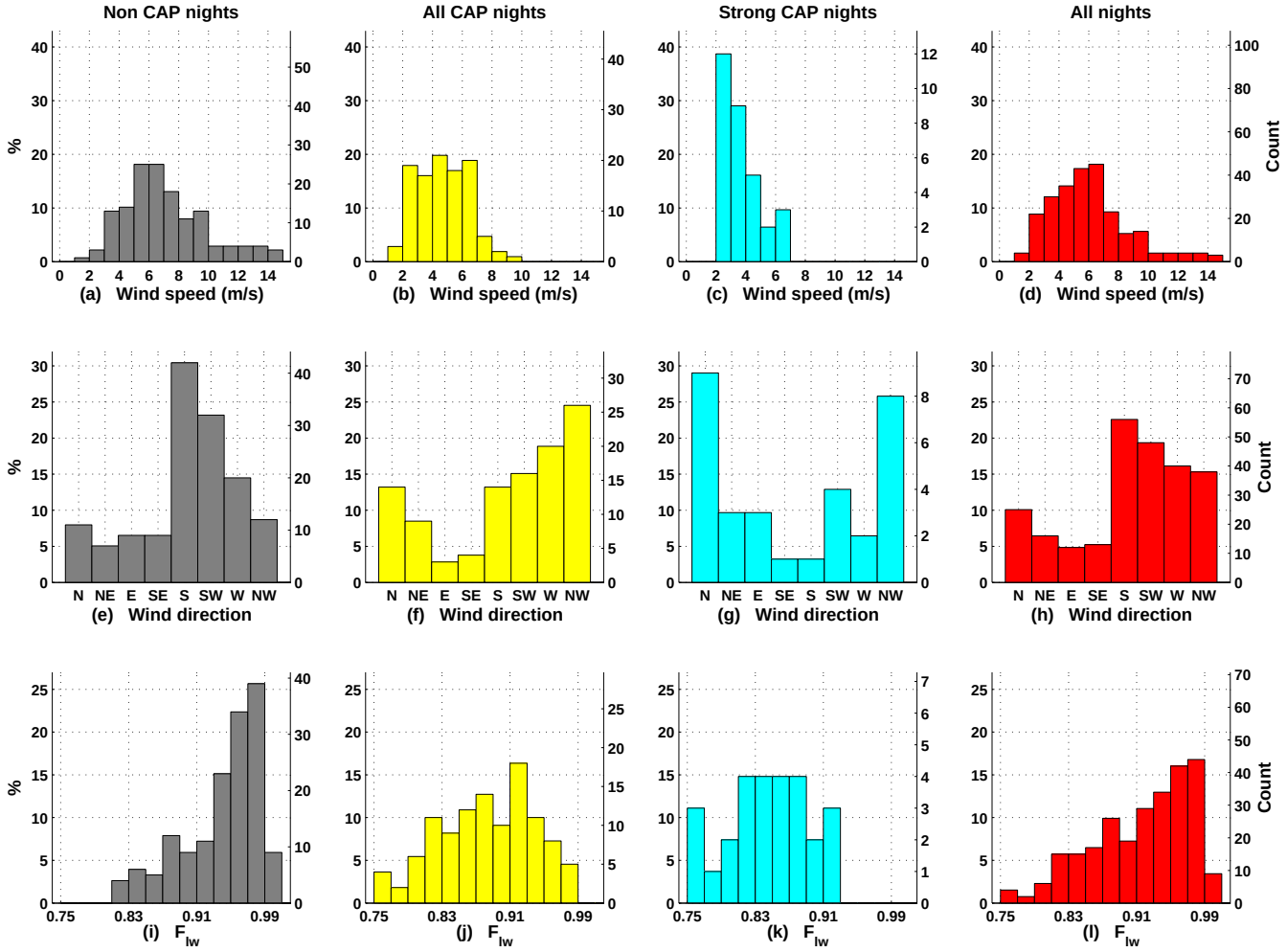

FIGURE 4.5: *Frequency distributions of wind speed (m/s), wind direction (45° segments) and the ratio of LW dn to LW up (F_{lw}), for; non CAP occurrences (grey), CAPs with an inversion stronger than 1° C (All CAP nights, yellow), CAPs with an inversion stronger than 4° C (blue), all nights (red). Winds are measured at the hill top site Springhill 30 m AGL.*

as the wind speed decreases. Over 90% of all CAPs (yellow histogram) occur when the above valley wind speed is between 2–7 m s^{-1} and CAPs rarely occur when the mean night-time wind speed exceeds 7 m s^{-1}. No strong CAP nights occur when the mean night-time ambient wind is below 2 m s^{-1}; mean might-time wind speeds that are rarely seen throughout the field campaign (see figure 4.5 (c) and (d)).

Strong CAPs are more likely to occur when the wind direction is from the N and NW. ∼55% of all strong CAPs occur when the mean night-time wind direction is from the N and NW. Strong CAP events occur less often when the wind is from the SE and S. The wind direction distribution is markedly different when comparing non CAP nights (figure 4.5(e)) to strong CAP nights (figure 4.5(g)). Strong CAPs are more likely when the wind is from the N and NW (∼55% of the time). These wind directions occur rarely during the field campaign – ∼25% of all nights. Strong CAPs are not favoured when wind directions from the S occur, which are seen most often during COLPEX (red histogram).

For the entire field campaign the distribution of night-time mean values of F_{lw} decreases almost linearly from values around 1 down to 0.75 (figure 4.5(l)), which suggests that clear skies and dry atmospheric conditions occur less often than either cloudy skies or an atmosphere that is high in water vapour content. There is a clear change in the distribution of F_{lw} from non CAP nights (figure 4.5(i)) to all CAP nights (figure 4.5(j)) and again to strong CAP nights (figure 4.5(k)). High values of F_{lw} are less likely and values decrease as the CAP strength increases. The distribution of F_{lw} shifts towards lower values during strong CAP occurrences with no strong CAPs seen when values of F_{lw} exceed 0.93, therefore strong CAPs are unlikely to form when values of F_{lw} exceed this value. There is no clear peak in the distribution of F_{lw} during strong CAP nights; however, 60% of strong CAPs occur when values of F_{lw} are between 0.81–0.91. Furthermore CAPs readily form when low values of F_{lw} occur and strong CAPs are more likely to form during these conditions.

Histograms showing the frequency distribution of mean sea level (msl) pressure and pressure gradient (PG) direction, are shown for; Non CAP nights, All CAP nights, Strong CAP nights and All nights, in figures 4.6 and 4.7. The pressure measurements are from UM global model analyse taken at 00:00 UTC each night (see methods 3.3.0.1). In figure 4.6, CAPs generally occur more often for high values of msl pressure. With the exception of two occasions, strong CAPs occur when the msl pressure is above 1007 hPa and over

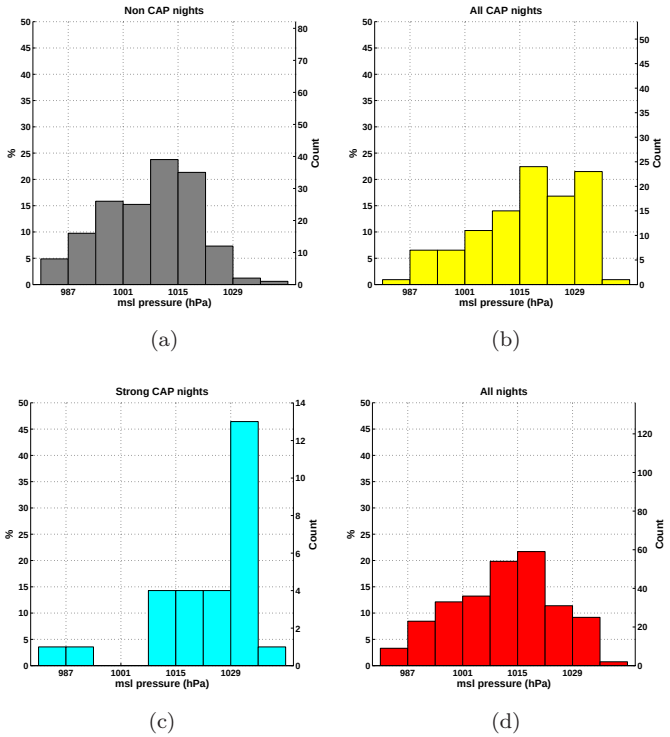

FIGURE 4.6: *Frequency distribution of msl pressure (hPa) for; (a) Non CAP nights, (b) All CAPs nights with an inversion stronger than 1°C, (c) Strong CAP nights with an inversion stronger than 4°C, and (d) All nights throughout the field campaign.*

45% of all strong CAPs occur when the msl pressure is between 1029–1036 hPa. There is a clear difference in distribution of CAP occurences from strong to weak CAPs. Weak CAPs occur across low and high msl pressure nights, but generally occur more often with increasing msl pressure.

In figure 4.7 strong CAPs occur more often when the PG direction is from the NE and E, which combined account for over 45% of all strong CAP occurrences. Strong CAPs occur least of all when the PG direction is from the S, SW, W and N. The distribution of weak CAPs is less distinct and more spread out than for strong CAPs. Weak CAPs occur more often when the PG is from the SE, S and SW, which is the same result seen for All nights in figure 4.7(d). The distribution frequencies of weak CAPs are more similar to the msl pressure frequency distributions of all nights in figure 4.7(d).

Figure 4.8 shows the normalised frequency distributions of wind speed, wind direction, F_{lw}, msl pressure and PG direction, for strong CAP occurrences (>4°C) as a percentage of all occurrences during the field campaign (see red histograms in figures 4.5, 4.6 and 4.7). These results clearly show that strong CAP nights occur more frequently with decreasing

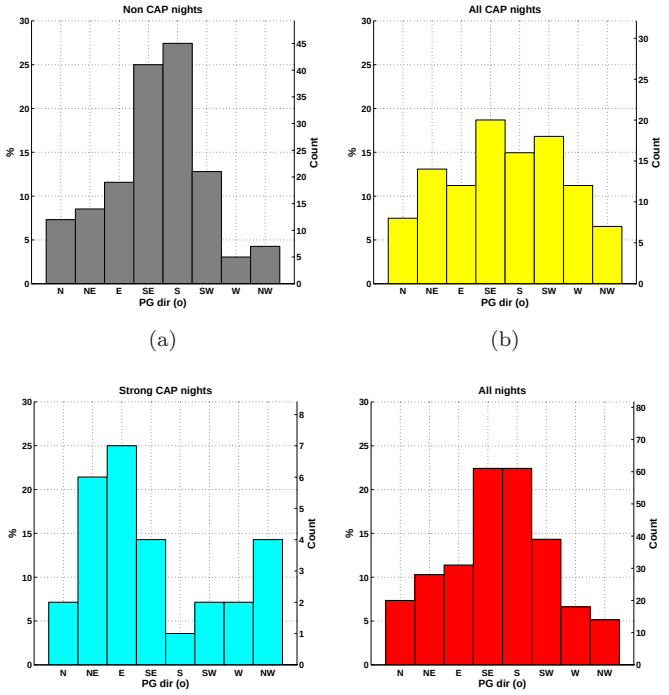

FIGURE 4.7: *As in figure 4.6, except frequency distributions of pressure gradient direction are shown in 45° segments. The PG direction is from high to low pressure.*

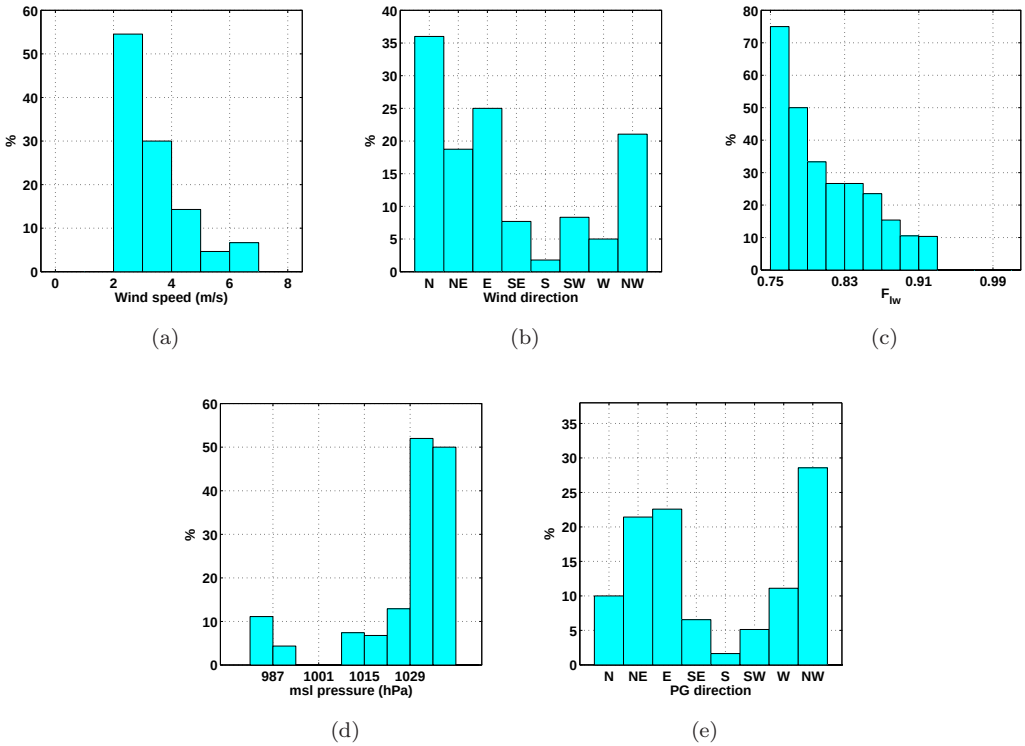

FIGURE 4.8: *Normalised frequency distributions showing the occurrence of strong CAPs (>4° C) as a percentage of the total observed for each bin thoughout the COLPEX field campaign.*

wind speed and decreasing F_{lw}. Strong CAPs also occur for 50% of all nights when the msl pressure is >1029 hPa.

Strong CAP forming nights occur over 20% of all nights when the wind direction is from E and NW, with the highest percentage occuring when from the N. Furthermore, <3% of all nights result in strong CAP nights when the ambient wind direction is from the S, therefore this is the least favoured wind direction for strong CAPs to form. Pressure gradient directions from the NE, E and NW are more likely to result in strong CAP nights than other directions, with these occuring over 20% of the time in each instance.

4.4.1 Relationship between synoptic components

The following results investigate the relationship between components of the synoptic meteorology and the CAP strength. Joint distribution functions for strong CAPs only are not conducted due to data limitations, i.e., only 31 nights in total are strong CAP forming nights. Additionally, gaps in different data sets often leads to fewer than 31 nights being compared. It should also be noted that some comparison of meteorological components using the COLPEX dataset have been conducted by Sheridan *et al.* (2013, figure 10), the results in figure 4.9 should be viewed as an extention of this.

For all comparisons shown in figure 4.9, CAPs strengths above 4°C are represented by dark blue filled circles (4 K/170 m). The clearest relationship between meteorological components is shown between msl pressure and wind speed (figure 4.9(c)). In this instance many strong CAP nights occur when the msl pressure is above 1025 hPa and the mean night-time wind speed at Springhill is <3 m s^{-1}. Additionally, many strong CAPs form when the msl pressure is both >1025 hPa and the wind direction has a northerly component (figure 4.9(a). Further to this low pressure situations are extremely uncommon when the mean ambient wind direction has an easterly component.

As shown previously in figure 4.5, the strongest CAPs tend to form when F_{lw} is less than 0.93. Figure 4.9(b) also indicates that very few strong CAPs occur when the wind direction has a southerly component and when they do occur values of F_{lw} are often relatively high, between 0.93 to 0.9, and values below 0.9 rarely occur. Interestingly, values of F_{lw} exceeding 0.9 rarely occur when the wind direction has an easterly component. Therefore combining results in figures 4.9(a) and 4.9(b), many strong CAP nights occur when; the

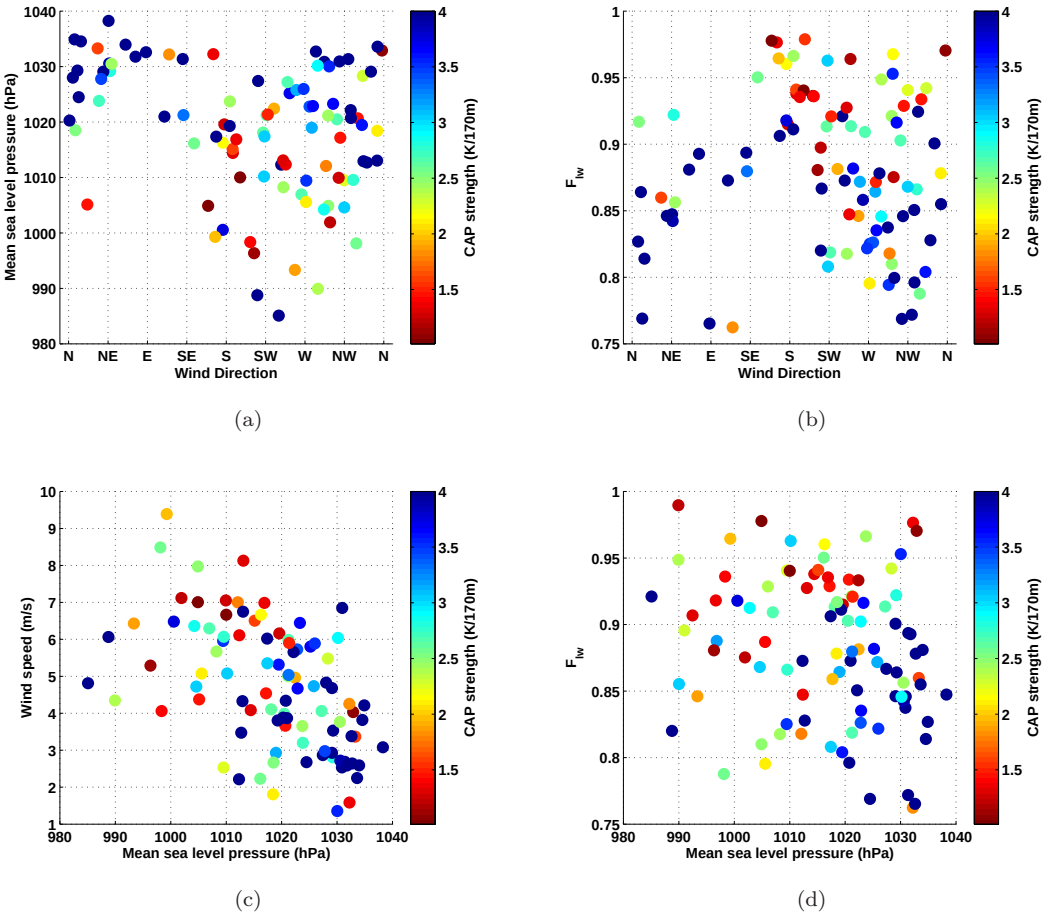

FIGURE 4.9: *Comparisons of night-time; (a) Springhill wind direction versus mean sea level (msl) pressure (hPa), (b) Springhill wind direction versus F_lw, (c) msl pressure versus Springhill wind speed, (d) msl pressure versus F_{lw}. All CAP strengths exceeding 4° C are represented by the maximum value of 4 K/170 m in the colour bar.*

ambient wind direction at Springhill has an easterly component, the air mass tends to be dry (low values of F_{lw}, e.g., 0.9), and has high atmospheric pressure (msl pressures >1020 hPa).

Figure 4.10(a) shows the relationship between the night-time synoptic PG direction and the mean night-time ambient wind direction at Springhill (30 m AGL) for weak (0–4°C) and strong (>4°C) CAPs nights. The expected geostrophic wind – based on the model pressure situation – is marked by the red solid lines. The PG and Coriolis force are assumed to exactly balance, therefore the wind direction is assumed to run parallel to the isobars and rotate clockwise around high pressure systems in the Northern Hemisphere, resulting in the geostrophic wind being rotated 90° clockwise to the PG direction.

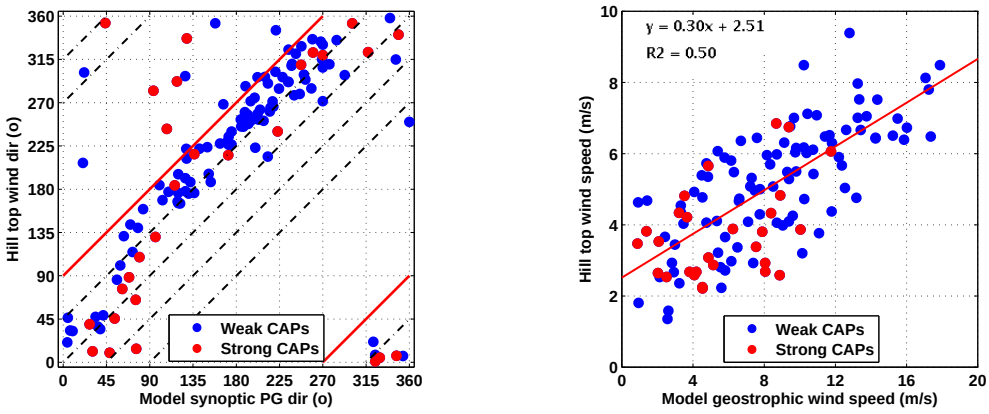

(a) (b)

FIGURE 4.10: *Comparisons of; (a) model PG direction at 00:00 UTC versus Springhill 30 m night-time mean wind direction, and (b) calculated model geostrophic wind speed (U_g) at 00:00 UTC versus Springhill 30 m night-time mean wind speed (U_{spring}). Red line in (b) shows the best fit using linear regression.*

For the most part the ambient wind is turned 45–90° clockwise to the synoptic PG direction; however, there is much variation, especially when the ambient wind is between 180–360°. The largest deviation away from 45–90° occurs in the upper-left part of figure 4.10(a), when the synoptic PG has an easterly component between 0–180° and the ambient wind direction is between 180–360°; many of these nights are strong CAP forming nights. There also appears to be a cluster of nights between 0–90° when the PG and ambient wind directions are similar. In these instances the ambient wind direction varies anticlockwise or clockwise to the synoptic PG direction between 0–45°, again many of these are strong CAP forming nights. A similar pattern is seen for some weak CAP nights also; however, the ambient wind for weak CAP nights is only rotated anticlockwise to the PG direction on two occasions.

A comparison of the model geostrophic wind speed U_g at 00:00 UTC each night (see methods 3.3.0.1), to the mean night-time ambient wind speed at Springhill U_{spring} (30 m AGL), is given in figure 4.10(b). Linear regression shows a relatively strong positive correlation between U_g and U_{spring}. Values of U_{spring} lower than 2 m s^{-1} only occur when U_g is below 4 m s^{-1}, but can be higher than 5 m s^{-1} under similar values of U_g. The R^2 calculation indicates that 50% of the variance in U_{spring} can be explained by U_g. Strong CAP nights do not occur when high wind speeds and high PGs occur.

In figure 4.5 the number of CAP nights (temperature inversions >1°C) that occur with

N and S ambient winds are the same, with 14 CAP nights in each case; however, there is only one strong CAP when the wind direction is from the S (temperature inversion <4°C) compared to nine when the wind direction is from the N. Subsequently there is a larger conversion of weak to strong CAPs when the wind direction is from the N than when from the S. Figure 4.11 shows wind roses for; (a) ambient wind speed at Springhill 30 m AGL,

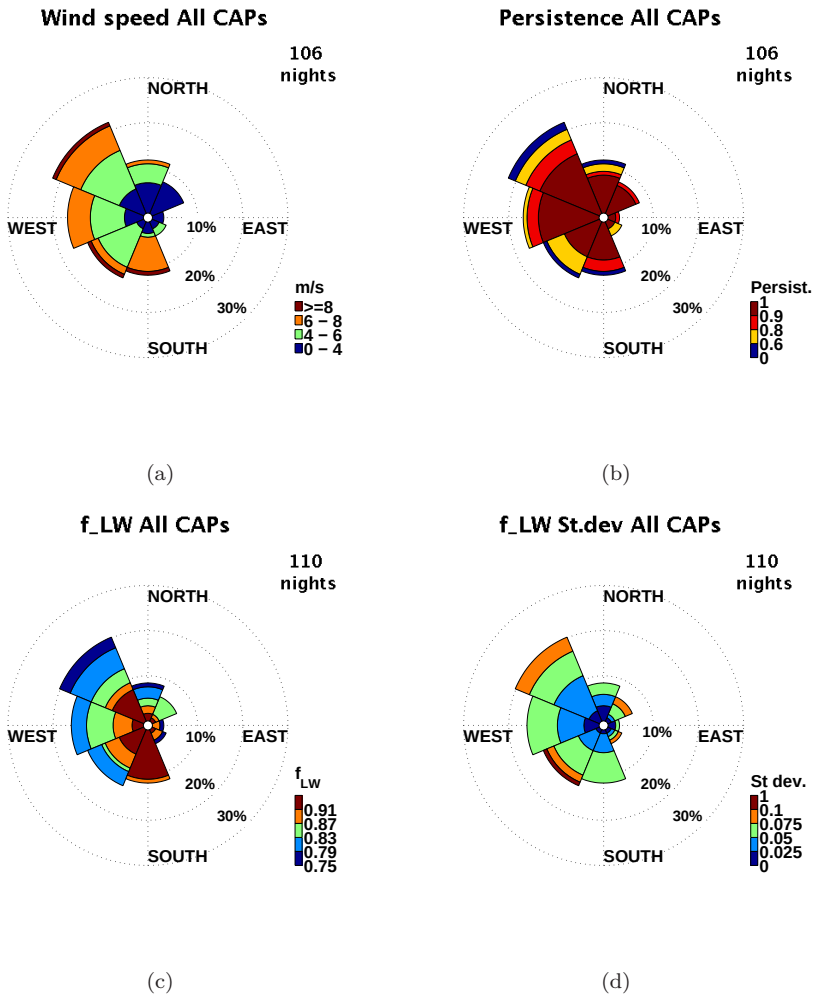

FIGURE 4.11: *Wind direction rose plots of wind speed at; (a) Springhill, (b) persistence of the wind, (c) night-time mean F_{lw} at Duffryn, and (d) the night-time standard deviation of F_{lw}. All plots are for CAP nights only.*

(b) wind persistence, (c) F_{lw} at Duffryn (2 m), and (d) the standard deviation of F_{lw}, for all CAP nights. In figures 4.11(a) and (c), the wind speed and F_{lw} values are much higher for S wind direction night than those when the wind direction is from the N and NW. Viewing figure 4.11(a) it is clear that the majority of CAPs that form during southerly wind directions are subject to wind speeds exceeding 6 m s^{-1}. Southerly wind directions also coincide with high values of F_{lw} (figure 4.11(c)).

Wind persistence (figure 4.11(b)) and the standard deviation of F_{lw} (figure 4.11(d)) serve as indicators of changeable conditions. There appears to be very little difference in distributions across all wind directions; however, winds from the SW are less persistent relative to other directions. SW winds also have larger standard deviations of F_{lw}. These results suggests that the synoptic conditions are more changeable when a SW wind direction prevails.

4.4.2 Summary

Results here show that strong CAPs are favoured when the following synoptic conditions prevail:

- Above valley ambient wind speeds <7 m s^{-1} the likelihood increases with decreasing wind.
- Above valley ambient wind directions from the N and NW.
- Values of $F_{lw} < 0.93$ and the likelihood increases with decreasing F_{lw}.
- High pressure situations above 1029 hPa and the likelihood increases with increasing msl pressure.
- PG directions from the NW, NE and E.

Results in figure 4.9 highlight that ambient wind directions with an easterly component often result in atmospheres that are dry (low values of F_{lw}) and have relatively high atmospheric pressure (msl pressures >1020 hPa). These three factors combined more often than not lead to strong CAPs (>4 K/170 m).

The ambient wind (Springhill 30 m AGL) appears to be more similar to the synoptic PG direction, than the expected geostrophic wind direction, for N and NE ambient wind directions. Additionally there are some instances when the ambient wind direction is rotated 90° clockwise to the geostrophic wind (180° clockwise to the PG direction); however, these situations only occur when the ambient wind direction is between 180–360° and are mostly CAP forming nights.

Results in figure 4.11 suggest that S wind directions rarely result in strong CAPs due more changeable conditions occurring for these wind directions. However, there appears to be no stand out reason as to why strong CAP nights form preferentially when the wind direction is from the N and NW, compared to other wind directions, which also experience low wind speeds and low values of F_{lw}.

4.5 Wind climatologies

The following wind climatology results are presented in two sections. The wind climatology of each site is shown in section 4.5.1 in the form of wind roses. Secondly, the relationship between the ambient wind (above valley wind) and the valley wind is shown in section 4.5.2. The ambient wind is represented by measurements taken at the hill top mast site Springhill at 30 m AGL. All locations used in the following analysis are indicated in pull out map figure 3.3.

4.5.1 Wind rose climatologies

The following wind rose climatology results are split into two sub sections; (1) wind measurements taken above 300 m ASL, and (2) wind measurements taken below 300 m ASL. The results are presented in this way since it is expected that sites located at similar altitudes will share much of the same characteristics. Sites located above 300 m ASL include; AWS in the upper parts of the valley or located near surrounding peaks, Burfield, and Springhill. Sites located below 300 m ASL include; AWS located along the Clun Valley floor (black valley in figure 3.3), AWS tributary valley sites (red, blue and magenta valleys in figure 3.3), and Duffryn.

For each site the wind climatology is shown for; (a) night-time winds only (Night), and (b) wind data during CAP nights only (CAP night). On occasions the wind climatology is shown for (c) daytime winds only (DAY), and (d) all field campaign wind data (All). As in section 4.3 previously, CAP nights are defined when a temperature inversion >1°C occurs during the night. All wind rose climatology results are from 10 minute mean data. The entire wind rose climatology is provided in Appendix B.

4.5.1.1 Sites above 300 m

Figure 4.12 shows the wind climatologies at Springhill, which is located on a hill top between the Burfield Valley and Clun Valley (see figure 3.3). The Springhill wind climatologies give an indication of the ambient wind that prevails throughout the field campaign. Wind climatologies are shown for measurements taken at 10 m and 30 m AGL. Overall, the wind speeds at 30 m are higher compared to those at 10 m. Most notably wind speeds exceeding 10 m s^{-1} occur most often at 30 m than at 10 m and more often than not, have a westerly wind component when they occur.

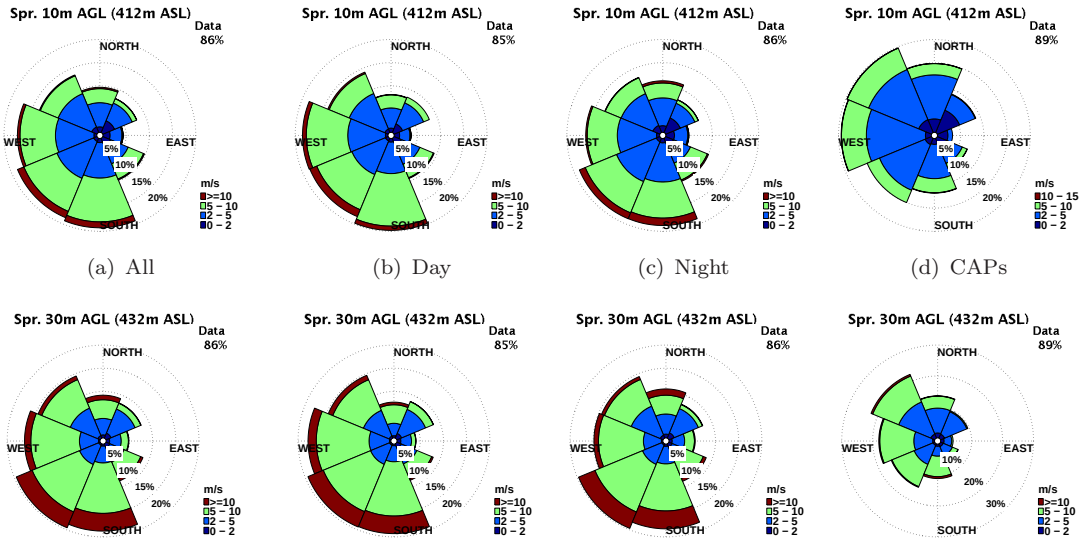

(a) All (b) Day (c) Night (d) CAPs

(e) All (f) Day (g) Night (h) CAPs

FIGURE 4.12: *Wind rose plots of 2 m wind speed and direction for Springhill, 10 m and 30 m AGL. Four wind rose plots are shown for each height, from left to right they are; (1) All wind data for the 204 day period from 29 September to 20 April, (2) for daytime wind data only, (3) for night-time wind data only, (4) for all CAP nights (inversion larger than 1° C). Wind speed (m s^{-1}) is represented using a colour scale. Each segment of the wind rose represents 45°. Percentage values under "Data" represent the total amount of data available for each climatology study.*

There is little change in the distribution of wind directions for All, Day and Night climatologies at Springhill. The wind climatology of CAP nights (figure 4.12(d) and (h)) is noticeably different compared to the other climatologies. As a general rule, this pattern is consistent across all climatologies at other sites, with the Night, Day and All climatologies, tending to be very similar (see Appendix B). Therefore the majority of the subsequent results are focused on comparisons between the CAP night and Night climatologies.

Winds with an easterly component occur least often generally. Referring to figure 4.12 specifically, easterly winds are less frequent and are weak (<5 m s^{-1}) when they do occur, rarely exceeding 5 m s^{-1} at 10 m at any location. At Springhill, during CAP nights the wind speeds are generally lower, never exceeding 10 m s^{-1} at 10 m and infrequently exceeding 10 m s^{-1} at 30 m. Winds from NW and W occur most often and winds from the S, SE, E and NE occur least often. However, there is more variability in the wind direction at 10 m than at 30 m, with NW winds occurring most often at 30 m.

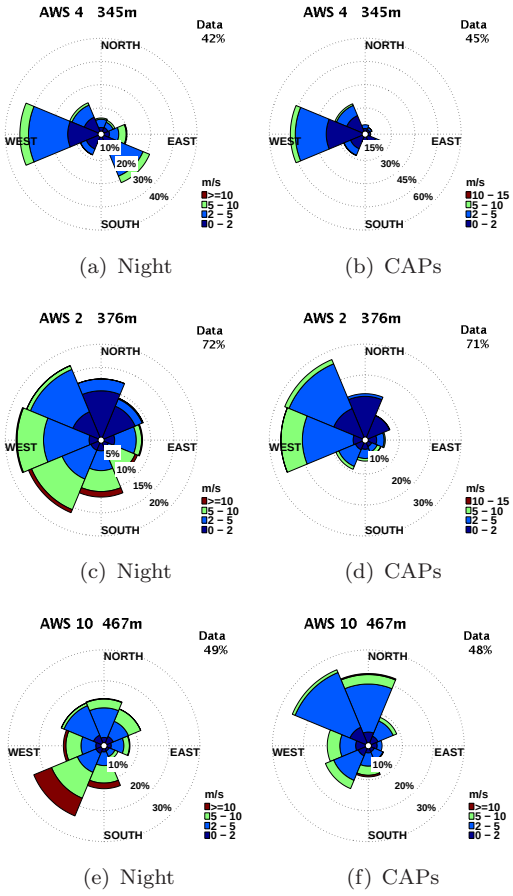

(a) Night (b) CAPs

(c) Night (d) CAPs

(e) Night (f) CAPs

FIGURE 4.13: *As in figure 4.12, except wind measurements are for all AWS located above 300 m ASL. All and Day climatologies are included in Appendix B. AWS measurements are at 2 m AGL.*

The Night and CAP night wind climatology for all AWS located above 300 m ASL, are shown in figure 4.13. The AWS climatology results in figure 4.13 share some characteristics with each other and to those seen at Springhill. Although there are noticeable differences in the wind climatologies of each AWS. Each have their own individual wind distribution pattern, which is likely to reflect the fact that each site is located in distinctly different geographical locations. As with the hill top site Springhill, the AWS wind climatologies

for All, Day and Night do not differ greatly at each individual site; however, as seen st Springhill the wind distribution is dramatically different during CAP nights.

Wind speeds rarely exceed 10 m s^{-1} across all AWS in figure 4.13, but do occur more often at the highest elevated site AWS 10. At AWS 10 high wind speeds tend to occur when the wind direction is from the W, SW and S; the same result observed at Springhill (figure 4.12). The lowest wind speeds occur at AWS 4, located in the upper part of the Clun Valley (see figure 3.3). The winds at AWS 4 are also the least variable compared other AWS located above 300 m and Springhill.

For Night climatologies, the winds at AWS 4 are mostly confined to the W and SE directions, which are roughly parallel to the local valley axis at that location – AWS 4 is located on a bend in the valley, directly up-valley the valley is orientated roughly W to E and directly down-valley is orientated NW to SE. During CAP nights, the SE winds are almost entirely absent and winds from the W occur more often for Day and Night climatologies. Results here clearly show that winds at AWS 4 are mostly confined to wind directions that reflect the local topography with winds aligned either up-valley or down-valley; predominantly down-valley during CAP nights.

At AWS 2 and 10 – both located on gentle slopes near hill top regions – the CAP night climatologies are noticeably different from All, Day and Night climatologies. For All, Day and Night climatologies, winds at AWS 2 and 10, like Springhill, are biased towards winds with a westerly component, mostly occurring from the W and SW respectively. The highest wind speeds occur at the highest elevated site AWS 10. During CAP nights the winds at AWS 2 are mostly confined to the NW and W, which are roughly perpendicular to the slope. Again winds from the E rarely occur at AWS 2 at any time. When winds from the N and NE occur at AWS 2, they extremely light ($\leq$2 m s^{-1}). At AWS 10, winds from the NW and N occur most often during CAP nights and wind speeds rarely exceed 5 m s^{-1}. The regions north of AWS 2 and AWS 10 are upslope, therefore both AWS are sheltered from the ambient wind when winds from this direction prevail.

Figure 4.14 shows the wind climatologies for the Burfield mast site at 2 m (AWS 1) and 30 m AGL. The Burfield site is located within in a bowl shaped region of the Burfield Valley (highlighted yellow in figure 3.3). The All, Day and Night climatologies (see Appendix B) at Burfield share similarities to those at AWS 10, AWS 2 and Springhill. Higher wind

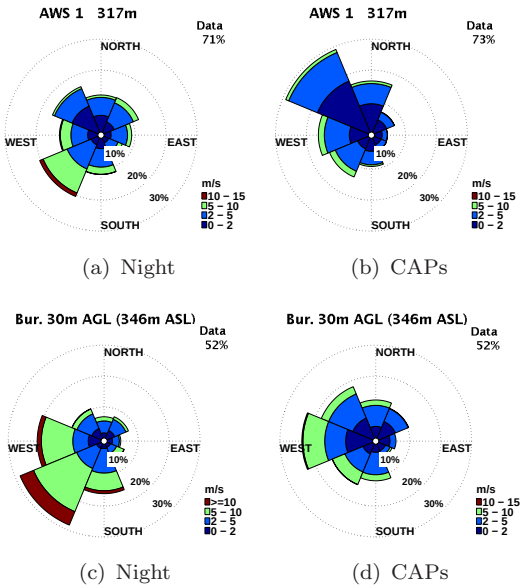

(a) Night (b) CAPs

(c) Night (d) CAPs

FIGURE 4.14: *As in figure 4.12, except wind is measured at the Burfield mast site, which includes AWS 1. Measurements are at* 2 *m (AWS 1) and* 30 *m AGL.*

speeds are more likely to occur with increasing height and higher wind speeds occur more often when wind directions are from the W, SW and S.

Wind directions from the SW occur most often at Burfield during All, Night and Day climatologies. During the Night, winds at 2 m are markedly different compared to those at 30 m. The winds are more varied at 2 m and although SW wind directions occur most often, wind directions from the NW, N, NE and E occur more often at 2 m than at 30 m. This is likely to be a characteristic of the lighter winds occurring with decreasing height. This part of the Burfield valley is also bowl shaped, unlike many parts of the Clun Valley that are relatively narrow. Additionally there are many small tributary valleys that feed into the Burfield Valley from the W, NW, N and NE, which may account for variability seen at 2 m AGL at Night.

During CAP nights, winds from the NW and W occur most often and are generally light, rarely exceed 5 m s^{-1} at 2 m and occasionally exceed 5 m s^{-1} at 30 m AGL. Winds from the W are most dominant at 30 m and are strongly favoured from the NW at 2 m, therefore the winds turn anticlockwise with height. The NW winds seen at 2 m during CAP nights are parallel to the main Burfield Valley axis and are down-valley, a similar result seen at AWS 4 also (see figure 4.13(b)). Again during CAP nights, winds with an easterly component rarely occur and infrequently exceed 5 m s^{-1} when they do.

4.5.1.2 Sites below 300 m

To follow are the wind climatology results for all sites located below 300 m (ASL). Figure 4.15 shows all AWS sited along the floor of the main Clun Valley (highlighted black in figure 3.3). In each case the wind speeds are low and rarely exceed 5 m s^{-1} at any time. The highest wind speeds are seen at AWS 6, located at the valley bottom near Clun (see figure 3.3). Wind speeds exceeding 5 m s^{-1} do occur on occasions but are limited to the W, SW, S and E. During CAP nights all winds are below 5 m s^{-1}. The lowest wind speeds occur during CAP nights and rarely exceed 2 m s^{-1} at all three AWS located along the Clun Valley floor (figure 4.15).

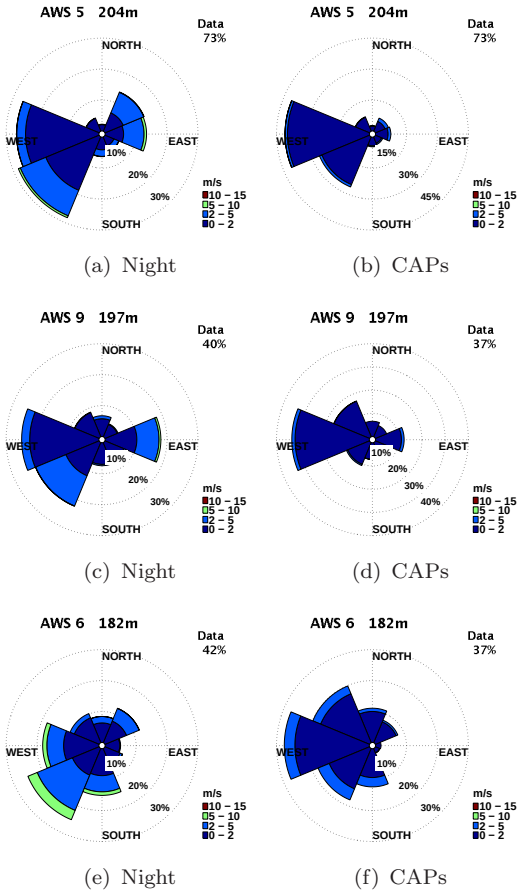

(a) Night (b) CAPs

(c) Night (d) CAPs

(e) Night (f) CAPs

FIGURE 4.15: *As in figure 4.12, except all AWS in this case are located below* 300 *m ASL along the floor of the Clun Valley.*

The AWS 5 and 9 wind rose results are similar, but there are some noticeable differences. AWS 5 and 9 are located less than 2 km apart and are at similar elevations (see figure 3.3). For Night climatologies the winds at AWS 5 tend are restricted to the four opposing

segments (W, SW, NW and E, same for Day also, see Appendix B), which are roughly aligned to the valley axis, trending from SSW to the NNE. Similarly at AWS 9 the Night wind climatologies are restricted to the W, SW and E, again being roughly aligned to the valley axis, which at AWS 9 is roughly orientated NNW to SSE. However, at AWS 9 the up-valley component is more restricted than the down-valley component.

More variation in the wind direction is seen at AWS 6 compared to AWS 5 and 9, which are located further up-valley to the west. During the Night, winds from the S, SW and W occur most often at AWS 6, a pattern mirrored by other AWS sites located at more exposed regions at higher altitudes, i.e., Springhill. During CAP nights lighter wind speeds are seen at all three AWS. Again more variation of the wind direction is seen at AWS 6 compared to AWS 5 and 9. However, winds with an up-valley direction from the E are almost completely absent, instead winds are predominantly down-valley having a westerly component.

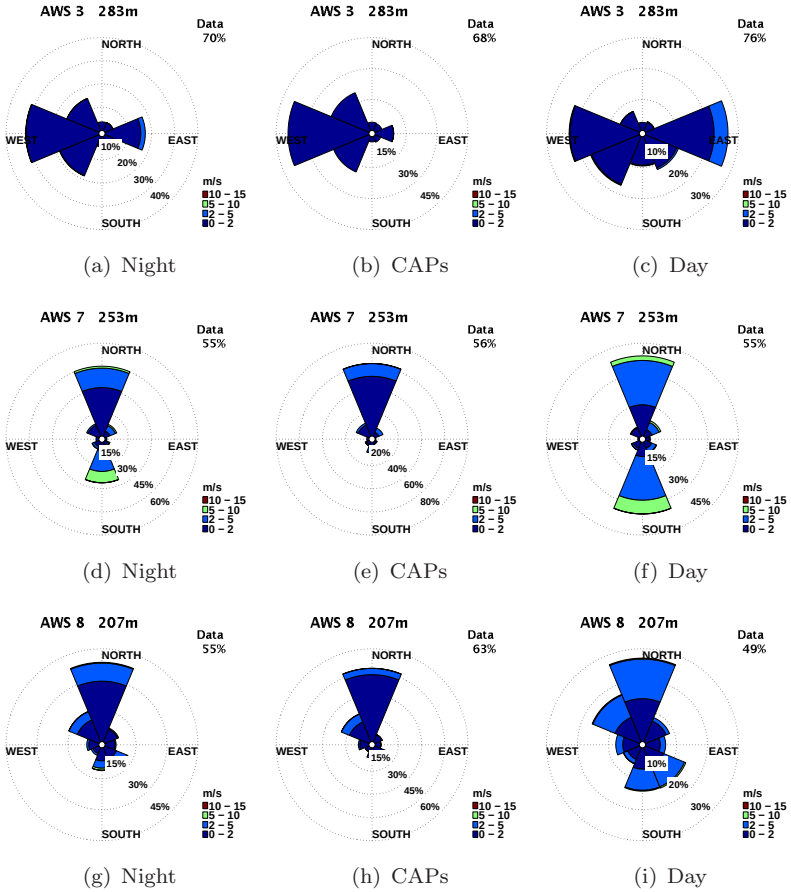

(a) Night (b) CAPs (c) Day

(d) Night (e) CAPs (f) Day

(g) Night (h) CAPs (i) Day

FIGURE 4.16: *As in figure 4.12, except all AWS in this case are located below* 300 *m ASL on the floor of tributary valleys that feed into the Clun Valley.*

Figure 4.16 shows the climatologies of AWS located in tributary valleys that connect to the main vein of the Clun Valley. AWS 3 is located in a small tributary valley (highlighted magenta in figure 3.3), which is roughly orientated W to E, slopes to the east and connects to the main vein of the Clun Valley near Duffryn. AWS 7 and 8 (highlighted blue and red in figure 3.3 respectively) are situated in larger tributary valleys, which are orientated roughly NW to SE and N to S respectively. Both connect to the main vein of the Clun Valley from the N. AWS 8 is the lowest elevated site and AWS 3 the highest.

As with other AWS sited below 300 m, the wind directions at all three tributary sites are strongly confined to wind directions that reflect the local orientation of the valley axis, aligned up or down-valley. The wind directions are strongly up or down-valley for both Day (see Appendix B) and Night climatologies. However, unlike AWS at other locations within the Clun Valley, up-valley winds at AWS 3 occur more often than the down-valley component during the day. The up-valley winds are also strongly confined to the E. In contrast the down-valley wind appears to be more variable being from the NW, W or SE, a similar pattern is seen at AWS 5 and 9 (figure 4.15). The wind speeds at AWS 3 are also lighter compared those at other sites, tending to be less than 2 m s^{-1}, except when up-valley winds from the E occur.

Stronger winds are seen at AWS 7 compared to most other valley floor sites, this is especially true for Day and Night climatologies. The wind directions at AWS 7 are strongly confined up and down-valley, from the N and S. The wind directions at AWS 8 are less confined than those at AWS 7. The up and down-valley winds at AWS 8 at night are more reminiscent of the patterns seen at AWS 5 and 9. One noticeable feature seen at AWS 8, are the down-valley NW and N winds, which are more prominent during the day than the up-valley winds from the S and SE; a pattern that is not mirrored at other locations (see Appendix B), this appears to be a local daytime phenomena seen at AWS 8 only.

The wind distribution of the tributary sites AWS 3, 7 and 8, changes for CAP nights. As seen at other valley floor locations down-valley winds are prominent, but up-valley winds are absent. The winds do not exceed 5 m s^{-1} at any time, which is true for all AWS located below 300 m ASL. During CAP nights the wind direction at AWS 7 is almost entirely confined to the N, occurring 60% of the time, which is a highest frequency sees across all sites and all climatologies.

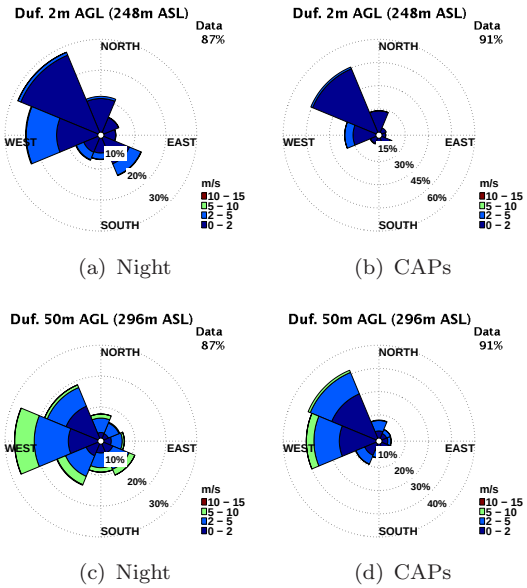

(a) Night (b) CAPs

(c) Night (d) CAPs

FIGURE 4.17: *As in figure 4.12, except wind is measured at the Duffryn mast site at* 2 *m and* 50 *m AGL. For* 10 *m and* 25 *m AGL results, See Appendix B.*

Figure 4.17 shows wind climatology results for the Duffryn mast site, located within the main vein of the Clun Valley (see figure 3.3). At Duffryn the valley is roughly orientated NW to SE; however, the smaller AWS 3 tributary valley joins the main vein of the Clun Valley just south of the Duffryn mast site. As seen at other locations, the wind directions are more varied and stronger at Night compared to those seen during CAP nights. Again the winds tend to be restricted to the local topography, with up and down-valley wind components seen most frequently. However, like some other AWS located below 300 m ASL, i.e., AWS 8 and AWS 6, up-valley winds rarely occur at any time.

For the Night climatologies at Duffryn, winds from the NW, W, SW and SE occur most often at all heights and the wind speed increases with height. At Night there is an anticlockwise turning of the wind with height, a characteristic observed at Burfield (figure 4.14), but not seen at Duffryn during the Day (Appendix B). During CAP nights winds from the NW occur most often at all heights and are generally light. At all heights higher winds occur more often when the wind direction is from W and winds from the W occur more often with increasing height away from the surface. During CAP nights winds from all other directions, other than those from the NW and W, occur infrequently and are weak when they do, always being less than 5 m s^{-1}. Therefore with the exception of AWS 9, up-valley winds rare at all sites located below 300 m ASL during CAP nights.

4.5.2 Ambient and valley wind relationships

The following results show the relationship between the ambient wind and the valley wind, for locations across the Clun Valley region. In order to report the following results, four physical mechanisms outlined by Whiteman *et al.* (1996) are referred to, these are discussed in the background section 2.4. In the Clun region, the distribution patterns will appear different to that shown in figure 2.11, simply because the valley orientation is different. Example wind patterns associated with each mechanisms, for valleys orientated north to south (AWS 7 and AWS 8) and west to east (AWS 5 and AWS 9), are given in Appendix A. The following results are primarily focused on measurements below the level of the surrounding hill tops. Sections 4.5.2.1 and 4.5.2.2 show results for AWS located in the main Clun Valley and connecting tributary valleys. Section 4.5.2.2 includes results for the Burfield Valley (see figure 3.3).

Frequency distribution plots are shown for each site. In all subsequent frequency distribution plots, the ambient wind direction is on the x-axis and is represented by measurements taken at the hill top site Springhill, 30 m AGL. The valley wind direction is on the y-axis. In section 4.5.2.1 and 4.5.2.2, frequency distributions are shown for:

1. Low wind speed nights, when the mean night-time ambient wind speed is <5 m s^{-1} (left figure).
2. High wind speed nights, when the mean night-time ambient wind speed is >5 m s^{-1} (centre figure).
3. Day-time winds (right figure).

Results showing the frequency distributions during strong CAP nights (inversions >4°C) are given in section 4.5.2.3.

4.5.2.1 Clun Valley

Wind direction frequency distribution plots are shown for sites located along the main vein of the Clun Valley in figure 4.18, which includes AWS 4, 5, 9 and 6. AWS 4 is the highest elevated site in the Clun Valley. It is roughly 2 km SW from the Clun Valley

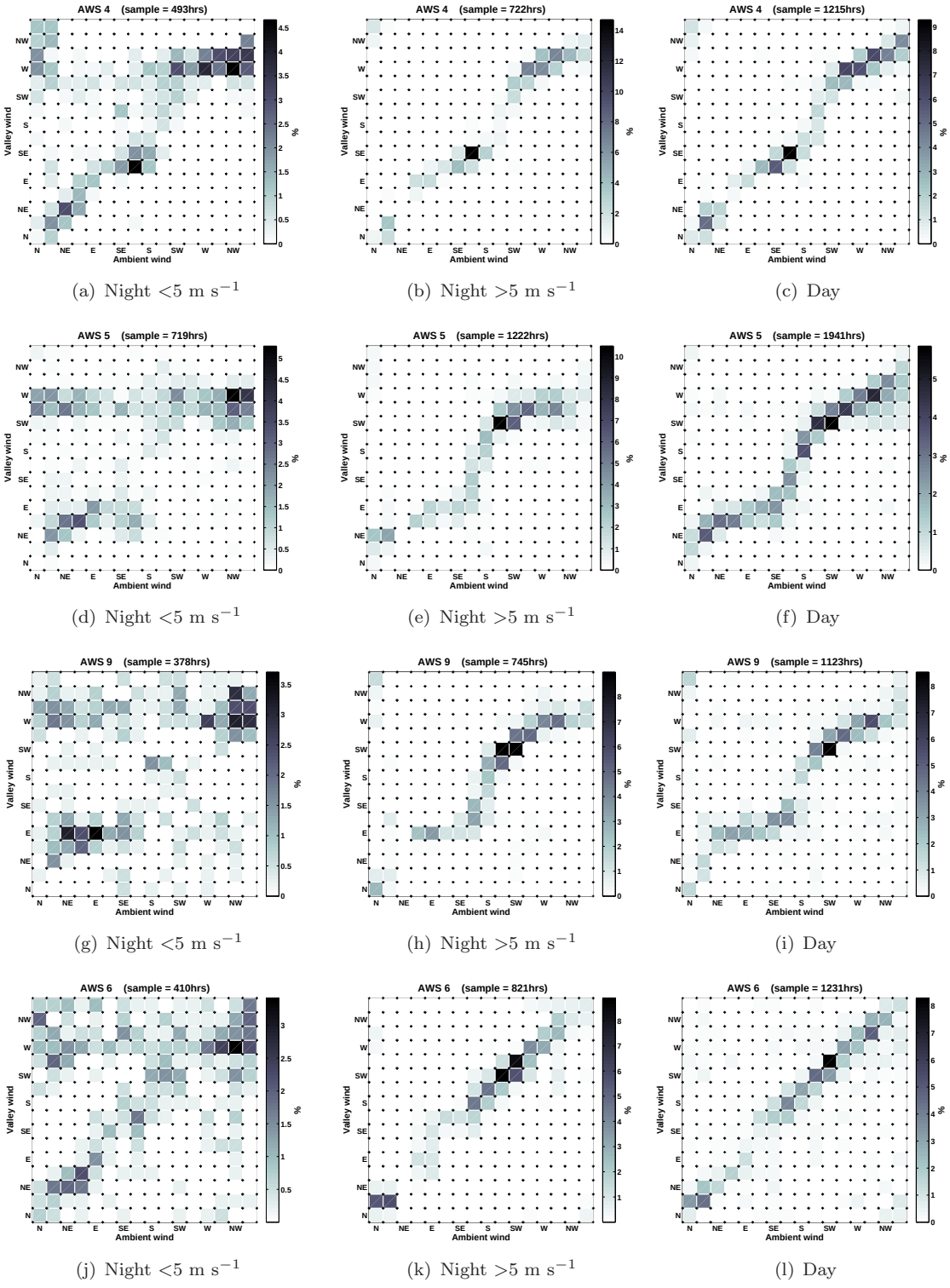

(a) Night <5 m s^{-1} (b) Night >5 m s^{-1} (c) Day

(d) Night <5 m s^{-1} (e) Night >5 m s^{-1} (f) Day

(g) Night <5 m s^{-1} (h) Night >5 m s^{-1} (i) Day

(j) Night <5 m s^{-1} (k) Night >5 m s^{-1} (l) Day

FIGURE 4.18: *Valley and ambient wind direction frequency distributions as a percentage for Clun Valley AWS locations. Ambient wind is Springhill* 30 *m AGL. Wind directions are binned into sixteen 22.5° segments. The total of the 16x16 array = 100%. Results are based on 1hr averages. Left figures show nights when the mean wind speed is <5 m s^{-1}. centre figures are for nights when the mean wind speed is >5 m s^{-1}, right figures daytime winds.*

head near Anchor (see figure 3.3). During the daytime (figure 4.18(c)) the valley wind mostly mirrors the ambient wind, following a pattern of downward momentum transport. However, the valley winds also show some evidence of forced channeling along the valley axis. The valley winds tend to be confined to the WSW, W and WNW when the ambient wind has a westerly component. The valley wind switches direction from an up-valley SE to a down-valley W wind direction when the ambient wind direction is from the S, SSW to SW, which is roughly perpendicular to the local axis. This pattern reflects forced channeling of the valley wind along the local valley axis, noting that AWS 4 is located at a bend in the valley at the junction of two tributary valleys (see figure 3.3). An almost identical pattern is seen during high wind speed nights (figure 4.18(b)).

For low wind speed nights (figure 4.18(a)), the frequency distribution pattern changes. The wind directions are more spread out, subsequently the distribution frequencies are smaller. Again patterns of downward momentum transport and forced channeling are apparent. Additionally there is a pattern of thermally driven down-valley winds from the WSW, W and WNW, which occur irrespective of the ambient wind direction. However, the thermally driven down-valley winds appear to be disturbed by forced channeling when the ambient wind has a westerly component and by downward momentum transport when the ambient wind has an easterly component. When ambient wind directions from the N and NE occur, valley winds from the SW clockwise to NNW are favoured. This variability in valley winds may be a result of valley flows from the more exposed regions to the north, where the tributary valley joins (see figure 3.3). Ambient wind directions that preferential cause forced channeling or thermally driven down-valley flows from this tributary valley, may have an increased influence on the valley winds at AWS 4.

The frequency distributions of the neighbouring sites AWS 5 and 9 are extremely similar (figure 4.18). Both are located near the centre of the Clun Valley at lower elevations than AWS 4. At first glance the high Night and Day frequency distributions at AWS 5 and 9 appear very similar to that seen at AWS 4, with the distribution following a pattern of downward momentum transport and forced channeling; however, the valley wind appears to be more characteristic of forced channeling with the valley winds more aligned to the valley axis. There is also some component of the valley wind that mirrors the ambient wind. For low wind speed nights, down-valley winds occur irrespective of the ambient wind direction, which follows a pattern of thermally driven down-valley winds, from the

W and WSW at AWS 5, from W and WNW at AWS 9. Forced channeling is also evident, recognised by the appearance of up-valley winds when the ambient wind has an easterly component (NNE to SSE). Downward momentum transport appears absent.

During low wind speed nights, up-valley winds from the E occur at AWS 9, when the ambient wind has a westerly component (SW to NW), which is not consistent with conventional patterns of thermally driven flows, forced channeling or downward momentum transport for a valley orientated west to east. The wind frequency distributions are lower and have more variability at AWS 9 compared to AWS 5 in general. This variability is most evident when NW to NE ambient winds occur. AWS 9 is more exposed to the N due to a presence of a small tributary valley (see figure 4.18). This result bares similarities to AWS 4, where the local valley wind is disturbed by winds from a neighbouring tributary valleys.

The frequency distribution patterns for AWS 6 are markedly different from those further up-valley at AWS 5 and 9. AWS 6 is located just west of Clun, at a low point in the valley (see figure 3.3). At AWS 6 downward momentum transport appears to be the dominant mechanism for valley winds during the daytime and high wind speed nights. In both instances the valley wind mirrors the ambient wind. However, during high wind speed nights, valley winds from the SSE are strongly favoured when ambient wind is from the E to SSE. Additionally, when the ambient wind is from the E, the valley wind varies from the SSE to ENE.

At AWS 6, a pattern of downward momentum transport is seen during low wind speed nights (figure 4.18(j)). Thermally driven down-valley flows are seen, with valley winds mostly from the W occurring irrespective of the ambient wind direction. The frequency distributions are small and more varied compared to other AWS, even so, there is little evidence of forced channeling. As with AWS 4 and AWS 9 previously, there appears to be more variability in the valley winds at AWS 6 when the ambient winds are aligned with more exposed regions, in this case when aligned to the AWS 8 tributary valley from the WNW through to the N. Again this highlights the possible effects of tributary valley flows when a large component of the ambient wind is aligned to the tributary valley in a down-valley direction.

4.5.2.2 Clun tributary valleys and Burfield Valley

AWS 3, 7 and 8 are situated in tributary valleys (highlighted blue, red and magenta in figure 3.3) and AWS 1 in the Burfield Valley (highlighted yellow in figure 3.3). The valley axis is orientated roughly W to E at AWS 3, roughly NW to SE at AWS 7, roughly N to S at AWS 8. At AWS 1 (Burfield Valley) the valley is mostly orientated NW to SE, but is less well defined.

The overall frequency distribution patterns seen at AWS 7 and AWS 3 are similar. At both, forced channeling is most evident for daytime and high wind speed nights (figure 4.19) and the distributions do not fit a pattern of downward momentum transport, as seen at AWS 6. For low wind speed nights, both thermally driven and forced channeling mechanisms are seen at AWS 3 and AWS 7. Similarly, the up-valley winds in each case represent forced channeling. Forced channeling of the valley winds down-valley are also likely, but are masked by the thermally driven down-valley winds that are seen. One difference between the two AWS is that the frequency distributions at AWS 3 are more spread compared to AWS 7: AWS 3 is more sheltered by the local topography, trees and bushes, therefore is less exposed to the ambient wind.

At AWS 8 the frequency distributions during the day (figure 4.19(i)) and for high wind speed nights (figure 4.19(h)) are dominated by downward momentum transport with the ambient wind strongly mirrored by the valley wind. On occasions valley winds from the north are seen for various ambient wind directions in the day, a pattern that is characteristic of down-valley drainage flows, which are expected to occur at night only. For low wind speeds nights (figure 4.19(g)) valley winds from the N or NNW occur for all ambient wind directions, following a pattern of thermally driven down-valley winds. When ambient winds have a westerly component (NNW to SSW), down-valley winds from the N and NNW are observed, which follows a pattern of either thermal driven flows or forced channeling. On the other hand the valley winds mirror the ambient winds when an easterly component of the ambient wind prevails (NNE to SSE), which follows a pattern of downward momentum transport. One factor that may contribute to this difference in behaviour is the existence of a gap in the terrain east of AWS 8, therefore AWS 8 is more exposed to ambient winds from the east.

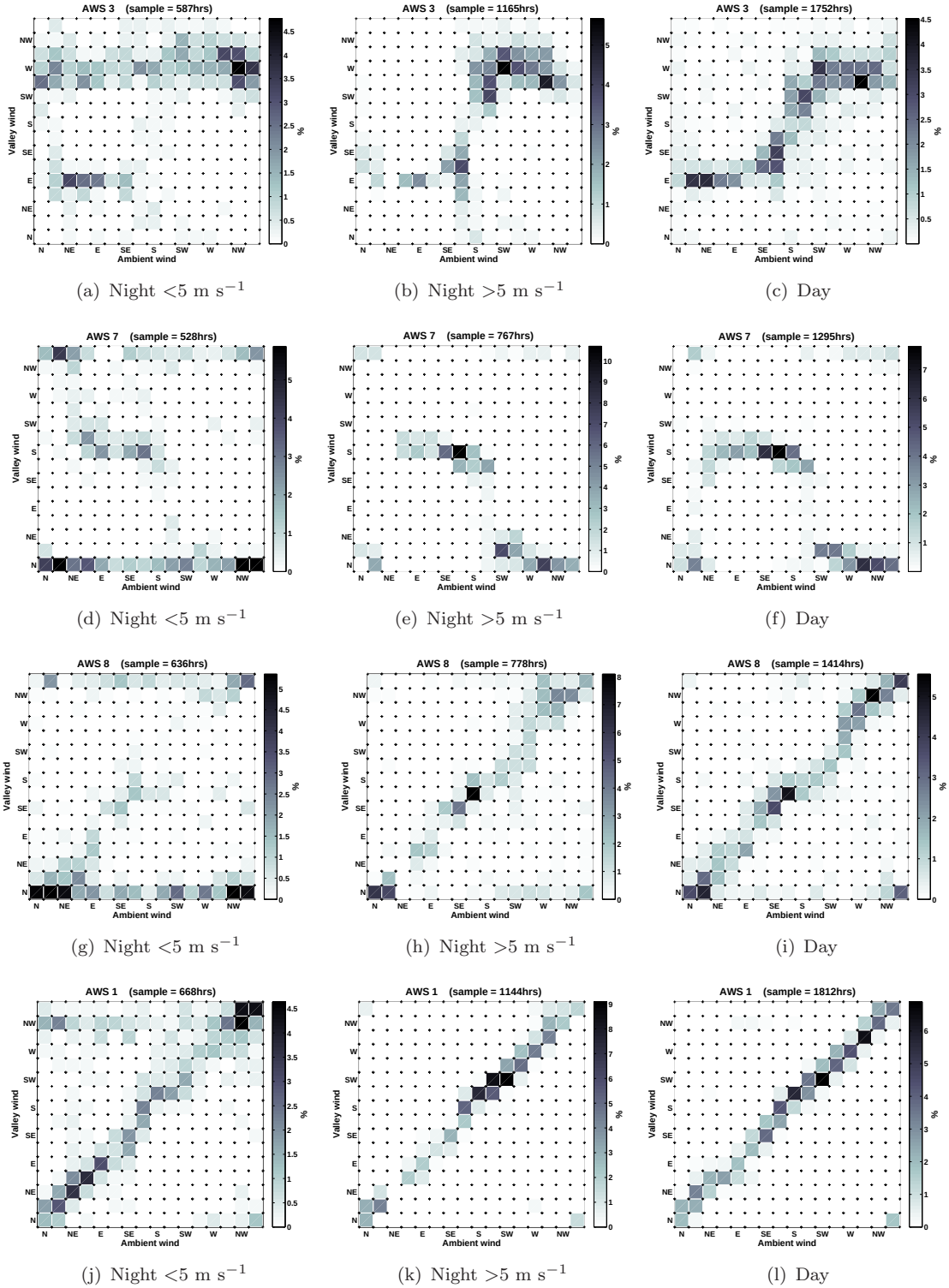

(a) Night <5 m s^{-1} (b) Night >5 m s^{-1} (c) Day

(d) Night <5 m s^{-1} (e) Night >5 m s^{-1} (f) Day

(g) Night <5 m s^{-1} (h) Night >5 m s^{-1} (i) Day

(j) Night <5 m s^{-1} (k) Night >5 m s^{-1} (l) Day

FIGURE 4.19: *As for figure 4.18, except valley wind measurements are from AWS located in tributary and Burfield valleys.*

At Burfield the frequency distribution patterns are less constrained by the valley compared to other locations. The area around AWS 1 is bowl shaped and the site is more exposed than many other valley floor locations, therefore this results is not surprising. Valley winds clearly mirror the ambient winds during the day (figure 4.19(l)) and for high wind speed nights (figure 4.19(k)), following a pattern of downward momentum transport. For low wind speed nights (figure 4.19(j)), down-valley winds are seen from the NW for all ambient wind directions, reflecting a pattern that is consistent with thermally driven down-valley winds.

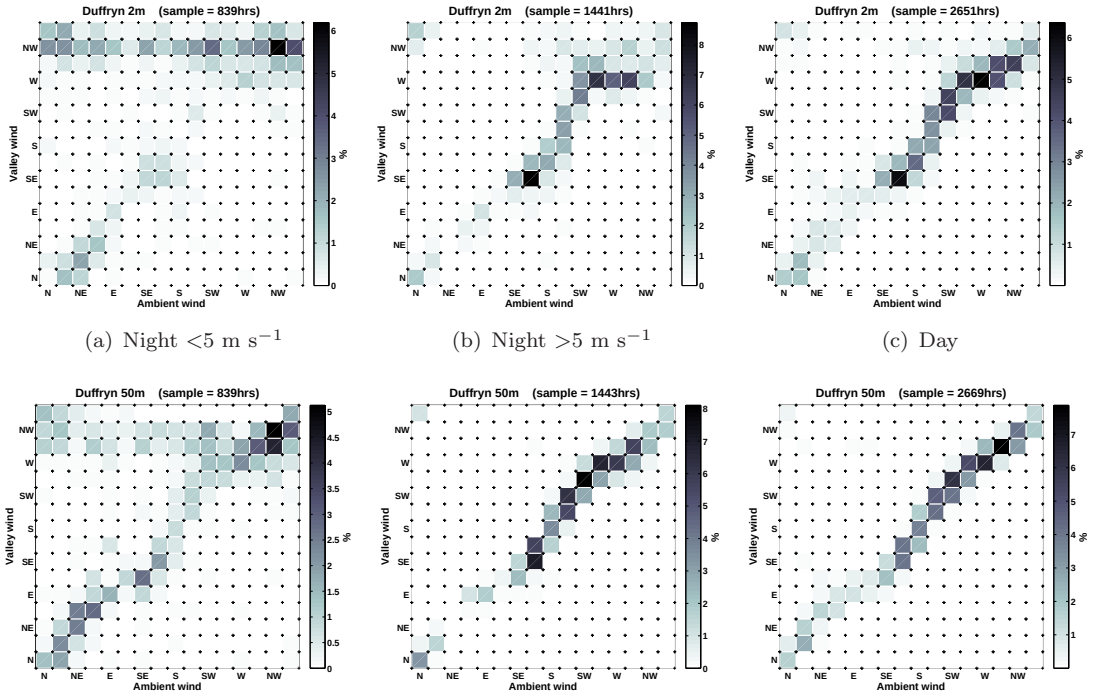

(a) Night <5 m s^{-1} (b) Night >5 m s^{-1} (c) Day

(d) Night <5 m s^{-1} (e) Night >5 m s^{-1} (f) Day

FIGURE 4.20: *As for figure 4.18, except valley wind measurements are for Duffryn at* 2 *m and* 50 *m AGL.*

Figure 4.20 shows wind direction distribution frequency's Duffryn at 2 m and 50 m AGL. Results for 10 m and 25 m as the results are similar. For daytime and high wind speed nights, the ambient wind is mostly mirrored by the valley wind, with some variation away from this pattern, therefore downward momentum transport appears to to be most dominant during these conditions. However, there is more deviation away from the downward momentum transport pattern with decreasing height. Valley wind directions from the W and WSW occur more often at 2 m for different ambient winds than seen at 50 m, this result follows a pattern that is consistent with more forced channeling of the flow at 2 m

than at 50 m, when ambient winds have a westerly component. The results at 50 m appear more similar to those at AWS 6 and AWS 1, with observations at 2 m more similar to those observed at AWS 4. Ambient winds with an easterly component rarely occur for observations at Duffryn during high wind speed nights; however, the few show that the valley wind is mirrored by the ambient wind, which s consistent with a pattern of downward momentum transport.

There are similarities at all heights during low wind speed nights (figure 4.20(a) for 2 m and (d) at 50 m). Thermally driven down-valley winds are confined to the NW at 2 m, but from the NW and WNW at 50 m. For all heights downward momentum transport is most prominent when ambient winds have an easterly component. Forced channeling and thermally driven down-valley winds are favoured when ambient winds have a westerly component at 2 m, with valley winds from the NW occurring more often than seen at 50 m. However, at 50 m downward momentum transport also appears to be occurring, with valley winds from the WNW occurring more often than seen at 2 m.

4.5.2.3 Strong CAP nights only

Figure 4.21 shows wind direction distribution frequencies for valley winds during strong CAP nights only (inversions >4°C). Primarily the valley wind distributions differ greatly during strong CAP nights compared to those shown for strong wind speed nights and daytime winds, instead they are more reminiscent of the results shown for weak wind speed nights. However, there are some consistent characteristic differences seen during strong CAP nights compared to the results for weak wind speed nights. Firstly, thermally driven down-valley winds are more prevalent across all sites. Secondly, downward momentum transport and forced channeling mechanisms are completely absent at some sites, appearing to be restricted to higher regions only, including AWS 1, AWS 3, AWS 4 and Duffryn 50 m.

As before, AWS 1, AWS 4 and Duffryn 50 m, have some wind distributions that are characteristic of downward momentum transport and AWS 3 has valley winds that are characteristic of forced channeling, with up-valley winds only occurring when the ambient wind has an easterly component. Additionally, across all sites during strong CAP nights, down-valley winds are seen most often when the ambient wind direction is from the NW to

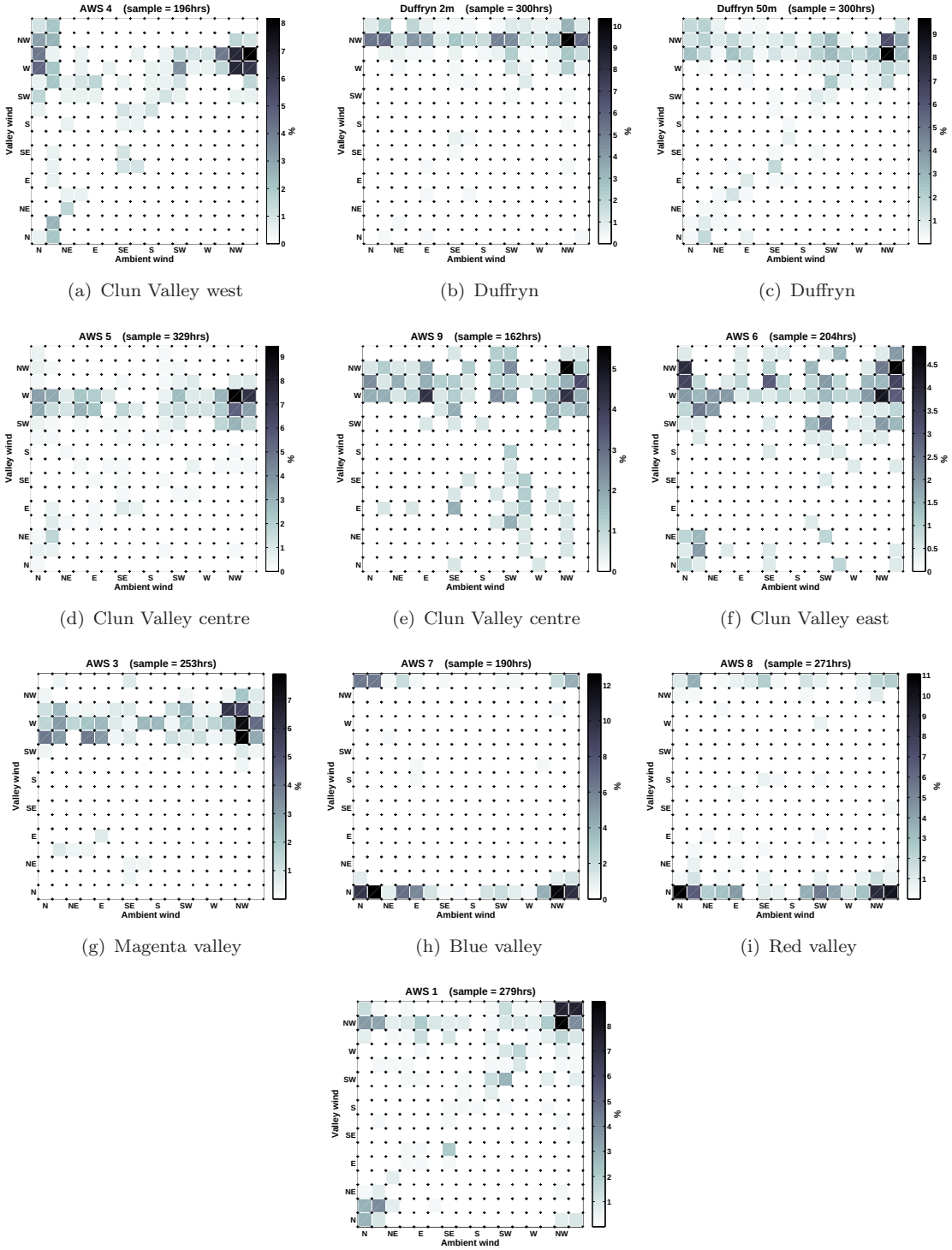

(a) Clun Valley west

(b) Duffryn

(c) Duffryn

(d) Clun Valley centre

(e) Clun Valley centre

(f) Clun Valley east

(g) Magenta valley

(h) Blue valley

(i) Red valley

(j) Yellow valley

FIGURE 4.21: *As for figure 4.18, except valley wind measurements are for strong CAP nights only.*

NNE, which is likely to reflect the increased likelyhood of strong CAPs forming during these wind directions. There is also more scatter in the wind distributions, with no apparent relationship between the ambient wind and the valley wind during strong CAP nights generally, when compared to other distributions shown previously.

Some other interesting distributions are seen. Most notably various up-valley wind components are seen at AWS 9. Up-valley winds are also seen during low wind speed nights for many ambient wind directions (figure 4.18(g)). However, the up-valley winds at AWS 9 are more common during CAP nights, especially when the ambient wind has a westerly component, which is in opposition to the up-valley winds.

There is also much variation in the valley winds at AWS 4 during CAP nights, when the ambient wind is from the N and NNE. A NNE ambient wind direction is aligned to the neighbouring tributary valley that connects to directly from the NNE, a characteristic also noted during weak wind speed nights also (figure 4.18(a)). At Duffryn the valley wind distributions differ depending on the ambient wind direction. Valley winds from the W are more common at both 2 m and 50 m when the ambient wind has a westerly component. Furthermore, at 50 m, SW valley winds are more common during westerly component ambient winds. Similarly, N to NE valley winds are frequently observed at AWS 6 when ambient wind is aligned with the AWS 8 tributary valley, from the NNW, N and NNE.

4.5.3 Summary

There is clear evidence of valley wind patters that reflect downward momentum transport, forced channeling and thermally driven flows. However, there is little or no evidence for pressure driven channeling of the valley winds. For daytime and high wind speed nights, more exposed regions, such as AWS 1 and AWS 6, are more likely to reflect downward momentum transport as a mechanism for valley winds and less exposed regions, such as the tributary valley sites AWS 3, AWS 7, AWS 8, are more likely to reflect forced channeling of the valley winds. There is evidence to suggest that ambient winds, which are aligned to neighbouring tributary valleys and/or more exposed regions, force a change in the regime of the valley wind pattern. This is most prominent at AWS 4, AWS 6, AWS 8 and AWS 9, of which AWS 4 and AWS 9 appear most affected by flows from neighbouring tributary valleys.

Thermally driven down-valley flows are most evident during strong CAP nights and are common across all sites shown. However, there is little evidence for up-valley thermally driven flows (anabatic winds), or at least they occur infrequently. One noticeable feature is the existence of an up-valley flow seen at the valley bottom site AWS 9, during both CAP nights and low wind speed nights. This is a particularly flat region of the valley. Additionally, a tributary valley joins from the north, which may have some influence on the up-valley winds seen during CAP nights.

4.6 Characteristics of the down-valley drainage flow at Duffryn

The following results provide an insight into the down-valley drainage flow at Duffryn, using observations gained from the 50 m mast. Figure 4.22 show night-time mean profiles of wind speed and $\Delta\theta$, for weak (1–4°C) and strong (above 4°C) CAP nights. $\Delta\theta$ is the difference in θ from 2 m, measured at 10 m, 25 m and 50 m. The wind speed and $\Delta\theta$ mean profiles for weak and strong CAPs are distinctly different. In both profiles wind speed and $\Delta\theta$ increase with height, but the similarities mostly end there. A stronger gradient in θ occurs during strong CAPs than during weak CAPs. Conversely, a weak gradient in wind speed occurs during strong CAP nights compared to weak CAP nights. The total mean $\Delta\theta$ from 2–50 m is 1.9 K for weak CAPs and 3.3 K for strong CAPs.

For both weak and strong CAPs the θ profiles are reminiscent of a log profile. The standard deviation of $\Delta\theta$ increases with height for weak CAPs but remains the same at all heights for strong CAPs. The standard deviation of $\Delta\theta$ is also slightly larger for strong CAPs than for weak CAPs, although this may in part be due to the smaller sampling size of strong CAP nights. The standard deviation of wind speed, for both weak and strong CAPs, increases with increasing wind speed, consequently the standard deviations are larger with increasing height AGL. However, the standard deviations are distinctly larger at all levels during weak CAPs compared to strong CAPs, which suggests that the wind speed profile is more variable during strong CAPs, when wind speeds tend to be weaker. The strongest gradient in wind speed and θ occurs between 2–10 m for both weak and strong CAP nights. Furthermore, for weak CAP nights the maximum mean wind speed is 2.3 m s^{-1} occurring at 50 m and for strong CAP nights is less, being 1.6 m s^{-1} at 50 m.

The minimum mean wind speed occurs at 2 m for both weak and strong CAP nights, but is less during weak CAP nights.

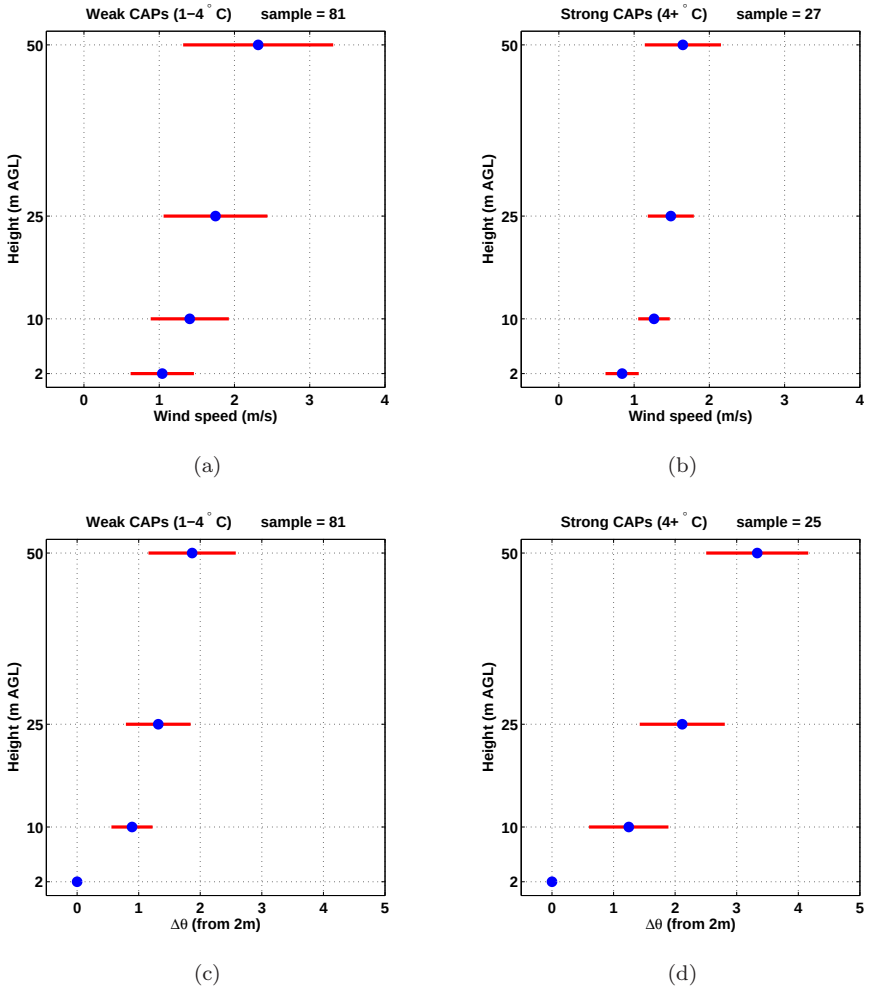

FIGURE 4.22: *Mean wind speed and $\Delta\theta$ profiles at Duffryn for weak and strong CAP nights. $\Delta\theta$ is the difference in θ from the mean measurements at 2 m. Error bars show the standard deviation of the sample mean.*

Wind rose plots of persistence are shown in figure 4.23(b) for Duffryn at 2 m and 50 m, for weak and strong CAP nights. The persistence is the ratio of the mean vector to mean scalar wind and has values that vary from 0–1. It gives an indication of how persistent the wind direction is. Values that approach 1 reflect persistent winds and increasing lower values reflect winds that are less persistent. For strong CAP nights the persistence and wind direction at 2 m, 10 m and 25 m are almost identical (10 m and 25 m not shown). At 50 m a large proportion of strong CAP occurrences have low persistent values (∼20%). As previously noted in figure 4.22(d), the standard deviation of θ is also largest at 50 m during strong CAP nights.

For weak CAP nights, lower values of persistence are seen at 2 m, 10 m and 25 m, compared to the corresponding heights during strong CAP nights, therefore winds during weak CAP nights are less persistent. This result supports those shown in figure 4.22, which show large standard deviations of wind speed during weak CAP nights compared to strong CAP nights.

Values of persistence appear to increase with height during weak CAP nights, which coincide with a wind direction shift from the NW favoured at 2 m to the W favoured at 50 m, which is not seen in strong CAP nights. At 2 m and 10 m the persistence, when NW winds occur, are lower than when winds from the W occur. Previously, results in figure 4.20 show that downward momentum transport is more prominent at 50 m than at 2 m, which is likely to relate to the change in wind direction distribution and increased persistence in the wind direction seen here, with W winds occurring more often at 50 m.

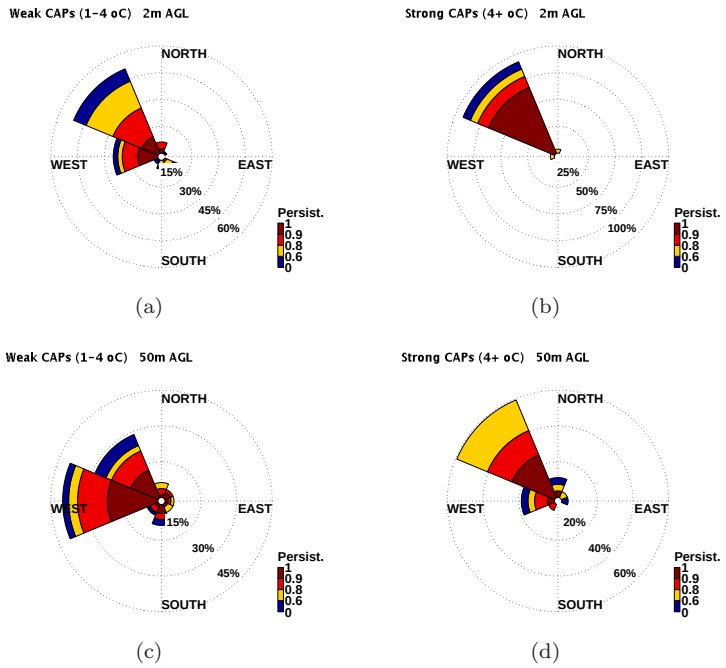

FIGURE 4.23: *Rose plots of 2 m and 50 m, wind direction and persistence measured at Duffryn, for weak CAP nights (a) and (c), and strong CAP nights (b) and (d).*

Of 111 CAP nights, when an inversion larger that 1°C was observed, the height of the mean maximum wind speed occurred at 10 m, 25 m and 50 m, on 3, 18 and 90 occasions respectively (2.7%, 16.2% and 81.1% respectively). For the 28 strong CAP nights observed (data dependent), where an inversion larger than 4°C was observed, the height of the mean maximum wind speed occurred at 10 m, 25 m and 50 m, on 2, 10 and 16 occassions

respectively (7.1%, 35.7% and 57.5% respectively). No wind speed maxima occur at 2 m. Results here suggest that the likelihood of the night-time mean maximum wind speeds to be below 50 m, increases when strong CAP nights occur. The mean wind speed profiles also suggest that the drainage flow jet peak height is lower during strong CAP nights compared to weak CAP nights; however, there is a large standard deviation of the 50 m wind speeds during weak CAP nights.

4.7 Discussion

The aim of this chapter is to discover and improve the understanding of CAPs that form in the Clun Valley region of Shropshire. This is achieved by gaining knowledge of; when and how often CAPs occur, what synoptic conditions favour CAP occurrence, how the synoptic conditions affect the strength of cooling observed, the relationship between the ambient wind and valley winds, during the day, non CAP and CAP nights.

4.7.1 Synoptic influence on CAP occurrences

Results from previous literature suggest that high ambient wind speeds exceeding 5–8 m s^{-1} (Barr & Orgill, 1989; Orgill *et al.*, 1992; Iijima & Shinoda, 2000; Whiteman *et al.*, 2001; Bogren *et al.*, 2000b; Vosper & Brown, 2008) and the presence of cloud cover (Bogren *et al.*, 2000b), in most instances, limits the formation of, or erodes pre-existing, CAPs. However, the possible influences of the wind direction, geostrophic pressure gradient and direction are less clear. Throughout COLPEX, CAP occurrences were very common. CAPs with an inversion <1°C occur 45% of the time and CAPs with inversions larger than 4°C occur 12% of the time.

It is clear from these results that CAPs favour development when; anticyclones dominate the synoptic weather, during clear skies and dry atmospheres, when low ambient wind speeds prevail and when the ambient wind has a northerly component. Furthermore, strong CAPs (inversions larger than 4°C) are favoured when the mean night-time msl pressure is >1008 hPa (figure 4.6). These situations occur during: the second week of September 2009, second week of October 2009, first two weeks of January 2010, the first

two weeks of March 2010, and in the first two weeks of April 2010 (figure 4.3). Strong CAPs were most frequent during October 2009 and the first two weeks of April 2010.

It is observed that cold weather conditions combined with snow cover, can lead to the formation of very strong CAPs, the same result observed by Whiteman (1982) in the Yampa Valley, Colorado, US. Two extreme CAPs were observed on consecutive nights from 6–8 January 2010, when particularly cold conditions prevailed and a generous snow cover present. The first of the two extreme CAP nights was the second largest temperature inversion of the entire 9–month field campaign and measured 9.3°C over the valley depth of $\sim$170 m . Over the three day period, the pressure situation changed little. A west to east PG persisted, but weakened with time and a cold N to NE wind persisted. The relative persistence of cold N to NE winds may have prevented snow melt during this period by reducing the flux of heat into the snow pack, which would have occurred if a warmer air mass had advected over the region for a reasonable length of time (McKay & Thurtell, 1978). Fresh snow also has a higher albedo, subsequently the snowpack may have remained in relative equilibrium with the air above, resulting in little exchange of heat. The continued presence of snowcover therefore led to the occurrence of strong CAPs forming during these two nights.

Interestingly, the mean night-time ambient wind speed at Springhill during the strong CAP forming night of 6–7 January, was 6.7 m s^{-1}. As seen in figure 4.5 there are five occasions when strong CAPs formed when the mean night-time wind speed exceeded 5 m s^{-1}, they are; 11-12 October 2009, 22-23 December 2009, 6–7 January 2010, 13-14 March 2010 and 7 April 2010, with maximum inversions of 4.5°C, 4.7°C, 9.3°C, 4.9°C and 4.7°C, with mean night-time ambient wind directions from the NW, SW, N, NW and NW respectively. In all instances the wind directions have a northerly or westerly component. Furthermore on three of these occasions the mean night-time wind speed is above 6 m s^{-1} (22-23 December 2009, 6–7 January 2010 and 13-14 March 2010). Possible reasons why strong CAPs occur when the mean night-time ambient wind speed is above 6 m s^{-1}, are:

1. CAP breakup did occur, but after the maximum CAP was observed.

2. The CAP formed during a period of light ambient winds, during a night of changeable synoptic weather conditions, i.e., during a CAP window (Dorninger *et al.*, 2011).

3. An already formed inversion within the valley was sufficiently strong enough not to be eroded as wind speeds increased – most likely during 6–7 January CAP night.

4. A warm bias at the hill top site caused by the advection of warmer air at the hill top, which may increase the stability within the valley and enhance the sensible heat flux divergence at the lowest levels for a period of time.

5. Other dynamical reason not yet known.

In the Clun Valley, strong CAPs rarely occur when the mean night-time ambient wind speed exceeds 7 m s^{-1} (figure 4.5(c)). This finding tends to agree with findings by others (Barr & Orgill, 1989; Orgill *et al.*, 1992; Iijima & Shinoda, 2000; Whiteman *et al.*, 2001; Bogren *et al.*, 2000b; Vosper & Brown, 2008). Results in figure 4.5 also show that strong CAPs are more likely to occur with decreasing ambient wind speeds. In this case approximately 38% of all strong CAPs formed when the ambient wind speed was between 2–3 m s^{-1}. Results by Bogren *et al.* (2000b) (see background figure 2.10), show that inversions larger than 1°C did not occur in a broad valley in the county of Älvsborg, Sweden (valley depths ∼40 m), when the hill top wind speed exceeded 2 m s^{-1}. Results here show that some weak CAPs occur when the mean night-time wind speed is above 7 m s^{-1}, but never occur when above 10 m s^{-1}. Iijima & Shinoda (2000) also noted that CAPs rarely occur in a hollow in the subalpine region of the Yatsugatake Range Japan, when the mean night-time wind speed is above 6 m s^{-1}.

With the knowledge that strong CAPs preferentially occur when the ambient wind speed is below 3 m s^{-1}, results in figure 4.10(b) can be used to suggest that a threshold value of 12 m s^{-1} geostrophic wind (PG = 1.5 Pa/km) or less is needed for strong CAPs to form; above this value and strong CAPs are unlikely to form. Note that in figure 4.10(b), when the model geostrophic wind is below 12 m s^{-1}, mean night-time wind speeds above 7 m s^{-1} occur on only one occasion, which is a weak CAP night.

It is also shown that CAP occurrence and strength are related to differences in wind direction and F_{lw} (the ratio of upwelling to downwelling LW radiation, see figure 4.5). Strong CAPs do not form when values of F_{lw} exceed 0.93 and strong CAPs are more likely to form with decreasing values of F_{lw} (figure 4.8(c)) – low values of F_{lw} reflect low values of atmospheric moisture and/or clear skies (Gudiksen *et al.*, 1992). Weak CAPs do form when values of F_{lw} exceed 0.93, but are likely to reflect nights when the atmospheric moisture

content is high or clouds form intermittently resulting in CAP windows (Dorninger *et al.*, 2011). Results by Vosper & Brown (2008) and Sheridan *et al.* (2013) show that CAP strength can mostly be explained by changes in U (a quantity of background wind speed, see background 2.3.4.2) and F_{lw}, with the variability seen likely to be related to factors such as varying winds and radiative conditions during CAP nights.

Strong CAPs occur most often when the mean night-time ambient wind direction is from the N (∼29%, figure 4.5,(g)). N wind directions occur rarely throughout the field campaign as a whole; however, over 35% of all N wind direction nights result in strong CAPs forming (figure 4.8(b)). In contrast, strong CAPs occur least often when the ambient wind direction is from the S, ∼3% of all nights and less than ∼3% of the time when S wind directions prevail () – S wind directions occur most often throughout during COLPEX (figure 4.5,(g)). Possible reasons why strong CAPs preferentially form when the synoptic wind is from the N are: (1) Lower wind speeds are more likely when the ambient wind direction is from the N; (2) Less cloud cover and/or low atmospheric water vapour content when the mean night-time wind direction is from the N, therefore low values of F_{lw} are more likely; (3) N winds are more indicative of less changeable conditions, i.e., low wind speeds and clear skies will persist throughout the night; (4) wind direction has a dynamical influence on CAPs, which is related to the geometry and orientation of the valley; (5) a combination of the reasons given, (6) other dynamical reason not yet known. When viewing 00:00 UTC analysis charts for each strong CAP when N winds are observed, the synoptic situation had weak pressure gradients over the UK associated with anticyclones or ridges centred over the UK, or located to the N, NW, W and SW. However, in many cases it is likely that the anticyclones are not static for the entire night-time period.

Results in figure 4.11 show that strong CAP nights rarely form when S wind directions prevail. Furthermore, S wind direction nights frequently coincide with mean night-time ambient wind speeds above 6 m s^{-1} and values of F_{lw} above 0.91. The results in figure 4.5 show that strong CAP nights do not occur when values of F_{lw} exceeded 0.93 and when mean night-time ambient wind speeds exceed 7 m s^{-1}. Combined these results emphasise that south wind directions are not favourable for strong CAPs. This is because S wind directions are associated with either mean night-time wind speeds exceeding 5 m s^{-1} and high values of F_{lw}, which reflect cloud cover and/or high content of atmospheric water

vapour. The occurrence of both may be indicative for the progression of frontal systems during these nights.

Wind direction and speed have been shown to have an effect on katabatic/drainage flows within other valleys, even when slopes are relatively well protected from direct exposure (Doran, 1991). Coulter *et al.* (1989) show that there was increased drainage from a tributary valley when the wind direction was opposite to the drainage direction, than when the ambient wind was aligned with the drainage flow. Results by Zängl (2005a) also highlight the potential impact of ambient winds on CAP persistence in large Alpine regions, highlighting that the geometry of valleys and their orientation to the large-scale flow (geostrophic) and PG, are particularly important factors. The tributary valleys of the Clun Valley are orientated in different directions with respect to the ambient wind, therefore it seems plausible that the structure of valley flows within neighbouring tributary valleys will differ as a results of changing ambient wind directions. Any change in structure of drainage flows can potentially affect; (1) the way cold air is redistributed through advection, (2) the amount of turbulent mixing generated by shear, resulting in (3) a change in the morphology and strength of the CAP as a whole.

The tendency of CAPs to form during anticyclones agrees with findings by Iijima & Shinoda (2000) and Kiess & Riordan (1987), in the subalpine region of the Yatsugatake Range in Japan and in North and South Carolina USA respectively, which show CAP occurrence and strength are strongly related to anticyclone weather patterns and weak pressure gradients. Iijima & Shinoda (2000) found that strong inversions formed preferentially during migratory anticyclone pressure situations that were accompanied by dry air. Iijima & Shinoda (2000) also show that CAPs occurred when wind speeds exceeded 6 m s^{-1} and suggests that these may be related to a high-level inversion created by anticyclonic subsidence (Yoshino (1972) cited Iijima & Shinoda (2000, p. 11)), this cannot be confirmed by results here but may offer one explanation. The evidence for any dependence of strong CAPs on pressure gradient direction is less clear; however, more NW pressure gradient nights result in strong CAPs forming (∼28%) than for other pressure gradient directions.

For the most part the ambient wind is turned 45–90° clockwise to the synoptic PG direction (see figure 4.10(a)). However, this does not appear to be the case when the PG direction and ambient wind directions are between 0–135° (N to SE). Instead the ambient wind appears similar, turned 0–45° clockwise or anticlockwise, when the PG is between 0–45°

and significantly different on three occasions when the PG direction is between 90–135°. Reasons for this are unknown, possible explanations are:

1. These conditions correlate with weak pressure gradients, which result in local wind forcings.
2. These conditions are preferential for meandering of the synoptic wind, which is particularly prominent if the flow approaches or is near approximate geostrophic balance (Oettl *et al.*, 2005).
3. Caused by significant backing of the ambient wind during stable conditions.
4. Decoupling of the ambient wind above the valley during strong stability, which may then be backed by frictional forces at the surface.

4.7.2 Characteristics of valley winds

Large differences in valley wind behaviour are seen across the Clun Valley region. It is expected that low geostrophic wind speeds above the valley and stable to neutral atmospheres at night, favour the development of either thermally driven down-valley/down-slope flows, or pressure driven channeling within the valley. High geostrophic wind speeds and neutral to unstable atmospheres, during the day or night, will favour the development of downward momentum transport or forced channeling mechanisms. Valley winds during daytime unstable atmospheres, will favour the development of up-valley/up-slope anabatic thermally driven winds.

Using pattern recognition, the forcing mechanism results in section 4.5.2 are summarised in figure 4.24 using octas to represent the ambient wind direction. Shown are the likely forcing mechanism of valley winds, for a given ambient wind direction (octas) during; (a) the daytime, (b) strong wind speed nights, and (c) strong CAP nights. White filled octas indicate valley winds that are either rare or did not occur. On occasions more than one valley forcing mechanism is observed, e.g., at AWS 8 during the day-time (figure 4.19(f)) wind patterns are a mixture of downward momentum transport and forced channeling, in this instance the pattern is identified as Mix (orange) in figures 4.24(a) and 4.24(b).

Day-time up-valley anabatic winds are completely absent from the climatology results. According to Rampanelli *et al.* (2004) the basic requirement for producing up-valley winds

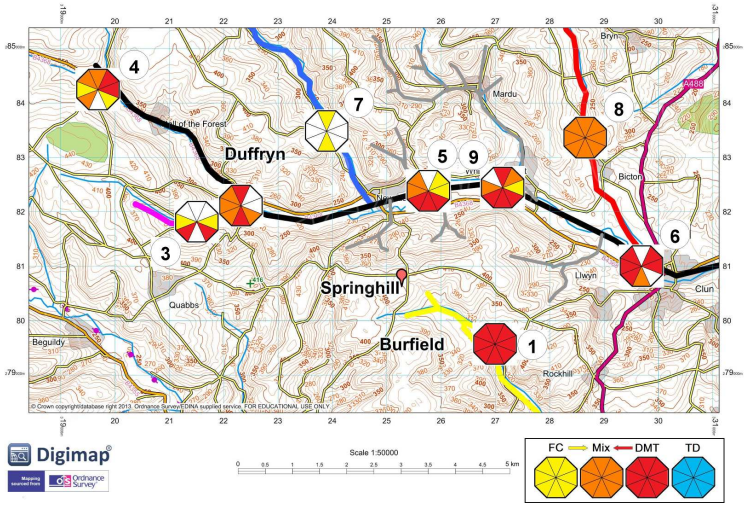

(a) Day-time

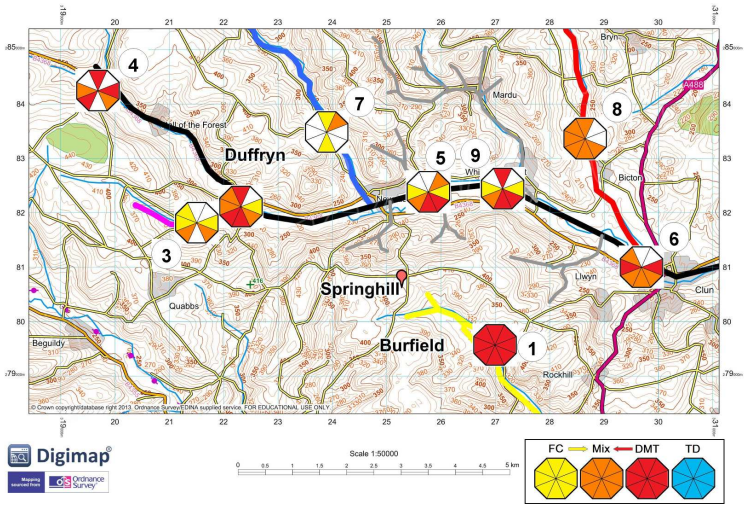

(b) Strong wind nights (>5 m s^{-1})

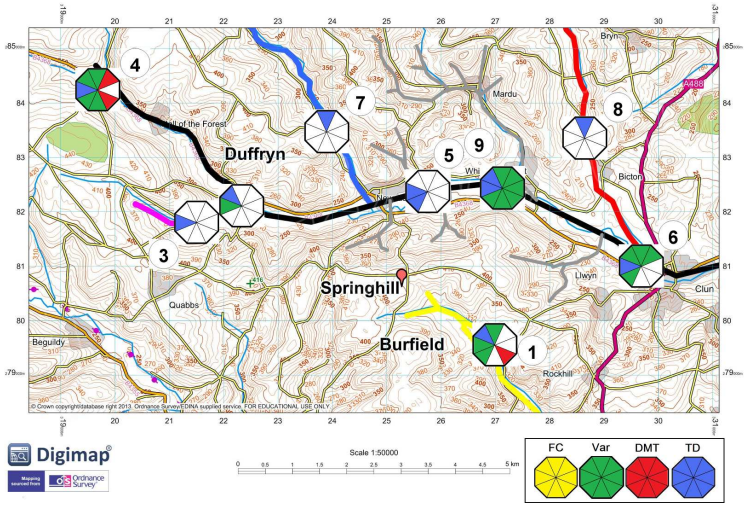

(c) Strong CAP nights (>4°C)

FIGURE 4.24: *Summary of valley winds and likely forcing mechanism at each site. The Key indicates the forcing mechanism; forced channeling (yellow), downward momentum transport (red) and thermally driven (blue). Additionally, Mix (orange) indicates evidence for both forced channeling and downward momentum transport. Var (green) indicates variable or unexplained wind patterns. ©Crown Copyright/database right 2013. An Ordnance Survey/EDINA supplied service.*

is for the valley to widen to a degree where it can be considered a plain. This basic requirement may not be met here, since the mouth of the Clun Valley lies roughly 15 km east of Clun and the valley does not widen significantly along its length. Anabatic winds may occur on occasions but are either infrequent, therefore not statistically recognised, or preferentially occur under the same conditions that favour forced channeling, therefore their appearance is masked.

During the day forced channeling and downward momentum transport are the dominant mechanism for valley winds (figure 4.24(a)). The occurrence of forced channeling and downward momentum transport is favoured at particular sites. Forced channeling is more prominent at narrow valley bottom sites AWS 3 and AWS 7 (figures 4.19(c) and 4.19(f) respectively). Both Whiteman & Doran (1993) and Weber & Kaufmann (1998) suggest that forced channeling is expected to be important for narrow valleys during unstable or neutral conditions, which appears to be the case here. In contrast, downward momentum transport is most prominent at AWS 1, AWS 6 and to some degree AWS 8 (figures 4.19(l), 4.18(l) and 4.19(i) respectively). These sites are located in less sheltered regions compared AWS 3 and AWS 7 (see figure 3.3). According to Whiteman & Doran (1993) broad valley regions, which are more open and less sheltered, are more likely to favour downward momentum transport during unstable and neutral atmospheres.

Forced channeling and downward momentum transport can occur at the same site, but occur preferentially depending on the ambient wind direction. One of the clearest examples of this occurs at AWS 4 during the day (figure 4.18(c) and 4.24(a)). When the ambient wind is from the more exposed region to the NE and E, the valley wind is also from these directions, reflecting downward momentum transport. However, when the ambient wind has a westerly component, i.e., SW, W and NW, valley wind directions from the W are most prominent, which is aligned to the local valley axis, a pattern consistent with forced channeling. further to this, during the day at AWS 5 and AWS 9 (figures 4.18(f) and 4.18(i)), forced channeling of the valley winds is seen during up-valley ambient wind directions, but is less noticeable for other wind directions. In both cases there is a narrowing of the valley in this direction, which is likely to accelerate the air as is is squeezed by the valley side walls.

Thermally driven down-valley winds are seen during low wind speed nights, but are very

prominent during strong CAP nights (see figure 4.24(c)). The clearest example of thermally driven flows occur at the tributary valley sites AWS 7 and AWS 8 (figures 4.21(h) and 4.21(i) respectively). At both locations down-valley winds from the N and NW occur frequently, irrespective of the ambient wind direction.

There is no evidence of pressure driven channeling, or at least the pattern associated with pressure driven channeling is hard distinguish using pattern recognition. The study by Whiteman & Doran (1993) uses the geostrophic wind (supergeostrophic wind) rather than an ambient wind to investigate the relationship between above valley winds and valley winds. Therefore the above valley wind in their study is rotated 90° clockwise to the synoptic PG (for a valley in the NH), i.e., the wind is supergeostrophic. From figure 4.10(a) it is clear that this is not necessarily the case for weak and strong CAP nights during COLPEX. In most instances the ambient wind at the hill top site Springhill (30 m AGL) is between 45–90° clockwise, but in some instances there is little difference. On occasions the ambient wind can be orientated slightly anticlockwise and in some instances appears almost random and independent from the synoptic pressure situation. Taking into account the pressure situation on a case by case basis, may improve the analysis, but it seems unlikely to show evidence of pressure driven channeling.

Both Whiteman & Doran (1993) and Gross & Wipperman (1987) show that pressure driven channeling of valley winds is prominent in the Tennessee and Rhine Valleys, which are larger than the Clun Valley. Weber & Kaufmann (1998) found that winds in narrow valleys with widths between 2–3 km, appear to be driven by forced channeling and in wider valleys with widths between 6–10 km, valley winds tend to be forced by the pressure driven channeling. Since the majority of the Clun Valley system has peak to peak widths less than 3 km, it seems unlikely based on the results by Weber & Kaufmann (1998) that pressure driven channeling will occur, or at least is not the dominant mechanism for valley winds. The relative closeness of the valley side walls and small depth of the Clun Valley, compared to the Tennessee and Rhine Valleys, mean that frictional forces will have a larger influence on valley winds in the Clun Valley. Whiteman & Doran (1993) also suggest that you would need large thermal differences along the valley to reproduce the magnitude of flows induced by the 'average' synoptic pressure gradient by thermally driven flows. It seems reasonable using interpretations by Whiteman & Doran (1993) and Gross & Wipperman (1987) to suggest that pressure driven channeling will contribute to some proportion of

the valley flow (i.e., a vector quantity of the overall wind speed and direction), providing a synoptic pressure gradient is present. Therefore pressure driven channeling may be occurring but is superimposed by other forcing mechanisms, which are more dominant and clearly identified in results here. Furthermore, pressure driven channeling may reduce valley wind speeds when the PG direction is aligned up-valley and increase valley wind speeds when aligned down-valley.

During strong CAP nights (figure 4.24(c)), valley wind patterns do not always fit the "ideal pattern" associated with each of the four valley wind mechanisms. An example of this occurs at AWS 9 – located in a particularly flat region of the Clun Valley. In this instance up-valley winds are observed during CAP nights (see AWS 9 in figures 4.15(d) and 4.21(e)), identified as Var (green) in figure 4.24. Additionally up-valley winds are not observed at the neighbouring site AWS 5. The neighbouring tributary valleys of AWS 9 may influence the local wind forcings resulting in the variable valley wind patterns seen. The impact of tributary valleys during strong CAP nights is most evident at AWS 4 (figure 4.21(a)); however, there is evidence to suggest that tributary valleys are contributing to the variability of valley winds at Duffryn, AWS 9, AWS 6 and Burfield also (figure 4.24(c)). In comparison to other valley floor locations, variable flow patterns are seen further down-valley at AWS 6 during strong CAP nights (see figure 4.21(f)). This particular site is known to be subject to highly variable winds, as noted in Price *et al.* (2011). The results in Price *et al.* (2011) highlight the occurrence of daytime westerly winds (259°) when ambient winds from NW (325°) occur at Springhill, but the mechanism that caused this backing of the wind during the day could not be determined. The climatology results in figure 4.18(j) suggest that forced channeling is a rare occurrence at AWS 6, instead downward momentum transport appears to be the dominant mechanism, therefore the occurrence of W valley winds during NW ambient winds, is not representative of the common daytime winds seen at AWS 6 in this study.

At the tributary valley site AWS 8, down-valley winds are seen during the day (figure 4.24(a)) irrespective of the ambient wind direction (see figure 4.19(i)). Observations by Coulter *et al.* (1989) show that drainage from a tributary valley continued after the main valley flow had reversed following sunrise, this continued drainage was attributed to continued radiative cooling of the slopes within the tributary valley and this drainage was

sufficiently strong enough to overcome the up-slope flow from the main valley. The down-valley flows seen during the day at AWS 6 in Price *et al.* (2011) and AWS 8 in results here, may be a result of continued cooling of nearby slopes, leading to rare daytime down-valley thermally driven flows, which may have a preference to occur under snow-covered conditions.

4.7.3 Duffryn drainage flow and evidence from tributary valleys

The drainage flow observed at Duffryn during strong CAPs, broadly agree with observations by Manins & Sawford (1979). There appears to be a large down-slope-flowing layer with very little directional shear during strong CAP nights in the layer between 10– 50 m. However, during weak CAP nights there is more directional shear between 25–50 m, which is likely to reflect the upper parts of the drainage flow being more susceptible to influences from the ambient atmosphere, through turbulent mixing during weak stability (Gudiksen *et al.*, 1992), therefore the upper regions of the drainage flow are more likely to be coupled to the atmosphere above at these times. Another explanation that the region around 50 m is more susceptible to influences from the neighbouring AWS 3 tributary valley during weak CAP nights.

The maximum wind speed height associated with the drainage flow exists above a strong thermal inversion, as seen by Manins & Sawford (1979). The maximum height of the drainage flow jet peak appears to vary between 10 m and some height above 50 m. The mean maximum wind speed occurs at 10 m, 25 m and 50 m, on 2, 10 and 16 occasions respectively (7.1%, 35.7% and 57.5% of strong CAPs respectively). The height of the maximum jet and depth of the drainage flow is likely to depend on a number of factors including; precipitation-evaporation effects causing non-radiative drainage events, wind shear above the valley, cloudiness, frontal passages and synoptic winds directed in the down-valley direction (Gudiksen *et al.* (1992)). Some investigations looking at the dependance of the drainage flow speed on CAP strength, wind direction and speed, were conducted but yielded no clear result, this was mostly due to data quantity, with the limiting factor being an inadequate amount of strong CAP nights for some wind directions. However, there is some evidence of a shallow drainage layer, or at least lower height of the wind speed maximum with stronger cooling. This analysis is likely to have benefited from;

a larger dataset, a taller tower with more measurements, and/or more frequent radiosonde measurements.

4.8 Chapter summary

Results here show that the formation of strong CAPs in the Clun Valley area are strongly correlated to anticyclonic weather patterns, weak synoptic pressure gradients, clear skies, dry atmospheres and low wind speeds. Specifically in the Clun Valley strong CAPs "preferentially" form when;

- Mean night-time wind speeds <7 ms^{-1} occur (model geostrophic wind speed below <12 ms^{-1}).
- Msl pressure is higher than 1007 hPa.
- Mean night-time ambient wind direction is from the N.
- Values of F_{lw} are below 0.93

The "ideal" conditions for strong CAPs to form, without snow-covered ground, are;

- Mean night-time wind speeds below 3 m s^{-1}.
- Msl pressure higher than 1029 hPa and pressure gradient below 1.5 Pa/km.
- Mean night-time ambient wind direction from the N, combined with pressure gradient direction from NW.
- Low values of F_{lw} i.e., <0.80, which reflect low amounts of column water vapour (i.e., greenhouse effect) and clear sky conditions.

There is insufficient evidence to identify exactly why strong CAPs are favoured for N ambient wind directions; however, N wind directions are often associated with cold air masses, which tend to be drier. Additionally, CAPs occur more often when a pressure gradient from the NW occurs, these results combined suggest that a high pressure centred to the NW of the Clun Valley region, with sufficiently backed winds to result in a N ambient wind direction (examples are seen in the bottom right of figure 4.10(a)). Based

on these criteria an illustration of the "ideal" synoptic situation for strong CAPs to form, is given in figure 4.25.

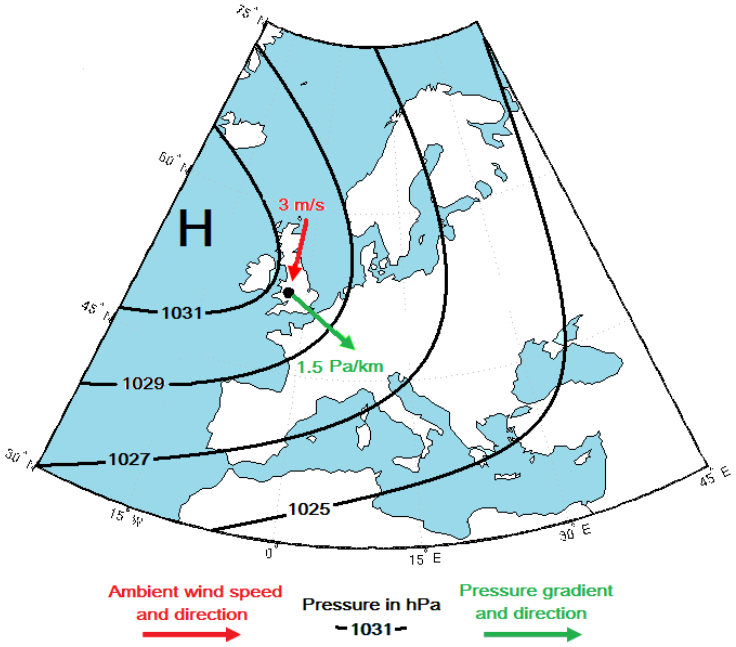

FIGURE 4.25: *Illustrated example of the "ideal" synoptic situation for strong CAPs to form in the Clun Valley region (marked by the black spot). The ambient wind is the hill top wind speed and direction.*

Ambient wind direction alone is likely to effect drainage flows in different tributary valleys differently, subsequently the temperature budget of the valley is likely to be modified as a consequence and the CAP strength affected; however, it is not known how important this process is for CAP formation and evolution in the Clun Valley and more broadly other valleys of similar scales, which have numerous tributary valleys with different orientations. Furthermore, wind directions from the N and NW roughly align with two main tributary valleys, plus a large section of the valley to the NW of Duffryn. An ambient wind aligned to the major tributary valleys in a down-valley direction, may preferentially form stronger CAPs, possibly by increasing stability, by reducing the amount of shear between the drainage flow and ambient wind. Further investigations are needed to explore this possibility. In this instance the interaction between the drainage flow and the ambient wind may be important for determining local stability and turbulence.

Investigations here looked at the relationship between ambient winds and valley winds using frequency distribution patterns. Three of the four mechanisms for valley winds outlined by Whiteman & Doran (1993) are observed; downward momentum transport, forced

channeling and down-valley thermally driven flows. Thermally driven up-valley anabatic winds, associated with daytime unstable atmospheres, and pressure driven channeling are not observed. The shape, depth and width of a valley, as well as the measurement height of the valley wind AGL, are key in defining which forcing mechanism is likely to be observed. The effects of the above valley wind on the valley wind change from site to site depending on characteristics of the local topography in terms of; the shape and orientation of the valley side walls, their proximity to the hill top, their proximity to the valley side walls (narrow/less narrow) and how the valley changes (narrowing or widening) in the direction of the ambient wind. An illustration of the likely occurrence of each mechanism, for sites at 2 m AGL, are shown in figure 4.26, with example locations from these results given.

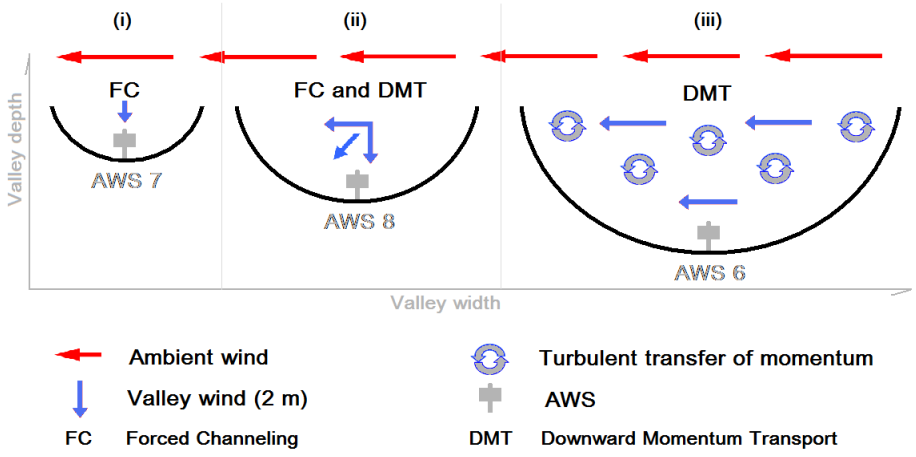

(a) Width and depth

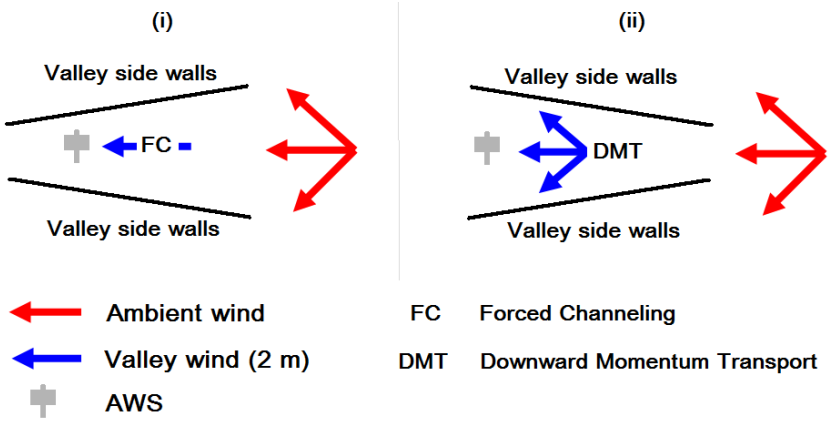

(b) Narrowing and widening

FIGURE 4.26: *Illustrated examples of forcing mechanisms occurring at 2 m AGL, depending on; (a) valley width and depth, (b) valley narrowing or widening.*

Patterns associated with downward momentum transport are known to occur during unstable and neutral atmospheres. Results here show that downward momentum transport is clearly favoured at less sheltered locations in the Clun Valley, e.g., AWS 6 (see figure 4.26(a)). The forced channeling mechanism is favoured at more sheltered regions in the Clun Valley, e.g., AWS 7 (see figure 4.26(a)). Broadly speaking, downward momentum transport is more likely to occur in wider valleys that have gently sloped sidewalls. The forced channeling mechanism is more likely to be observed in narrow valleys with steep sidewalls (figure 4.26(a)). At some locations both patterns of downward momentum transport and forced channeling are seen (such as AWS 8), this clearly shows that a balance exists that defines which of the two mechanisms will occur. Downward momentum transport occurs preferentially when the up-wind region is more exposed, i.e., a narrowing of the valley in the direction of the ambient wind, and the forced channeling mechanism occurs preferentially when the up-wind region of the valley is more confined, i.e., a widening of the valley in the direction of the ambient wind, as illustrated in figure 4.26(b).

Thermally driven down-valley winds (drainage flows) dominate the valley wind regime in the lowest parts of all valleys during CAP nights. In this instance the valley winds show no relationship to the ambient wind and instead appear decoupled. The absence of pressure driven flows is likely to be a consequence of valley depth, length, width, and the presence of the thermally driven flows. Furthermore, the valleys are not sufficiently deep enough for pressure driven flows to form between the drainage flow and the ambient wind. The Clun valley may not be sufficiently long enough for a large pressure gradient to be imposed on the valleys length. Evidence here suggests that drainage flows from tributary valleys affect wind patterns in neighbouring valleys. These results clearly show how the valley wind mechanism depends on valley geometry – depth, height, length, narrowing, widening – but does not quantify this. The results summarised by figure 4.24, may serve as a tool for identifyting the likely valley wind mechanism to occur in other regions similar in scale to the Clun Valley.

A climatology of the Duffryn drainage flow has been summarised here; however, there remains some uncertainty in how the structure of the drainage flow at Duffryn will change depending on time, CAP strength, ambient wind direction and speed. These results show that the depth and height of the maximum jet decrease with increasing CAP strength; however, this result is uncertain and further investigations are needed. Clearly it would

be beneficial to investigate a strong CAP event, using the "ideal" criteria outlined here to understanding how CAPs form, evolve and break up in the Clun Valley.

Chapter 5

An "ideal" case study of cold-air-pooling; IOP 16, 4–5 March 2010

5.1 Introduction

Results in chapter 4 show the importance of the synoptic conditions on controlling CAP strength, in terms of the total amount of cooling observed on any given night across the Clun Valley depth (170 m). Using the COLPEX observational dataset, this case study investigation aims to understand how CAPs evolve, during conditions that are "ideal" for strong CAPs to form. After initial investigations it was found that although the synoptic conditions appeared "ideal", the CAP was still prone to disturbance by other nocturnal meteorological phenomena.

Currently there are very few detailed studies of CAPs in smaller terrain types, such as the Clun Valley region. Little is known about how CAPs evolve and what controls their evolution in such a region. Zängl (2005a) suggests that CAP erosion by turbulent mixing from above plays a comparatively minor role in deep valley systems. Furthermore, findings by Zängl (2003) suggest that turbulent mixing can be important for shallow CAPs. It seems likely that turbulent mixing from above will play a comparatively larger role in smaller valleys with smaller valley depths, compared to large deep mountainous valleys,

which have been extensively studied before. Changes in wind speed (Orgill *et al.*, 1992) and direction (Coulter *et al.*, 1989) are also known to affect the structure of drainage flows in valleys, which will subsequently affect the evolution of the CAP as a whole.

This chapter presents results of observations gathered during IOP 16, issued for the night of 4–5 March 2010. Based on conclusions in chapter 4, the synoptic conditions that prevail on the night of IOP 16, fit the "ideal" criteria for strong CAPs to form; there is little evidence for cloud cover, a high pressure system dominates the UK weather, the pressure gradient across the region is weak and light ambient winds prevail with a mean night-time wind direction from the NW (320°). By conducting a detailed study of IOP 16, the aim of this chapter is to understand how the CAP evolves during these "ideal" conditions. Is CAP evolution uninterrupted and insensitive to changes in the synoptic conditions, and/or other meteorological phenomena? If so how do these changes affect the CAP as it evolves and breaks up.

An introduction to IOP 16, outlining the general synoptic conditions and justification of using IOP 16 as a case study to investigate, is given in section 5.2. Section 5.3 gives an overview of the CAP cycle, from formation to break up. The CAP appeared disturbed by three distinct phenomena during the evolution and break up phase of the CAP, each of these disturbances are investigated in sections 5.4, 5.5 and 5.6 respectively. A summary of the findings from this chapter are given in section 5.7.

5.2 Calling of IOP 16 and synoptic weather overview

The weather forecast leading up to the 4–5 March 2010 suggested that this night would be ideal for CAPs to form, which led to the calling of IOP 16. The UK synoptic weather situation over the 48hr period from 4–5 March 2010 was dominated by a high pressure system. Centred off the west coast of Ireland the high pressure ridge extended across the UK into mainland western Europe and had a relatively high central msl pressure of 1035 hPa (see figure 5.1). The west to east (high to low) pressure gradient across the UK was relatively weak. An estimate of the pressure gradient that existed across the Clun Valley region at 00:00 UTC on the 5 March, is ∼1.0 Pa/km (figure 5.1(a)). There was a small southeast movement of the high pressure centre and a slight increase in the pressure gradient between 00:00–12:00 UTC (see figures 5.1(a) and 5.1(b)). For the first part of

the night, between 16:00–00:00 UTC, a light geostrophic wind (< 5 m s^{-1}) from the N prevailed. Between 00:00–12:00 UTC the geostrophic wind strengthened to $\sim$8 m s^{-1} and changed direction towards the NNW.

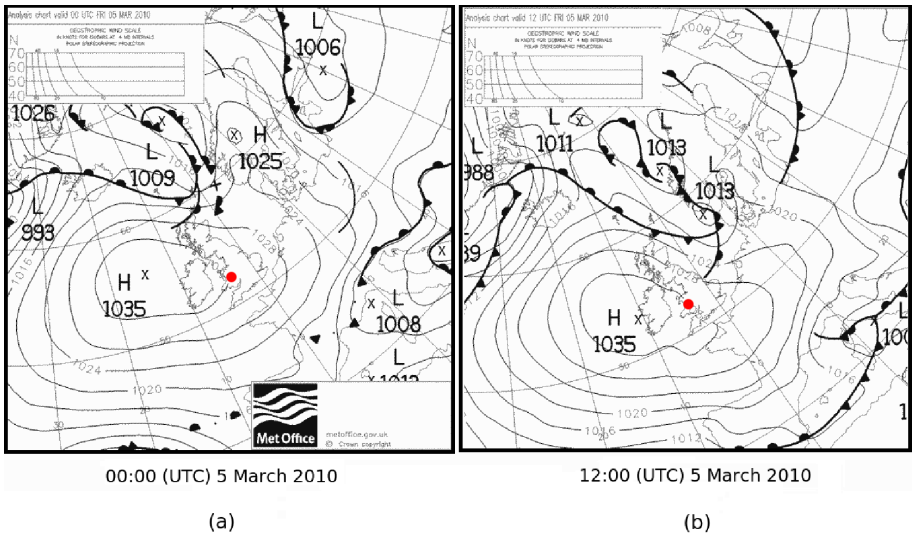

FIGURE 5.1: *Met Office surface analysis charts for 5 March 2010 at (a) 00:00 UTC and (b) 12:00 UTC. Red filled circle is the approximate location of the Clun Valley.*

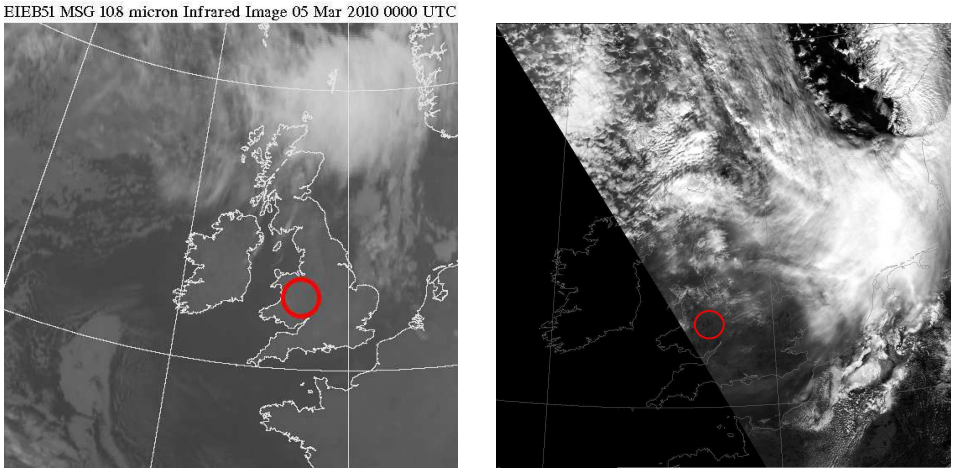

FIGURE 5.2: *(a) Infrared satellite image centred over the UK at 00:00 (UTC) on 5 March 2010. (b) NASA MODIS satellite image centred over the UK at 11:58 (UTC) on 5 March 2010. The Clun Valley region is located within the red circle.*

The infrared satellite image in figure 5.2(a), taken at 00:00 UTC on the 5 March, indicates no medium or high level cloud and little evidence for low level cloud at this time; however, mist or fog formation in valleys, such as the Clun Valley, may be hard to distinguish from the backround radiation of the land surface. The MODIS satellite image in figure 5.2(b),

at 11:58 UTC on the 5 March, also shows little evidence for cloud cover over the Clun Valley region. The presence of the high pressure ridge, low geostrophic wind speeds and little evidence for cloud cover or fog, imply that the synoptic weather conditions are ideal for CAP formation in the Clun Valley region.

The mean night-time ambient wind direction and speed, measured at Springhill 30 m AGL, for IOP 16 was 319° (NW) and 2.7 m s^{-1} respectively. The mean night-time F_{lw} measured at Duffryn 2 m AGL, was 0.77. These characteristics fit the "ideal" criteria for strong CAPs to form as outlined by the findings in chapter 4.

5.3 Overview of CAP cycle

As previously stated, the synoptic pressure situation appears to change relatively little throughout the diurnal cycle, with some movement of the high pressure centre from west to east towards the UK (figure 5.1). A pressure increase of 5 hPa is measured at the hill top site AWS 2 (376 m ASL) over the 24hr period (not shown). Measurements from the radiosondes launched at Duffryn also show an increase in height of the 500 hPa isobar level from 523.9 dm at 16:00 UTC to 529.2 dm at 05:30 UTC. This suggests that the high pressure is building over the Clun Valley region during the night of IOP 16.

Table 5.1 shows meteorological variables measured by the AWS during IOP 16. The lowest minimum θ observed occurred at the Clun Valley floor site AWS 5 (204 m ASL, see figure 3.3), measuring 265.2 K. This minimum occurred soon after local sunrise (06:50 UTC) on 5 March. The highest minimum θ observed was 272.8 K at the hill top site AWS 2 (376 m ASL), occurring at 04:05 UTC. The largest difference in minimum and maximum θ is 14 K, occurring at the valley bottom site AWS 5. The minimum change in θ was observed at the hill top site AWS 2, measuring 7.7 K.

Environmental temperatures below 0°C occur across all AWS at some point during the night. In-field observations taken by Met Office scientists at Duffryn reported clear skies, bright stars and small amounts of cirrus seen on occasions, up until 00:31 UTC (see table 3.7 in chapter 3). Further reports at 05:35 UTC record very hard ground, medium frost deposition, clear skies, with small amounts of cirrus on the horizon. Ground frost appears likely across the entire Clun Valley region during the night. By 09:00 UTC it was sunny,

AWS	Potential temperature				Wind dir.			Wind spd.		
	Min θ K	Time UTC	Max θ K	Time UTC	Day 1 °	Night °	Day 2 °	Day 1 m s^{-1}	Night m s^{-1}	Day 2 m s^{-1}
1	269.8	01:25	278.9	11:55	67	315	341	3.3	0.8	3.6
2	272.8	04:05	280.5	14:55	68	320	314	1.9	1.9	3.2
3	268.2	06:35	280.2	11:35	93	255	294	1.5	0.5	0.6
5	265.2	06:55	279.2	11:55	70	268	300	2.7	0.8	1.6
7	267.7	04:45	278.9	11:55	175	355	6	2.2	1.5	2.5
8	266.1	05:35	279.3	14:55	48	352	340	1.6	1.2	2.5
9*	266.3	05:35	278.7	11:55	79	301	311	2.1	0.4	1.2
10*	272.7	03:15	279.5	14:55	80	2	–	3.3	2.0	–

TABLE 5.1: *AWS data summary for the 24hr period from 12:00 UTC on 4 March 2010. *No data coverage for AWS 10 from 04:10–12:00 UTC on 5 March (79% coverage over entire night-time period), and AWS 9 between 06:15–08:25 UTC (84% coverage over entire night-time period).*

clear with some frost remaining in the shadows. At 11:00 UTC the conditions remained sunny and clear, with no frost present.

Visibility measurements at both Duffryn and Springhill did not record values low enough to represent fog formation (fog is defined when values of visibility fall below 1 km). At Springhill the night-time minimum visibility occurred at 02:45 UTC measuring 10.9 km and at Duffryn occurred at 03:45 UTC measuring 3.7 km. There were no observations of fog noted at Duffryn; however, local variations in humidity are possible and local fog formations at times cannot be completely dismissed.

The spatial evolution of the CAP across the entire Clun Valley region is shown by the terrain maps in figure 5.3. The plots show 2 m θ, 2 m winds (black arrows), 50 m winds at Duffryn (T1), and 30 m winds at both Springhill (T2) and Burfield (T3) (red arrows), for the 10min mean time periods centred at; (a) 14:05 UTC, (c) 18:05 UTC, (c) 22:05 UTC on the 4th March, and (d) 02:05 UTC, (e) 06:05 UTC and (f) 10:05 UTC on 5th March. The plots in figure 5.3 clearly show how the CAP develops in the bottom of the valley first and that the lowest sites remain the coldest locations until the CAP breaks up following sunrise. The plots also show how the wind direction within the valley changes as the CAP forms. The valley winds become orientated down-valley, reflecting thermally driven down valley flows, which appear decoupled from the ambient wind above. Through the night the ambient wind at Springhill (T2, red vector) changes with time, from a NE wind direction at 18:05 UTC (figure 12(c)), to a NW wind direction at 06:05 UTC (figure

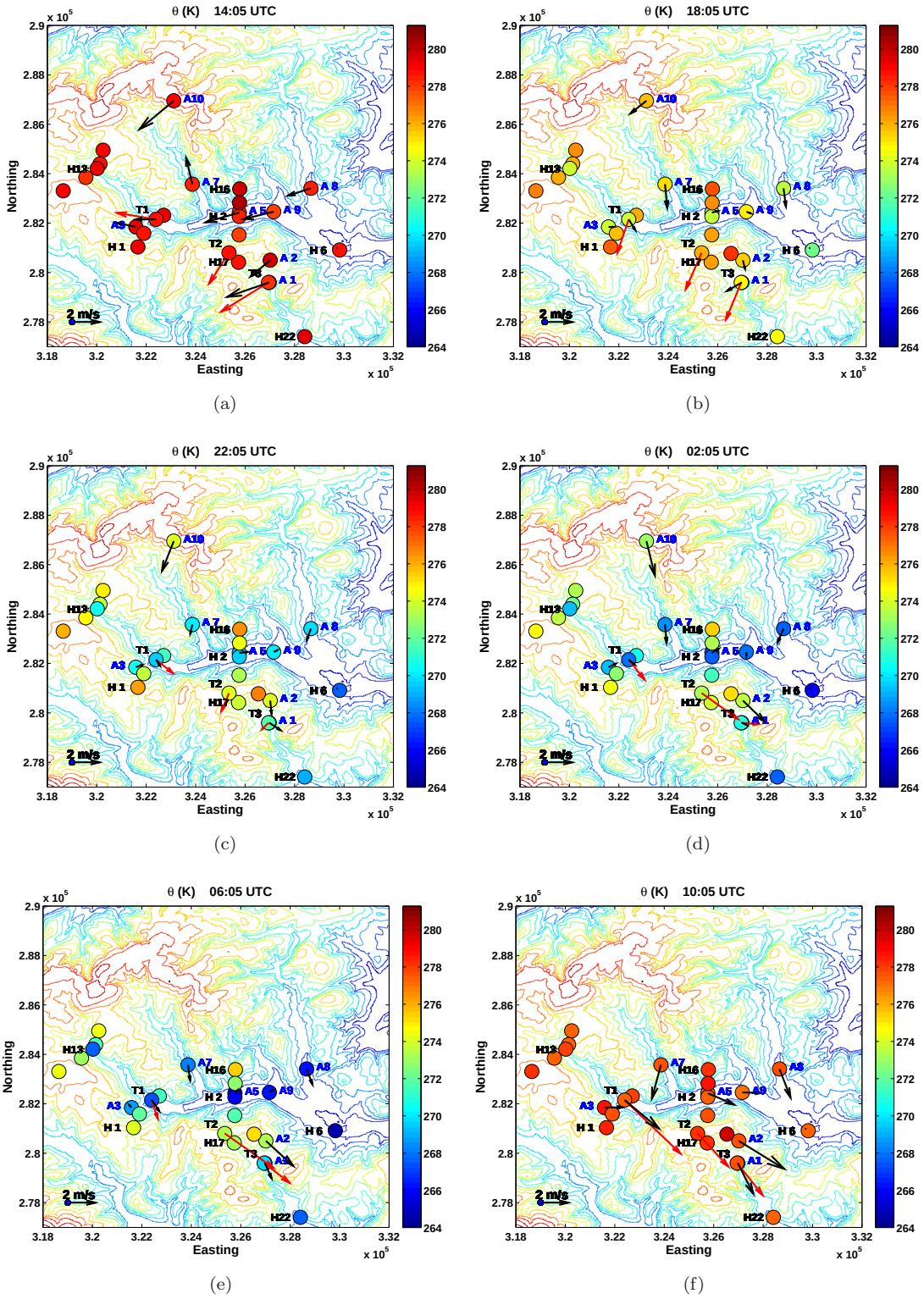

(a) (b) (c) (d) (e) (f)

FIGURE 5.3: *Left figures show 2 m θ, 2 m winds (black arrows), 50 m winds at Duffryn (T1), 30 m winds at both Springhill (T2) and Burfield (T3) (red arrows). Left figures are for 10min mean periods centred at: (a) 14:05 UTC, (c) 18:05 UTC, (c) 22:05 UTC, (d) 02:05 UTC, (e) 06:05 UTC, and (f) 10:05 UTC. Wind direction is from vector averaged winds and the magnitude is the mean wind speed (scalar).*

5.3(e)). One further observation is that some of the lowest sites, including AWS 6, AWS 9 (Clun Valley) and HOBO 22 (Burfield Valley), continue to remain cooler than those above by 10:05 UTC some 3hrs after local sunrise (figure 5.3(f)).

A more detailed overview of the 24hr cycle, from 12:00 UTC on 4 March 2010, is summarised by the time-series plots in figure 5.4, which consist of; (a) 2 m θ, (b) environmental lapse rate (ELR), (c) 2 m relative humidity (RH), and (d) 2 m water vapour mixing ratio (M_r). Additional results showing the evolution of the energy budget at the three mast sites throughout IOP 16 are provided in Appendix C.

The 2 m θ time series (figure 5.4(a)) shows measurements at sites located across the Clun Valley region, at difference heights ASL. At all locations cooling starts ∼2hrs prior to local sunset (17:57 UTC) at around 16:00 UTC. From ∼19:00 UTC, AWS 5 and 8 (green and red), two valley bottom sites at similar elevations, are clearly colder than those above forming a temperature inversion (a positive environmental lapse rate). Prior to sunset the ELR is negative (figure 5.4(b)), which reflects a well mixed boundary-layer and a small decrease in temperature with height. In figure 5.4(b) the blue time series is the ELR calculated using all HOBO and AWS 2 m temperature measurements. The red filled circles show the Clun Valley ELR using radiosondes launched from Duffryn. The blue time series error bars indicate the amount of variability in temperature across all AWS and HOBOs at each time interval (see methods chapter 3.4.3 for ELR methods used).

As the inversion forms around sunset, the ELR changes from negative to positive. A positive ELR is characteristic of temperature increasing with height ($\partial T/\partial z > 0$), i.e., CAP formation. After sunset there is a positive increase in the ELR with time until sunrise. Following sunrise (∼07:00 UTC) a negative ELR ensues. Initially the ELR appears to increase relatively uninterrupted from sunset until ∼22:00 UTC. However, between 22:00–23:30 UTC and 02:30–03:30 UTC the ELR decreases, appearing to recover between with a small peak at ∼02:30 UTC. Between 04:00–06:00 UTC the ELR increases to a 24hr peak, representing a rapid strengthening of the CAP in the final two hours before sunrise.

Following sunrise the temperature inversion begins to break down during the morning transition. From ∼07:00 UTC (∼1hr after sunrise), a rapid warming is seen across all regions, resulting in the temperature inversion breaking down around ∼09:00 UTC and a negative ELR ensues (figure 5.4(b)). By ∼09:00 UTC, temperatures across all sites appear

similar although as previously noted some of the lowest sites, including AWS 6, 9 and HOBO 22, continue to remain cooler by 10:05 UTC (figure 5.3(f)). At 09:00 UTC, AWS 3 is noticeably warmer than other sites in figure 5.4(a) (see figure 5.3(f) also). The mean daytime wind speed at AWS 3 on 5 March is notably less than other sites (see table 5.1). AWS 3 is located on a small south-east facing slope and is likely to be subject to increased incoming *SW* radiation during the morning hours compared to many other locations. AWS 3 is also more sheltered by vegetation compared to other locations. Combined these characteristics are likely to explain why AWS 3 is warmer during this period compared to other sites.

A notable feature of the 2 m θ time series (figure 5.4(a)) are the numerous warming events that occur during the night, across a number of sites, which occur within an overall cooling trend. One example occurs at the hill top site AWS 10 between 20:00–22:00 UTC and again at Burfield between 03:00–04:00 UTC. At times there are noticeable differences between the radiosonde ELR (red circles) and the 2 m temperature ELR (blue solid line, figure 5.4(b)). The dips in the ELR appear to be associated with the larger, more sustained warming events, which occur across a number of sites. Furthermore, the increase in ELR towards the end of the night (from 3:30 UTC) appear to be mostly attributed to a warming of some higher regions of the valley and continued cooling within the lowest regions of the valley also. Small intermittent warming/mixing events are seen across all sites throughout the night and appear similar in scale to the averaging period (10 minutes, figure 5.4(a)). These smaller warming/mixing events are likely to be caused locally, by one of the following mechanisms outlined by Banta *et al.* (2004): (a) local shear, (b) local pulsations, (c) local obstacle effects, or (d) the convergence or divergence of local drainage flows.

As with the evolution of 2 m θ and the ELR, there is also variability in the evolution of RH and the mixing ratio (M_r) during IOP 16. A time series of RH and M_r, for the valley floor site HOBO 2 (202 m ASL) and the hill top site HOBO 16 (362 m ASL), are shown in figures 5.4(c) and (d) respectively. Before sunset RH and M_r are similar at both sites, falling at both locations from 76–78% RH at 12:00 UTC to 60–64% RH at 16:00 UTC. The fall in RH coincides with a drop in M_r. RH increases at both locations from 16:00 UTC until sunset ($\sim$17:57 UTC). M_r remains relatively unchanged over this period, therefore the change in RH is primarily caused by the decrease in temperatures.

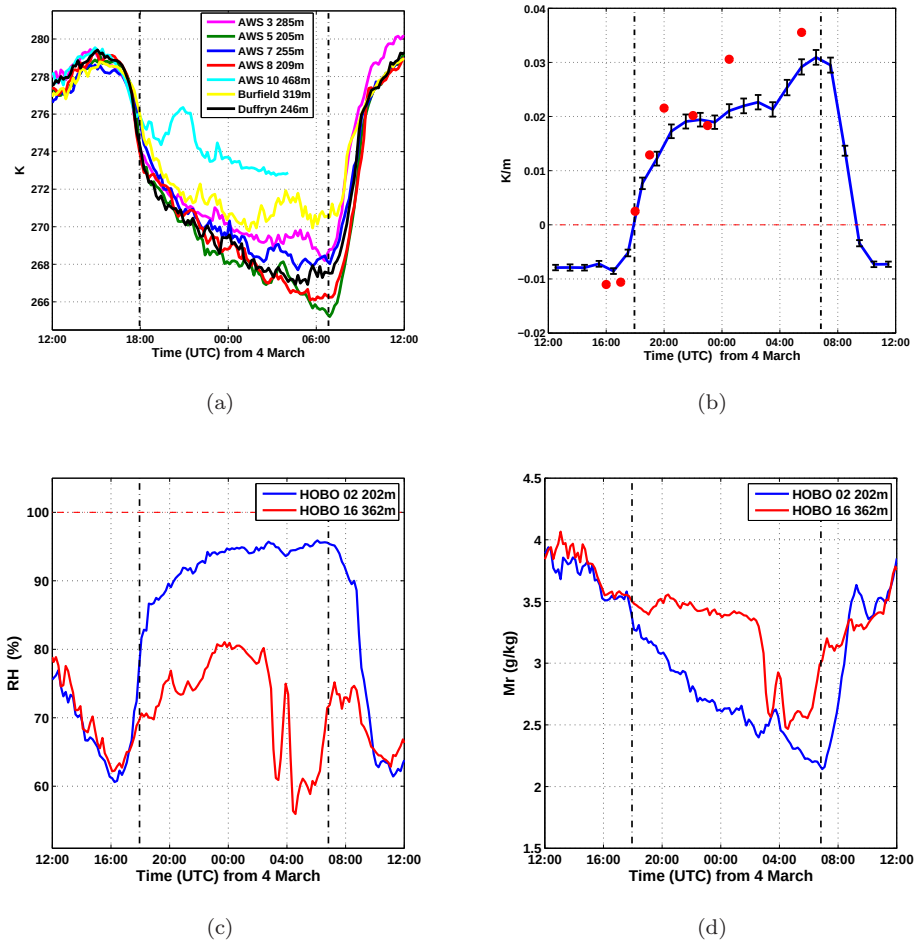

FIGURE 5.4: *24hr time series of (a) 2 m θ, (b) Clun Valley environmental lapse rate (ELR), (c) RH and (d) water vapour mixing ratio (M_r). Dashed vertical black lines show local sunset and sunrise times (calculated using NOAA solar calculator). In figure (b) the blue solid line is the ELR calculated using 2 m temperature from AWS, HOBO and mast sites. The red markers are the ELR calculated using radiosonde measurements launched from Duffryn (0–400 m AGL).*

After sunset an increase in RH and a decrease in M_r is seen at the valley floor site HOBO 2; however, M_r at the hill top site HOBO 16 remains relatively unchanged over the same period, subsequently values of RH and M_r begin to diverge between the hill top and the valley bottom (HOBO 2 and HOBO 16 respectively). Increases in RH are seen at both HOBO 16 and HOBO 22, but are less pronounced at HOBO 16. This trend continues until a peak in RH occurs at ∼03:00 UTC measuring ∼95% at HOBO 2 and ∼80% at HOBO 16. This peak in RH at ∼03:00 UTC also coincides with a small peak in the ELR seen at this time. The fact that M_r appears to drop continuously in the valley but remains relatively unchanged at the hill top, suggests that the moisture at the valley bottom site

is being continuously removed – by frost or dew deposition – as the air pools along the valley floor.

Soon after ∼02:30 UTC a dramatic drop in M_r is seen at the hill top site HOBO 16 and values appear to briefly match those seen at the valley bottom site HOBO 2. This coincides with a marked decrease in RH from ∼ 80% to ∼ 60%, which generally persists from 03:00–07:00 UTC. Over the same period RH changes very little at the valley bottom site HOBO 2, remaining around 95% with M_r continuing to fall reaching a minimum around sunrise. There is one marked spike in M_r at both locations around 04:00 UTC, which coincides with increasing θ at both AWS 3 and Burfield in figure 5.4(a), following a decrease in the ELR seen before 04:00 UTC in figure 5.4(b). The drop in RH seen at the hill top site HOBO 16 over this period, may in part be due to an increase in the ambient temperature (i.e., the ambient air that is advecting in is warmer than previously in the night).

The temperatures in the lowest regions approach the point of freezing around sunset (figure 5.4(a)), therefore frost deposition may be occurring in these regions throughout the night. However, the temperatures at the hill top site HOBO 16 do not drop below freezing for the entire night, but remain around 1°C for much of the period between 00:00–07:00 UTC (not shown). A brief fall in temperatures to ∼0°C occur at ∼04:00 UTC, which coincide with the spike in RH and M_r. Since the temperature measurements are taken at ∼2 m AGL, it seems likely that the ground below HOBO 16 may well be low enough for frost to occur, therefore the removal of moisture (decrease in M_r) by frost deposition may be occurring also.

After sunrise values of RH and M_r at the hill top and valley floor sites begin to converge as the ELR becomes negative and a subsequent break down in the temperature inversion is seen by ∼10:00 UTC. After 10:00 UTC, RH and M_r return to values seen before sunset the previous evening and persist thereafter. This pattern in the diurnal cycle of RH and M_r is repeated across comparable sites, where elevated sites record much lower values of RH during the night and a marked decrease in RH is seen between 02:00 and 07:00 UTC.

Many of the changes in RH, M_r, θ and ELR (figure 5.4) appear related. The LIDAR profiles shown in figure 5.5 show a number of anomalies that occur in the region at and above the Valley, measured at Duffryn, during the night and morning hours of IOP 16. Specifically, three episodes have been highlighted; Episode 1, Episode 2 and Episode 3.

The start of each episode coincides with a change in behaviour of RH, M_r, θ and/or the ELR.

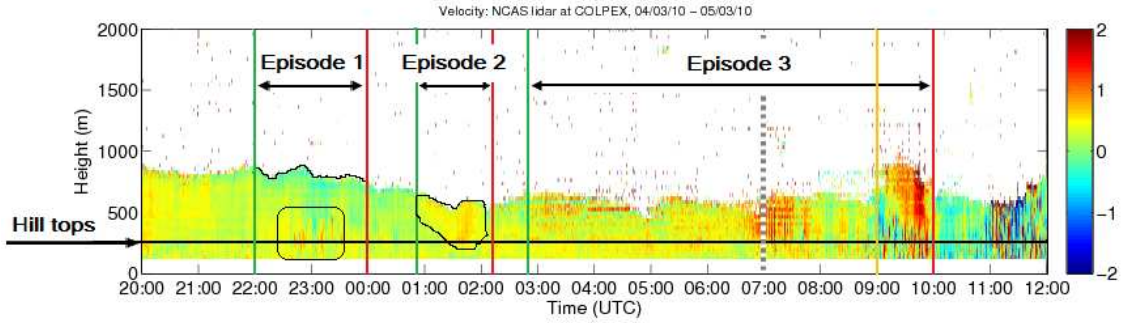

(a)

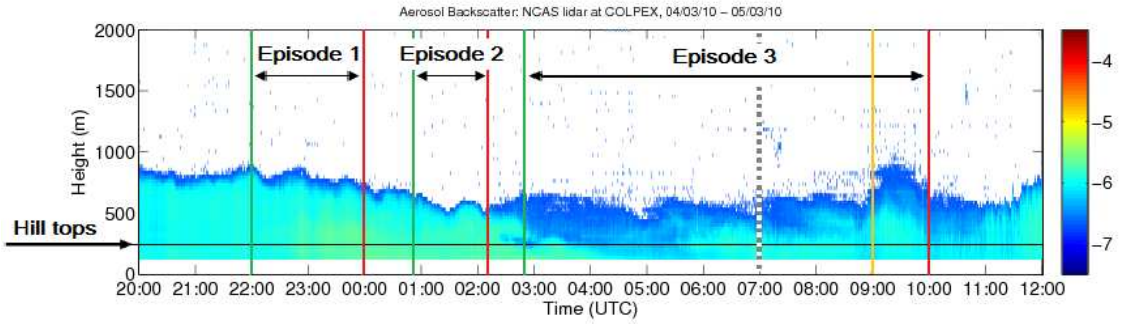

(b)

FIGURE 5.5: *Time series of LIDAR measurements taken at Duffryn showing vertical profiles of; (a) vertical velocity and (b) backscatter, from 4–5 March 2010. The vertically dashed grey line indicates the time of sunrise.*

Episode 1 is characterised by intermittent increases and decreases in vertical velocities in the hill top regions (figure 5.5(a)), between ∼22:30–23:30 UTC. Over the period between 22:00–23:00 UTC a wave like structure is also seen at the top of the LIDAR profiles.

A wave like structure is also seen in the LIDAR profile during Episode 2, at ∼01:30 UTC; however, the vertical velocity profile is distinctly different when compared to Episode 1, with no intermittent behaviour seen. Instead the vertical velocity profile is characteristically more turbulent in appearance. A region of higher vertical velocities is seen that descends with time, reaching the hill top regions around 01:45 UTC. This region of increased vertical velocities fizzle out around 02:00 UTC.

The period outlined by Episode 3 is much longer than either Episodes 1 or 2. Episode 3 appears typically more turbulent, with higher vertical velocities seen in the LIDAR

profile, begininning soon after the end of Episode 2. Episode 3 is also associated with less backscatter generally (figure 5.5(b)), which is indicative of either a drier atmosphere, i.e., less condensate, or a cleaner atmosphere, i.e., less aerosol. Evidence from the RH, M_r and θ time series in figure 5.4 over the same time period, suggest that the reduced backscatter in Episode 3 is associated with warmer, less humid air. Two further features are seen in the LIDAR profile during Episode 3 (figure 5.5(a)), associated with increased vertical velocities. The first occurs around sunrise at ∼07:00 UTC and the second between 09:00–10:00 UTC, during the period when the CAP finally breaks up.

5.3.1 Summary

It has been shown that a strong inversion forms within the Clun and Burfield valleys during the night of IOP 16. As expected during an ideal CAP forming night, an inversion first forms around sunset, following a period of rapid cooling across all regions. The inversion is strongest around sunrise and breaks down in the late morning some 3–3.5hrs after sunrise, between 10:00–10:30 UTC. A change in the ambient wind direction occurs at the hill top site Springhill 30 m AGL, turning anticlockwise with time from a NE direction around sunset, to a NW direction by sunrise.

Interestingly the evolution of θ, RH, M_r and ELR, all show fluctuations throughout the night. These changes highlight the complexity of the CAP evolution during IOP 16, under apparently "ideal" synoptic conditions. There appear to be noticeable warming periods at some locations amid an overall cooling trend. The ELR does not increase linearly with time and there are two noticeable dips in the ELR seen at ∼23:30 and ∼3:30 UTC, with a small peak occurring between at ∼02:30 UTC.

RH at the hill top regions remain relatively low compared to valley bottom sites; however, values of M_r are higher at the hill tops than at the valley bottom sites, although a general decrease is seen at both locations throughout the night, with the decrease in M_r largest at the valley bottom site. The results suggest that the larger decrease of M_r within the valley may be due to frost deposition and the subsequent loss of moisture to the surface, since the valley floor sites appear to be cold enough for frost deposition to occur throughout the night following sunset.

Three episodes of interest have been highlighted in the LIDAR profiles. Each of these episodes are associated with an anomaly in the LIDAR occurring in the region at and above the hilltops. Furthermore, each of these episodes coincides with a change in the behaviour of RH, M_r, θ and/or the ELR, which suggests that the CAP is being disturbed by phenomena that are not site specific. The focus of following investigations is on these three episodes.

5.4 Episode 1; gravity wave activity

The following results focus on the evolution of the CAP between 22:00–00:00 UTC, defined as Episode 1. Episode 1 is characterised by intermittent increases and decreases in vertical velocities seen in the LIDAR profile measured at Duffryn (figure 5.5(a)), from ∼22:30–23:30 UTC. The increases and decreases in vertical velocities have a periodic nature, which is unlike the vertical velocity profile seen at other times during the night. These intermittent increases (red) and decreases (blue) in vertical velocities occur in the region at and just above the hill tops, between 200–400 m AGL (relative to Duffryn). There are between 6–8 intermittent increases in the vertical velocity over this 1hr period. A wave like structure is also seen at the top of the LIDAR profile between 22:00–23:00 UTC, with a peak seen just prior to 23:00 UTC. Between the intermittent increases in vertical velocity, there is a small period of sustained downward vertical velocities soon after 23:00 UTC, which extend throughout the 125–800 m LIDAR profile. Higher values are concentrated in the region between 150–250 m AGL.

Prior to Episode 1, a temperature inversion formed around sunset across the valley depth (figure 5.4(a)). A positive ELR ensued and increased with time (figure 5.4(b)), as the inversion established and the CAP continued to grow (see figure 5.3). Over the same period, values of RH and M_r at the hill top and valley bottom sites diverge and this difference generally increases with time. RH increased with time across all regions, but more so at the valley bottom regions (figure 5.4(c)).

At the start of Episode 1 (∼22:00 UTC) the ELR ceases to increase and instead decreases over the following hour or so, which suggests an interuption of the CAP growth. Between 22:00–23:30 UTC there are noticeable increases in θ at a number of sites located across the Clun Valley region, at different heights; including AWS 10, Burfield, AWS 3, AWS 7 and

Duffryn (figure 5.4(a)). In each case these increases are larger in magnitude and in length of time, compared to the smaller more intermittent increases often seen before and after. Viewing figure 5.4(a), sites located in the bottom most part of the valley are less affected during this period, including AWS 5 and AWS 8. Over the same period the RH measured at the hill top site HOBO 16, also increases sharply from 22:00–23:30 UTC. At the same time a region of increased backscatter is seen in the LIDAR profile between ∼150–400 m AGL, indicating higher levels of condensate in the region below 400 m AGL during this period (figure 5.5(b)).

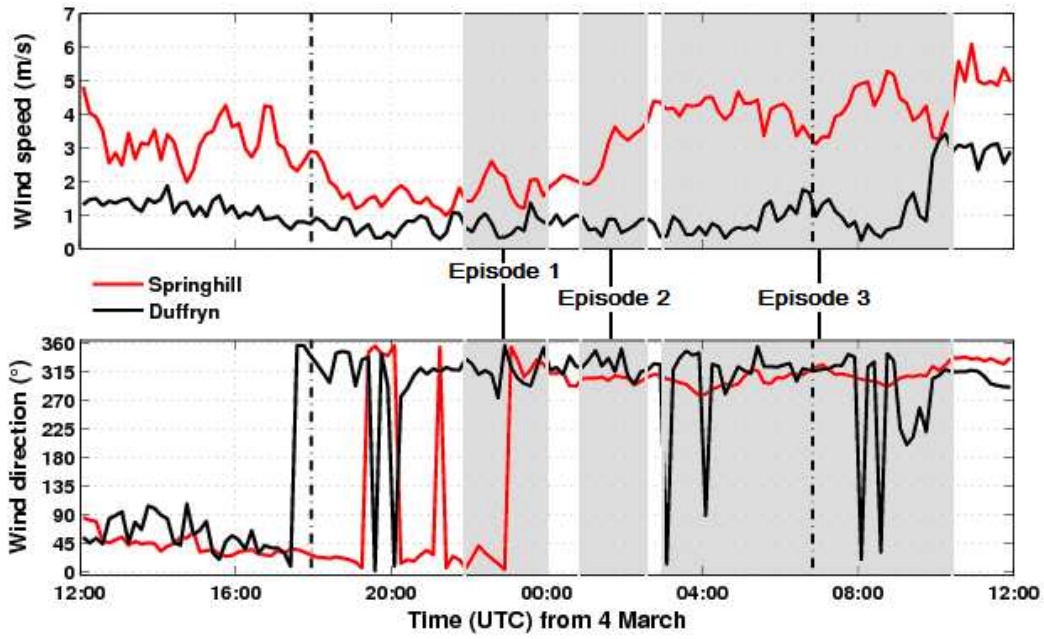

FIGURE 5.6: *Wind speed and direction for the 24hr period from 12:00 UTC 4 March.*

There are some noticeable changes in the behaviour of the ambient wind at Springhill and within the valley at Duffryn during Episode 1. This is shown by the time series in figure 5.6. A relatively abrupt change in wind direction is seen at Springhill, turning anticlockwise with time from a NE at 22:35 UTC, turning to a NW by 23:35 UT. Over the same period, an anticlockwise turning of the wind is seen at the hill top sites AWS 10 and AWS 2 (not shown), although neither are directly aligned to those seen at Springhill.

Prior to Episode 1, the 50 m wind at Duffryn (figure 5.6) generally persisted in a down-valley direction after the CAP started to form prior to sunset. However, the 50 m wind at Duffryn is no longer aligned down-valley at 23:05 UTC, instead the 50 m wind is from the SW, a direction that is aligned with the axis of the AWS 3 tributary valley that joins from

the SW (see figure 3.3). Variation away from a down-valley wind is seen at other sites during this period also. A down-valley wind returns at Duffryn by 23:35 UTC. This result shows that the thermally driven flow (drainage flow) that was established at Duffryn prior to Episode 1, breaks down, or is at least affected over this period, but recovers soon after. This is further emphasised by vertical profiles from Duffryn over the period shown in figure 5.7. The profiles of wind speed, TKE, wind direction and wind persistence, change over the period from 22:05–23:35 UTC. At 22:05 UTC the wind speed and direction profiles (see figure5.3(c) also) are very similar to those seen soon after sunset and are consistent with a thermally driven down-valley drainage flow from the NNW. In the middle of Episode 1 at 23:05 UTC (red profile), the wind speeds have decreased across the entire profile, the wind direction at 50 m has changed to a SW, aligned with the AWS 3 tributary valley and the wind in the upper parts of the drainage flow at 25 m and 50 m AGL, are less persistent. By 23:35 UTC the drainage flow has re-established, the wind speeds have increased across the 2–25 m layer and the 50 m wind speed and direction are similar to those seen at the start of Episode 1 at 22:05 UTC.

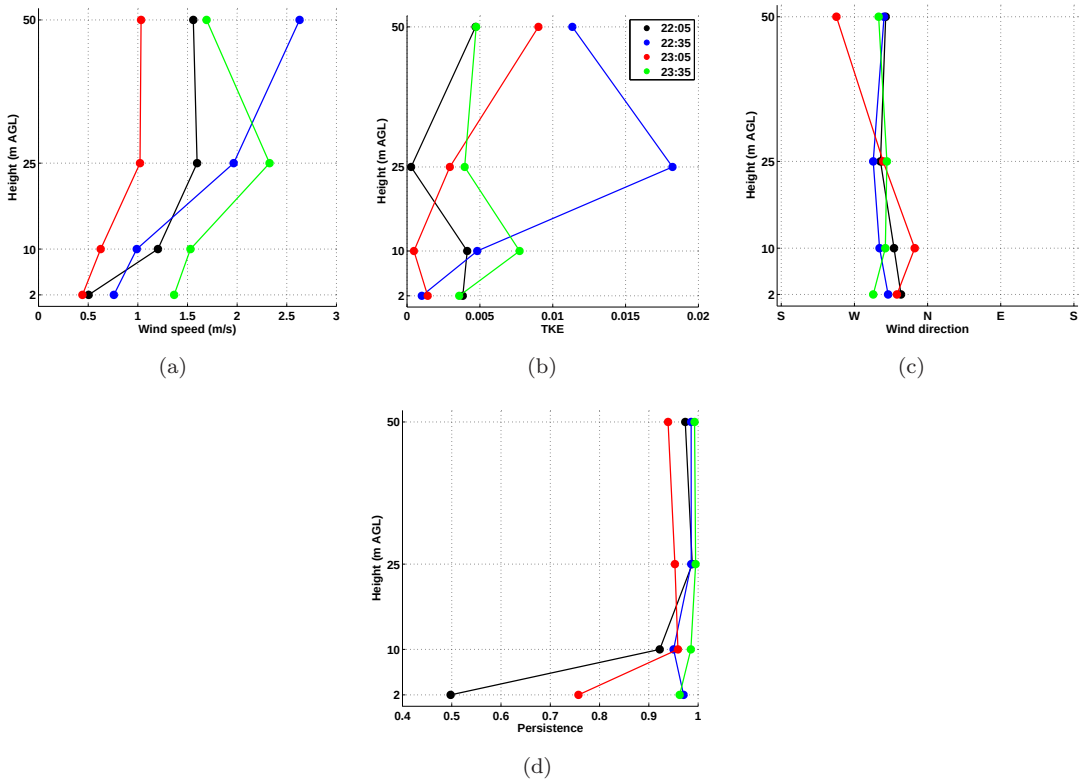

FIGURE 5.7: *Duffryn 10min mean profiles of (a) wind speed, (b) TKE, (c) wind direction and (d) wind direction persistence. Mean intervals are centred at 22:05 UTC (black), 22:35 UTC (blue), 23:05 UTC (red) and 23:35 UTC (green).*

Figure 5.8 shows radiosonde profiles launched from Duffryn before, during and after Episode 1 at 22:02, 23:01 and 00:35 UTC. The layer between 100–400 m AGL – from 50 m above the Duffryn mast to ∼200 m above the local hill tops – has cooled over the period from 22:02–23:01 UTC. From 23:01–00:30 UTC the layer between 600–900 m has warmed. Furthermore at 22:02 UTC, a sharp inversion is seen at 700 m that descends with time and is less well defined by 00:30 UTC. The winds strengthen from 22:02–00:30 UTC over the region between 200–800 m and turn anticlockwise throughout the layer. The majority of the wind direction rotation occurs between the region directly above the hill tops, between 200–400 m AGL, changing from a NE to WNW. This result compares well with the observations seen at Springhill in figure 5.6. For the region between 0–400 m AGL – from the valley floor to ∼200 m above the hill tops – the valley winds are different in all three profiles: however, at 23:01 UTC the profile appears noticeably different. Unlike other profiles, the wind speed increases linearly with height from 0–175 m AGL, with a decrease seen between 175–300 m AGL. The wind direction is down-valley at the lowest regions, which corresponds to the Duffryn mast; however, unlike the profiles at 22:02 and 00:30 UTC, the wind direction turns clockwise with height up to 300 m, then anticlockwise between 300–400 m. The 23:01 UTC radiosonde profile corresponds with the increase in downward vertical velocities seen in figure 5.5(a), during a period where a wave like structure is also seen at the top of the LIDAR profiles in figure 5.5.

Figure 5.9 shows radiosonde ascent rate profiles for the corresponding radiosondes launched from Duffryn shown in figure 5.8. Each of the radiosonde profiles display different characteristics. At 22:02 UTC a decrease in ascent speeds is seen between 200–800 m, followed by a rapid increase between 800–1, 000 m. A decrease in the ascent rate implies an increase in the downward component of wind, or the existence of a warmer layer of air relative to the region above or below the balloon as it ascends. The corresponding radiosonde profile shows a linear θ profile across this region, therefore the evidence suggests the decrease in ascent rate between 200–800 m at 22:01 UTC is due to increase in downward momentum. This also coincides with a layer of very little wind shear between the hill tops and ∼600 m (figure 5.8(c)).

There is a rapid increase in the ascent rate between 800-1,000 m, which implies less downward motion. Above 1,000 m the ascent rate returns to a value similar to the background ascent rate. The 23:01 UTC ascent profile appears distinctly different compared to the

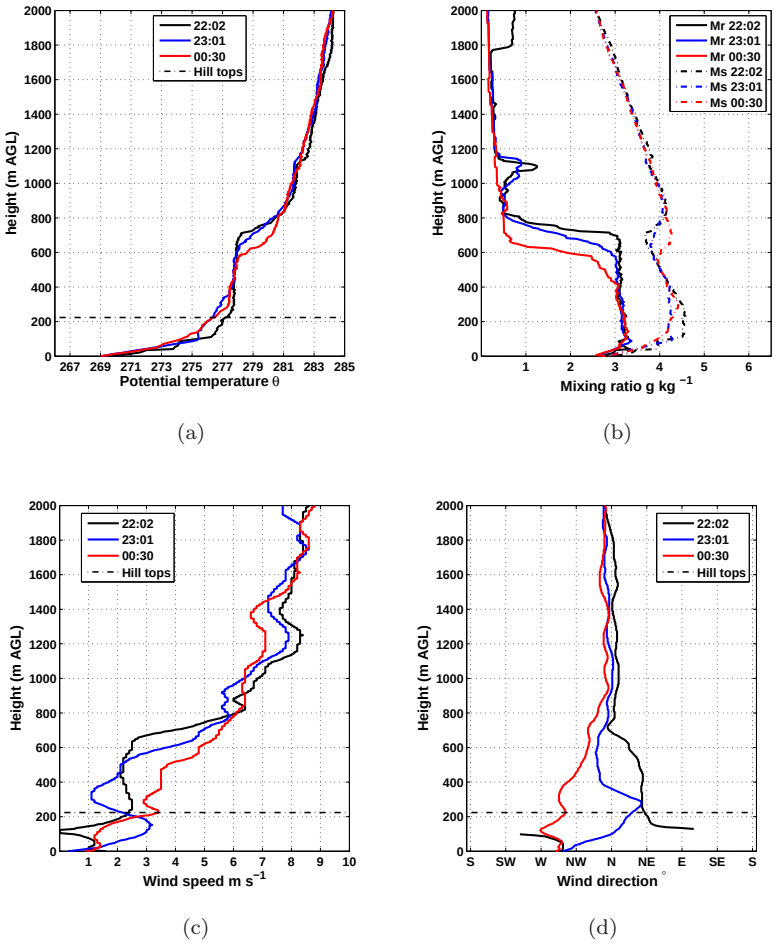

FIGURE 5.8: *Above are three radiosonde profiles launched from Duffryn at 22:02, 23:01 and 00:30, of; (a) potential temperature, (b) water vapour mixing ratio (M_r) and saturation mixing ratio (M_s), (c) wind speed, and (d) wind direction.*

profiles before and after (22:02 and 00:30 UTC respectively). In this instance there are two noticeable periods of decreasing ascent rates. The first is between ∼1–1.5 km and the second between ∼3.1–4 km. As before the decrease in ascent rate implies an increase in down-ward momentum in the absence of any warming with height. There is a very small, almost negligible temperature inversion that exists at ∼3.8 km (not shown), otherwise there is no warming associated with these changes in ascent rate. Relative to the other profiles, the ascent profile at 00:35 UTC show less variation in the ascent rates. The ascent rate profiles at 22:02 and 23:01 UTC (figure 5.9), show marked changes that are not related to any change in θ. In the absence of any large temperature changes, these decreases and increases in ascent rate are an indicator of wave activity in the atmosphere (Lalas & Einaudi, 1980).

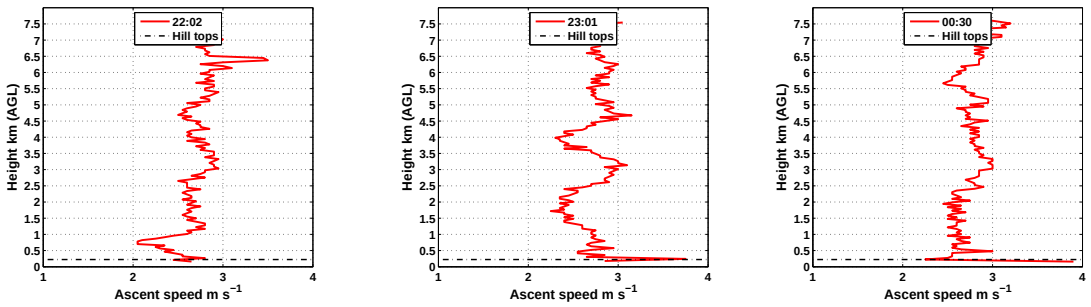

(a) (b) (c)

FIGURE 5.9: *Radiosonde ascent speed profiles at 22:02 (a), 23:01 (b) and 00:30 UTC (c).*

Zängl (2005a) suggests that turbulent erosion may become relevant when the formation of orographic gravity waves accelerates ambient airflow down into a valley and maintains very strong vertical shear on top of a cold pool. The results here clearly indicate that a disturbance, likely to be a gravity wave, caused a redistribution of air in some parts of the valley, warming some lower regions and cooling some higher regions. Therefore for a short period the gravity wave activity arrested the growth of the CAP. The drainage flow at Duffryn is also disrupted during Episode 1, particularly at 23:05 UTC. There is a notable change in wind direction at 50 m, changing from a down-valley wind to a cross valley WSW wind at 23:05 UTC. The WSW wind may indicate the presence of a drainage flow from the neighbouring AWS 3 tributary valley.

This disturbance of the CAP evolution, likely to be caused by a gravity wave, may not have affected all regions of the Clun Valley and results here give no clear evidence either way. The possible signature of a drainage flow from the AWS 3 tributary valley, may indicate that the AWS 3 drainage flow was uninterrupted, or less prone to the gravity wave activity. The upper parts of drainage flows are known to be particularly susceptible to breakdown through turbulent mixing by its proximity to the free atmosphere, lack of terrain sheltering and generally weaker density gradients than lower regions of a valley (Gudiksen *et al.*, 1992). The ambient wind speed at Springhill over this period remains below 3 m s^{-1}, for this reason the ambient wind speed does not appear to be the cause of drainage flow erosion, since erosion is not expected to occur until ambient wind speed exceed 5 m s^{-1} (Orgill *et al.*, 1992).

Combined, these results lend supporting evidence for gravity wave activity in the atmosphere during Episode 1 (figure 5.8). The exact cause of the gravity wave(s) is not known.

A sudden change in the ambient wind direction at Springhill is seen at ∼23:00 UTC in figure 5.6 and in the radiosonde profiles in figure 5.8. The gravity wave(s) may be caused by wind speed and/or directional shear within the atmosphere, or by other means such as orographic generation. Another possible explanation is that the gravity wave activity is generated locally in the form of a hydraulic jump. Hydraulic jumps are hypothesised by Adler *et al.* (2012) to be the cause of warm air intrusions in to Arizona's Meteor crater during CAP nights; one of the few studies of CAPs conducted on similar scales.

5.5 Episode 2; acceleration of ambient wind

During Episode 2, increases in vertical velocities (∼1 m s^{-1}) are seen above the valley at 600 m AGL, which descend with time from 01:00 UTC reaching the hill top regions at 200 m AGL by ∼01:30 UTC. As in Episode 1, a wave like structure is seen at the top of the LIDAR profiles in Episode 2; however, on this occasion there are no intermittent increases in the vertical velocities (figure 5.5). The region of increased vertical velocities dissipates out around 02:00 UTC. The disturbance in Episode 2 (1:00–2:30 UTC) appears to have a relatively small impact on the CAP evolution compared to Episodes 1 and 3; however, some warming of higher regions is seen, most evident at Burfield (see figure 5.4(a)). A warming of higher regions, with continued cooling of lower regions, will result in an increase of the valley ELR. A small peak in the ELR is seen at the end of Episode 2 at 02:30 UTC (figure 5.4(b)).

The increase in vertical velocities in Episode 2 coincide with a change in the ambient wind direction and a sudden increase in the ambient wind speed from 2–4.5 m s^{-1} (see figures 5.6) – the ambient wind speed generally remains below 2 m s^{-1} from sunset to 01:00 UTC. The acceleration of the ambient wind over this 1.5hr period equates to a mean acceleration of ∼4.6 x 10^4 m s^{-2}. Orgill *et al.* (1992) suggest that ambient wind accelerations exceeding ∼4.6 x 10^4 m s^{-2} can lead to the erosion of drainage flows, which will affect the CAP evolution.

A change in the Duffryn drainage flow structure also occurs during Episode 2. The jet peak height of the drainage flow is lower (25 m) during Episode 2, compared to other periods when the CAP is undisturbed. This is seen in the 01:35–02:35 UTC vertical profile in figure 5.10(a). During undisturbed periods the peak jet height of the Duffryn drainage

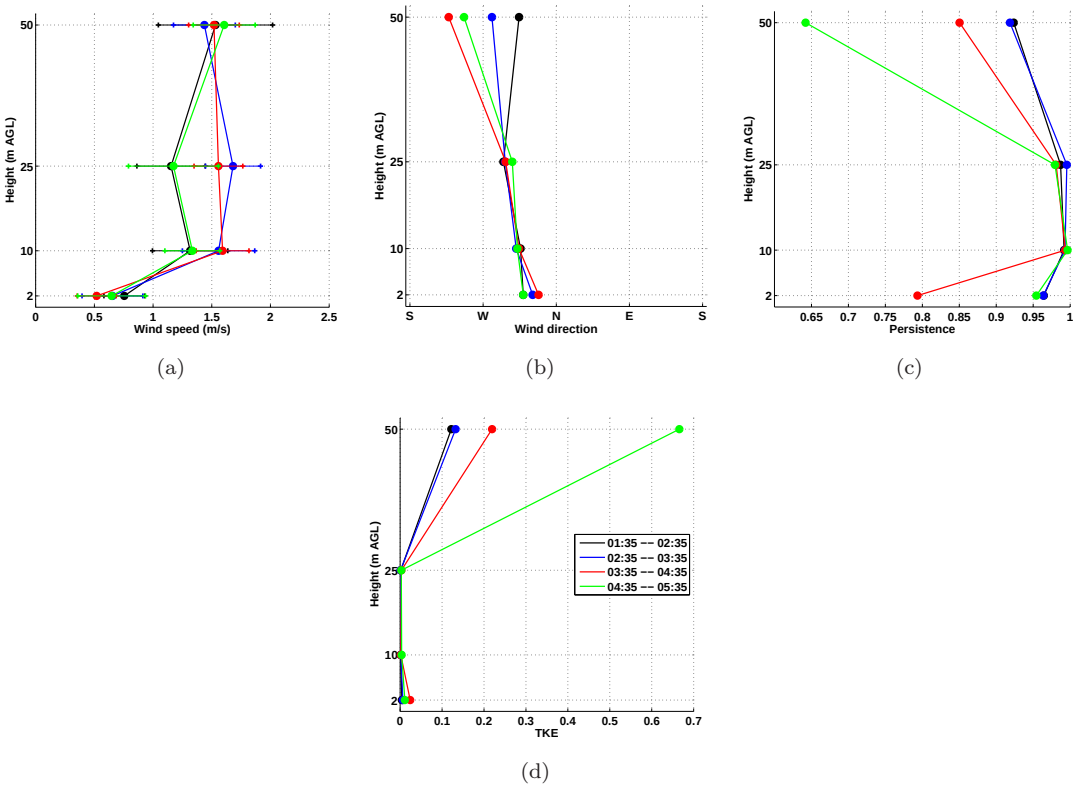

FIGURE 5.10: *Duffryn vertical profiles of; (a) wind speed, (c) wind direction, (d) wind direction persistence and (b) TKE. For 1hr mean intervals; 01:35–02:35 UTC (black), 02:35–03:35 UTC (blue), 03:35–04:35 UTC (red) and 04:35–05:35 UTC (green).*

flow in IOP 16 is typically seen at 25 m, 50 m or some height above 50 m AGL. When the ambient wind speed stops increasing at ∼02:30 UTC, the region of increased vertical velocities dissipate out (figure 5.5(a)) and the typical drainage flow structure at Duffryn is re-established (blue profile in figure 5.10). This result does not reflect the climatology findings in chapter 4, figure 4.22, which show that the Duffryn drainage flow peak jet height is on average higher during weaker CAP nights, although there are large standard deviations in the 50 m wind climatology during weak CAP nights.

Figure 5.11 shows the evolution of the bulk Richardson number (Ri_b, see background equation 2.2) during IOP 16. Ri_b is shown for the regions between Springhill 30 m AGL and; 5.11(a) Burfield, 5.11(b) Duffryn. Values of $Ri_b > 1$ represent laminar flow (strong stability), when $0.25 < Ri_b < 1$ the atmosphere is in transition between laminar and turbulent flow, and when $0.25 > Ri_b$ the air column is said to be turbulent (see background section 2.2.2.)

For the three hour period preceding 02:00 UTC, the region above Burfield and Duffryn

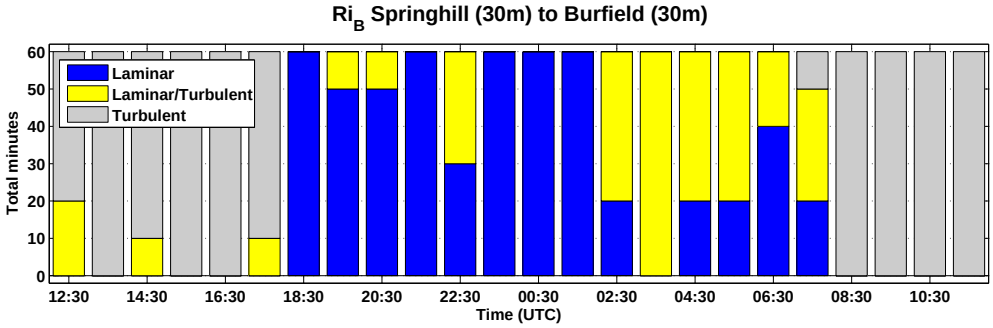

(a)

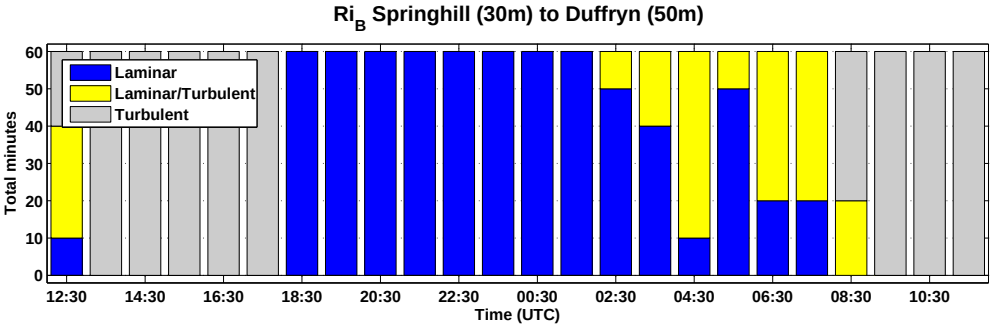

(b)

FIGURE 5.11: *Bulk Richardson number (Ri_B) representing the regions between Springhill 30 m AGL and; 5.11(a) Burfield 30 m AGL, 5.11(b) Duffryn 50 m AGL.*

is characteristically laminar; however, between 02:00–03:00 UTC, both are characteristically laminar/turbulent for part of the 1hr period and Burfield laminar/turbulent for the majority of this 1hr period. Viewing figure 5.11, Episode 2 appears to be in a transition period from laminar to more laminar/turbulent flow.

The results combined suggest that the increase in ambient wind speed seen at Springhill during Episode 2 (figure 5.6), is caused/related to an increase in vertical velocities seen in the LIDAR profile (figure 5.5). A subsequent increase in shear driven turbulence causes warmer air to be mixed down in more sensitive regions, including the upper parts of the Duffryn drainage flow and Burfield, which is highlighted further by the Ri_b results in figure 5.11. Therefore the evidence here suggests that the disturbance in Episode 2 is associated with a decrease in stability in the hill top regions, which subsequently leads to more sensitive regions – such as Burfield – being subject to some warming.

5.6 Episode 3; nocturnal low level jet

Viewing the LIDAR vertical velocity profile in figure 5.5(a), Episode 3 appears distinctly different in character to both Episode 1 and 2. In this instance the vertical velocities are characteristically more turbulent. The increase in vertical velocities are present across much of the LIDAR profile depth between 200–600 m. The increased vertical velocities also persist for a longer period of time. Episode 3 is associated with less backscatter (figure 5.5(b)), which is indicative of either drier air, i.e., less condensate, or cleaner air, i.e., less aerosol. The RH and M_r time series in figure 5.4, suggest that the region of reduced backscatter is less humid.

At the start of Episode 3 there is a noticeable dip in the ELR at ∼03:30 UTC. From 04:00–06:00 UTC the Clun Valley region ELR rapidly increases. This suggests either a warming at elevated sites, a cooling at valley floor sites, or a combination of both. In fact both are occurring (see figure 5.4(a)). As a point of further interest, towards the end of the night, weak up-valley winds are observed at the valley bottom sites AWS 5 and AWS 9 (not shown). This characteristic is seen in the climatology results for AWS 9 (see chapter 4), figures 4.15 and 4.21(e)). The up-valley winds observed at AWS 5 and 9, coincide with an accelerated cooling event at these two sites (figure 5.4(a)), this may be caused by one of the following:

1. Extra stability at the valley bottom caused by warming of higher regions, leading to increased decoupling of the lower regions of the valley, therefore increased sheltering from the ambient winds and an increase in the sensible heat flux divergence.

2. Advection of cold air up-valley; as the CAP in lower regions continues to cool uninterrupted, an “overspill” of cold air advects up-valley.

3. Potential pooling of elevated major tributary valleys, causing colder drainage flows to enter the valley system, as noted by Neff & King (1989).

4. Drainage flows can weaken as the stronger down-valley flow expands and the temperature inversion in the valley grows and strengthens (Haiden & Whiteman, 2005). This may have further feedbacks by modifying the way the CAP evolves later in the night, such as blocking the normal CAP outflow region.

As in Episode 1 and 2, the Duffryn drainage flow is again affected during Episode 3, particularly at 50 m (figure 5.6). Variations in the wind direction, increases in TKE and decreases in wind persistence are seen over this period (figure 5.10). The Duffryn vertical wind speed profile at 05:05 UTC is almost identical to that seen during Episode 2 at 02:05 UTC. As in Episode 2, there is a lowering of the drainage flow peak jet height to 10 m AGL at 05:05 UTC (figure 5.10). Throughout much of Episode 3 the ambient wind speed remains between 4–5 m s^{-1} from 03:30–06:00 UTC, which follows an acceleration of the ambient wind seen in Episode 2 (figure 5.6). The ambient wind speeds during this period are the highest seen throughout the entire night of IOP 16. Orgill *et al.* (1992) show that even well established drainage flows are significantly affected when the ambient wind speed exceeds 5 m s^{-1}, which is particularly true for upper slope regions. In these instances the existing CAP is likely to be eroded from the top down by shear induced turbulence. As emphasised before, many studies have highlighted the importance of the above valley ambient wind speed, which can erode pre-existing CAPs and drainage flows, when the wind speed exceeds 5–8 m s^{-1} (Barr & Orgill, 1989; Orgill *et al.*, 1992; Iijima & Shinoda, 2000; Whiteman *et al.*, 2001; Bogren *et al.*, 2000b; Vosper & Brown, 2008). The Ri_b results in figure 5.11 clearly indicate that the regions above both Burfield and Duffryn, are more turbulent after 02:00 UTC when the ambient wind speed at Springhill approaches 5 m s^{-1}, therefore the change in behaviour of the Duffryn drainage flow is caused by the increased wind speeds, which reduce the stability of hill top regions during Episode 3.

The change in the wind speed and direction following Episode 2, appear to be part of a synoptic change that occurs during the night. Viewing figure 5.12, the radiosonde profiles launched from Duffryn show the development of a strong jet above the valley during the night. At the hill top regions (∼200 m AGL) the wind speed at 05:35 UTC is ∼4.5 m s^{-1}. Above the hill top regions there is a strong wind speed gradient with height, reaching a peak of ∼9 m s^{-1} at ∼1,000 m AGL. A jet peak of ∼9 m s^{-1} is roughly proportional to, or slightly higher than (supergeostrophic) the expected geostrophic wind speed estimated from the surface analysis chart in figure 5.1. The wind speed gradient corresponds to a clockwise turning of the wind with height, veering from a NW at the hill tops to a N at the height of the jet peak (∼1,000 m AGL). At the height of the jet peak the wind direction (N) is approximately geostrophic when viewing the surface analysis charts in figure 5.1.

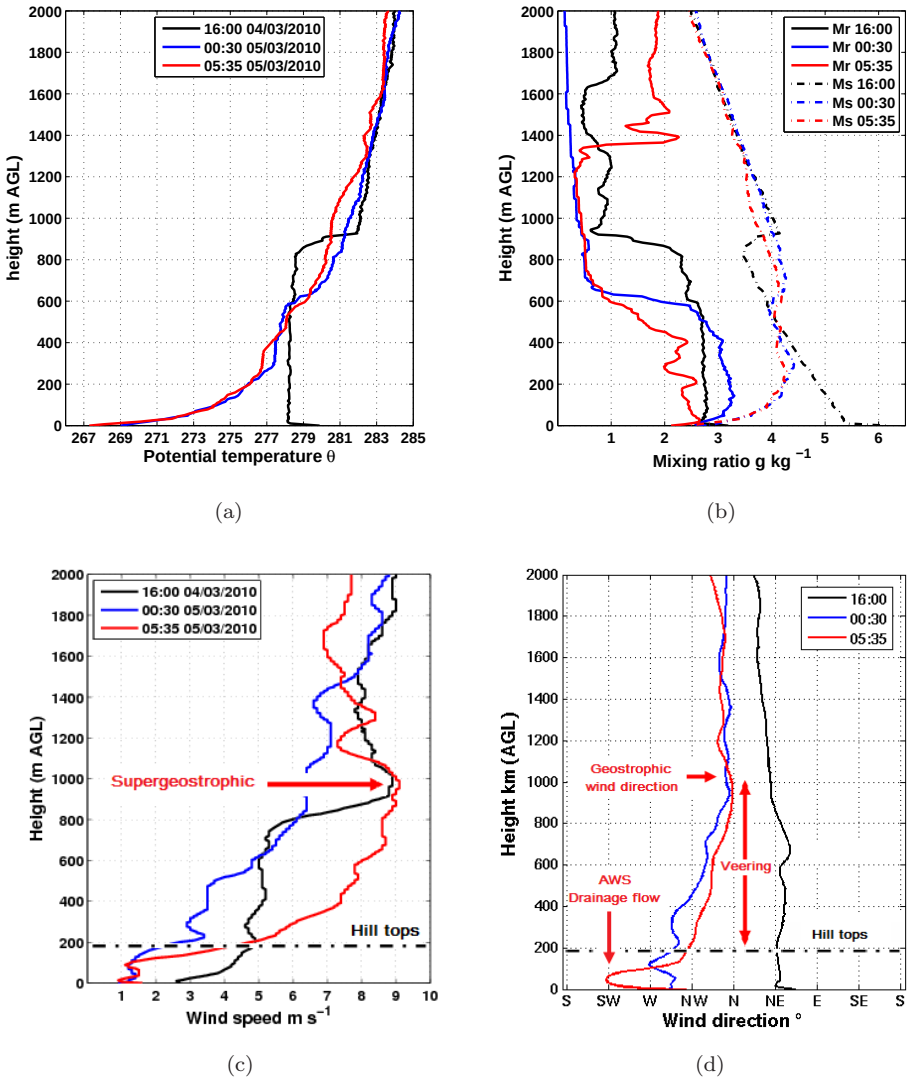

FIGURE 5.12: *Above are three radiosonde profiles launched from Duffryn at 16:00, 00:30 and 05:35 UTC, showing (a) potential temperature, (b) water vapour mixing ratio (solid lines) and saturation mixing ratio (dashed lines), (c) wind speed and (d) wind direction.*

Many of the characteristics seen in the 05:35 UTC radiosonde profile, are characteristic of a nocturnal low level jet (NLLJ) as described by Thorpe & Guymer (1977). NLLJs are known to form preferentially inland during the night above near surface inversions, when fine weather conditions prevail and little or no cloud cover (Thorpe & Guymer, 1977) – conditions that are synonymous with the formation of CAPs. According to Thorpe & Guymer (1977) a pronounced supergeostrophic wind maximum is expected within a few hundred meters of the ground and the jet maximum is expected to occur at, or slightly above the nocturnal inversion layer. These characteristics are seen in other studies of NLLJs also, such as the recurrence of a NLLJ over the the Great Plains of the US (see

Whiteman, 2000, p. 168). Since NLLJs and CAPs are favoured under the same conditions, it seems reasonable to assume that the occurrence of both simultaneously is likely for inland regions in the UK.

Figure 5.13 shows a composite of mean radiosonde wind speed profiles from five CAP nights during COLPEX; IOP 4, 5, 10, 16 and 17 (see methods, table 3.7). Two mean profiles are shown for each IOP night, taken at similar times relative to sunset at; (a) the early evening (figure 5.13(a)), and (b) the morning some time before sunrise (figure 5.13(b)). It should be noted that the CAP growth was disturbed by the formation of fog during the morning of IOP 10 (11/12/2009, red profile in figure 5.13(c)).

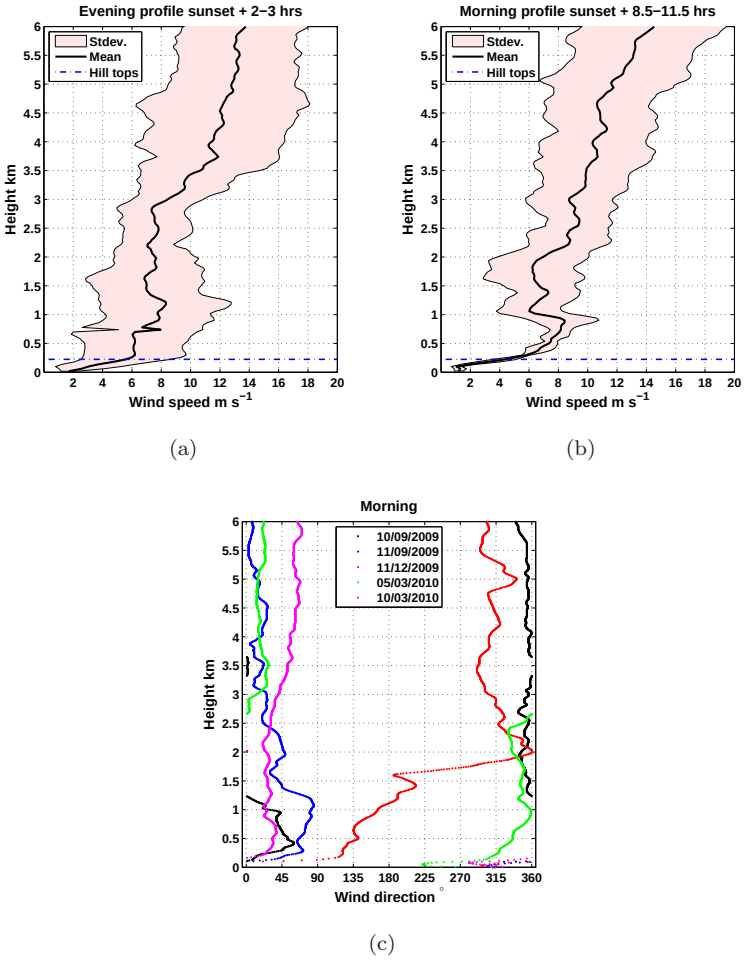

FIGURE 5.13: *Figures (a) and (b) show the mean wind speed profiles during the early evening and morning, for five sonde profiles launched on different IOP nights at similar times. The red shaded region is the standard deviation from the mean. Figure 5.13(c) shows the morning radiosonde profiles of wind direction for IOPs 4, 5, 10, 16 and 17.*

The radiosonde wind speed profiles below 1,000 m AGL are more similar during the morning profiles (figure 5.13(b)) than the profiles from the previous evening (figure 5.13(a)), which is highlighted by the smaller standard deviations. The morning profiles show the following characteristics; (1) a jet peak of between 7–12 m s^{-1} in the region between 500–1,000 m AGL, (2) a veering of the wind direction with height, (3) the wind direction at the peak jet height is aligned with the expected geostrophic wind direction for each IOP (figure 5.13(c)). These three characteristics are indicative of a NLLJ that forms in the boundary-layer during high atmospheric pressure, when a stable inversion layer forms at the ground surface (Thorpe & Guymer, 1977).

This similarity between the radiosonde profiles during the morning hours suggest that the characteristics associated with the formation of NLLJs, are a recurring feature when CAPs are observed in the Clun Valley region. A recurring NLLJ that favours development during the same synoptic conditions as CAP occurrences, will directly affect the ambient wind speed, stability and subsequently the CAP evolution and strength. NLLJs may therefore be a recurring controlling factor on CAP occurrence, evolution and breakup in the Clun Valley region. You may expect the same to be true for other valleys in other inland regions of the UK. Particularly the NLLJ may be important towards the end of the night, when the wind speed above the valley is strongest as the NLLJ peaks before sunrise – if this is the case.

Two further features are seen in the LIDAR profile in Episode 3 towards the end of the CAP cycle (figure 5.5(a)). The first occurs around sunrise at ∼07:00 UTC and the second occurs between 09:00–10:00 UTC, when the CAP finally breaks up. The coldest temperatures experienced during IOP 16 occur around sunrise (06:55 UTC) at the lowest elevated sites (see figure 5.3(e)). With reference to the AWS the coldest temperatures are observed at the Clun Valley floor site AWS 5 at 06:55 UTC (see table 5.1). At the same time a 24hr peak in the ELR occurs (figure 5.4(b)), suggesting that the temperature difference from the valley floor to the hill top regions is largest at this time. Warming is seen across all regions between 07:35–08:35 UTC, but the rate of warming is highest in the lowest regions at valley floor locations (such as AWS 6 and AWS 5). By 08:35 UTC (∼1.5hrs after sunrise) a CAP still persists in valley bottom regions, with temperature differences of 6 K seen between the lowest site HOBO 6 and some hill top sites.

At ∼10:00 UTC values of θ (figure 5.4(a)), RH (figure 5.4(c)), M_r (figure 5.4(d)), wind speed and direction (5.6) converge, with measurements at the valley bottom mirroring those seen at the hill tops. Over the same period the Duffryn drainage flow breaks up and the vertical profiles of wind speed, θ and TKE, exhibit those of a typical daytime CBL profile by 10:30 UTC (not shown). The final break up of the CAP between 09:00–10:00 UTC, coincides with the two regions of increased vertical velocities that exist above the valley (figure 5.5(a)). The first is an elevated region that descends with time from 09:00–10:00 UTC. The second region remains between 150–400 m AGL over the period and is more intermittent in behaviour (some similarities to Episode 1). At 10:00 UTC, the regions of increased vertical velocities become almost indistinguishable. The descending region of increased vertical velocities may reflect downward momentum transport of the NLLJ, which is seen in the atmosphere above the valley in the 05:35 UTC radiosonde profile; however, there are no radiosonde profiles launched after 05:35 UTC, therefore from an observational point of view there is no way to confirm the existence of the NLLJ at this time. What is clear from these results is that by 10:35 UTC, approximately 3 hours 40 minutes after local sunrise, the CAP has completely broken up and this is finally achieved by a mixing down of momentum from above, which results in a complete coupling of the boundary-layer, with a CBL ensuing.

Figure 5.14 shows vertical profiles of wind speed and direction from a COLPEX model simulation of IOP 16 (for model description see background section 2.5.1). The vertical profile is taken from a valley floor location ∼600 m up valley to the west of the intersection of the AWS 7 tributary and main Clun Valley (see detachable map figure 3.2). A number of interesting phenomena are seen in the COLPEX model simulation that confirm some of the observations described previously in Episodes 1, 2 and 3. What is clear is that the model confirms the increase in wind speeds seen in the observations during the evolution of CAP between the hill tops and 1 km AGL. The COLPEX model also shows a region of higher wind speeds that descend with time during Episodes 2, which corresponds well to the descending region of increased vertical velocities seen in the LIDAR (figure 5.5(a)). The higher wind speeds then remain at the hill top level throughout Episode 3. Intermittent increases are seen in the region at and above the hill tops and a peak in the ambient wind speed occurs around 04:00 UTC; again the observations at Springhill show this peak in the ambient wind at 04:00 UTC (figure 5.6). In the model simulation the higher wind speeds follow a marked change in wind direction during Episode 1, from a NE to a WNW. This

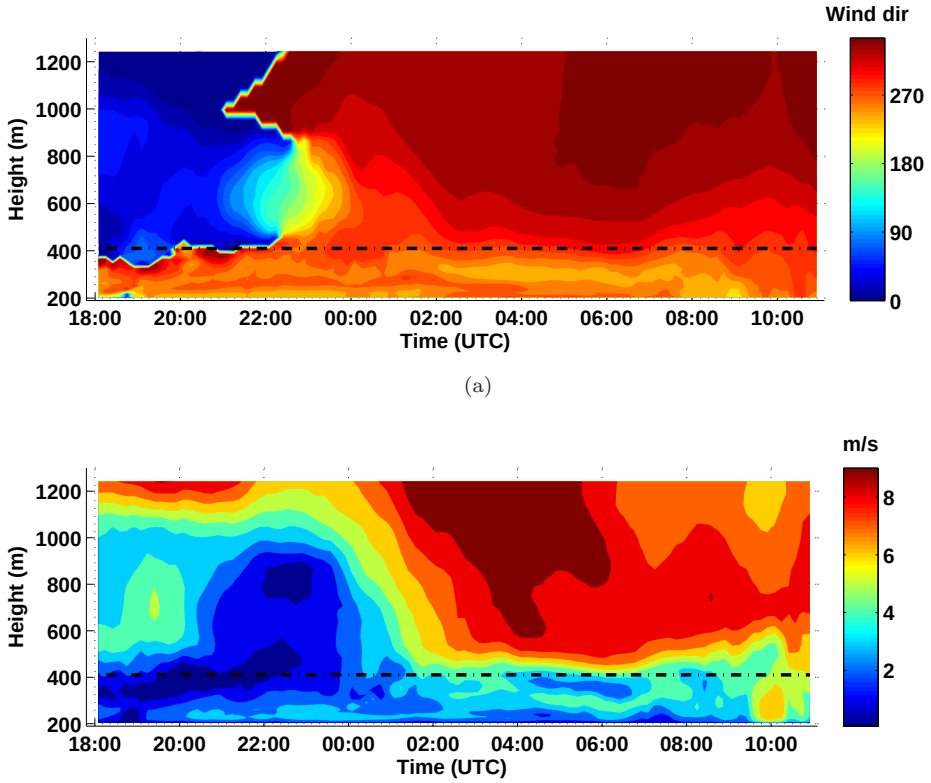

(a)

(b)

FIGURE 5.14: *COLPEX model simulation of wind speed and direction. From a valley bottom site located ∼600 m up valley from the intersection between the AWS 7 tributary valley and main Clun Valley (see pull out map figure 3.2). COLPEX model simulation conducted by Dr. John Hughes.*

is associated with a sheering of the wind in the region above the hill tops. This change in wind direction during Episode 1 is also seen in the observations at Springhill (figure 5.6). The sudden change in wind direction during Episode 1 coincides with the gravity wave activity.

5.7 Summary

It is clear from results presented here that the CAP evolution during IOP 16 is not uninterrupted, despite the fact that the synoptic conditions are "ideal" for strong CAPs to form. Instead the evolution of the CAP is disturbed, but not to the extent that the CAP breaks down, instead the CAP growth is arrested. This is clear when viewing the evolution of the valley ELR (figure 5.4(b)). The ELR increases uninterrupted until ∼22:00 UTC, at which point the evolution of the ELR changes. The disturbance of the CAP evolution is

characterised by the behaviour of the LIDAR vertical velocity profile, with three episodes highlighted:

Episode 1 – Between 22:30–23:30 UTC.

Episode 2 – Between 01:00–02:30 UTC.

Episode 3 – Between 03:00–11:00 UTC (4hrs after local sunrise).

An illustration for the sequence of events that disturb the CAP evolution during IOP 16, are given in figure 5.15.

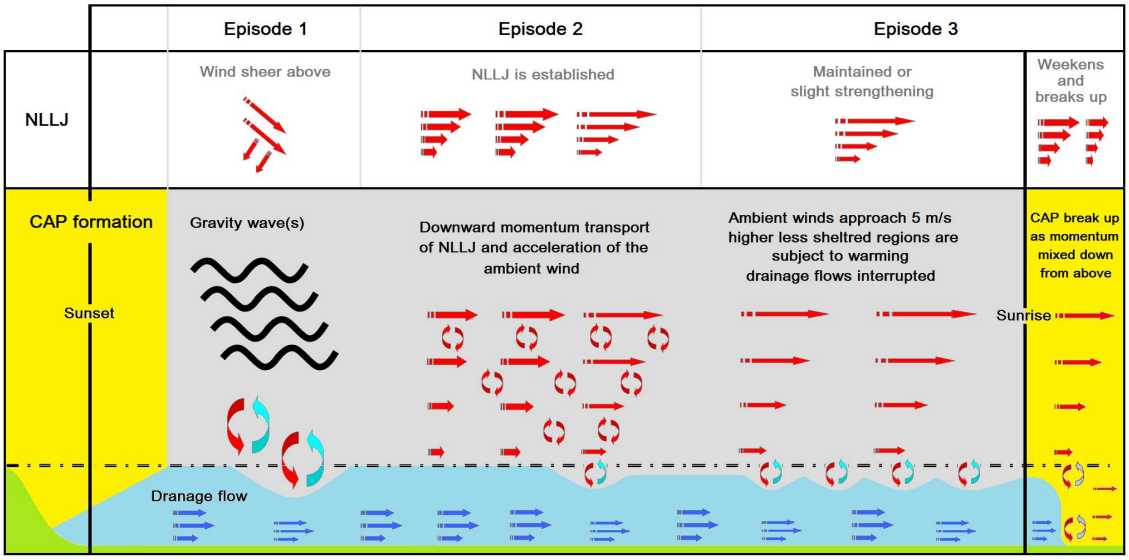

FIGURE 5.15: *Illustration showing the sequence of events that disturb the CAP evolution during IOP 16.*

The disturbance of the CAP evolution in Episode 1 is attributed to gravity wave activity. The exact cause of the gravity wave(s) is not determined; however, both observations and COLPEX model simulation show a marked change in the wind direction and speed with height at this time. The gravity wave(s) may be generated by this shear in wind direction and speed with height. The change in wind speed and direction appears to signify the early stages of NLLJ development, therefore the gravity wave(s) could be caused/related to the developing NLLJ and may even propagate ahead. Other possible causes include orographic generation, possibly in the form of a hydraulic jump.

Episode 2 is characterised by a region of increased vertical velocities that descend over a 1.5hr period and an acceleration of the ambient wind speed at the hill top level. This

feature is a product of the developing NLLJ. In this instance Episode 2 signifies the arrival of the NLLJ at the hill top regions, as momentum is mixed down from above. This occurs at ∼02:00 UTC when the ambient wind speed stops accelerating and the region of increased vertical velocities dissipates out. In Episode 3 the NLLJ continues to develop into the morning. According to the COLPEX model results, the NLLJ starts to dissipate at the same time as the CAP weakens after sunrise. The final break up of the CAP occurs some 3.5hrs after sunrise and the evidence suggests that this is the final moments of the NLLJ, as momentum is mixed down from above. The overriding factor that causes the disturbances during the CAP evolution, and possible contributes to the timing of CAP breakup, is the development of the NLLJ throughout the night.

Initial investigations suggest a synoptic feature, that is characteristic of a NLLJ, reoccurs with some consistency during other CAP nights. It seems unlikely that the occurrence of CAPs and NLLJs are limited to the Clun Valley region alone. The development of a NLLJ is likely to be a consistent controlling factor on CAP evolution and breakup in other regions of the world, which are similar in scale to the Clun Valley.

Chapter 6

Investigations of CAPs using model simulations

A number of uncertainties arose from investigations conducted during chapter 4 and 5. Firstly, results in both chapters highlighted the possibility of slope flows. Investigations during IOP 16 showed that some elevated regions became much colder than regions below during the initial stages of CAP formation. This suggests that drainage/slope flows may be occurring, emanating from cold air drainage of higher regions (slope flows). Results in chapter 4 suggest that slope flows may be reccurring at two of the highest sites AWS 2 and 10, which are located on gentle slopes.

The IOP 16 case study in chapter 5 showed that a drainage flow at Duffryn forms soon after sunset, a result shared by high resolution model investigations by Vosper *et al.* (2013b). The drainage flow tended to persist throughout the night, but was interrupted at times. During these interuptions the height of the drainage flow jet peak was lower. Results in chapter 4 show that the peak jet height of the Duffryn drainage flow is lower during strong CAP nights (>4°C) compared to weak CAP nights (<4°C), therefore the results are conflicting.

Due to lack of data it was not possible to investigate the dependence of drainage flow structure on wind speed and direction for strong CAP nights in chapter 4. Therefore it is not known how the structure of the Duffryn drainage flow changes with wind direction, speed and/or stability. Findings in Chapter 4 show that many sites located near confluence

regions of tributary valleys are subject to fluctuations in wind direction during strong CAP nights (see figure 4.24(c)). It is not yet known how and when drainage flows from other tributary valleys form and more specifically how these drainage flows interact at a confluence region. Additionally, it is not yet known if the investigations of IOP 16, conducted in chapter 5 and by Vosper *et al.* (2013b), are representative studies of typical CAP formations in the Clun Valley region.

It has been shown by Coulter *et al.* (1989) that wind direction can affect drainage flows. In this instance Coulter *et al.* (1989) showed that there was increased drainage from a tributary valley when the wind direction was opposite to the drainage direction, than when the ambient wind was aligned with the drainage flow. This highlights the potential for drainage flow interactions at confluence zones, to be different depending on the ambient wind direction. This is likely to have subsequent effects on drainage flow dynamics from case to case, which will modify the flow structure of the entire valley system, subsequently affecting local stability and CAP dynamics as a whole. To date few investigations have focused on the characteristics and role of drainage flows from multiple tributary valleys on CAP formation, evolution and breakup. For this reason there is a current gap in knowledge with respect to the very basic principle of tributary valley interactions during CAP nights.

Recent model investigations of CAPs have focused on understanding the dynamics that govern the temperature change in the lowest region of valleys using numerical model investigations (Vosper & Brown, 2008; Vosper *et al.*, 2013b), with a view to use this knowledge to devise simple parametrisation or downscaling for use in real-time weather forecasting models (Sheridan *et al.*, 2013). Specifically Sheridan *et al.* (2013) shows how a non-dimensional valley depth (NH/U) – where $Fr = NH/U$ – can be used as a measure for the amount of sheltering from the free atmosphere that is occurring in the lowest valley regions. This sheltering mechanism can lead to a net cooling of valley bottom regions that is driven by a divergence in the sensible heat flux (see Vosper *et al.*, 2013b).

Findings by Sheridan *et al.* (2013) show that this sheltering mechanism ($F_r = NH/U$) was found to have a relationship to CAP strength. Additionally, beyond a critical value (NH/U close to 1), CAP strength no longer increases, at which point the the valley is said to be decoupled from the ambient wind.

The hypothesis here is that wind direction is likely to have some impact on stability and thus the amount of sheltering that is occurring from site to site, especially when tributary valleys are orientated in different directions with respect to the main component of the ambient wind. For example, if the ambient wind direction is from the W, a site located at the centre of a west to east orientated valley, is not aligned preferentially for sheltering to occur compared to a site located in a neighbouring valley that is orientated 90°, i.e., north to south. Considering the finding by Vosper & Brown (2008) and Sheridan *et al.* (2013), it seems plausible that any dependence on sheltering caused by preferential orientation to the ambient wind direction, is likely to be most evident during the intital stages of CAP formation, before a critical value of NH/U is reached and a decoupling of valley bottom regions occur.

Two investigations are conducted here:

1. Using high resolution model simulations, of multiple strong CAP nights with different ambient wind speeds and directions, understand the occurrence, structure, timing of formation, evolution and breakup of two neighbouring drainage flows for a number of CAP nights.

2. Understand the potential effects of wind direction on sheltering/decoupling of valley bottom regions during the early stages of CAP formation. This will be achieved by applying a similar method used by Sheridan *et al.* (2013) to calculate NH/U. However, investigations here will look at the across and along valley components of wind (U) separately, and will broadly assess how NH/U changes across Clun Valley floor regions, for a number of valleys that are orientated in different directions relative to the ambient wind.

A brief outline of each case study is given in section 6.1, with comparisons of temperature from model and observations, which give some perspective of the COLPEX model representation of CAPs during these nights. Section 6.2 shows model vertical cross sections of; (1) a confluence region of valleys, and (2) the main Clun Valley, for a number of CAP nights. For each case, values of Fr_U and the ratio of cross valley wind component U to the along valley wind component V, are shown in 6.3. This is an initial investigation in to the possible effects of sheltering across the Clun Valley region during CAP formation. Discussions are given in section 6.4, followed by a summary of the findings in section 6.5.

6.1 An overview of case studies used

To follow is a brief description of five strong CAP nights, which are used in subsequent investigations. These nights are chosen because a strong CAP formed each night, during synoptic conditions that favoured strong CAPs to form, as outlined by findings in chapter 4. Additionally four of the nights are IOP nights, therefore have good data coverage. Table 6.1 gives a summary of the nights used in these investigations. A surface analysis chart at 00:00 UTC is shown in figure 6.1 for each night.

The maximum CAP strength exceeded 4°C for all nights shown in table 6.1. In each case the maximum CAP strength occurred within the last hour preceding sunrise. The mean ambient wind speed at Springhill is below 5 m s^{-1} in all cases. The mean night-time ambient wind direction is different, but all have a northerly wind component. The night-time length is similar, varying between ∼10.5 to ∼13hrs. The pressure situation at 00:00 UTC for all nights is broadly similar (figure 6.1) – the UK weather is dominated by a high pressure system. The msl pressure for the Clun Valley region at 00:00 UTC – using the UM global analysis data (see methods 3.3.0.1) – varies little from case to case between 1029–1038 hPa. The pressure gradient is also weak for all nights, being below 0.8 Pa/km for four of the five nights. The exception is IOP 17 (1.22 Pa/km), which has the lowest msl pressure (1029 hPa).

The observations given in table 6.1 show that the CAP nights appear broadly similar, in terms of the synoptic conditions, although there are small differences. A time-series comparing high resolution model simulations and observations of 2 m temperature at Springhill and Duffryn, are shown in figure 6.2 for each CAP night in table 6.1. A description of the COLPEX model is given in Chapter 2 section 2.5.1. The main purpose of this comparison is to broadly understand how the model represents the CAPs, i.e., does the model show a developing temperature inversion across the depth of the Clun Valley during each night. The model is then used as a tool for investigations in section 6.2.

The COLPEX version of the Met Office Unified Model has been shown to represent CAPs well (Price *et al.*, 2011; Vosper *et al.*, 2013a,b). Additionally the study by Vosper *et al.* (2013b) was focused on model simulations and comparisons during IOP 16. Some model and observation results were also presented in Price *et al.* (2011) of IOP 4. The model

Case study	Date	Max CAP °C	Time of max CAP hh:mm	Mean WD °	Mean WS m s^{-1}	Mean f_{LW}	Ngt. length hh:mm	msl P hPa	PG Pa/km	PG dir. °
IOP 4	9–10 Sep 2009	5.7	00:28	7 (N)	4.2	0.83	10:57	1035	0.54	347 (N)
IOP 5	10–11 Sep 2009	6.6	00:51	46 (NE)	3.0	0.85	11:01	1038	0.72	54 (NE)
IOP 16	4–5 Mar 2010	6.7	00:01	320 (NW)	2.7	0.77	12:53	1031	0.58	270 (W)
IOP 17	10–11 Mar 2010	4.8	00:20	40 (NE)	2.9	0.85	12:28	1029	1.22	27 (NE)
APR 9	09–10 Apr 2010	5.5	00:58	353 (N)	2.2	0.86	10:27	1034	0.66	44 (NE)

TABLE 6.1: *Summary of case studies. Max CAP is the maximum temperature inversion to occur during the night-time. The time of the maximum CAP is hours and minutes (hh:mm) before local sunrise (when multiple maximums occur the first instance is shown). Mean wind direction (WD) and speed (WS) are the night-time mean for the IOP measured at Springhill* 30 *m AGL.*

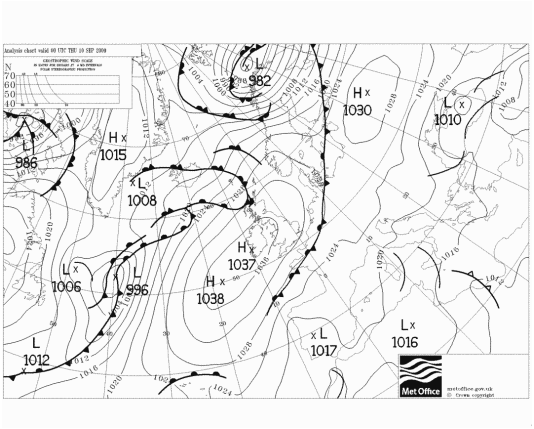

(a) 10/09/2009

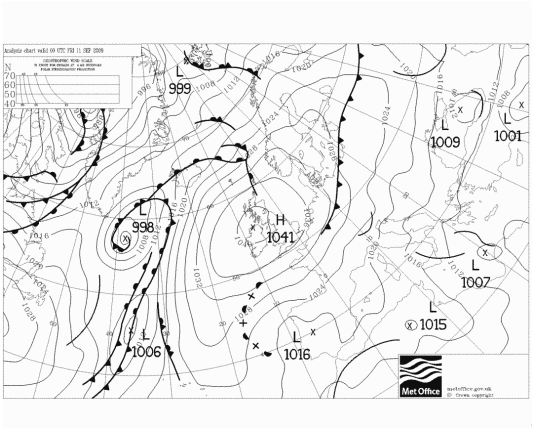

(b) 11/09/2009

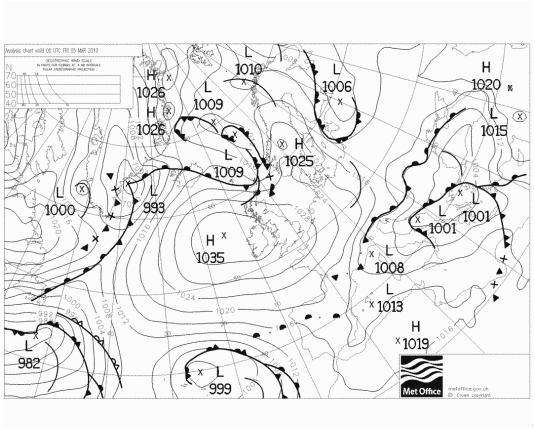

(c) 05/03/2010

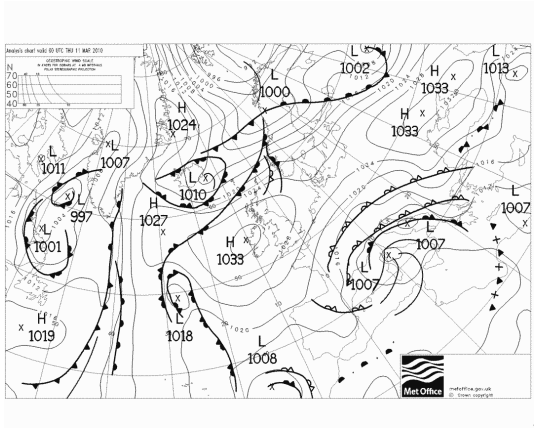

(d) 11/03/2010

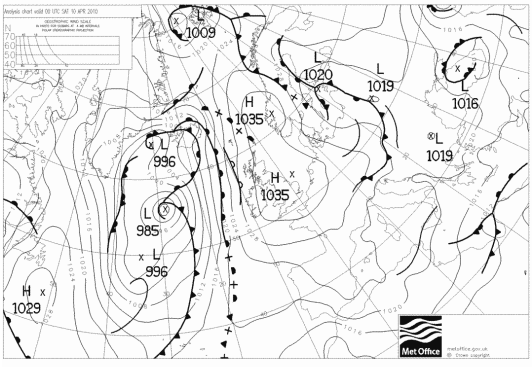

(e) 10/04/2010

FIGURE 6.1: *Surface analysis charts at 00:00 UTC for; (a) 10 September 2009, (b) 11 September 2009, (c) 5 March 2010, (d) 10 March 2010, and (e) 9 April 2010.*

simulations used here were conducted by Dr. John Hughes (University of Leeds); however, further data processing was conducted after.

For all five CAP nights, cooling starts before sunset. The model simulations clearly show the development of a temperature inversion that strengthens with time. In each case an inversion forms around or soon after sunset (figure 6.2). The model broadly agrees with the observations in all cases; however, there are some noticeable periods when the observations and model do not agree. The model temperature time-series of Springhill appears to agree extremely well with the observations during the night, but the model does have a cold bias during the day. The model representation of temperature at Duffryn agrees to within 2°C of the observations for most of the time; however, there is one noticeable period when the model is bias cold by over 2°C, which occurs during the evening of IOP 17. This period of cold bias in the model coincides with in-field reports of stratoculumus (8/8 octas) at 20:29 UTC (see methods table 3.7). It appears that the stratocumulus was not present in the model, or at least does not prevent CAP formation after ∼20:00 UTC. Since there is an emphasis on using the model as a tool to investigate CAP occurrence, this cold bias has little bearing on investigations here.

6.2 Model investigations

Using COLPEX model simulations (see Chapter 2 section 2.5.1), the following results aim to further understand the occurrence, structure, timing of formation and evolution of drainage flows in two adjoining valleys. The results are presented as a time slice of two vertical cross sections of model data. The locations and orientations of these cross sections are identified in figure 6.3. Cross section 1 (C1) cuts along the AWS 7 tributary valley in a down-valley direction and crosses perpendicular to the main Clun Valley. Cross section 2 (C2) is parallel to C1 and located ∼600 m west from C1. This cross section cuts the main Clun Valley only. Both cross sections are rotated −21° relative to polar north. In all subsequent cross sections the wind vectors are 2D horizontal components only, projected on to the vertical plane. When wind directions are horizontal they are aligned with the AWS 7 tributary valley axis and when vertical they are aligned with the main Clun Valley axis (figure 6.3), i.e., a horizontal wind vector pointing to the right in figure 6.4(a) represents winds that are in a down-valley direction with respect to the AWS 7 valley, vertical wind

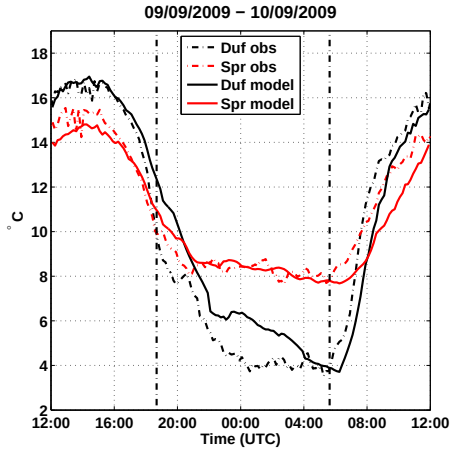

(a) 09-10/09/2009

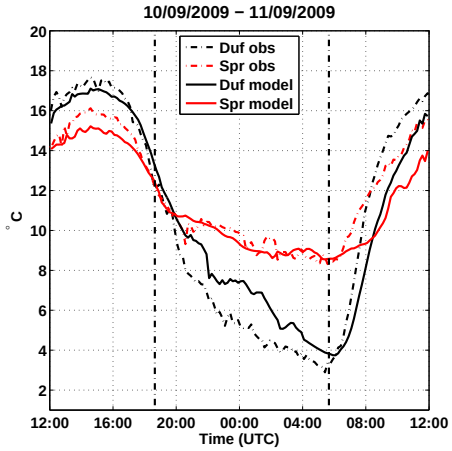

(b) 10-11/09/2009

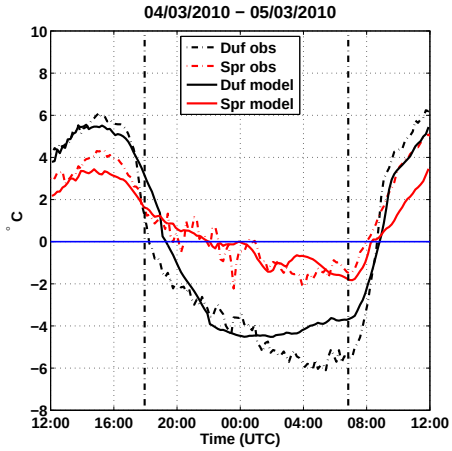

(c) 04-05/03/2010

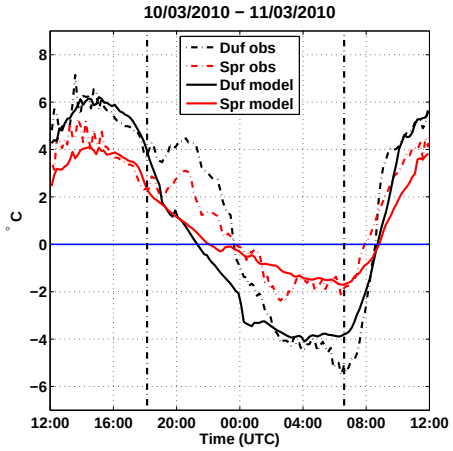

(d) 10-11/03/2010

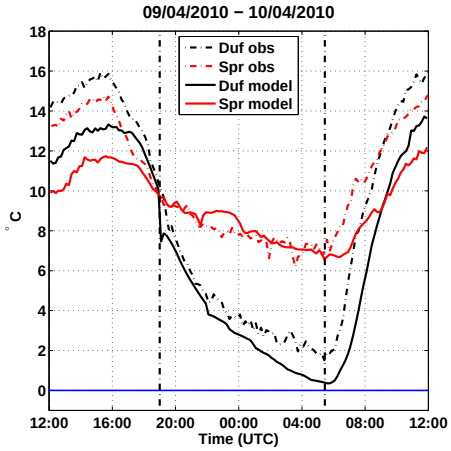

(e) 09-10/04/2010

FIGURE 6.2: *Comparisons of temperature from COLPEX model simulations (solid lines) and observations (dashed lines), for the hilltop site Springhill (red) and the valley floor site Duffryn (black), for; (a) 9-10 September 2009, (b) 10-11 September 2009, (c) 4-5 March 2010, (d) 10-11 March 2010, and (e) 9-10 April 2010.*

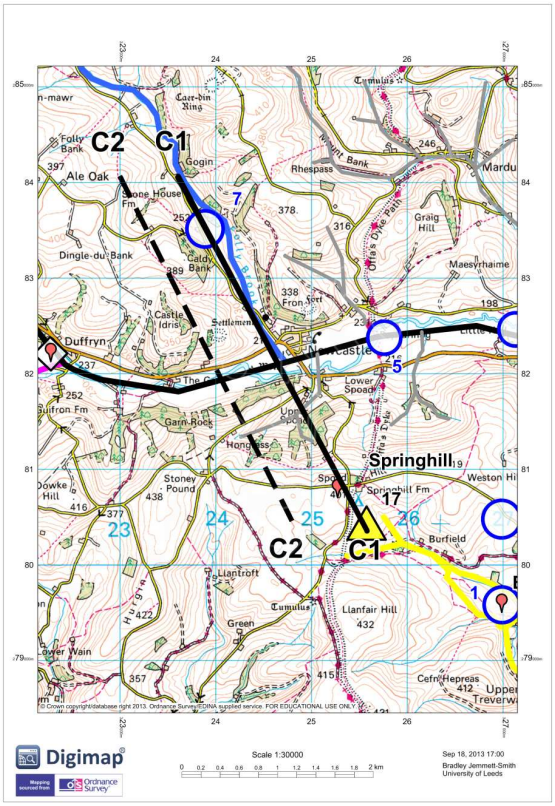

FIGURE 6.3: *Map showing cross sections C1 and C2. ©Crown Copyright/database right 2013. An Ordnance Survey/EDINA supplied service.*

vectors pointing up are representative of winds that are aligned down-valley with respect to the main Clun valley, i.e., from roughly WSW to ENE viewing figure 6.3.

6.2.1 CAP formation and evolution

The following results show C1 and C2 cross sections for the period during CAP formation and evolution. In future each CAP night is referred to using the case study name given in table 6.1, i.e., CAP night 10–11 March 2009 will be referred to as IOP 17. The cross sections shown in figure 6.4 represent the mean period from 0–1hrs after sunset. Cross sections are shown for all CAP nights in table 6.1. Left figures show results for the cross section C1 ((a), (c), (e), (g), (i)) and right figures for cross section C2 ((b), (d), (f), (h), (j)). This format will be repeated for all subsequent cross section figures.

In figure 6.4 an inversion has formed in all CAP nights. The CAP is least developed in IOP 17 and most developed in APR 9. In APR 9 the θ profile is strongly stratified right

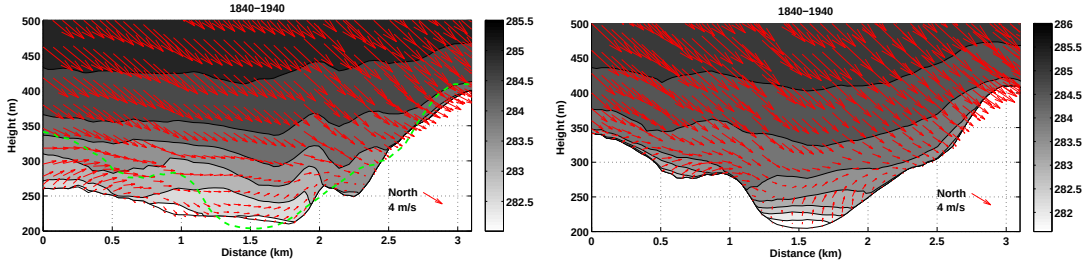

(a) IOP 4, C1

(b) IOP 4, C2

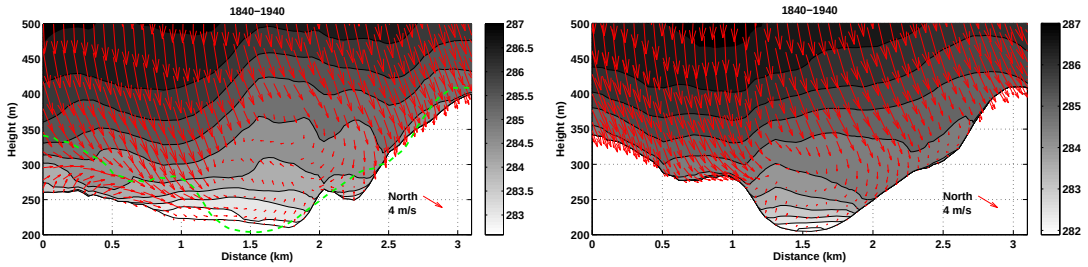

(c) IOP 5, C1

(d) IOP 5, C2

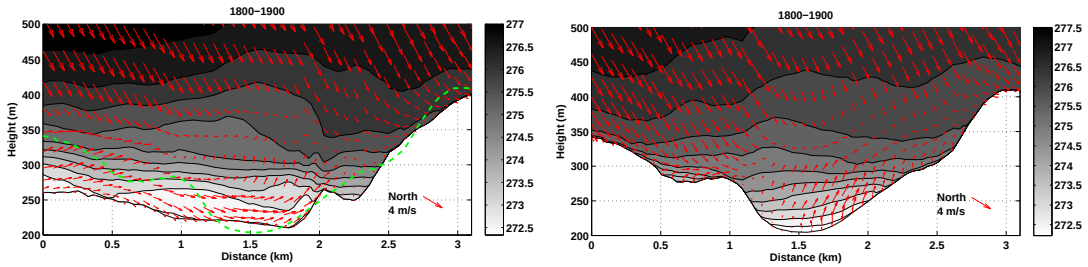

(e) IOP 16, C1

(f) IOP 16, C2

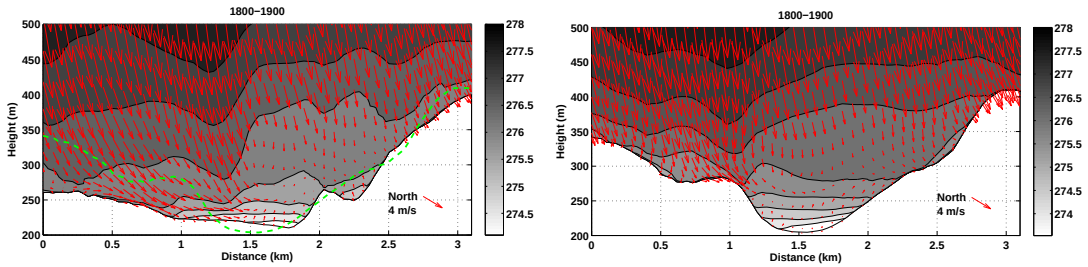

(g) Mar 10, C1

(h) Mar 10, C2

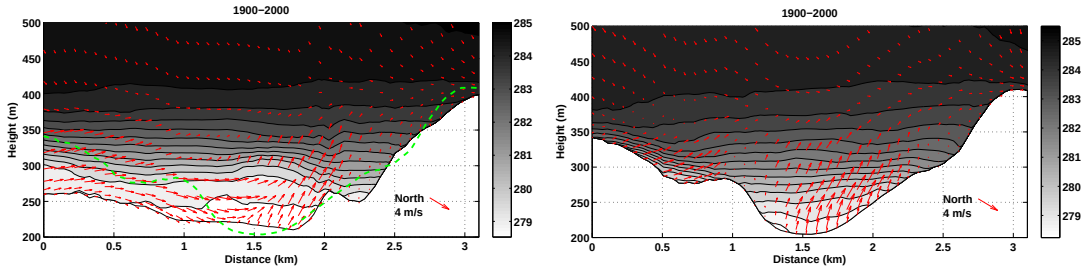

(i) APR 9, C1

(j) APR 9, C2

FIGURE 6.4: *Vertical cross-sections along the AWS 7 tributary valley and across the main Clun Valley, showing 1hr average vector winds and θ. Arrows are 2D horizontal components of the vector projected on to the vertical plane. Cross sections C1 and C2 are rotated 21° relative to polar north. Results are hourly averages between 0–1hr following sunset. The location of C1 and C2 are shown in figure 6.3. The green dashed lines in left figures (C1) shows the terrain height of C2.*

up to the hill top regions. The ambient wind speeds in APR 9 are the lowest seen of all cases. There is some evidence of drainage flow development in the AWS 7 side valley (C1) and in the main Clun Valley for all CAP nights; however, the AWS 7 valley drainage flow is restricted to bottom levels only and the Clun Valley drainage flow is less evident in IOP 4, IOP 5 and IOP 17. In IOP 16 and APR 9, drainage flows are seen in both valleys, i.e., wind directions are from left to right in C1 (figures 6.4(e) and 6.4(i)), aligned with the AWS 7 valley axis, and are from top to bottom in C2 (figures 6.4(f) and 6.4(j)), aligned with the Clun Valley axis. The strongest winds associated with the Clun Valley drainage flow, in both IOP 16 and APR 9, are located near the southern valley side wall (right). The wind speeds associated with the Clun Valley drainage flow in APR 9, are also stronger than those seen in IOP 16. IOP 16 is also less stratified and has a weaker θ gradient across the valley depth compared to APR 9.

The Clun Valley drainage flow is less evident in C1 where the drainage flows meet during both IOP 16 and APR 9, compared to C2 (Clun Valley only). In IOP 16 the drainage flow from the AWS 7 valley appears to undercut or override the Clun Valley drainage flow and colder air is seen to run up the side wall of the south slope. Similarly, cold air is draining from the AWS 7 valley in IOP 4, which results is cold air running up the side wall of the south facing slope, except in this case appears to override the Clun Valley drainage flow completely. In APR 9 the AWS 7 drainage flow appears to split the northern side (left) of the Clun Valley drainage flow, neither overriding or undercutting the the Clun Valley drainage flow. The θ gradient in the valley bottom of APR 9 is less in C1 (6.5(i)) compared to C2 (6.5(j)), where the AWS 7 and Clun Valley drainage flows meet. This suggests that the two drainage flows cause mixing, which results in an upward bulge of cold air (6.5(i)), i.e., a net cold contribution of cold air from the AWS 7 drainage flow.

One general observation is that the characteristics of the drainage flows and θ profiles are more similar when comparing IOP 4 to IOP 16 and again when comparing IOP 5 to IOP 17. The ambient winds in IOP 5 and IOP 17 are extremely similar also. Both are aligned almost directly up the main Clun Valley. Also, in both cases the drainage flows are almost completely absent and the θ profile is less stratified compared to other cases. One further observation is that a region of weak winds is seen in both IOP 5 and IOP 17 cross sections, which is likely to reflect a weak drainage flow in the Clun Valley. The winds that derive from the AWS 7 valley are much stronger, but do not appear to be related

to drainage of cold air, except for the very lowest level maybe. Instead the valley winds may be caused by forced channeling along the valley axis, a characteristic associated with neutral atmospheres (see chapter 4).

The cross sections in figure 6.5 are for the 1hr mean period between 3–4hrs following sunset. At this time IOP 16 and APR 9 clearly have the most stratified boundary-layers. The general characteristic of both IOP 16 and APR 9 appear very similar. The ambient wind speed has decreased in IOP 16 and is now similar to that seen in APR 9. In both IOP 16 and APR 9, drainage flows from the AWS 7 valley are seen; however, have only a small impact on the strong drainage flow that has formed in the Clun Valley, deflecting the upper part of the Clun Valley drainage flow towards the south slope. Furthermore, in both instances the air is coldest in the Clun Valley compared to the cold air draining from the AWS 7 valley. In both IOP 16 and APR 9, the θ gradient is much less in the Clun Valley bottom region compared to region above between $\sim$270–350 m.

IOP 5 and IOP 17 continue to be similar. The ambient wind in both cases remains similar in both speed and direction and the θ profiles are similar also. A well stratified θ gradient exists in the Clun Valley, associated with a relatively weak drainage flow; however, above $\sim$250 m ASL the θ gradient is less and θ is less stratified too. One difference seen is the development of a drainage flow from the AWS 7 valley in IOP 17, which is at least less clear in IOP 5. IOP 4 seems to be somewhere between the regimes of IOP 5/IOP 17 and IOP 16/APR 9. The wind speeds are similar to those seen in IOP 5 and IOP 17, but the wind direction is rotated further towards the N being from the NNE. A Clun Valley drainage flow is evident; however, there is little evidence of drainage from the AWS 7 valley, or at least the drainage flow is weak. The θ gradient at the bottom of the Clun Valley is also much stronger compared to all other cases.

Figure 6.6 show cross section results for the 1hr mean period between 9–10hrs after sunset. At this point in time a Clun Valley drainage flow is seen in all CAP nights. However, the Clun Valley drainage flow is less well defined in IOP 16, which has been subject to an increase in ambient wind speed and a change in wind direction to the NW. The increase in wind speed in IOP 16 has dramatically affected the characteristics of the CAP compared to the 1hr mean profiles between 3–4hrs (figures 6.5(e) and (f)). As well as the apparent disruption of the Clun Valley drainage flow, θ is less stratified. One consequence of the increase in wind speeds and direction change in IOP 16, is the erosion of a CAP in a small

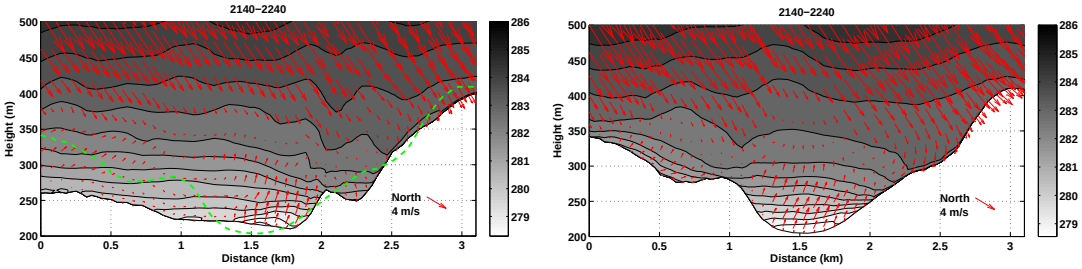

(a) IOP 4, C1

(b) IOP 4, C2

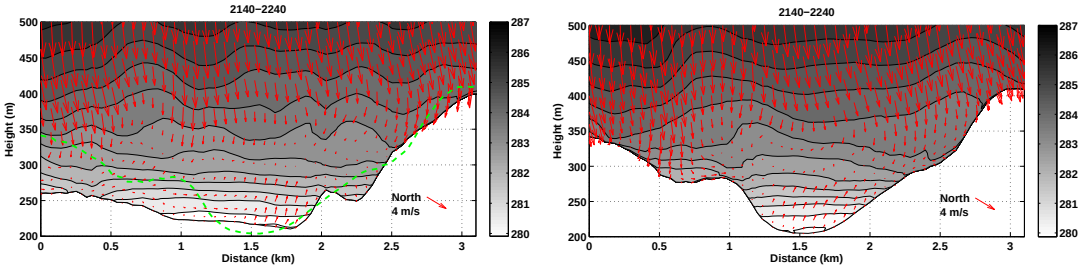

(c) IOP 5, C1

(d) IOP 5, C2

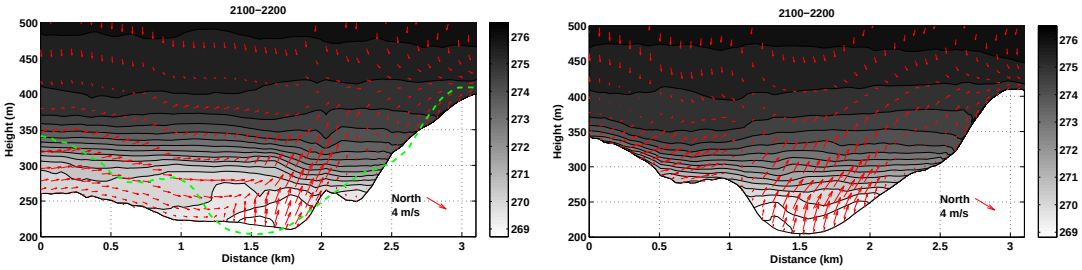

(e) IOP 16, C1

(f) IOP 16, C2

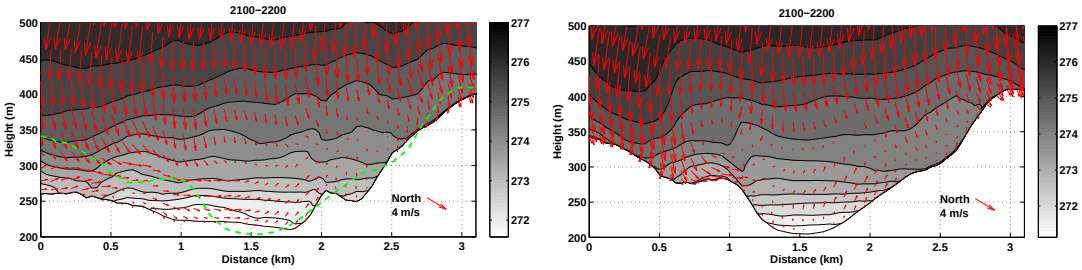

(g) IOP 17, C1

(h) IOP 17, C2

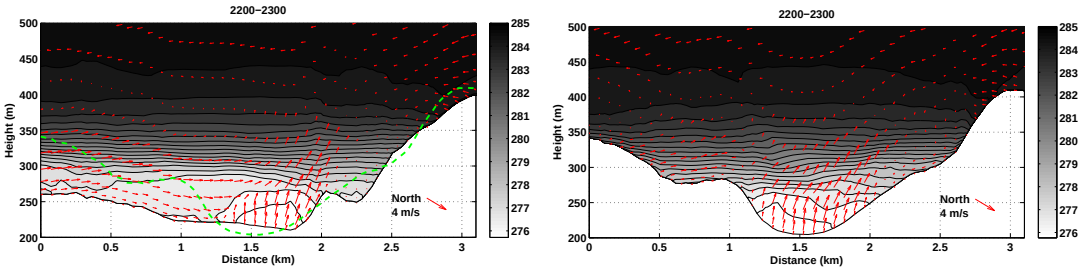

(i) APR 9, C1

(j) APR 9, C2

FIGURE 6.5: *As in figure 6.4 except results are for hourly averages between 3–4 hrs following sunset.*

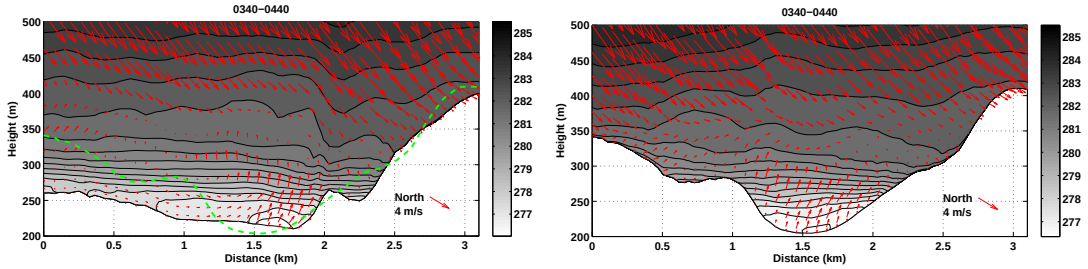

(a) IOP 4, C1

(b) IOP 4, C2

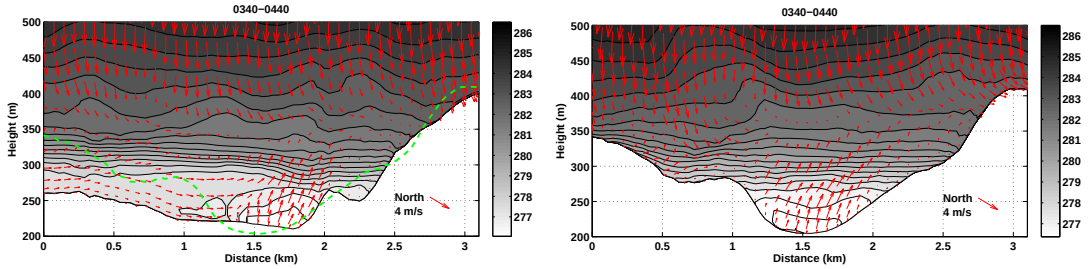

(c) IOP 5, C1

(d) IOP 5, C2

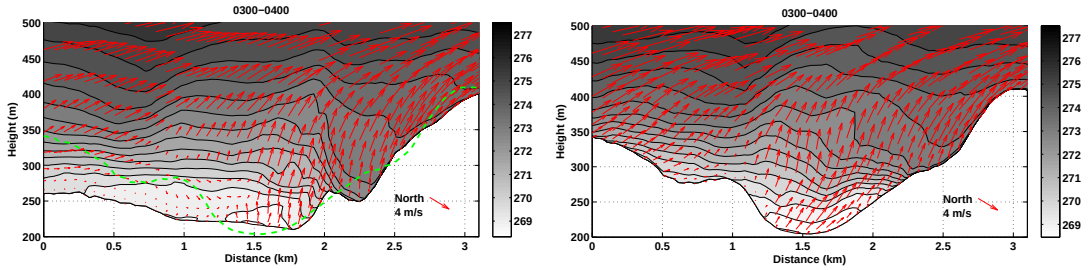

(e) IOP 16, C1

(f) IOP 16, C2

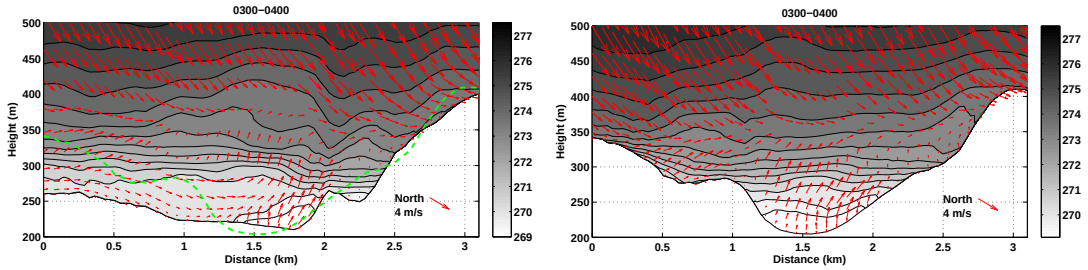

(g) IOP 17, C1

(h) IOP 17, C2

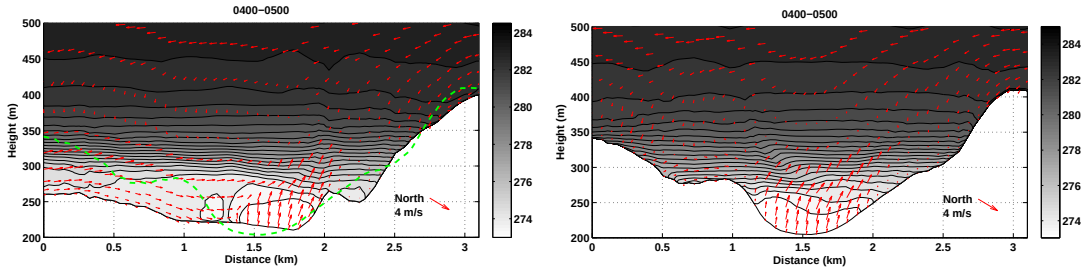

(i) APR 9, C1

(j) APR 9, C2

FIGURE 6.6: *As in figure 6.4 except results are for hourly averages between 9–10 hrs following sunset.*

tributary valley above and to the south of the Clun Valley (figure 6.6(e)). The winds in the small valley are aligned to the valley axis, which is indicative of forced channeling. The inversion in the Clun Valley and AWS 7 tributary valley remain intact, although the AWS 7 drainage flow has weakened.

The other CAP nights are broadly similar in characteristic at this time. Although the light ambient wind speed night of APR 9, continues to be the most stratified and has the strongest θ gradient below the level of the hill tops. Another feature seen in APR 9 is the relatively weak θ gradient that is seen in the lowest 50 m or so in the Clun Valley and AWS 7 valley.

One consistent feature across all C1 profiles between 9-10hrs after sunset (left figures in 6.6) is a pocket of relatively cold air associated with the drainage flow in the Clun Valley bottom, which is colder than any cold air draining from the AWS 7 valley. Therefore the AWS 7 drainage flow either halts at the confluence zone with the Clun Valley drainage flow, or flows above and mixes. This results in a gradual turning of the winds in this region. Additionally in all instances, except for IOP 16, the colder air within the Clun Valley is pushed towards the south sidewall by the AWS 7 drainage flow.

IOP 4 continues to be different to other CAP nights at this time. The most noticeable difference is that the CAP which formed is shallower compared to other CAP nights. Additionally, with the exception of IOP 16, the AWS 7 valley drainage flow is weaker than in other CAP nights and is also weaker than the Clun Valley drainage flow.

6.2.2 CAP breakup

The following results show model cross sections for the morning transition period during CAP breakup. Cross sections C1 and C2 are shown in figure 6.7 for the 1hr mean period between 0–1hrs following sunrise. As before cross sections are shown for all CAP nights in table 6.1. In figure 6.7, the left figures show results for cross section C1 ((a), (c), (e), (g), (i)) and right figures for cross section C2 ((b), (d), (f), (h), (j)).

When compared to the 1hr mean period between 9–10hrs after sunset (figure 6.6), there is very little warming up to 1hr following sunrise. IOP 16 continues to be the least stratified case and there remains little distinction between the Clun Valley drainage flow and the

ambient wind. On the other hand APR 9 continues to be the most stratified in terms of θ. In IOP 16 there continues to be a lack of drainage flow from the AWS 7 valley. In IOP 16 there is a bank of cold air within the AWS 7 valley (figure 6.7(e)). As seen before there is no CAP in the small valley to the south of the Clun Valley, which is much warmer than regions at similar elevations, a characteristic not seen in the other cases.

Common features seen in the remaining four CAP cases (IOP 4, IOP 5, IOP 17, APR 9) include the presence of a drainage flow in the Clun Valley, a drainage flow from the AWS 7 valley and an elevated CAP in the small valley to the south of the Clun Valley. Additionally in all five cases, an elevated core of cold air is seen in the main Clun Valley. In IOP 4, IOP 5 and IOP 17, the CAP in the Clun Valley is slanted towards the north facing slope to the south in cross section C2 (figure 6.7(b) (d) and (h)), this is likely to reflect the south facing slopes being warmer following sunrise.

In figure 6.8 results for cross sections C1 are shown for the 1hr mean periods between 1–2hrs ((a), (c), (e), (g), (i)) and 2–3hrs ((b), (c), (f), (h), (j)) following sunrise for each CAP night (see table 6.1). During these periods the breakup of the CAPs is clearly occurring.

The CAP is most persistent in APR 9 and least persistent in the less stratified IOP 16. Although even in IOP 16 a small pocket of cold air remains on the north facing slope of the Clun Valley between 2–3hrs after sunrise (figure 6.8(e)). In all cases there is little evidence of drainage flow from the AWS 7 valley 1–2 hrs following sunrise. However, there is some evidence of continued drainage in the Clun Valley in IOP 4, IOP 17 and APR 9, possibly IOP 16 also.

In the mean period between 1–2hrs following sunrise, two cold cores remain, which are associated with the Clun Valley and AWS 7 valley respectively (left figures in 6.8). Furthermore, the CAPs in the small valley to the south of the Clun Valley have mostly eroded in IOP 4 and IOP 17, and completely eroded in IOP 16, which occurred much earlier.

By 2–3hrs following sunrise (right figures in 6.8), the CAPs are mostly eroded, with the exception of the strong CAP forming night of APR 9. The wind speeds in APR 9 have increased and but are less than those seen in IOP 17. In all cases a small skin of warm temperature is seen in the AWS 7 valley. At this time there is no evidence of drainage flows in any case. Valley winds are aligned either up-valley, down-valley or roughly aligned

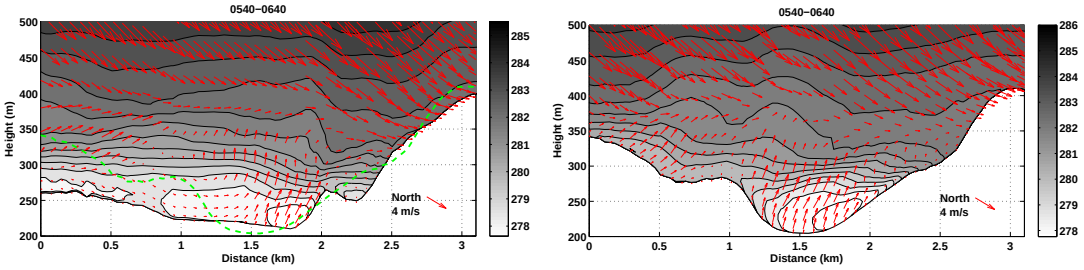

(a) IOP 4, C1

(b) IOP 4, C2

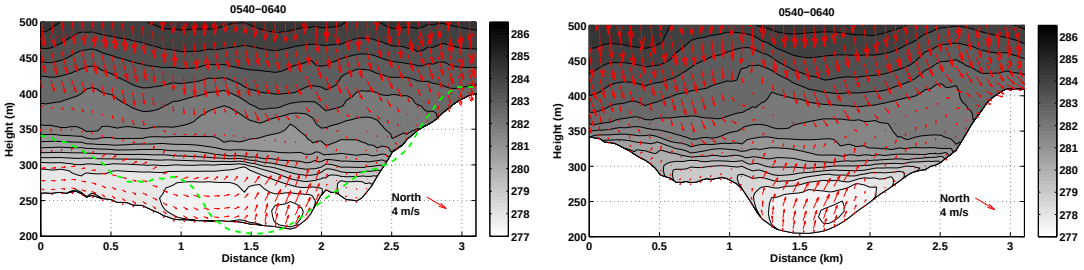

(c) IOP 5, C1

(d) IOP 5, C2

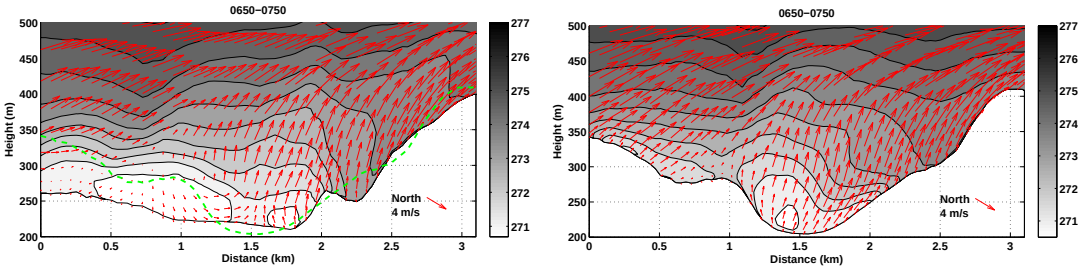

(e) IOP 16, C1

(f) IOP 16, C2

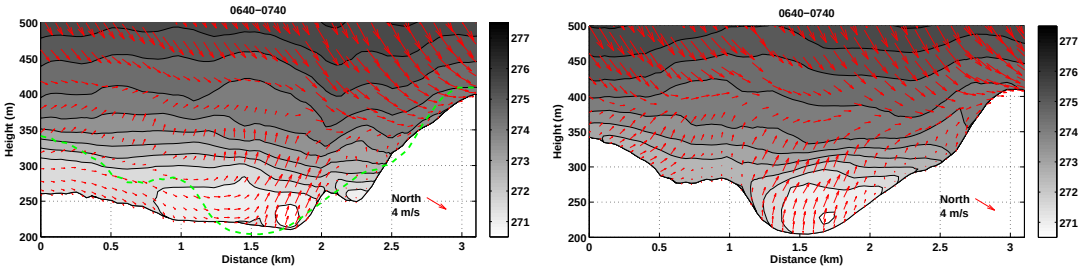

(g) IOP 17, C1

(h) IOP 17, C2

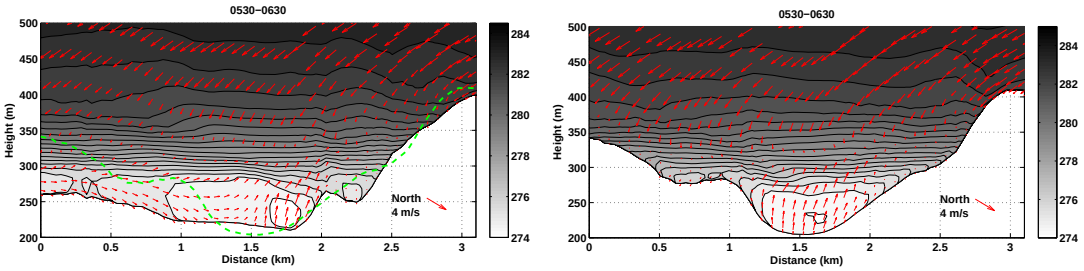

(i) APR 9, C1

(j) APR 9, C2

FIGURE 6.7: *As in figure 6.4 except results are for hourly averages between 0–1 hrs following sunrise.*

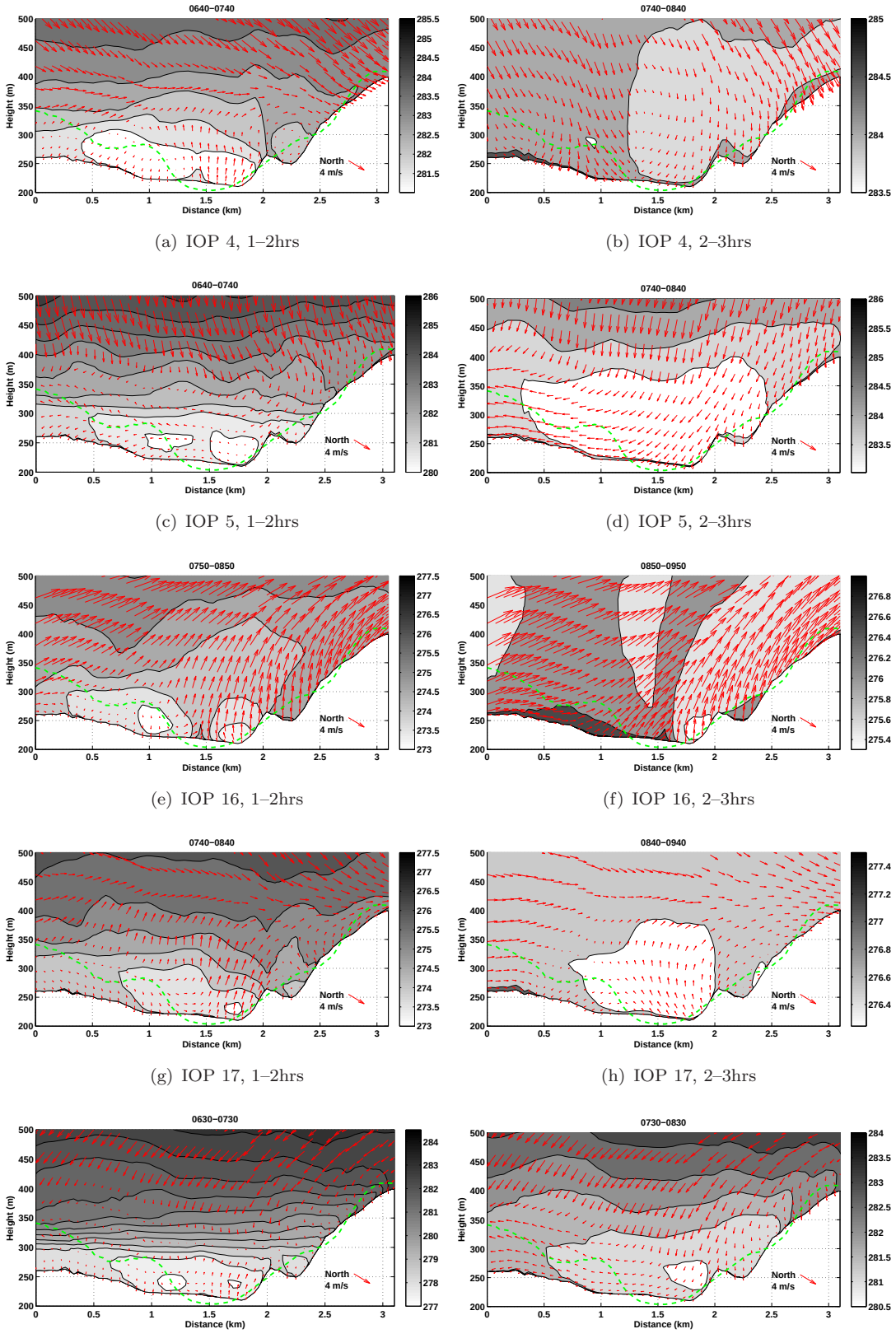

(a) IOP 4, 1–2hrs

(b) IOP 4, 2–3hrs

(c) IOP 5, 1–2hrs

(d) IOP 5, 2–3hrs

(e) IOP 16, 1–2hrs

(f) IOP 16, 2–3hrs

(g) IOP 17, 1–2hrs

(h) IOP 17, 2–3hrs

(i) APR 9, 1–2hrs

(j) APR 9, 2–3hrs

FIGURE 6.8: *As in figure 6.4 except results are for cross sections C1 only. Hourly averages are between 1–2 hrs (left) and 2–3hrs (right) following sunrise.*

with the ambient wind, as seen in IOP 16. Although not shown, the CAPs in all cases completely breakup between 3–4hrs following sunrise.

6.3 Investigations of NH/U

The aim here is to conduct initial investigations into the potential affects of wind direction on sheltering/decoupling of valley bottom regions, during the early stages of CAP formation. This is achieved by applying a similar method used by Vosper & Brown (2008) and Sheridan *et al.* (2013), used to define the amount of sheltering that is occurring in valley bottom regions using an inverse Froude number $Fr = NH/U$. Results by Sheridan *et al.* (2013) suggest that valley bottom regions become decoupled from the ambient wind when a critical value of $NH/U \simeq 1$.

The method for calculating NH/U used here is similar to that used by Sheridan *et al.* (2013). The valley depth H, is calculated using the difference in height from a 10x10 m grid box and the height of the mean 2 km grid box of the surrounding region (terrain data supplied by Ordnance Survey (2007)). Dr. Peter Sheridan provided the data for the background Brunt-Väisälä frequency N and wind speed U, which are used in investigations by Sheridan *et al.* (2013) of the Clun Valley region also. U and N are hourly background values, calculated using the UK4 configuration of the Met Office Unified Model (see Davies *et al.*, 2005; Lean *et al.*, 2008) over the lowest 150 m AGL. N is calculated using bulk value differences in θ and U averaged over the same layer (Sheridan *et al.*, 2013).

In this instance the cross valley component of U is investigated, referred to as U_{cross} in future where $Fr_U = NH/U_{cross}$. The Clun Valley region is divided – rather robustly – in to five valley zones (VZ). These zones are characterised by the general orientation of the local valley axis. The five valley sections and their orientations with respect to polar north, are shown below and are identified in figure 6.9:

VZ 1 – Clun Valley west, rotated $-45°$.

VZ 2 – AWS 7 valley, rotated $-30°$.

VZ 3 – AWS 8 valley, rotated $-10°$.

VZ 4 – Clun Valley middle, rotated $+80°$.

VZ 5 – Clun Valley east, rotated −80°.

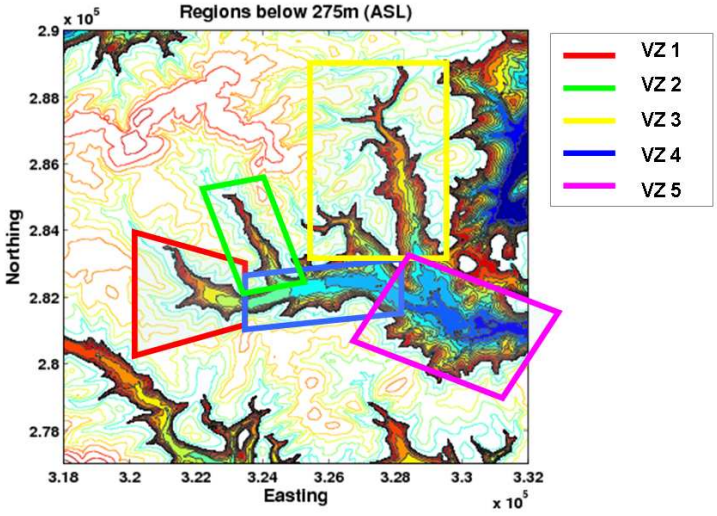

FIGURE 6.9: *Map of the Clun Valley Zones (VZ). All coloured terrain regions are below 275 m and represent ∼ 26% of the domain area. Values are m AGL and contour intervals are 10 m. ©Crown Copyright/database right 2007. An Ordnance Survey/EDINA supplied service.*

Investigations here will broadly assess how $Fr_U = NH/U_{cross}$ changes across Clun Valley floor regions (below 275 m, regions highlighted in figure 6.9) for a number of valleys orientated in different directions and for a number of case studies (listed in table 6.1). For each case study the following are shown: (1) Fr_U for all valley zones and regions below 275 m ASL. (2) model simulations of 1hr mean $\theta - 273.15$, for comparative periods (plots provided by Dr. John Hughes, University of Leeds). (3) ratio of the cross valley wind component to the along valley wind component, i.e., U_{cross}/V_{cross}. In all subsequent figures of Fr_U and U/V, the upper end of the colour scale is set to 5, therefore values above 5 may occur but are not indicated.

Figure 6.10 shows the results for IOP 4 (left) and IOP 5 (right), for the 1hr mean intervals following sunset from 19:00–20:00 UTC. In both instances values of Fr_U are generally close to 1 across most valley bottom regions; however, Fr_U is slightly above 1 in some regions of IOP 5 (figures 6.10(a) and (b)). In both IOP 4 and IOP 5, most cooling is observed in VZ 4 (figures 6.10(c) and (d) respectively). For IOP 5 this region of most cooling corresponds to the same region where high values of Fr_U are seen (VZ 4), i.e., more decoupling/sheltering is occurring.

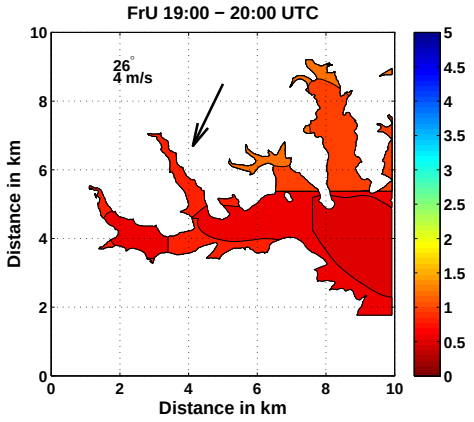

(a) IOP 4

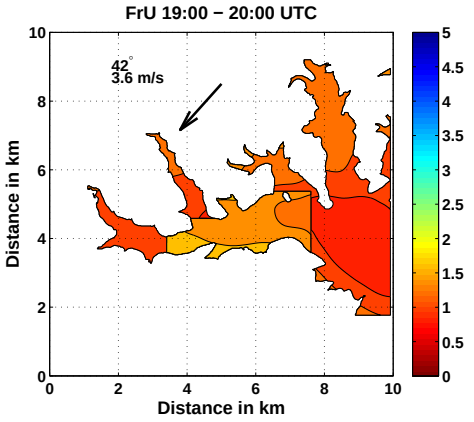

(b) IOP 5

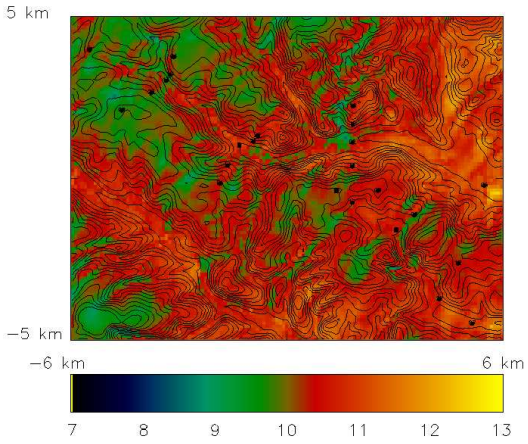

(c) IOP 4, 19:00–20:00 UTC

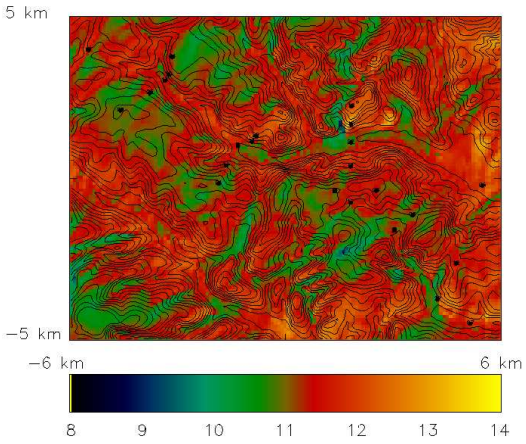

(d) IOP 5, 19:00–20:00 UTC

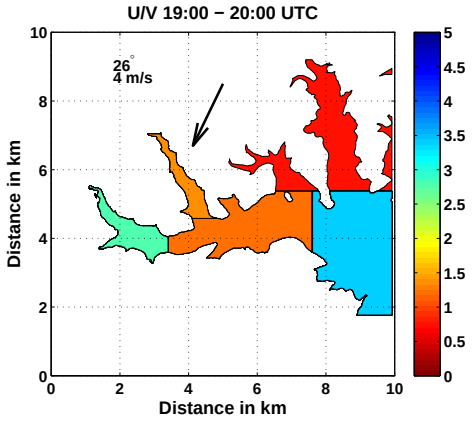

(e) IOP 4

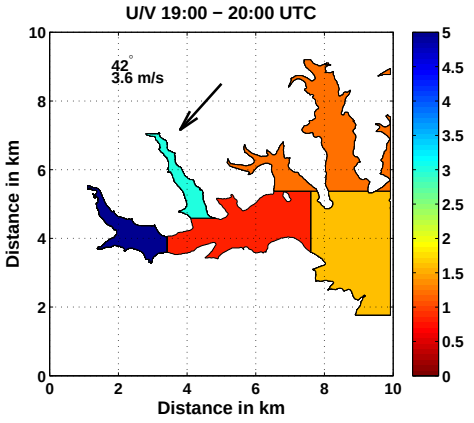

(f) IOP 5

FIGURE 6.10: *IOP 4 and IOP 5 early evening values of;* Fr_U *(a) and (b),* θ*+273.15 (c) and (d), and the ratio of* U/V *wind components (e) and (f).*

For both IOP 4 and IOP 5, the warmest valley bottom region is VZ 5, which in both cases corresponds to the lowest values of Fr_U. For both IOP 4 and IOP 5, it is clearly seen in figures 6.10(d) and 6.10(d) that some elevated regions are colder than many valley bottom regions at this time, with the exception of some areas in VZ 4 as previously mentioned.

The corresponding results for IOP 16 and IOP 17 are shown in figure 6.11 (left and right figures respectively). As in IOP 4 and IOP 5, many elevated regions are much colder at these times compared to valley bottom regions. In both IOP 16 and IOP 17, the amount of cooling in valley bottom regions is less at this time. However, there is more cooling of valley bottom regions generally in IOP 16 compared to IOP 17. Additionally the values of Fr_U in IOP 17 are much lower than those seen in IOP 4 and IOP 5. There is no clear pattern of cooling in IOP 16 at this time. In IOP 17, valley regions VZ 1 and VZ 2 are warmer than other regions, which corresponds to larger values of U/V, i.e., the cross valley wind component is much larger than the along valley wind component V.

Figure 6.12 shows the results of APR 9. Compared to other cases the values of Fr_U are much higher (above 5.0). At the same time the valley bottom regions are much colder than the hill top regions. In this instance many valley bottom regions have similar values of θ; however, the warmest region appears to be VZ 4, specifically the confluence region of the Clun Valley and AWS 7 tributary valley.

Generally it seems that high values of Fr_U correspond to more cooling of valley bottom regions compared to hill top regions; however, some quantitative assessment of this is needed, but was not possible here to time constraints. There is little evidence to suggest any relationship exists between the amount of decoupling/sheltering and the wind components of U and V; however, further investigations are needed to prove of disprove this.

6.4 Discussion

6.4.1 Drainage flows

Using high resolution model simulations, the aim of investigations here are to understand the occurrence, structure, timing of formation and evolution of two neighbouring drainage

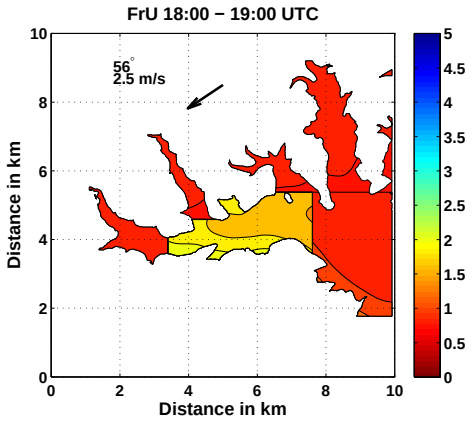

(a) IOP 16

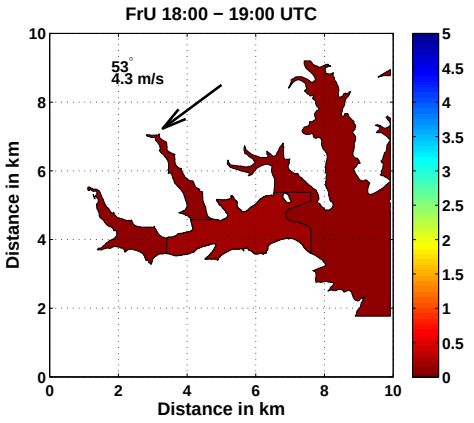

(b) IOP 17

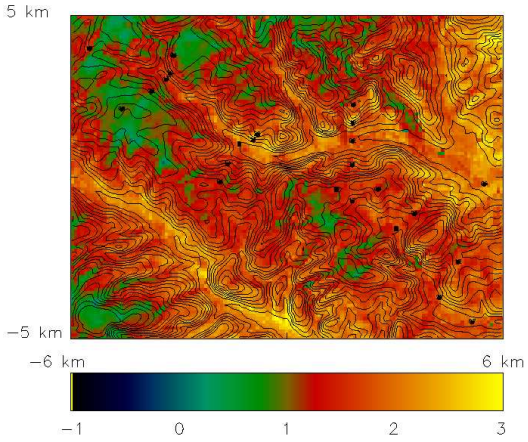

(c) IOP 16, 18:00–19:00 UTC

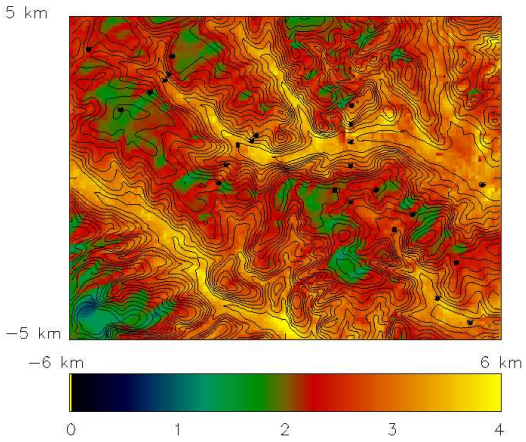

(d) IOP 17, 18:00–19:00 UTC

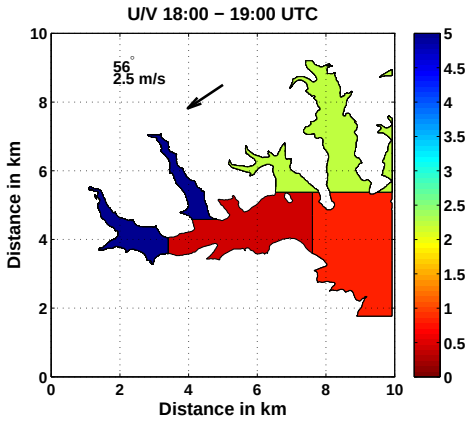

(e) IOP 16

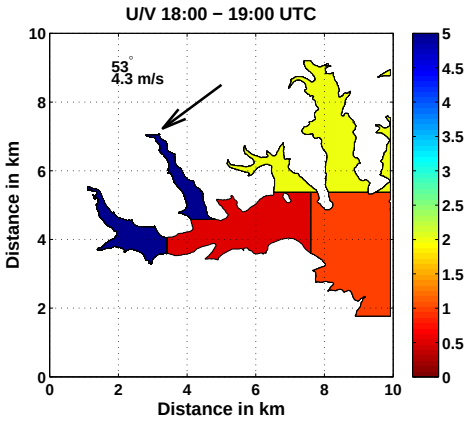

(f) IOP 17

FIGURE 6.11: *As in figure 6.10 except for IOP 16 and IOP 17.*

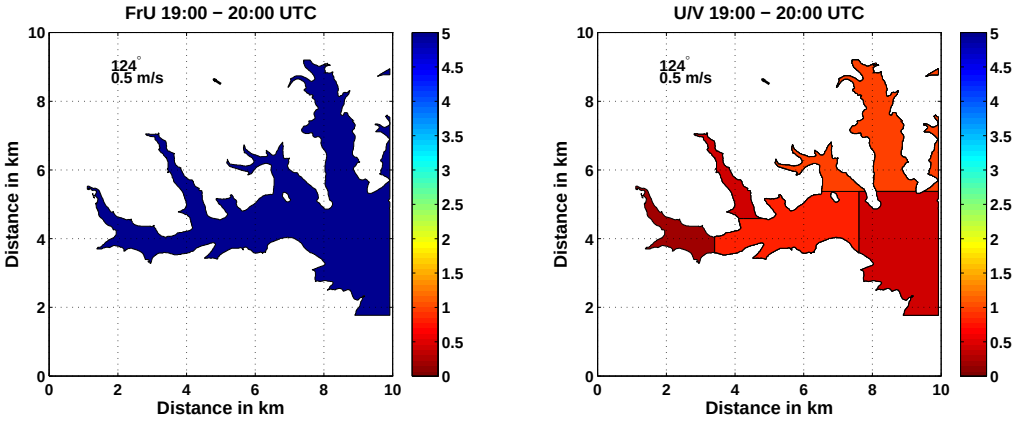

(a) APR 9

(b) APR 9, 19:00–20:00 UTC

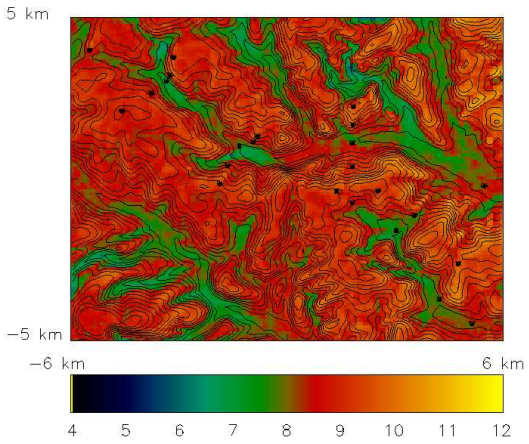

(c) APR 9

FIGURE 6.12: *As in figure 6.10 except for APR 9.*

flows, for a number strong CAP nights with different ambient wind speed and directions. During the initial stages of CAP formation an inversion is seen in all CAP nights soon after local sunset. In the interval between 0–1hrs, the CAP is least developed in the less stratified, high wind speed IOP 17 case and most developed in the well stratified, low wind speed APR 9 case. There is evidence of drainage flow development in both the AWS 7 side valley and in the main Clun Valley in all cases; however, the Clun Valley drainage flow is strongest in the most developed CAP nights, IOP 16 and APR 9.

In IOP 4 and IOP 16, which have similar wind directions, the drainage flow from the AWS 7 valley overrides or undercuts the Clun Valley drainage flow. As a consequence the colder Clun Valley drainage flow air is pushed up against the south side wall that opposes the AWS 7 valley. Additionally, in IOP 4, IOP 16 and APR 9, the drainage flow from the AWS

7 valley contributes a net cooling to the lowest 100 m or so, although as a consequence, some of the coldest air in the Clun Valley is mixed out as the two flows meet.

Interestingly in IOP 5 and IOP 17, the AWS 7 drainage flow is less evident. Both IOP 5 and IOP 17 have similar wind directions and speeds, which are aligned in an up-valley direction with respect to the Clun Valley. Furthermore, the Clun Valley drainage flow is less noticeable compared to other cases at this time. Results by Coulter *et al.* (1989) show that there was increased drainage from a tributary valley when the wind direction was opposite to the drainage direction, than when the ambient wind was aligned with the drainage flow. The results here suggest the opposite may be occurring, although this would need to be investigated further.

For the intervals between 3–4hrs after local sunset, two regimes are apparent: (1) During weak wind speed nights (IOP 16 and APR 9), strong drainage flows are seen, resulting in more turbulence that subsequently causes mixing and the formation of a weak θ gradient in bottom most part of the valley. Above the drainage flow a strong θ gradient exists. (2) During higher wind speed nights (IOP 5 and 17, which both have winds aligned in an up-valley direction with respect to the Clun Valley), weaker drainage flows are seen, subsequently there is less turbulence and mixing, which results in strong stratified conditions in valley bottom regions. Additionally, results of IOP 4 suggest that even when similar wind speeds occur, differences in wind direction result in the development of strong drainage flows, as seen in the Clun Valley. In this instance a strong θ gradient in the bottom 50 m is seen. At the same time little drainage is seen in the AWS 7 valley.

The most apparent change by 9–10hrs following sunrise, is the change in wind speed and direction in IOP 16, which greatly disrupts the CAP, which is less stratified as a consequence. The disruption of IOP 16 was noted in the case study investigation in chapter 5. Here a small shallow tributary valley to the south of the Clun Valley, is completely eroded by the change in synoptic wind. Additionally there is no clear decoupling of the drainage flow from the ambient wind at this time and the AWS 7 drainage flow is less apparent. Investigations by Mahrt *et al.* (2010) show that large wind direction shifts in drainage flows tend to occur when the drainage flow is intermittent, this occurs on nights when the synoptic flow is more significant or the cooling weaker. This type of behaviour may be characteristic of the drainage flows seen in IOP 16 during the period of disruption.

Despite the disruption of IOP 16 after 9–10hrs of CAP development there is a regime that is consistent across all CAP nights. The following characteristics are common across all CAP nights: (1) A Clun Valley drainage flow has established and is associated with a relatively well mixed layer that has a small θ gradient. (2) Above this relatively well mixed layer there is a strong θ gradient and a low wind speed region that separates the valley winds from the ambient winds. (3) A drainage flow from the AWS 7 valley has established – even if weak in some instances – which pushes the colder Clun Valley air toward the south valley side wall. Previously in chapter 5 it was noted that the drainage flow at Duffryn was often interrupted. During these periods the wind direction shifted to a more westerly or south-westerly direction, which often aligned with the AWS 3 tributary valley to the SW. It was hypothesised that this may have been caused by a drainage flow originating from the AWS 3 valley. Results here suggest that this may well have been the case.

One further characteristic seen at this time is that the CAP in IOP 4 is more restricted to lower regions compared to other CAP nights. This may be related to the fact that the drainage flow from the AWS 7 valley is weaker and is associated with relatively warm air, therefore in this case the drainage of air from the AWS 7 valley may have a smaller net contribution of cold air to the lowest 50 m AGL in IOP 4, compared to other CAP nights. Or this may be a characteristic of CAP development when NNE wind directions prevail, which are persistent thoughout IOP 4.

The results shown for the morning transition show that the CAP in IOP 16 breaks up first. It was also noted that the erosion of a small tributary valley to the south of the Clun Valley occurred earlier in the night. Combined these results suggest that the synoptic conditions during the later stages of IOP 16 were not ideal for CAPs. However, in this instance a strong CAP had already formed prior to these less favourable conditions occurring. It should be noted that the model temperature time series diverged from the observations during this period, with warmer temperatures seen in the model at Duffryn compared to the observations.

For all CAP nights, drainage flows in both the AWS 7 and the Clun Valley, persist for the first 0–1hr period following sunrise. The small tributary valley south of the Clun Valley erodes first in all CAP nights. This result suggest that higher regions are more sensitive to CAP erosion from above. In all cases CAP breakup occurs between 2–4hrs after sunrise.

The last CAP to be errode is APR 9, which is the strongest CAP night, in terms of the θ gradient and stratification of θ. This result suggests that stronger CAPs take longer to breakup.

6.4.2 Cross valley wind component and NH/U

The aim here was to conduct initial investigations into the potential affects of wind direction on sheltering/decoupling of valley bottom regions. Specifically during the early stages of CAP formation, for a number of CAP forming nights. Generally the results in section 6.3 show limited evidence of any preferential cooling or warming due to the orientation of the valley axis to the wind direction, i.e., the cross valley or along valley wind components. In one instance, IOP 4, there does appear to be some agreement between the observed cooling in the valley regions VZ 4, when values of Fr_U were above 1. According to results by Sheridan *et al.* (2013) values above 1 for Fr suggest a decoupling of these regions with respect to the ambient wind. However, it seems unreasonable to draw any conclusions from this result alone.

What is clear from these results, is that high values of Fr_U correspond well to more cooling observed in valley bottom regions. Specifically this was most evident when values Fr_U were above 1. However, some cooling of lower regions are also observed when values of Fr_U are below 1, but are less pronounced. With the exception of APR 9 – which had the highest values of Fr_U – regions above were often cooler than many valley bottom regions. The cooling of some valley bottom regions and not others is likely to be due to two reasons: (1) local in-situ cooling via sheltering/decoupling is highly variable. (2) The cooling was due to the advection of air from colder regions above.

6.5 Summary

Combined with the corresponding results in section 6.2.1 and findings from investigations conducted by Vosper *et al.* (2013b) of IOP 16, it is clear that advection of cold air from higher regions, in the form of drainage flows, can play a large role in cooling some valley bottom regions during the initial stages of CAP formation. Furthermore the occurrence and strength of drainage flows may have some dependence on wind direction and/or speed

above the valley. During the early evening, between 3–4hrs following sunrise, weak ambient wind speed nights can result in the early formation of strong drainage flows, that induce turbulent mixing, which results in weak near surface inversions (0–50 m AGL). Higher wind speed nights can result in weaker drainage flows with reduced turbulent mixing, which results in stronger near surface inversions (0–50 m AGL). This result highlights a potential negative feedback on local stability and stratification, whereby strong forming CAPs can lead to strong drainage flows forming, which can cause increased turbulent mixing in the lowest regions that in turn reduces the θ gradient in valley bottom regions. This may also highlight a potential misconception of CAPs. Where stronger CAPs have stronger near surface inversions. A plot showing comparisons of bulk Richardson number (Ri_b), should emphasis this point, but unfortunately this was not possible due to time constraints.

As the night progresses, and the CAP continues to grow, the characteristics of the drainage flows and CAPs appear more similar from case to case. In all cases strong drainage flows are seen in the Clun Valley and weaker stratification occurs as a consequence of increased turbulent mixing, as occurs in the light wind speed case above.

Investigations here attempted to assess the potential relationship between sheltering/decoupling of valley bottom regions to the cross valley wind component, where $Fr_U = NH/U_{cross}$. There was no clear indication that the cross valley wind component was an important controlling factor for cooling by sheltering/decoupling of valley bottom regions. However, with increasing Fr_U, more cooling was seen across all regions generally. This result suggests that Fr_U can be a useful indicator of decoupling/sheltering which results in cooling of valley bottom regions. However, does not appear to be a useful tool for identifying specific regions that may be more sensitive to the wind direction.

Chapter 7

Conclusions

To date there has been limited investigations of CAPs in small terrain types, where valley widths are less than a few kilometres and valley depths less than a few hundred metres. A unique dataset of measurements obtained from the COLPEX field campaign conducted in the Clun Valley region of Shropshire, are presented here. A summary of the major findings from this thesis follow. A response to questions posed in the introduction (chapter 2) are given.

7.1 Summary of major findings

Unfortunately the data quality of some instruments was poor. Cold wet conditions were prevalent during nights throughout the COLPEX field experiment, which caused a number of relative humidity and temperature sensors to fail. This resulted in poor data coverage of relative humidity. Additionally a hardware design flaw caused the Leeds University AWS data loggers to fail frequently. Due to this the AWS data coverage was generally poor. These issues combined limited the investigations to some degree.

1. A short 9–month climatology study of CAPs was conducted. The aim was to give a detailed account of CAP occurrence in the Clun Valley region of Shropshire, England.

   (a) CAPs occur frequently throughout the 9–month field campaign. The night-time maximum difference in temperature, between a hill top site (372 m ASL) and

a valley bottom site (202 m ASL), was used as a measure for CAP strength for each night. Weak CAPs, defined as temperature inversions larger than 1°C, occur on 45% of all nights. Strong CAPs, defined as temperature inversions larger than 4°C, occur 12% of all nights. Strong CAP events occur most frequently during the second week of September 2009, second week of October 2009, first two weeks of January 2010, the first two weeks of March 2010 and in the first two weeks of April 2010. Particularly strong CAPs formed during periods of snow cover, specifically on consecutive nights from 6–8 January 2010, which resulted in inversion strengths of 9.3°C and 9.9°C respectively.

(b) It was found that CAPs favour development when anticyclones dominate the synoptic weather situation, during clear skies and dry atmospheres, when low ambient wind speeds prevail and when the ambient wind direction was from the N. The pressure situation for each night was based on Met Office UM global model analysis taken at 00:00 UTC each night. The dryness of the atmosphere and the amount of cloud cover is inferred from the ratio of incoming to the amount of out going LW radiation (F_{lw}). The findings show that stronger CAPs "preferentially" form when:

- the mean night-time msl pressure is >1008 hPa.
- the mean night-time ambient wind speed is <7 m s^{-1} (geostrophic wind speeds <12 m s^{-1}) and are more likely to occur with decreasing ambient wind speed.
- the mean night-time ambient wind direction has a northerly or easterly wind component.
- values of F_{lw} are below 0.91 and are more likely to occur with decreasing values of F_{lw}, i.e., drier atmospheres (greenhouse effect).

Furthermore, from the findings it can be inferred that the "ideal" conditions for strong CAPs to form, without snow-covered ground, are:

- when the msl pressure is >1029 hPa and the PG is <1.5 Pa/km.
- when the mean night-time ambient wind speed is below 3 m s^{-1}.
- When the mean night-time ambient wind direction is from the north.
- When low values of F_{lw} occur, i.e., <0.80.

An illustration of the ideal synoptic situations has been given by figure 4.25, which may serve are a useful predictive tool for the potential of strong CAPs to form in the UK.

(c) A thorough investigation of the wind climatology was conducted to assess the relationship between ambient winds and valley winds for daytime, night-time and CAP nights. The emphasis was on identifying which of the four mechanisms outlined by Whiteman & Doran (1993) are observed during each of these times. Observations are focused on a network of AWS located across valley bottom regions in neighbouring valleys. Each site is located in surroundings that are topographically different. The four mechanisms for valley winds outlined by Whiteman & Doran (1993) are; forced channeling, downward momentum transport, pressure driven channeling and thermally driven flows. Each has a unique signature that is identifiable using distribution patterns of ambient wind against valley winds.

Results showed that pressure driven channeling and daytime thermally driven flows are not observed. Downward momentum transport, forced channeling and night-time thermally driven down-valley winds are prominent. Both downward momentum transport and forced channeling mechanisms are observed; however, both mechanisms favour development at specific locations. Downward momentum transport occurs most often in less sheltered locations. Forced channeling of the valley winds occurs most often in locations where the valleys are more narrow. Forced channeling is also observed when the valley narrows in the direction of the ambient wind and downward momentum transport when the valley widens in the direction of the ambient wind. Illustrated examples of these mechanisms in the Clun valley are given by figure 4.26.

The valley wind behaviour changes dramatically from daytime to strong CAP nights. Thermally driven down-valley winds are very prominent. This behaviour is indicative of valley winds that are decoupled from the ambient wind. Additionally unconventional patterns are observed. Up-valley winds are seen at two valley bottom locations during CAP nights and on occasions winds are aligned with neighbouring tributary valleys. Results in chapter 5 indicate that the night-time up-valley flows are caused by advection of colder air up-valley.

2. Using the criteria found in chapter 4, which outlines the "ideal" synoptic conditions for strong CAPs to form, a detailed case study investigation of a strong CAP forming night was conducted (chapter 5). The case study chosen was IOP 16 on 4–5 March 2010. The mean night-time ambient wind was from the NW and measured 2.7 m s^{-1}, the mean night-time F_{lw} measured 0.77, the msl pressure over the region at 00:00 UTC measured 1031 hPa, the pressure gradient at 00:00 UTC was 0.58 Pa/km and the maximum CAP strength was 6.7°C occurring around sunrise. The aim of the case study was to investigate the formation, evolution and break up of a strong CAP night in the Clun Valley region, during synoptic conditions that were "ideal" for strong CAPs to form. Initial investigations showed that the CAP evolution was not undisturbed, therefore despite the "ideal" synoptic conditions the CAP was still prone to disturbance by other nocturnal phenomena.

   (a) Cooling of all regions occurred 1–2hrs before sunset and a small inversion formed ∼1hr prior to sunset in the valley bottom. For the first few hours the CAP grew uninterrupted and a drainage flow was established and maintained at the valley bottom site Duffryn; however, the evolution of the CAP was interrupt some 4hrs after sunset.

   (b) Three Episodes of CAP evolution disruption are highlighted and are attributed to different phenomena, which in each case resulted in warmer air being introduced into the valley and the Duffryn drainage flow being interrupted. With the aid of high resolution model simulations of IOP 16, using the COLPEX version of the Met Office Unified Model, these results suggest that all three disturbances are part of a sequence of events that are attributed to the formation of the NLLJ during the night.

   The disturbance in Episode 1 was caused by gravity wave activity, possibly caused by strong wind shear (direction and speed) in the atmosphere above at this time. The wind shear appears to indicate the initial development of the NLLJ in the atmosphere above (∼1 km). The exact cause of the gravity wave activity is not determined. The gravity wave activity may have been formed though orographic generation, locally in the form of a hydraulic jump. This result highlights how sensitive CAPs in small terrain types are to disruption or break up by gravity wave activity, an observation rarely made before. However,

gravity wave activity is hypothesised by Adler *et al.* (2012) to be the cause of warm air intrusions into CAPs that form in Arizona's Meteor Crater, which is of similar scale to the Clun Valley, i.e., widths less than a few kilometres and depths less than a few hundred metres.

The disturbance during Episode 2 is less pronounced than that caused by the gravity wave(s) in Episode 1. In Episode 2 a region of increased turbulence descends to a level similar to the hill tops over a 1.5hr period. This phenomena in Episode 2 is attributed to the downward momentum transport of the evolving NLLJ over this 1.5hr period. This coincided with an increase in wind speeds from 2–4.5 m s^{-1}. When the ambient wind speed stopped increasing, the region of increased turbulence stopped. Orgill *et al.* (1992) suggests that ambient wind accelerations exceeding 4 x 10^{-4} m s^{-2} can lead to the erosion of drainage flows. The mean acceleration of the ambient wind over this period was ∼4.6 x 10^{-4} m s^{-2}.

The disturbance in Episode 3 is over a longer period of time compared to Episode 1 and 2. An increase in turbulence of the regions at and above the hill top regions are attributed to the continued evolution of the NLLJ, which resulted in the highest ambient wind speeds seen during the night, occurring in the early morning hours prior to sunrise.

(c) The final breakup of the CAP occurred some ∼3.5hrs after sunrise. In the initial stages of CAP breakup, warming is seen across all regions, but mostly in lower regions of the valleys. During CAP breakup the CAP top is eroded with time by shear driven turbulence from above, associated with the weakening NLLJ. The final breakup of the CAP occurs suddenly, caused by downward momentum transport of the NLLJ to the valley bottom. After this time the CAP and NLLJ cease to exist.

A comparison of radiosonde profiles for a number of strong CAP forming nights were made. The results show a pattern of wind speed and direction was consistent with characteristics of a NLLJ forming during other CAP nights also. This highlights the possibility of NLLJs being a consistent controlling factor on CAP evolution and breakup in the Clun Valley region and other inland regions across the world that are similar in scale. Further investigations are needed to confirm these findings.

3. A number of questions arose from the findings in Chapter 4 and 5 with regards drainage flows on CAP formation, evolution and breakup: (1) How does the Duffryn drainage flow develop with time? (2) How do cold air drainage flows contribute to CAP formation for a number of CAP nights? (3) How do drainage flows interact at a confluence region? A comparison of multiple CAP nights is conducted in chapter 6 using COLPEX model simulations. The focus here is to understand the structure, timing of formation, evolution and breakup of CAPs for a number of CAP nights.

   The pattern of drainage flow development was not the same across all cases. When drainage flows occur they are not necessarily seen in both neighbouring valleys, this is likely to be caused by differences in local stability, which will be dependent on local valley width, depth and orientation of the ambient wind direction to the valley. Low wind speed nights resulted in the early development of drainage flows, which tended to be stronger than in other cases. The stronger drainage flow led to increased mixing of valley bottom regions, which caused weaker stratification of valley bottom regions. However, in strong wind speed cases, weaker drainage flows formed first, which resulted in less turbulent mixing of valley bottom regions and stronger near surface stratification. This result suggests that there is a negative feedback on near surface stability resultsing in weaker near surface θ gradients.

   This result highlights a potential misunderstanding of CAP characteristics in valleys. It is generally assumed that CAPs have stronger θ gradients from the ground upwards and that this gradient will increase with increasing CAP strength. Weaker drainage flows may infact lead to increased stability locally, therefore a stronger cooling of valley bottom regions by sheltering/decoupling.

4. An investigation into the potential affects of the cross valley wind component on sheltering/decoupling (NH/U) in valley bottom regions, during the early stages of CAP formation was conducted. There is no strong evidence showing that the cross valley wind component had any bearing on sheltering/decoupling. However, as a general rule of thumb, as NH/U_{cross} increased, more cooling in valley bottom regions was observed. The results here suggest that there is little benefit of taking into account any effects of wind direction in relation to valley orientation when estimating the amount of decoupling/sheltering that is occurring. Drainage flows are likely to be efficient at redistributing cold air during the early stages of CAP

formation. Drainage flows can therefore mask the effects of cooling caused by a decoupling/sheltering of valley bottom regions. Results here suggest that future attempts to use NH/U as a downscaling tool for CAP prediction, should concentrate on other factors, such as the potential impacts from other nocturnal phenomena, such as gravity waves.

7.2 Recommendations for future research

One of the key aims of this thesis was to improve knowledge of CAPs in small-scale terrain typical of many parts of the UK. Throughout investigations in chapters 4 and 5, a number of further questions arose. Some initial investigations aimed at answering these questions in chapter 6. A number of phenomena have been shown to influence CAP evolution and breakup, including; drainage flows from multiple valleys, gravity wave formations, short accelerations in wind speed and the development of a NLLJ. To accurately predict CAPs in smaller terrain types, these processes and phenomena need to be resolved, or understood further for use in parametrisation or downscaling techniques.

In chapter 4 it was found that strong CAPs had a tendency to form preferentially when the ambient wind direction was from the N. Unfortunately it has not been determined why this is. It was hypothesised that N wind directions may favour strong CAP formation due to the fact that these wind directions are mostly aligned with many of the major tributary valleys in the Clun Valley region. However, it may be that N wind directions are indicative of synoptic conditions that favour strong atmospheric stability. One way to test this relationship is to conduct 3D idealised model simulations. Using an idealised V shaped valley and keeping the synoptic conditions the same, the valley could be rotated with respect to the wind direction (and pressure situation). This study should prove or disprove this hypothesis. A number of further sensitivity studies could be conducted, such as changing; (1) the pressure situation (identifying the existence of pressure driven channeling), (2) the depth, width and shape of the valley, (3) the background stability.

Due to data limitations it was not possible to investigate the dependence and structure of the Duffryn drainage flow on CAP strength, wind direction and speed. Model results in chapter 6 show some differences in the Clun Valley drainage flow structure for a number of CAP nights. Specifically is appeared that strong drainage flows form in strongly stratified

nights; however, the drainage flows can increase turbulence in the lowest regions of the valley, which result in less stratification of valley bottom regions. The model investigations mentioned above could be extended to investigate the impacts of these factors on drainage flows also. If drainage flow structure is different under different wind directions, this would impact how CAPs form and evolve.

It was highlighted in chapter 5 that gravity wave activity affected the evolution of the CAP during IOP 16; however, the mechanism of the gravity wave activity was not determined. Investigations using large eddy model simulations of IOP 16 may identify possible mechanisms of generation. The radiosonde profiles launched at the time could be used as input parameters for the background meteorology. Results may highlight if the conditions favour the development of a hydraulic jump, therefore dismissing this as a possibility.

Results in chapter 5 highlighted the possible recurrence of a NLLJ in the atmosphere above the Clun Valley during CAP nights. To confirm this comparisons could be made to model simulations of these nights. Additionally it would be beneficial to conduct further analysis – using model simulations or observations (radiosondes) of many CAP nights – in the Clun Valley or a similar region, could be made to confirm if the NLLJ is a reccurring nocturnal phenomena. Further analysis could be conducted to see how the NLLJ changes in strength and or season (length of day).

The results in chapter 4 highlighted the "ideal" and "preferential" synoptic conditions for CAPs to form. Further statistical analysis of the COLPEX dataset, continuing on the analysis in chapter 4, could potentially be adapted for use as a weather forecasting tool, in the form of a CAP outbreak-risk look up table.

References

Adler, B., Whiteman, C., Hoch, S., Lehner, M. & Kalthoff, N. (2012). Warm-Air Intrusions in Arizona's Meteor Crater. *Journal of Applied Meteorology and Climatology*, **51**, 1010–1025.

Anfossi, D., Oettl, D., Degrazia, G. & Goulart, A. (2005). An analysis of sonic anemometer observations in low wind speed conditions. *Boundary-Layer Meteorology*, **114**, 179–203.

Banta, R., Darby, L., Fast, J., Pinto, J., Whiteman, C., Shaw, W. & Orr, B. (2004). Nocturnal low-level jet in a mountain basin complex. Part I: Evolution and effects on local flows. *Journal of Applied Meteorology*, **43**, 1348–1365.

Barr, S. & Orgill, M. (1989). Influence of external meteorology on nocturnal valley drainage winds. *Journal of Applied Meteorology*, **28**, 497–517.

Barry, R.G. (2008). *Mountain Weather and Climate; third edition*. Cambridge University Press, New York, USA.

Best, M., Pryor, M., Clark, D., Rooney, G., Essery, R., Ménard, C., Edwards, J., Hendry, M., Porson, A., Gedney, N. *et al.* (2011). The Joint UK Land Environment Simulator (JULES), model description–Part 1: energy and water fluxes. *Geoscientific Model Development*, **4**, 677–699.

Billings, B., Grubisic, V. & Borys, R. (2006). Maintenance of a mountain valley cold pool: A numerical study. *Monthly Weather Review*, **134**, 2266–2278.

Blackadar, A. (1957). Boundary layer wind maxima and their significance for the growth of nocturnal inversions. *Bulletin of the Amererican Meteoroligical Society*, **38**, 283–290.

Bodine, D., Klein, P., Arms, S. & Shapiro, A. (2009). Variability of Surface Air Temperature over Gently Sloped Terrain. *Journal of Applied Meteorology and Climatology*, **48**, 1117–1141.

Bogren, J., Gustavsson, T., Karlsson, M. & Postgård, U. (2000a). The impact of screening on road surface temperature. *Meteorological Applications*, **7**, 97–104.

Bogren, J., Gustavsson, T. & Postgård, U. (2000b). Local temperature differences in relation to weather parameters. *International Journal of Climatology*, **20**, 151–170.

Bootsma, A. (1976). Estimating minimum temperature and climatological freeze risk in hilly terrain. *Agricultural Meteorology (Netherlands)*.

Browning, K.A., Morcrette, C.J., Nicol, J., Blyth, A.M., Bennett, L.J., Brooks, B.J., Marsham, J., Mobbs, S.D., Parker, D.J., Perry, F. *et al.* (2007). The convective storm initiation project. *Bulletin of the American Meteorological Society*, **88**, 1939–1955.

Carrera, M., Gyakum, J. & Lin, C. (2008). Observational study of wind channeling within the St. Lawrence River Valley. *Journal of Climatology and Applied Meteorology*, **48**, 2341–2361.

Clements, C., Whiteman, C. & Horel, J. (2003). Cold-air-pool structure and evolution in a mountain basin: Peter Sinks, Utah. *Journal of Applied Meteorology*, **42**, 752–768.

Coulter, R., Orgill, M. & Porch, W. (1989). Tributory fluxes in to Bruch Creek Valley. *Journal of Applied Meteorology*, **28**, 555–568.

Cullen, M., Davies, T., Mawson, M., James, J., Coulter, S. & Malcolm, A. (1997). An overview of numerical methods for the next generation UK NWP and climate model. *Atmosphere-Ocean*, **35**, 425–444.

Cuxart, J., Yagüe, C., Morales, G., Terradellas, E., Orbe, J., Calvo, J., Fernández, A., Soler, M., Infante, C., Buenestado, P. *et al.* (2000). Stable atmospheric boundary-layer experiment in Spain (SABLES 98): a report. *Boundary-Layer Meteorology*, **96**, 337–370.

Davies, T., Cullen, M., Malcolm, A., Mawson, M., Staniforth, A., White, A. & Wood, N. (2005). A new dynamical core for the Met Office's global and regional modelling of the atmosphere. *Quarterly Journal of the Royal Meteorological Society*, **131**, 1759–1782.

Doran, J. (1991). The effects of ambient winds on valley drainage flows. *Boundary-Layer Meteorology*, **55**, 177–189.

Dorninger, M., Whiteman, C., Bica, B., Eisenbach, S., Pospichal, B. & Steinacker, R. (2011). Meteorological Events Affecting Cold-Air Pools in a Small Basin. *Journal of Applied Meteorology and Climatology*, **11**, 2223–2234.

Drobinski, P., Steinacker, R., Richner, H., Baumann-Stanzer, K., Beffrey, G., Benech, B., Berger, H., Chimani, B., Dabas, A., Dorninger, M. *et al.* (2007). F ohn in the Rhine Valley during MAP: A reveiw of its multiscale dynamics in complex valley geometry. *Quarterly Journal of the Royal Meteoroogical Society*, **133**, 897–916.

Eden, P. (2009a). August 2009 Very wet in the north and west, dry in the south-east. *Weather*, **64**, i–iv.

Eden, P. (2009b). July 2009 A hot start, then very unsettled with several heavy falls of rain. *Weather*, **64**, i–iv.

Eden, P. (2009c). November 2009 Very mild and exceptionally wet. *Weather*, **65**, i–iv.

Eden, P. (2009d). October 2009 Rather dull but dry; cool first three weeks but a warm finish. *Weather*, **64**, i–iv.

Eden, P. (2009e). September 2009 A disturbed start, then generally dry and warm. *Weather*, **64**, i–iv.

Eden, P. (2010a). April 2010 Dry and very sunny. Frequent warm days but rather cold nights. *Weather*, **65**, i–iv.

Eden, P. (2010b). December 2009 Coldest since 1996: frequent snow after mid-month. *Weather*, **65**, i–iv.

Eden, P. (2010c). February 2010 Coldest since 1996. Coldest winter quarter since 1978–1979. *Weather*, **65**, i–iv.

Eden, P. (2010d). January 2010 very cold and snowy first half; nondescript second half. *Weather*, **65**, i–iv.

Eden, P. (2010e). March 2010 Dry, sunny but cold first half; unsettled but much warmer second half. *Weather*, **65**, i–iv.

Farrugia, P. & Micallef, A. (2006). Comparative analysis of estimators for wind direction standard deviation. *Meteorological Applications*, **13**, 29–41.

Fernando, H. & Weil, J. (2010). Whither the Stable Boundary Layer?: A Shift in the Research Agenda. *Bulletin of the American Meteorological Society*, **91**, 1475–1484.

Fitzjarrald, D. & Lala, G. (1989). Hudson Valley fog environments. *Journal of Applied Meteorology*, **28**, 1303–1328.

Garratt, J. & Brost, R. (1981). Radiative cooling effects within and above the nocturnal boundary layer. *Journal of Atmospheric Sciences*, **38**, 2730–2746.

Gregory, D. & Rowntree, P. (1990). A mass flux convection scheme with representation of cloud ensemble characteristics and stability-dependent closure. *Monthly Weather Review*, **118**, 1483–1506.

Gross, G. & Wipperman, F. (1987). Channeling and countercurrent in the upper Rhine Valley; Numerical simulations. *Journal of Alimate and Applied Meteorology*, **26**, 1293–1304.

Gudiksen, P., Leone, J., King, C., Ruffieux, D. & Neff, W. (1992). Measurements and modelling of the effects of ambient meteorology on nocturnal drainage flows. *Journal of Applied Meteorology*, **31**, 1023–1032.

Gustavsson, T. (1995). A study of air and road-surface temperature variations during clear windy nights. *International Journal of Climatology*, **15**, 919–932.

Gustavsson, T., Karlsson, M., Bogren, J. & Lindqvist, S. (1998). Development of temperature patterns during clear nights. *Journal of Applied Meteorology*, **37**, 559–571.

Haiden, T. & Whiteman, C.D. (2005). Katabatic flow mechanisms on a low-angle slope. *Journal of applied meteorology*, **44**, 113–126.

Hart, K., Steenburgh, W. & Onton, D. (2005). Model forecast improvements with decreased horizontal grid spacing over finescale intermountain orography during the 2002 Olympic Winter Games. *Weather and Forecasting*, **20**, 558–576.

Heywood, G. (1933). Katabatic winds in a valley. *Quarterly Journal of the Royal Meteorological Society*, **59**, 47–58.

Hobby, M. (2010). Personal communication. *University of Leeds and NCAS*.

Hoch, S., Calanca, P., Philipona, R. & Ohmura, A. (2007). Year-round observation of longwave radiative flux divergence in Greenland. *Journal of Applied Meteorology and Climatology*, **46**, 1469–1479.

Holden, J., Derbyshire, S. & Belcher, S. (2000). Tethered balloon observations of the nocturnal stable boundary layer in a valley. *Boundary-Layer Meteorology*, **97**, 1–24.

Iijima, Y. & Shinoda, M. (2000). Seasonal changes in the cold-air pool formation in a subalpine hollow, central Japan. *International Journal of Climatology*, **20**, 1471–1483.

Kaimal, J. & Finnigan, J. (1994). *Atmospheric boundary layer flows: their structure and measurement*. Oxford University Press, USA.

Kiess, R.B. & Riordan, A.J. (1987). The Statistical Relationship between the Synoptic-Scale Pressure Field and the Development and Morning Transition of Surface Inversions at Two Rural Sites. *Journal of Climate and Applied Meteorology*, **26**, 1000–1013.

King, J. & Giles, B. (1997). *Regional Climates of the British Isles*. Routledge London.

Kossmann, M. & Sturman, A. (2003). Pressure-driven channeling effects in bent valleys. *Journal of Applied Meteorology*, **42**, 151–158.

Kouznetsov, R., Tisler, P., Palo, T. & Vihma, T. (2012). An evidence of very shallow summertime katabatic flows in Dronning Maud Land, Antarctica. *Journal of Applied Meteorology and Climatology*.

Lalas, D. & Einaudi, F. (1980). Tropospheric gravity waves: Their detection by and influence on rawinsonde balloon data. *Quarterly Journal of the Royal Meteorological Society*, **106**, 855–864.

Lean, H., Clark, P., Dixon, M., Roberts, N., Fitch, A., Forbes, R. & Halliwell, C. (2008). Characteristics of high-resoloution versions of the met office unified model for forecasting convection over the united kingdom. *Monthly Weather Review*, **136**, 3408–3424.

Lee, T., Pielke, R., Kessler, R. & Weaver, J. (1989). Influence of cold pools downstream of mountain barriers on downslope winds and flushing. *Monthly Weather Review*, **117**, 2041–2058.

Lindkvist, L., Gustavsson, T. & Bogren, J. (2000). A frost assessment method for mountainous areas. *Agricultural and Forest Meteorology*, **102**, 51–67.

Lock, A., Brown, A., Bush, M., Martin, G. & Smith, R. (2000). A new boundary layer mixing scheme. Part I: Scheme description and single-column model tests. *Monthly Weather Review*, **128**, 3187–3199.

Madelin, M. & Beltrando, G. (2005). Spatial interpolation-based mapping of the spring frost hazard in the Champagne vineyards. *Meteorological Applications*, **12**, 51–56.

Mahrt, L. (1989). Intermittent of atmospheric turbulence. *Collections*.

Mahrt, L. (2006). Variation of surface air temperature in complex terrain. *Journal of Applied Meteorology*, **45**, 1481–1493.

Mahrt, L. (2008a). Bulk formulation of surface fluxes extended to weak-wind stable conditions. *Quarterly Journal of the Royal Meteorological Society*, **134**, 1–10.

Mahrt, L. (2008b). Mesoscale wind direction shifts in the stable boundary-layer. *Tellus A*, **60**, 700–705.

Mahrt, L., Richardson, S., Seaman, N. & Stauffer, D. (2010). Non-stationary drainage flows and motions in the cold pool. *Tellus A*, **62**, 698–705.

Manins, P. & Sawford, B. (1979). Katabatic winds: A field case study. *Quarterly Journal of the Royal Meteorological Society*, **105**, 1011–1025.

Manners, J., Vosper, S. & Roberts, N. (2012). Radiative transfer over resolved topographic features for high-resolution weather prediction. *Quarterly Journal of the Royal Meteorological Society*, **138**, 720–733.

May, P.T. (1995). The Australian nocturnal jet and diurnal variations of boundary-layer winds over Mt. Isa in North-eastern Australia. *Quarterly Journal of the Royal Meteorological Society*, **121**, 987–1003.

Mayr, G., Armi, L., Arnold, S., Banta, R., Darby, L., Durran, D., Flamant, C., Gabersek, S., Gohm, A., Mayr, R. *et al.* (2004). Gap flow measurements during the Mesoscale Alpine Programme. *Meteorology and Atmospheric Physics*, **86**, 99–119.

McKay, D. & Thurtell, G. (1978). Measurements of the energy fluxes involved in the energy budget of a snow cover. *Journal of Applied Meteorology*, **17**, 339–349.

Miloshevich, L., Vömel, H., Whiteman, D. & Leblanc, T. (2009). Accuracy assessment and correction of Vaisala RS92 radiosonde water vapor measurements. *Journal of Geophysical Research*, **114**, D11305.

Moraes, O.L., Acevedo, O.C., Degrazia, G.A., Anfossi, D., da Silva, R. & Anabor, V. (2005). Surface layer turbulence parameters over a complex terrain. *Atmospheric Environment*, **39**, 3103–3112.

Neff, W. & King, C. (1989). The accumulation and pooling of drainage flows in a large basin. *Journal of Applied Meteorology*, **28**, 518–529.

Nygaard & Wolff (2010). Use of Ultrasonic wind sensors in Norway. *Conference on Meteorological and Environmental Instruments and Methods of Observation Helsinki, Finland, 30 August - 1 September 2010*, **Poster 3.21**.

Oettl, D., Goulart, A., Degrazia, G. & Anfossi, D. (2005). A new hypothesis on meandering atmospheric flows in low wind speed conditions. *Atmospheric Environment*, **39**, 1739–1748.

Oke, T.R. (1987). *Boundary Layer Climates; second edition*. Routledge London.

Ookouch, Y., Segal, M., Kessler, R. & Pielke, R. (1984). Evaluation of soil moisture effects on the generation and modification of mesoscale circulations. *Monthly Weather Review*, **112**, 2281–2292.

Ordnance Survey (2007). OS MasterMap [NTF geospatial data], Scale 1:1250: Updated: May, Using: EDINA Digimap Ordnance Survey Service. ⟨`http://edina.ac.uk/digimap`⟩, accessed: March 2008.

Orgill, M.M., Kincheloe, J.D. & Sutherland, R.A. (1992). Mesoscale influences on nocturnal valley drainage winds in Western Colorado valleys. *Journal of applied meteorology*, **31**, 121–141.

Pal Arya, S. (1988). *Introduction to Micrometeorology*. Academic Press, Inc , London.

Pal Arya, S. (1999). *Air pollution Meteorology and Dispersion*. Oxford University Press, Inc , New York, USA.

Parker, M. & Raman, S. (1993). A case study of the nocturnal boundary layer over a complex terrain. *Boundary-Layer Meteorology*, **66**, 303–324.

Pearson, G., Davies, F. & Collier, C. (2009). An analysis of the performance of the UFAM pulsed Doppler lidar for observing the boundary layer. *Journal of Atmospheric and Oceanic Technology*, **26**, 240–250.

Poulos, G. & Zhong, S.S. (2008). An Observational History of Small-Scale Katabatic Winds in Mid-Latitudes. *Geography Compass*, **2**, 1798–1821.

Pozdnoukhov, A., Foresti, L. & Kanevski, M. (2009). Data-driven topo-climatic mapping with machine learning methods. *Natural hazards*, **50**, 497–518.

Price, J. (2010). Personal communication. *UK Met Office*.

Price, J., Vosper, S., Brown, A., Ross, A., Clark, P., Davies, F., Horlacher, V., Claxton, B., McGregor, J., Hoare, J., Jemmett-Smith, B. & Sheridan, P. (2011). COLPEX: Field and Numerical Studies Over a Region of Small Hills. *Bulletin of the American Meteorological Society*, **92**, 1636–1650.

Rampanelli, G., Zardi, D. & Rotunno, R. (2004). Mechanisms of up-valley winds. *Journal of the atmospheric sciences*, **61**, 3097–3111.

Renfrew, I.A. & Anderson, P.S. (2002). The surface climatology of an ordinary katabatic wind regime in Coats Land, Antarctica. *Tellus A*, **54**, 463–484.

Reuten, C., Steyn, D., Strawbridge, K. & Bovis, P. (2005). Observations of the relation between upslope flows and the convective boundary layer in steep terrain. *Boundary-Layer Meteorology*, **116**, 37–61.

Rogers, R.R. (1979). A Short Course in Cloud Physics. *A short course in cloud physics., by Rogers, RR. Elmsford (NY, USA): Pergamon Press, 227 p.*, **1**.

Rolland, C. (2003). Spatial and seasonal variations of air temperature lapse rates in alpine regions. *Journal of Climate*, **16**, 1032–1046.

Rotach, M. & Zardi, D. (2007). On the boundary-layer structure over highly complex terrain: Key findings from MAP. *Quarterly Journal of the Royal Meteorological Society*, **133**, 937–948.

Savov, P., Skakalova, T., Kolev, I. & Ludwig, F. (2002). Lidar investigation of the temporal and spatial distribution of atmospheric aerosols in mountain valleys. *Journal of Applied Meteorology*, **41**, 528–541.

Schmidli, J., Poulos, G., Daniels, M. & Chow, F. (2009). External influences on nocturnal thermally driven flows in a deep valley. *Journal of Applied Meteorology and Climatology*, **48**, 3–23.

Sheridan, P., Smith, S., Brown, A. & Vosper, S. (2010). A simple height-based correction for temperature downscaling in complex terrain. *Meteorological Applications*, **17**, 329–339.

Sheridan, P., Vosper, S. & Brown, A. (2013). Characteristics of cold pools observed in narrow valleys and dependence on external conditions. *Quarterly Journal of the Royal Meteorological Society*.

Smith, R. (1990). A scheme for predicting layer clouds and their water content in a general circulation model. *Quarterly Journal of the Royal Meteorological Society*, **116**, 435–460.

Smith, S., Brown, A., Vosper, S., Murkin, P. & Veal, A. (2010). Observations and Simulations of Cold Air Pooling in Valleys. *Boundary-Layer Meteorology*, **134**, 85–108.

Stewart, J.Q., Whiteman, C.D., Steenburgh, W.J. & Bian, X. (2002). A climatological study of thermally driven wind systems of the US Intermountain West. *Bulletin of the American Meteorological Society*, **83**, 699–708.

Stull, R.B. (1988). *An introduction to Boundary layer Meteorology*. Kluwer Academic Publishers, Dordrecht, Netherlands.

Tang, Y., Lean, H.W. & Bornemann, J. (2012). The benefits of the Met Office variable resolution NWP model for forecasting convection. *Meteorological Applications*.

Thorpe, A. & Guymer, T. (1977). The nocturnal jet. *Quarterly Journal of the Royal Meteorological Society*, **103**, 633–653.

Van de Wiel, B., Ronda, R., Moene, A., De Bruin, H. & Holtslag, A. (2002). Intermittent turbulence and oscillations in the stable boundary layer over land. Part I: A bulk model. *Journal of the atmospheric sciences*, **59**, 942–958.

Vosper, S. & Brown, A. (2008). Numerical simulations of sheltering in valleys: The formation of nighttime cold-air pools. *Boundary-Layer Meteorology*, **127**, 429–448.

Vosper, S., Carter, E., Lean, H., Lock, A., Clark, P. & Webster, S. (2013a). High resolution modelling of valley cold pools. *Atmospheric Science Letters*.

Vosper, S., Hughes, J., Lock, A., Sheridan, P., Ross, A., Jemmett-Smith, B. & Brown, A. (2013b). Cold pool formation in a narrow valley. *Quarterly Journal of the Royal Meteorological Society*.

Weber, R. & Kaufmann, P. (1998). Relationship of synoptic winds and complex terrain flows during the MISTRAL field experiment. *Journal of Applied Meteorology*, **37**, 1486–1496.

Weigel, A. & Rotach, M. (2004). Flow structure and turbulence characteristics of the daytime atmosphere in a steep and narrow Alpine valley. *Quarterly Journal of the Royal Meteorological Society*, **130**, 2605–2628.

Whiteman, C. (1982). Breakup of temperature inversions in deep mountain valleys: Part I. Observations. *Journal of Applied Meteorology*, **21**, 270–289.

Whiteman, C. (2000). *Mountain meteorology: fundamentals and applications*. Oxford University Press, USA.

Whiteman, C. & Doran, J. (1993). The relationship between overlying synoptic-scale flows and winds within a valley. *Journal of Applied Meteorology*, **32**, 1669–1682.

Whiteman, C. & McKee, T. (1982). Breakup of temperature inversions in deep mountain valleys: Part II. Thermodynamic model. *Journal of Applied Meteorology*, **21**, 290–302.

Whiteman, C., Allwine, K., Fritschen, L., Orgill, M. & Simpson, J. (1989a). Deep valley radiation and surface energy budget microclimates. Part I: Radiation. *Journal of Applied Meteorology*, **28**, 414–426.

Whiteman, C., Allwine, K., Fritschen, L., Orgill, M. & Simpson, J. (1989b). Deep valley radiation and surface energy budget microclimates. Part II: Energy budget. *Journal of Applied Meteorology*, **28**, 427–437.

Whiteman, C., McKee, T. & Doran, J. (1996). Boundary layer evolution within a canyonland basin. Part I: Mass, heat, and moisture budgets from observations. *Journal of Applied Meteorology*, **35**, 2145–2161.

Whiteman, C., Bian, X. & Zhong, S. (1999). Wintertime evolution of the temperature inversion in the Colorado Plateau Basin. *Journal of Applied Meteorology*, **38**, 1103–1117.

Whiteman, C., Zhong, S., Shaw, W., Hubbe, J., Bian, X. & Mittelstadt, J. (2001). Cold pools in the Columbia Basin. *Weather and Forecasting*, **16**, 432–447.

Whiteman, C., De Wekker, S. & Haiden, T. (2007). Effect of dewfall and frostfall on nighttime cooling in a small, closed basin. *Journal of Applied Meteorology and Climatology*, **46**, 3–13.

Whiteman, C., Muschinski, A., Zhong, S., Fritts, D., Hoch, S., Hahnenberger, M., Yao, W., Hohreiter, V., Behn, M., Cheon, Y. *et al.* (2008). Metcrax 2006. *Bulletin of the American Meteorological Society*, **89**.

Wilson, D.R. & Ballard, S.P. (1999). A microphysically based precipitation scheme for the UK Meteorological Office Unified Model. *Quarterly Journal of the Royal Meteorological Society*, **125**, 1607–1636.

Wood, N. & Mason, P. (1993). The pressure force induced by neutral, turbulent flow over hills. *Quarterly Journal of the Royal Meteorological Society*, **119**, 1233–1267.

Worthington, R.M. (1999). Alignment of mountain wave patterns above Wales: A VHF radar study during 1990–1998. *Journal of Geophysical Research: Atmospheres (1984–2012)*, **104**, 9199–9212.

Wyngaard, J. (1990). Scalar fluxes in the planetary boundary layer?theory, modeling, and measurement. *Boundary-Layer Meteorology*, **50**, 49–75.

Zängl, G. (2003). The impact of upstream blocking, drainage flow and the geostrophic pressure gradient on the persistence of cold-air pools. *Quarterly Journal of the Royal Meteorological Society*, **129**, 117–137.

Zängl, G. (2005a). Dynamical aspects of wintertime cold-air pools in an Alpine valley system. *MONTHLY WEATHER REVIEW-USA*, **133**, 2721.

Zängl, G. (2005b). Wintertime Cold-Air Pools in the Bavarian Danube Valley Basin: Data Analysis and Idealized Numerical Simulations. *Journal of Applied Meteorology*, **44**, 1950–1971.

Zhong, S., Li, J., Whiteman, C., Bian, X. & Yao, W. (2008). Climatology of the high wind events in the Owens Valley, California. *Monthly Weather Review*, **136**, 3536–3552.

Appendix A

.1 Valley wind forcings for valleys orientated north to south and west to east.

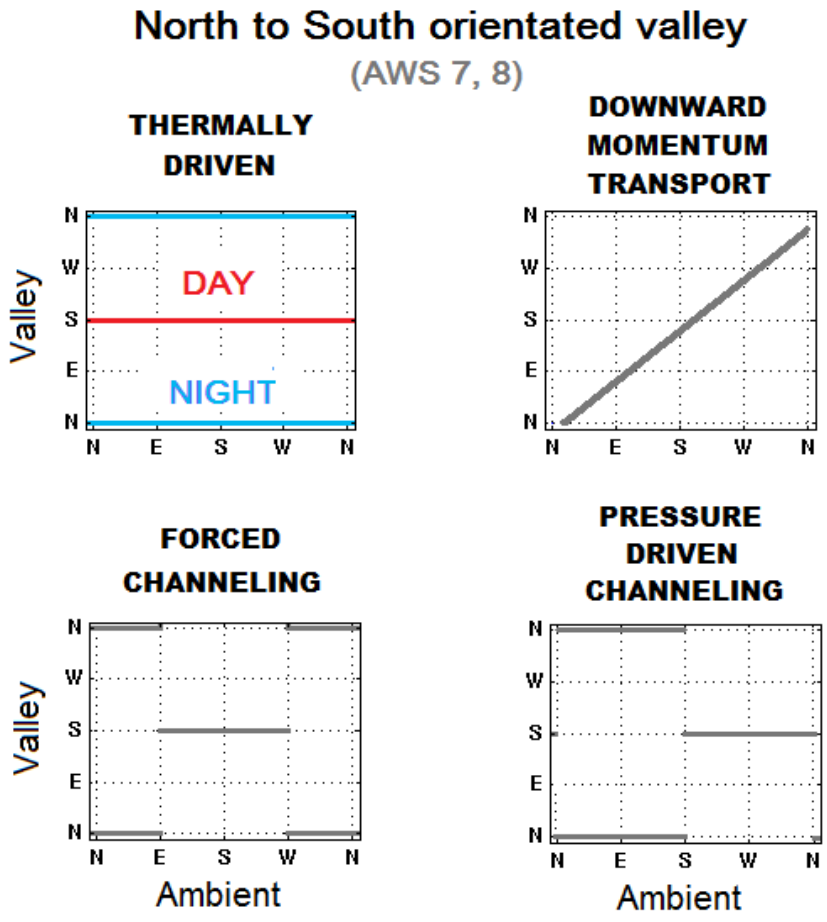

FIGURE 1: *Valley wind forcing examples for a valley orientated north to south.*

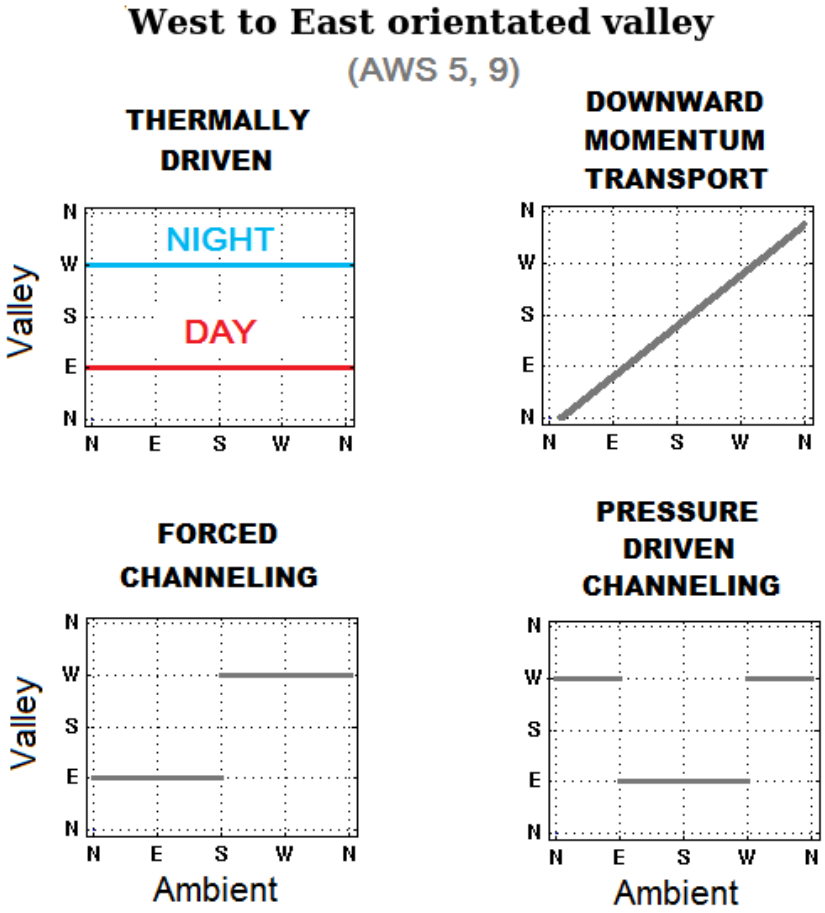

FIGURE 2: *Valley wind forcing examples for a valley orientated west to east.*

Appendix B

Wind rose plots showing all wind climatology, obtained during the COLPEX field campaign from July 2009 to April 2010, are shown in the following sections.

.2 Springhill mast site

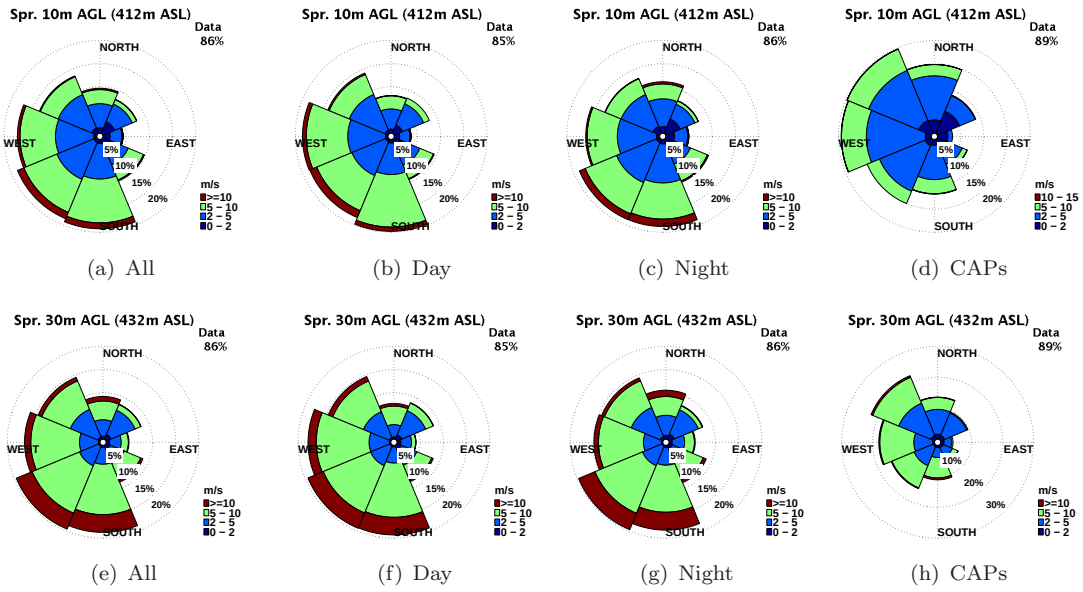

(a) All (b) Day (c) Night (d) CAPs

(e) All (f) Day (g) Night (h) CAPs

FIGURE 3: *Wind rose plots of* 2 *m wind speed and direction for Springhill,* 10 *m and* 30 *m AGL. Four wind rose plots are shown for each height, from left to right they are; (1) All wind data for the 204 day period from 29 September to 20 April, (2) for daytime wind data only, (3) for night-time wind data only, (4) for all CAP nights (inversion larger than* 1° *C). Wind speed (m* s^{-1}*) is represented using a colour scale. Each segment of the wind rose represents* 45°*. Percentage values under "Data" represent the total amount of data available for each climatology study.*

.3 Burfield mast site

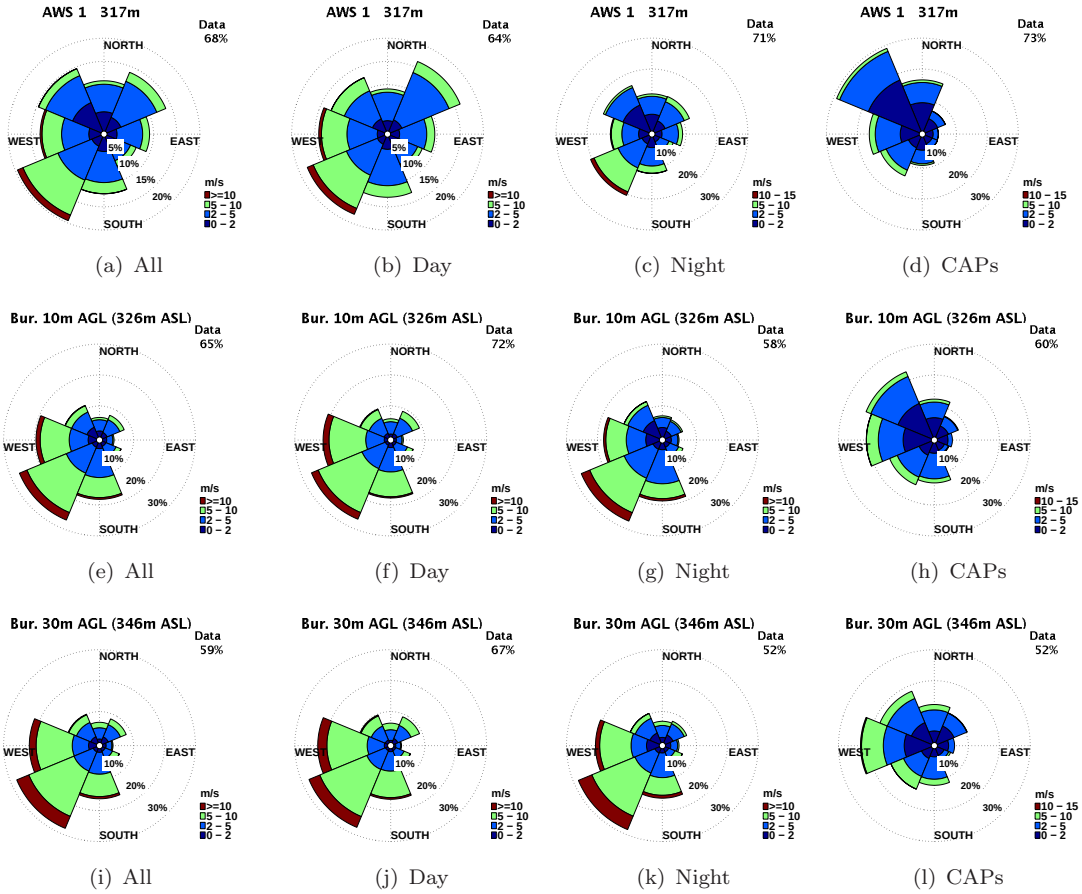

(a) All (b) Day (c) Night (d) CAPs

(e) All (f) Day (g) Night (h) CAPs

(i) All (j) Day (k) Night (l) CAPs

FIGURE 4: *As in figure 3, except wind is measured at the Burfield mast site, which includes AWS 1. Measurements are at* 2 *m (AWS 1),* 10 *m and* 30 *m AGL.*

.4 Duffryn mast site

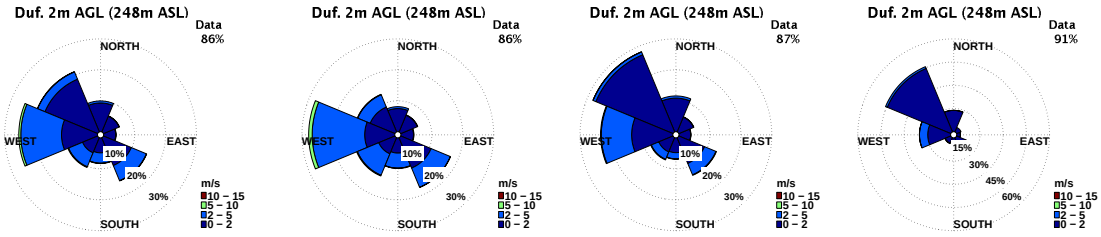

(a) All

(b) Day

(c) Night

(d) CAPs

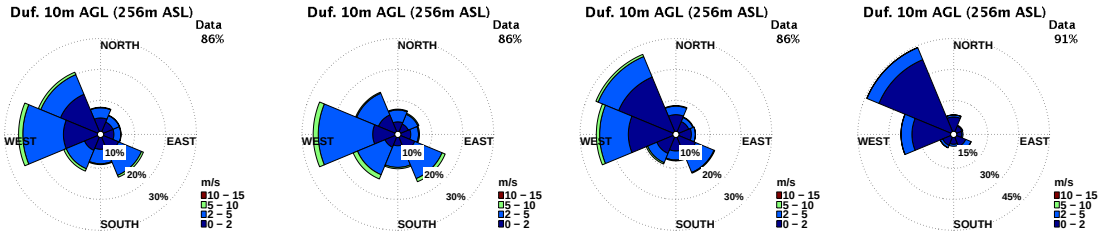

(e) All

(f) Day

(g) Night

(h) CAPs

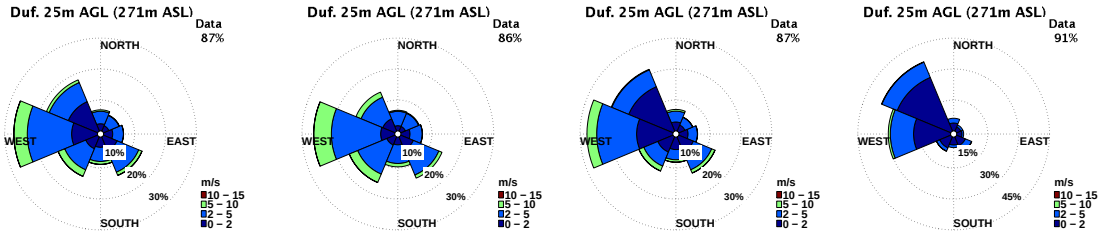

(i) All

(j) Day

(k) Night

(l) CAPs

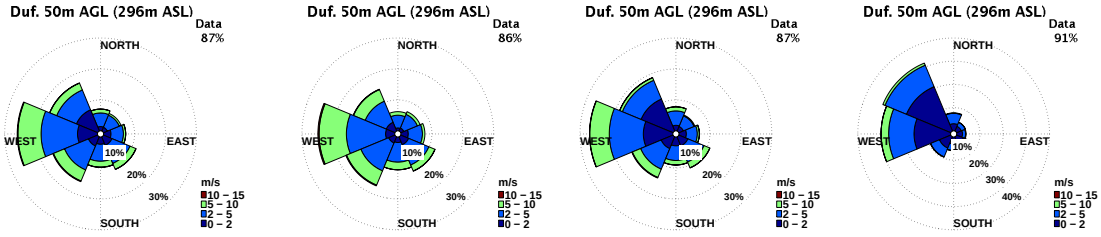

(m) All

(n) Day

(o) Night

(p) CAPs

FIGURE 5: *As in figure 3, except wind is measured at the Duffryn mast site at* 2 *m,* 10 *m,* 25 *m and* 50 *m AGL.*

.5 AWS cited above 300 m ASL; AWS 1, 2, 4 and 10

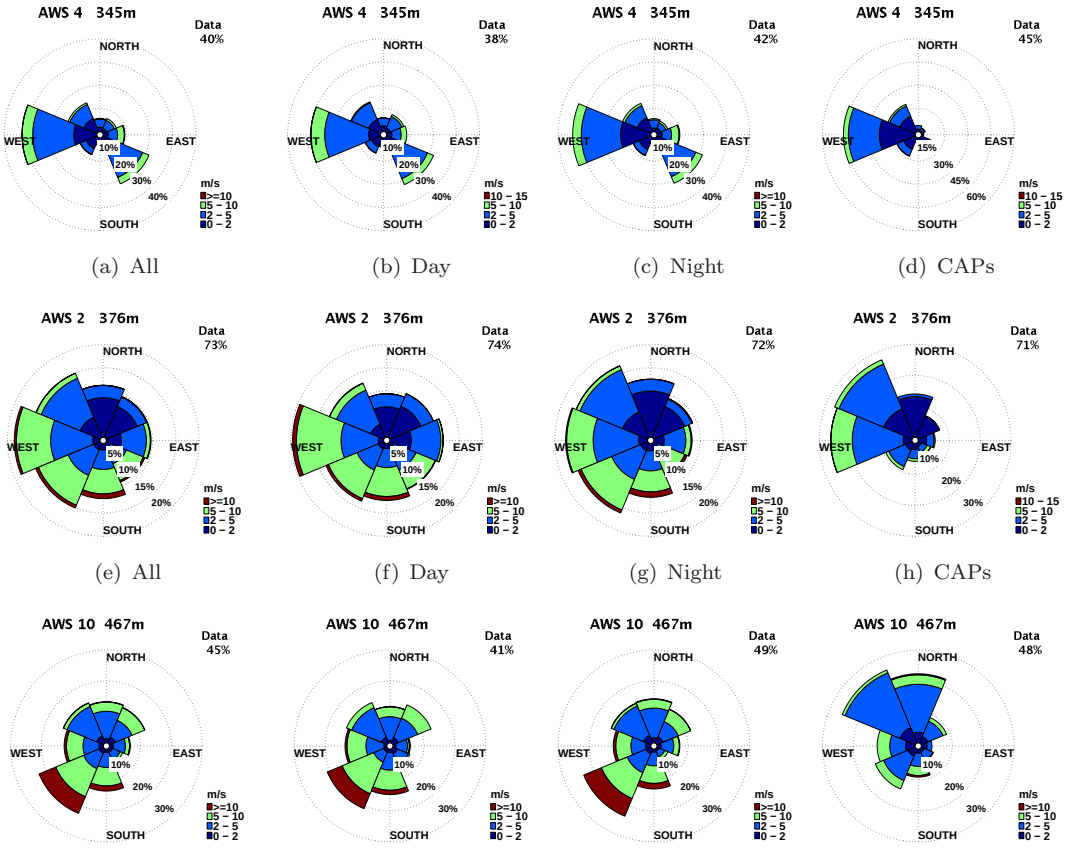

(a) All (b) Day (c) Night (d) CAPs

(e) All (f) Day (g) Night (h) CAPs

(i) All (j) Day (k) Night (l) CAPs

FIGURE 6: *As in figure 3, except wind measurements are for all AWS located above 300 m ASL. AWS measurements are at 2 m AGL.*

.6 AWS cited below 300 m ASL in the main Clun Valley; AWS 5, 9, 6

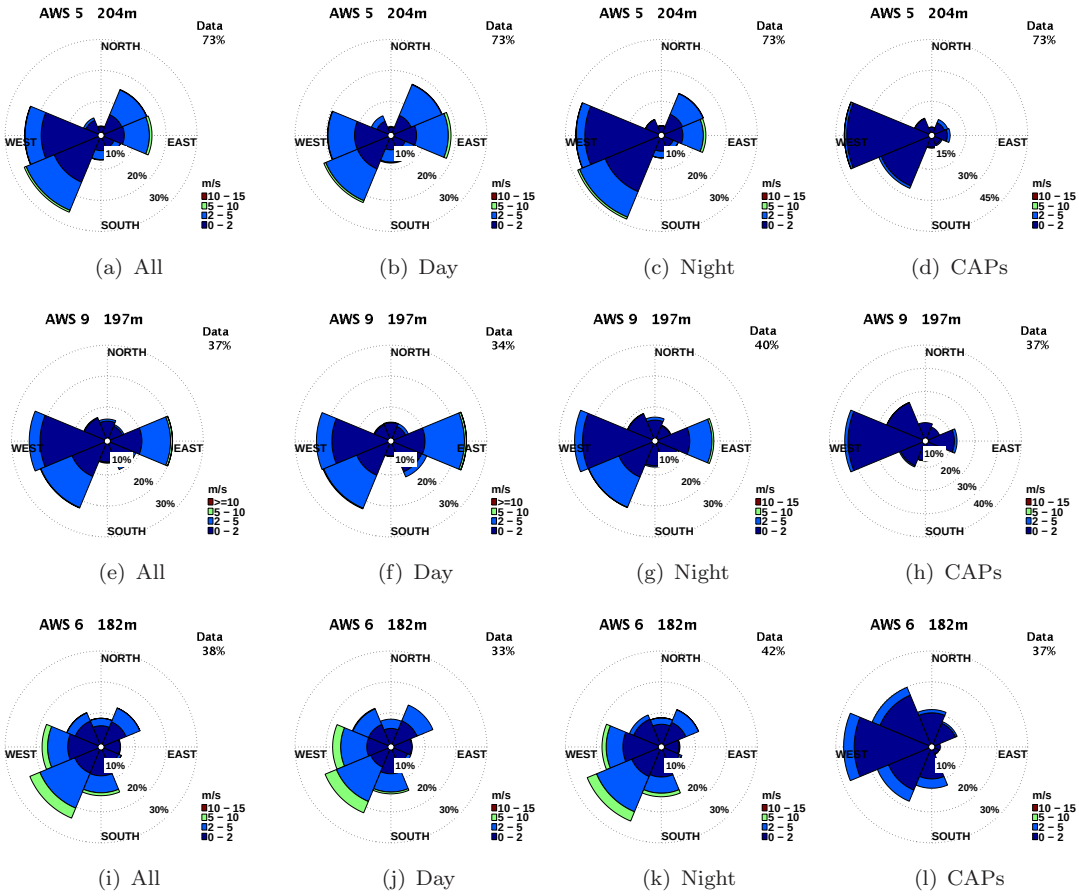

(a) All (b) Day (c) Night (d) CAPs

(e) All (f) Day (g) Night (h) CAPs

(i) All (j) Day (k) Night (l) CAPs

FIGURE 7: *As in figure 3, except all AWS in this case are located below* 300 *m ASL along the floor of the Clun Valley.*

.7 AWS cited below 300 m ASL in tributary valleys; AWS 3, 7, 8

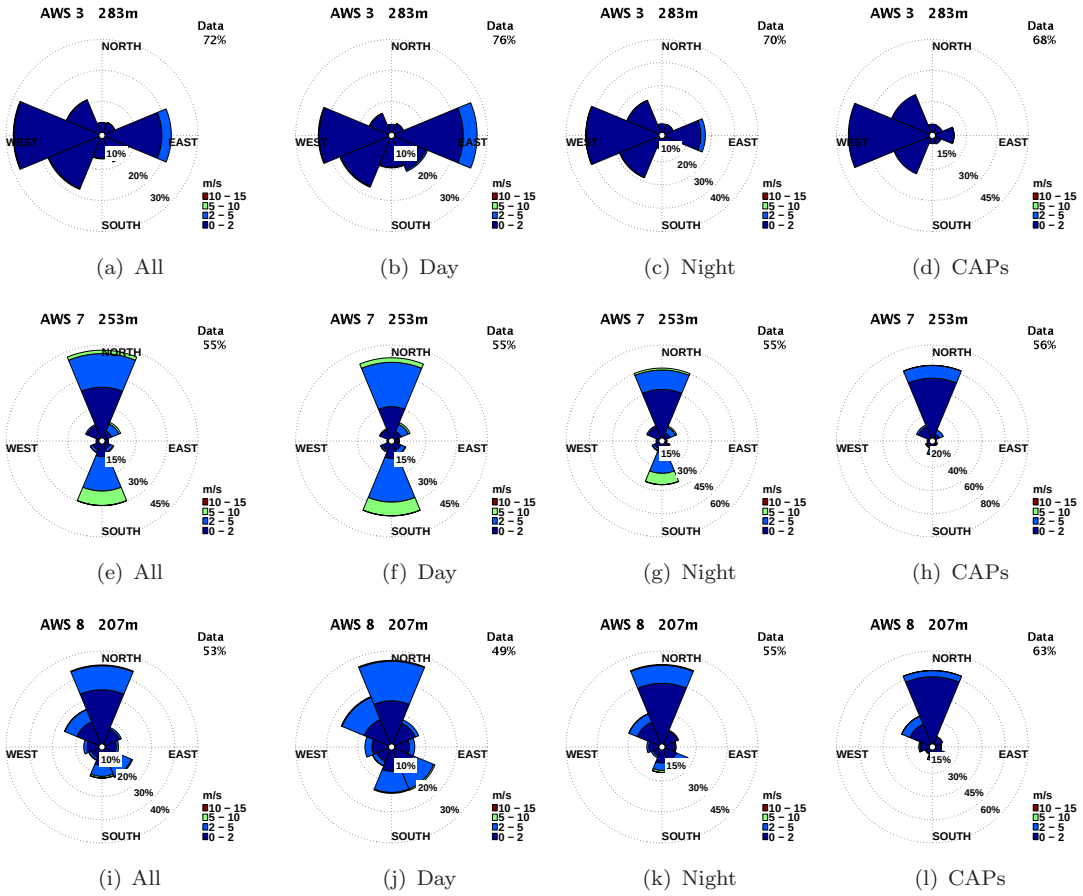

(a) All (b) Day (c) Night (d) CAPs

(e) All (f) Day (g) Night (h) CAPs

(i) All (j) Day (k) Night (l) CAPs

FIGURE 8: *As in figure 3, except all AWS in this case are located below* 300 *m ASL on the floor of tributary valleys that feed into the Clun Valley.*

Appendix C

Appendix C includes discussion on the energy budget components at the three mast sites Burfield, Duffryn and Springhill.

.8 Diurnal cycle of energy components

Time series showing components of the energy budget at Burfield, Duffryn and Springhill are given in figure 9(a), (b) and (c) respectively. In each case the LW, SW and R_{net} radiation measurements are taken at 2 m AGL and H at 10 m AGL. Note that the sign convention used here means that H contributes a net upward sensible heat flux when positive and a net downward sensible heat flux when negative.

Both H and R_{net} start to decline soon after midday at all sites as the contribution of SW declines with time, but both values are initially smaller at Burfield compared to Duffryn and Springhill. H begins to approach 0 by 16:00 UTC at Springhill and Burfield, with negative values (downward flux) seen by 17:00 UTC. In comparison H approaches 0 later at Duffryn ($\sim$17:00 UTC). By sunset H is negative at all three sites and is smallest at Duffryn and largest at Burfield.

From 20:00 UTC, H remains negative (net downward flux) at Springhill and becomes more negative towards the end of the night. At Burfield H is negative and relatively small throughout the night. H is more negative between 04:00–08:00 UTC, but values are not as negative to those observed at Springhill. At Duffryn H remains mostly negative and is very small generally with larger standard deviations at times compared to both Burfield and Springhill. At times H at Duffryn approaches zero but remains negative (net downward flux). At sunrise there is a peak negative value in H at Duffryn; however, this

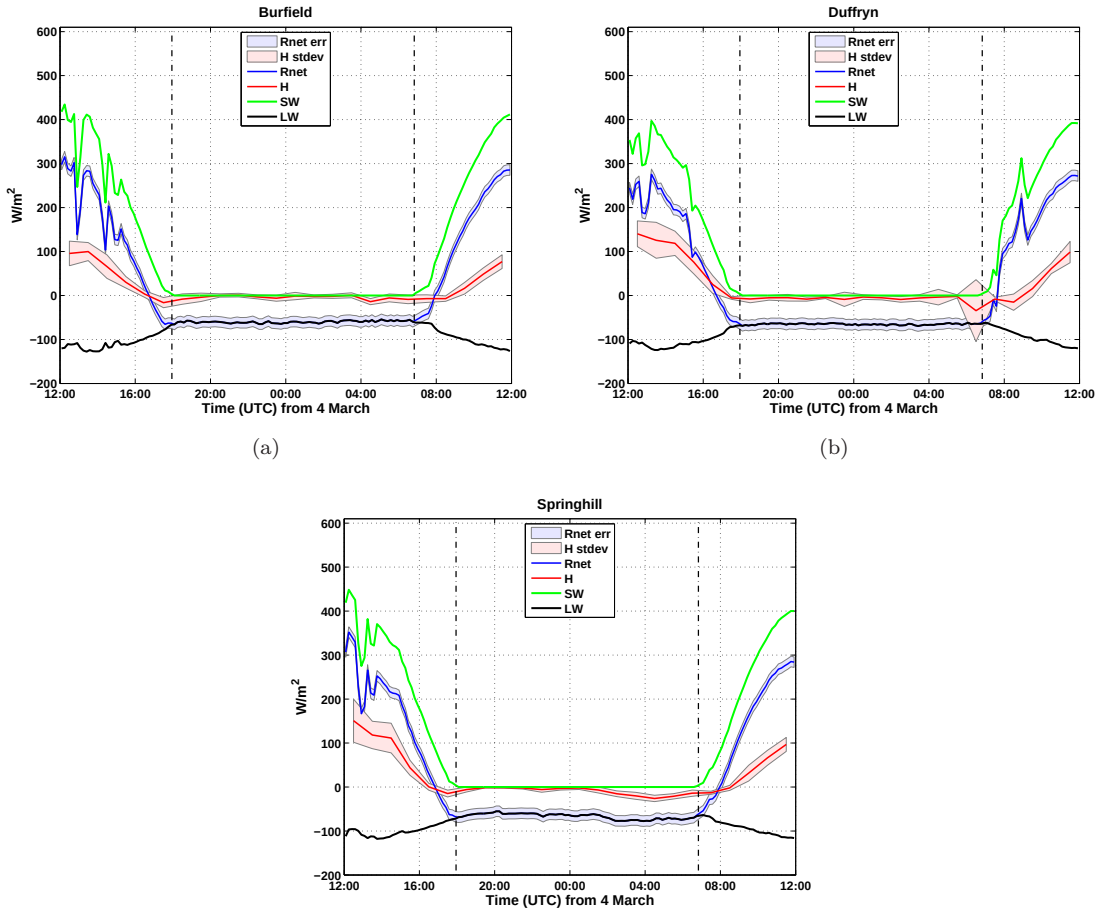

FIGURE 9: *Components of the energy budget at Burfield, Duffryn and Springhill. In each case the LW, SW and R_{net} radiative components are measured at 2 m and H measured at 10 m AGL. The R_{net} error is the expected measurement error from all components of the LW and SW instruments combined and is expected to be no more than ±12 W/m^2. The standard deviation of H is from 1hr mean data.*

is accompanied by a large standard deviation of the hourly mean data, a pattern not seen at the other sites.

During the night R_{net} appears to become more negative with time at Springhill, but almost no change is seen at the other two mast sites. The error of R_{net} is relatively large in comparison to the small changes in LW that occur throughout the night. The relative importance of this error is highlighted by the plots in figure 10, which provide a summary of the contribution of R_{net} to the overall cooling of the layer between 2–50 m AGL at Duffryn. Figure 10(a) shows time series of LW_{2m}, LW_{50m} and $LW_{50m} - LW_{2m}$, from sunset to sunrise. The errors shown are the combined radiometer measurement errors (see methods section 3.1.3 for radiometer errors and data quality issues).

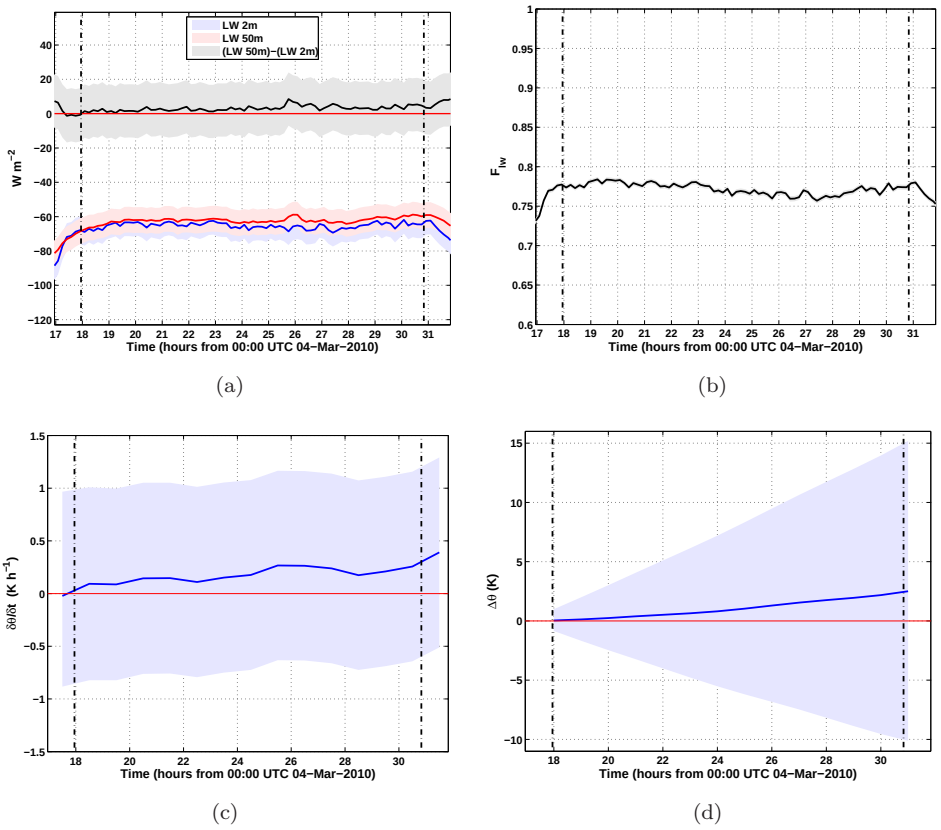

FIGURE 10: *Summary of LW radiative flux measurements at Duffryn showing time series of: net LW at 2 m, 50 m and $LW_{50m} - LW_{2m}$ (a), F_{lw} (b), 1hr mean $\delta\theta/\delta t$ due the radiative flux divergence (c) and cumulative change ($\Delta\theta$) in $\delta\theta/\delta t$ due to the radiative flux divergence (d). Shaded regions denote the error based on the maximum measurement error of the radiometers.*

The time series in figure 10(a) shows that the difference between LW_{2m} and LW_{50m} is relatively small with respect to the error. Thoughout the night there is a larger upward flux of LW_{2m} compared to LW_{50m}, which suggests a net convergence (warming) of LW between the two layers; however, it is clear that the combined measurement error is larger than this difference. The results suggest that the radiative flux divergence (see background section 2.13), contributes a net warming of between 0–0.3 K/hr (measurement error ± 1, figure 10(c)). By sunrise the radiative flux divergence contributes to a net warming contribution of $\sim$2.5 K. Considering the total combined measurement error of LW is ± 12.5, it is clear that the size of this error is significant and can potentially lead to large uncertainties when looking at the net contribution of LW to the overall cooling (or warming) of a layer (as illustrated in figure 10). What is clear is that F_{lw} changes very little during the night, remaining between 0.75–0.8, with a minimum of $\sim$0.76 occurring around 0:30 UTC (figure 10(b)).

.9 Duffryn sensible heat flux divergence during the evening transition

The characteristics of a CBL existing between 15:35–16:35 UTC, have been identified in terms of wind, θ and TKE in figure 13 previously. Furthermore, during the following 3hrs the characteristic associated with a CBL are replaced by those of a SBL (or NBL) profile. At all three mast sites, H at 10 m is positive (transfer of heat away from the surface) between 12:00–16:00 UTC (figure 9). Sometime between 16:00 UTC and sunset at 17:57 UTC, H becomes negative at all sites, resulting in a net transfer of heat towards the surface. The change in sign of H roughly coincides with the change in sign of R_{net} also, from positive to negative, as the supply of SW is cut-off during sunset. This results in a net radiative flux away from the surface (see figure 10). After sunset H remains small and negative, and R_{net} negative, for the remainder of the night at all mast sites (between ~60–80 W/m^2).

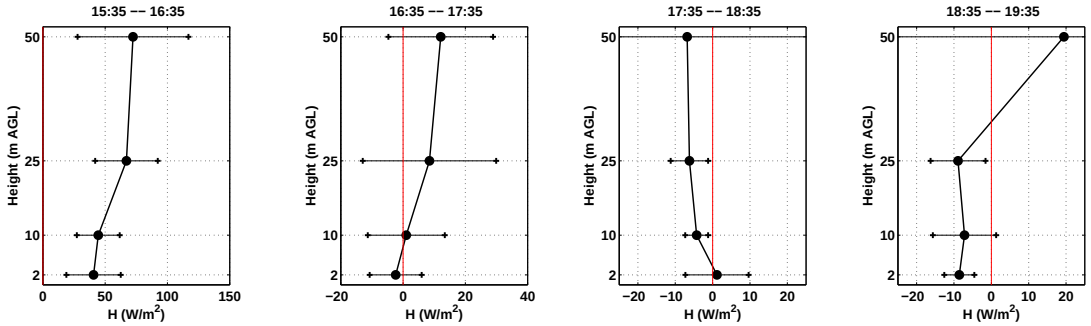

FIGURE 11: *Duffryn vertical profiles of mean 1hr sensible heat flux (H) for time intervals: 15:35–16:35 (a), 16:35–17:35 (b), 17:35–18:35 (c) and 18:35–19:35 (d). Error bars are the standard deviation of the 1hr mean.*

The profiles in figure 11 give further insight into the BL evolution in terms of the vertical evolution of H measured at Duffryn during the initial stages of CAP formation. H is measured at 2, 10, 25 and 50 m AGL, using an averaging period of 10 minutes. Profiles are shown for 1hr mean flux intervals; 2hrs before sunset (15:35–16:35) figure 11(a), 1hr before sunset (16:35–17:35) (b), during sunset (17:35–18:35) (c) and 1hr after sunset (18:35–19:35) (d).

The H profile between 15:35–16:35 UTC (figure 11(a)) shows that heat is being transferred away from the surface at all heights (positive). H decreases with time from 2hrs before sunset (figure 11(a)) to sunset (figure 11(c)) at all levels. However, the profile before sunset (figure 11(b)) suggests a divergence in H, therefore the vertical transport of heat provides a net cooling contribution at this time. The reverse is seen 1hr later in the mean profile covering sunset (between 17:35–18:35 UTC), with a net convergence in H seen between all heights. This suggests a net warming contribution by the vertical transport of heat at this time. Since this is a period of rapid cooling, the cooling contributions are likely to be from a net divergence of R_{net} and horizontal advection of colder air, through cold drainage flows.

The sign of H changes becoming negative between 2–25 m, 1hr after sunset (figure 11(d)), which suggests a transfer of heat downwards towards the surface. Between 18:35–19:35 UTC (figure 11(d)), the profile of H suggests that more heat is being transferred towards the surface at 2 m than is being transferred down from 10 m, therefore there is a net divergence in H between 2–10 m for this 1hr period. This would result in a net cooling contribution to the layer between 2–10 m, due to a divergence of H over this period. At the same time the reverse is seen between 10–25 m and an extremely large divergence (cooling) contribution is seen between 25–50 m. However, the standard deviation of the 1hr mean H at times is noticeably large, especially at 50 m, during and following sunset (figures 11(c) and (d) respectively). In fact the standard deviation of H is rarely small relative to the size of the negative values seen, which suggests that H is highly variable over the 1hr mean intervals. Therefore some perspective needs to be taken when viewing these results.

.10 Summary

It has been shown that the mean quantities of the sensible heat flux (H) at Duffryn, generally reduce with time following sunset. H changes sign, from a net upward flux to a net downward flux, some time between 16:35–18:35 UTC (figure 11). H appears to change sign at the lowest levels. However, it is clear that there is much variation in H within the hourly mean samples across the entire Duffryn mast profile. Specifically there appear to be large standard deviations at 50 m for the mean periods around and just after sunset

(figures 11(c) and (d) respectively). The values of H appear similar and have less variation at 2, 10 and 25 m AGL generally, remaining between -10 and 0 during the two evening profiles (11(c) and (d)). Ignoring results at 50 m, the results suggest that the gradient in H provides a net cooling contribution before sunset during the mean intervals of 15:35–16:35 UTC (figure 11(a)) and 16:35–17:35 UTC (figure 11(b)) and a net warming contribution during the period covering sunset from 17:35–18:35 UTC (figure 11(c)).

Following sunset, between 18:35–19:35 UTC (figure 11(d)), the gradient in H provides a net cooling contribution between 2–10 m and a net warming term between 10–25 m. High resolution model simulations of IOP 16 over this period (18:00–19:00 UTC) by Vosper *et al.* (2013b), using volume averaged quantities of valley floor locations, show that H provides a very small cooling contribution to the 10–25 m layer at valley floor locations. Furthermore, the 10–25 m layer is associated with the main component of the Duffryn drainage flow, which may provide a net cooling contribution at this time also, i.e., cooling via advection.

The relative consistency of the H at 2, 10 and 25 m, suggest that the signal is reliable for some interpretation and/or as a means to compare against other observations or modelling experiments. However, given the size of the error, it seems unreasonable to draw definitive conclusions with regards to the amount of net cooling (warming) contribution due to the divergence (convergence) of H across these data. The values of H shown here for the period before and during CAP formation, at 2, 10 and 25 m, do compare relatively well to the model simulations conducted by Vosper *et al.* (2013b) (as shown), for a region that typifies the Duffryn mast site. Model simulations of this IOP conducted by Vosper *et al.* (2013b), suggest that although the values of H are small and negative (~ -5 W m^{-2}), after 17:00 UTC, and the gradient of H is large enough to provide a net cooling contribution at 2 m of approximately -2 K h^{-1}.

Additionally, the measurement error of the LW radiative fluxes is relatively small with respect to the large quantities of LW measured during the night; however, these errors become important and relatively large when investigating the radiative flux divergence of LW across the layer between 2 m and 50 m (see figure 10). This results in a large uncertainty in the overall cooling (warming) contribution of the radiative flux divergence (convergence) to the change in observed θ at Duffryn. Investigations by Hoch *et al.* (2007) show how observations of radiative fluxes can be successful and reliable in estimating the

net cooling (warming) from the divergence (convergence) in the radiative flux components of the energy budget, providing the right techniques are used.

Vosper *et al.* (2013b) also highlight the uncertainties from drawing conclusions of the energy budget components using point data sources only. The model simulations of CAP formation by Vosper *et al.* (2013b), show that the net contribution of advection and surface heat fluxes to the amount of cooling or warming, can be highly variable in time and space during CAP formation. Additionally it is very hard to measure the contribution from advection using observations, which is likely to be important for drainage flows. For these reasons, providing models are highly resolved and at least some comparison to observations are made, models are likely to be a better tool for investigating the overall dynamics of CAPs, more specifically the evolution of the energy budget.

.11 IOP 16 CAP formation

The following results focus on the formation of the CAP during the evening transition period, between 15:35–19:35 UTC (local sunset is estimated to be 17:57 UTC). The results are followed by a discussion of CAP formation.

Previously in section **??** is was shown that cooling started across the Clun Valley region roughly 2hrs before sunset. A temperature inversion formed between the hill tops and the valley bottom around sunset and a positive ELR ensued, which continued to increase with time. Values of RH and M_r at the hill top and valley bottom, begin to diverge as the inversion forms. RH becomes increasingly higher at the valley bottom and M_r decreases.

Prior to the establishment of the inversion, the wind in the valley at Duffryn is aligned to the ambient wind at Springhill, although the valley wind speed is less than the ambient wind speed. The Duffryn wind direction changes roughly 30 minutes before local sunset, with a down-valley wind direction seen. This change appears to be just before the inversion first forms. Across all three mast sites the contributions of H and R_{net} to the surface energy budget also reverse $\sim$30 minutes prior to sunset, resulting in a net upward flux of R_{net} (cooling contribution) and a net small downward flux of H (warming contribution). The contribution of H remains small for the remainder of the evening.

A more complete picture of CAP formation over the entire Clun Valley region is shown by the 2D terrain plots in figure 12. The terrain data for all subsequent 2D terrain plots shown in chapter 5 are supplied by Ordnance Survey (2007). The left plots in figure 12 show 10min averages of θ and wind across the Clun Valley region using HOBO, AWS and mast site data. Black arrows show 2 m wind, red arrows show 50 m wind at Duffryn (T1), 30 m wind at Burfield (T3) and 30 m wind at Springhill (T2). The 30 m wind at Springhill will also be referred to as the ambient or above valley wind. The wind arrows are vector averaged wind direction and wind speed (scalar). The right plots in figure 12 show the change in 1hr mean θ over the 1hr period shown ($\Delta\theta$). Figures (a) and (b) are $\sim$1 hr before sunset, (c) and (d) are for the period around sunset, (e) and (f) are for the period $\sim$1hr after sunset.

Figure 5.4(a) shows that cooling starts $\sim$2hrs prior to sunset and accelerates around $\sim$1 hr before local sunset at $\sim$17:00 UTC. Before 17:00 UTC the difference in θ across all sites is very small, < 1 K across the entire Clun Valley region at 17:05 UTC (as seen in figure 12(a)). Cooling is occurring across all sites between 16:05–17:05 UTC (figure 12(b)), but the rate of cooling varies, despite little difference in θ being apparent at this time (figure 12(a)). Many sites in the lowest regions of the valleys, such as HOBO 6 and AWS 8, are cooling faster than locations above; however, not all valley bottom sites are cooling at the same rate. At the centre of the main Clun Valley, AWS 5 and 9, are cooling at a rate slower than other valley floor sites further up-valley (Duffryn) and further down-valley (HOBO 6). For reasons not known the tributary valley site AWS 7 is also cooling at a rate that is more similar to AWS 5 and 9 compared to other valley floor locations nearby. Furthermore the hill top sites AWS 10, AWS 2 and HOBO 17, appear to be cooling faster than many other regions at lower elevations.

At this time (17:05 UTC) the valley winds are either aligned with the ambient winds at Springhill or follow the contours of the valley (figure 12(a)). The ambient wind at Springhill (T2 30 m AGL) is from the NW and is ~ 4 m s^{-1}. The valley winds at Duffryn, AWS 5 and 9, are aligned to the ambient wind at Springhill; however, at the three tributary valley sites AWS 3, 7 and 8, the wind direction is aligned to the valley axis, orientated up-valley at AWS 3 and down-valley at AWS 7 and 8. The valley winds are also lighter than those seen at higher elevations close to the hill tops, such as AWS 2, although the

50 m wind at Duffryn is an exception to this and is similar in magnitude and direction to the ambient wind at Springhill.

By 18:05 UTC – soon after local sunset (17:57 UTC) – the lowest elevated site within the Clun Valley, HOBO 6, is clearly the coldest site (figure 12(c)). From 17:05–18:05 UTC, HOBO 6 experiences the most cooling out of all sites across the region, between 4–6 K (figure 12(d)). Other regions along the valley floor, within both the Burfield and Clun Valleys, are clearly cooler than many regions above; however, the highest elevated site AWS 10 (469 m ASL) is cooler than many sites at lower elevations near hill tops, such as HOBO 1 (391 m ASL) and HOBO 16 (362 m ASL). Therefore, with respect to all 2 m θ measurements, θ does not increase linearly with height during this period. AWS 9 (199 m ASL) is also warmer in comparison to other regions both up and down-valley and has cooled at a slower rate, therefore at this point in time there appears to be a warm temperature gradient towards the Clun Valley centre at AWS 9.

There are noticeable changes in the 2 m valley winds from 17:05 to 18:05 UTC. The Clun Valley floor locations Duffryn, AWS 5 and 9, no longer mirror the ambient wind direction at 18:05 UTC (figure 12(c)). Instead the valley winds are lighter and appear to be aligned with the valley axis in a down-valley direction. The valley wind at these locations therefore appears decoupled from the ambient wind (Springhill). However, the 50 m wind at Duffryn still mirrors the ambient wind and the magnitude has remained similar to that seen at 17:05 UTC. Therefore at this point in time the 50 m wind at Duffryn (red at T1) appears to remain coupled with the ambient wind. The 2 m wind at Duffryn is also more characteristic of those seen at other valley floor sites, rather than those seen above at 50 m. The valley wind at AWS 3, located in the small tributary valley SW from Duffryn, has also changed to a down-valley wind direction. Furthermore, the 2 m wind at Burfield and AWS 2 has also changed, reducing in speed and changing direction with respect to the ambient wind at Springhill. The wind direction at AWS 2 appears to be parallel to the local slope angle (N–S), which may be characteristic of a slope flow, caused by the sinking of negatively buoyant cold air.

One noticeable difference between the valley floor sites AWS 3, 5, 9 and Duffryn, to the tributary sites AWS 7 and 8, is that the 2 m winds are stronger in the N–S orientated tributary valleys, which are aligned with the ambient wind and down-valley. Additionally. at 18:05 UTC the wind speed at AWS 7 is higher than at 17:05 UTC and is cooling at a

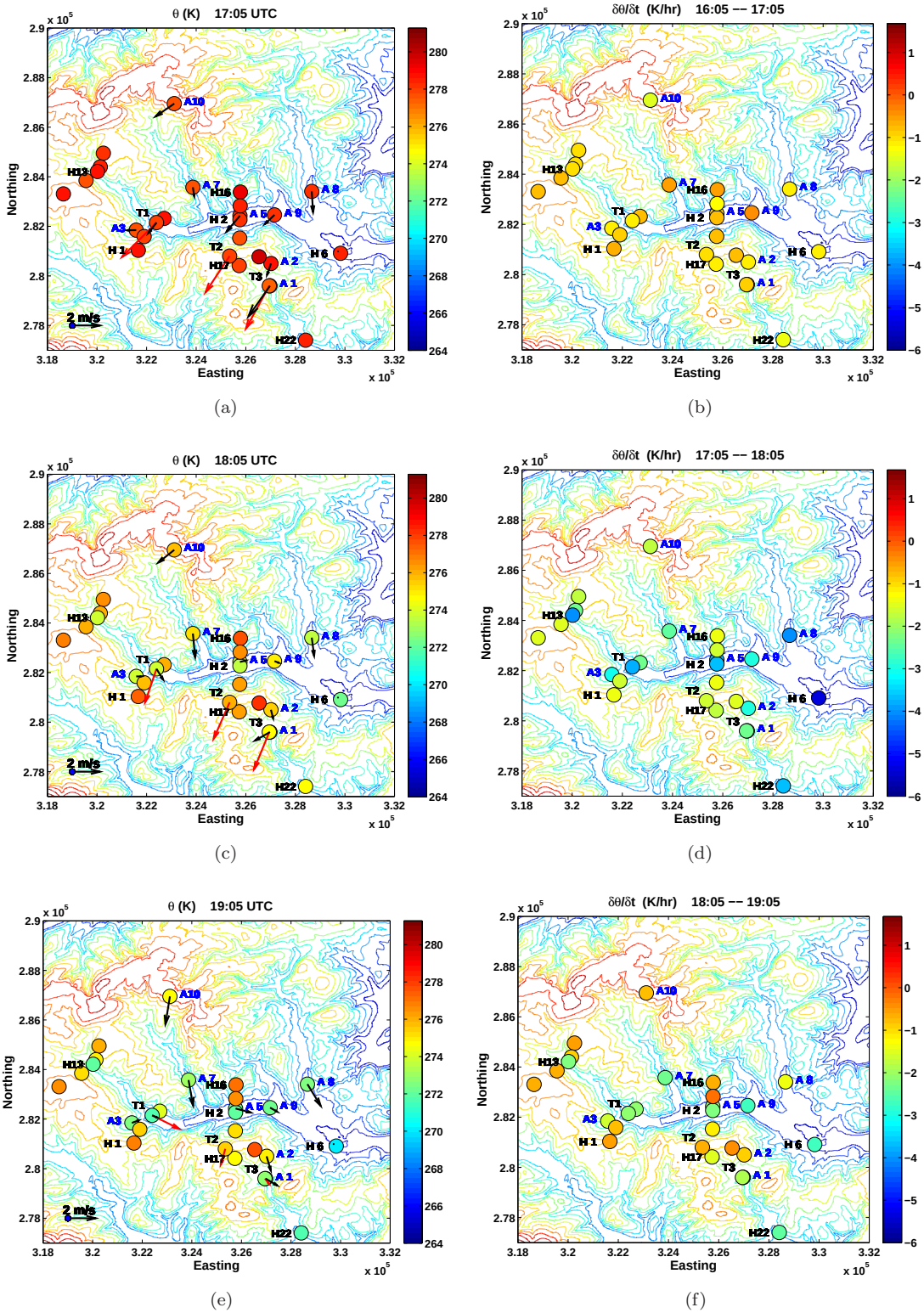

FIGURE 12: *Left figures show 2 m θ, 2 m winds (black arrows), 50 m winds at Duffryn (T1), 30 m winds at both Springhill (T2) and Burfield (T3) (red arrows). Left figures are for 10min mean periods centred at: 17:05 UTC (a), 18:05 UTC (c) and 19:05 UTC (e). Right figures are the change in 1hr mean θ (Δθ) for time intervals: 16:05–17:05 UTC (b), 17:05–18:05 UTC (d) and 18:05–19:05 UTC (f). Contours are 25 m intervals. Terrain height varies from 150 m (blue) to 525 m (red) ASL. Wind direction is calculated from vector averaged winds and the magnitude is the mean wind speed (scalar).*

slower rate than other valley floor sites including AWS 5, 8 and 9. The increase in wind speed and reduced cooling at AWS 7 appear to be related.

By 19:05 UTC the lowest elevated site HOBO 6 continues to be the coldest site (figure 12(e)). Generally θ appears to increase with height; however, AWS 10 continues to be cooler than many regions at lower elevations. Between 18:05–19:05 UTC (figure 12(f)) the cooling rate has decreased for many sites compared to 1hr previously (figure 12(d)) and the greatest cooling continues to occur at the lowest elevated site HOBO 6. There is some evidence to suggest that the cooling rate decreases with height at this time, although there are some noticeable exceptions to this, such as AWS 8, which is cooling at a much slower rate compared to other valley floor sites at this time.

The ambient wind at Springhill has decreased significantly by 19:05 UTC (figure 12(e)) although the wind direction remains similar to that seen at 18:05 UTC (figure 12(c)). The 30 m wind at Burfield has also decreased and the wind direction no longer mirrors the ambient wind direction at Springhill and is instead similar to the 2 m wind at Burfield in both speed and direction, being roughly orientated down-valley. At Duffryn the 50 m winds are the highest seen across the region, with the possible exception of AWS 10. The Duffryn 50 m wind is no longer aligned with the ambient wind, instead the 50 m wind is aligned with the corresponding 2 m wind in a down-valley direction (NW). The valley winds at AWS 5 and 9 continue to be orientated roughly down-valley, but have increased in speed since 18:05 UTC, although remain less than 2 m s^{-1}. Meanwhile the valley wind speeds at the tributary valley sites, AWS 7 and 8, remain higher than those at other valley floor locations.

As noted previously, the evolution of the 2 m and 50 m winds at Duffryn are different during CAP formation. The development of a down-valley wind is clearly seen at 2 m by 18:05 UTC (figure 12(c)) and at 50 m by 19:05 UTC (figure 12(e)). The vertical evolution of the CAP at Duffryn (2–50 m AGL) is shown in figure 13 using 1hr mean profiles of θ (a), wind speed (b), wind direction (c), persistence of the wind (d) and the turbulent kinetic energy (TKE) (e), at four time intervals during the evening transition. Before sunset, between 15:35–16:35 UTC (black), θ is highest at 2 m and changes little with height up to 50 m. The wind direction mirrors the ambient wind , being from the NW across the entire 2–50 m profile (figure 13(c)). The wind direction is also very persistent (figure 13(d)) and there appears to be a logarithmic increase in wind speeds with height (figure 13(b)).

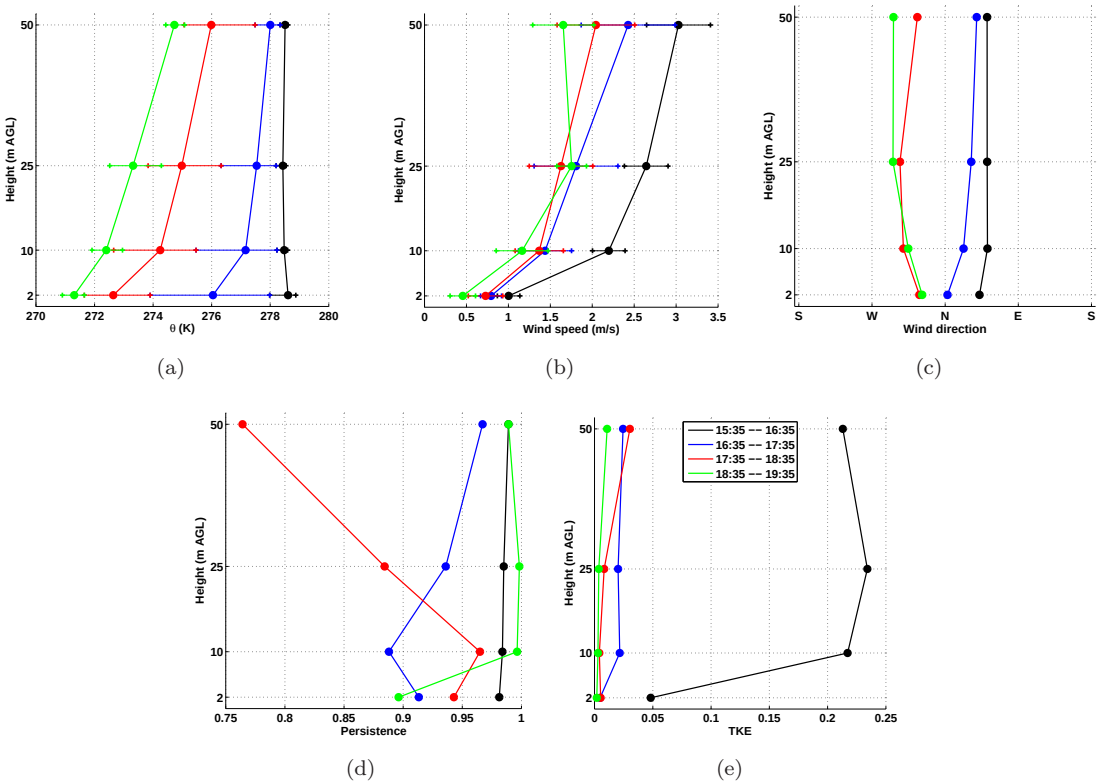

FIGURE 13: *Duffryn vertical profiles of 1hr mean θ (a), wind speed (b), wind direction (c), wind direction persistence (d) and TKE (e). Profiles are shown for 1hr intervals: 15:35–16:35 UTC (black), 16:35–17:35 UTC (blue), 17:35–18:35 UTC (red) and 18:35–19:35 UTC (green). Error bars in (a) are θ minimum and maximum and in (b) are the standard deviation of the 1hr mean.*

All these characteristics are consistent with a daytime CBL profile, where turbulence is primarily driven by buoyant thermals generated by heating of near surface air.

At ∼1hr prior to sunset, between 15:35–16:35 UTC (green), some of the characteristics associated with a CBL profile are no longer seen. The amount of TKE is reduced across the entire mean profile compared to 1hr previous (black in figure 13(e)) and a 2 K θ inversion has formed between 2–50 m. The strongest θ gradient is at the lowest region between 2–10 m and the gradient decreases rapidly with height.

The wind speed has decreased at all levels, but most notably between 10–50 m. The typical CBL logarithmic wind speed profile seen in the 15:35–16:35 UTC mean profile (black in figure 13(b)) is not seen 1hr later in the 16:35–17:35 UTC mean profile (blue in figure 13(b)). There is a small change in wind direction at all levels, but the change decreases with increasing height. The persistence of the wind direction is also less at all levels, but

is least persistent at 2 and 10 m, where the wind speeds are lower and both the wind direction and θ have changed most.

Cooling has continued at all heights with a θ gradient maintained by the 17:35–18:35 UTC profile (red). Wind speed has continued to decrease at all levels, but is most noticeable at 25 and 50 m. The wind direction has changed across the entire profile and no longer mirrors the ambient wind at Springhill. Instead the wind direction is orientated roughly down-valley from the NNW at 2 and 50 m, but from the NW at 10 and 25 m. The persistence of the wind direction decreases significantly with height, being least persistent at 50 m. The TKE also increases with height peaking at 50 m, but continues to decrease with time at all heights.

Cooling continues during the early evening (green in figure 13(b)), with most cooling observed between 10–25 m. The wind speed profile no longer increases with height across the entire profile, instead the peak wind speed is seen at 25 m, decreasing above and below. The wind direction profile is similar to that seen 1hr previous (red). The winds at 25 m and 50 m continue to be orientated roughly down-valley, but have a more westerly component being from the WNW. The change in the persistence profile appears to be most dramatic. Between 10–50 m the wind direction is extremely persistent and is clearly least persistent at 2 m, where the wind speed is lowest and the most cooling is observed. The amount of TKE at this time (green in figure 13(e)) is the least observed, showing that the amount of turbulence has decreased with time during the evening transition.